

REPORT DOCUMENTATION PAGE

Public reporting burden for this collection of information is estimated to average 1 hour per response, including the time for reviewing information, searching existing data sources, gathering the data needed, and completing and reviewing this collection of information. Send comments regarding this burden estimate or any other aspect of this collection of information, including suggestions for reducing this burden, to Washington Headquarters Services, Directorate for Information Operations and Reports (0704-0188), Washington, DC 20540-6001. Respondents should be aware that notwithstanding any other provision of law, no person shall be subject to a penalty for failing to provide information unless it is specifically required by law. **PLEASE DO NOT RETURN YOUR FORM TO THE ABOVE ADDRESS.**

AFRL-SR-BL-TR-02-

the
ing
-
antly

0293

1. REPORT DATE (DD-MM-YYYY) 14-02-2002		2. REPORT TYPE Final		3. DATES COVERED (from - to) 15-11-1998-11-11-2001	
4. TITLE AND SUBTITLE Combined Asymptotics and Numerical Methods in Transonic Store Interactions				5a. CONTRACT NUMBER F49620-99-C-0005	
				5b. GRANT NUMBER	
				5c. PROGRAM ELEMENT NUMBER	
6. AUTHOR(S) N. Malmuth, V. Shalaev and A. Fedorov				5d. PROJECT NUMBER 2304/BV	
				5e. TASK NUMBER	
				5f. WORK UNIT NUMBER	
7. PERFORMING ORGANIZATION NAME(S) AND ADDRESS(ES) Rockwell Scientific Company LLC 1049 Camino Dos Rios Thousand Oaks, California				8. PERFORMING ORGANIZATION REPORT NUMBER 71153.FTR	
9. SPONSORING / MONITORING AGENCY NAME(S) AND ADDRESS(ES) Air Force Office of Scientific Research 801 N. Randolph Street Room 832 Arlington, VA 22203-1977				10. SPONSOR/MONITOR'S ACRONYM(S) AFOSR/NM	
12. DISTRIBUTION / AVAILABILITY STATEMENT unlimited				11. SPONSOR/MONITOR'S REPORT	
13. SUPPLEMENTARY NOTES				<p>DISTRIBUTION STATEMENT A Approved for Public Release Distribution Unlimited</p> <p>20020315 042</p> <p>AIR FORCE OFFICE OF SCIENTIFIC RESEARCH (AFOSR) NOTICE OF TRANSMITTAL DTIC: THIS TECHNICAL REPORT HAS BEEN REVIEWED AND IS APPROVED FOR PUBLIC RELEASE LAW AER 120-12. DISTRIBUTION IS UNLIMITED.</p>	
14. ABSTRACT Combined asymptotic and numerics procedures were coupled with dynamics equations to simulate two and three-degree of freedom store separation from cavities. New solutions were obtained that provide insight into how the shear layer can interact with the body motion and cause re-contact and ricochet with the parent body. The theoretical models simulated these phenomena by adjustment of initial launch conditions such as initial plunge and pitch velocities among other lumped groups. Details of the structure of the near and far fields of the separating store were obtained by a combination of asymptotic analysis and function theory. Trajectory bifurcation producing a quick transition from one pitch trajectory to another was correlated with shear layer interactions and our experiments. This also produced a jump in the phase of oscillatory pitch. Transonic flows were considered and the significance of wave drag to the trajectory history was assessed within the nonlinear framework of Karman-Gudererly transonic small disturbance theory.					
15. SUBJECT TERMS store separation, stage separation, subsonic flow, transonic flow, weapons bays, cavity flows, shear layers					
16. SECURITY CLASSIFICATION OF:			17. LIMITATION OF ABSTRACT	18. NUMBER OF PAGES	19a. NAME OF RESPONSIBLE PERSON
a. REPORT UNCLASSIFIED	b. ABSTRACT UNCLASSIFIED	c. THIS PAGE UNCLASSIFIED	none	181	Dr. Norman D. Malmuth (805)-373-4154

Combined Asymptotics and Numerical Methods In Transonic Store Interactions

Final Technical Report

Contract No. F49620-99-0005

15 Nov 98 - 11 Nov 01

Prepared for:

Air Force Office of Scientific Research
AFOSR/NM
Directorate of Mathematical and Information Sciences
Bldg 410
Bolling AFB, DC 20332-6448
ATTN: Dr. Arje Nachman

Prepared by:

N.D. Malmuth, V. Shalaev, and A. Fedorov
Rockwell Scientific
1049 Camino Dos Rios
Thousand Oaks CA 91360

February 2002

 **ROCKWELL
SCIENTIFIC**

Copy #

9

Overview

Combined Asymptotic and Numerical Methods in Transonic Store Interactions

AFOSR Contract No. F49620-99-0005

Dr. Norman Malmuth, Principal Investigator
Rockwell Scientific Company, Thousand Oaks, California

Phone: (805) 373-4154

Fax: (805) 373-4775

E-mail: nmalmuth@rwsc.com

Co-Investigators/Subcontractors

Vladimir Shalaev and Alexander Fedorov
Moscow Institute of Physics and Technology
Moscow, Russia

Foreword

This overview describes the objectives, work carried out and results obtained in this project in accord with the final reporting requirements. A more detailed section entitled "Details of Analytical Studies" follows which describes the analytical approaches, results and parametric studies of our rapid turn-around models of store separation. Preprints and reprints of selected papers constitute the final section to provide a self-contained description of our effort under the contract.

Objectives

Perform research to study store interaction with cavity bay shear layers relevant to separation and delivery with emphasis on

- application of asymptotic and numerical methods to description of store release
- study of vorticity interactions in cavity shear layers
- coupling of dynamics and fluid dynamics store release aspects

The foregoing objectives are in response to AEDC, Wright Labs (ARCTIC), and Eglin who have stressed the importance of *internal* store separation from weapons bays because of the possibilities of interaction of their highly active shear layers with the store motion. AEDC stressed a unit problem approach in which the details of the interaction of the cavity flow should be understood rather than concentration on the complete vehicle. In response to Air Force needs, we have focused on store separation from a rectangular cavity. This provides an excellent launching pad for our future studies in stage separation for access-to-space and other flight vehicles. The former subject has a high priority in the

SLI program under which second and third generation reusable launch vehicles are being developed.

Status and Accomplishments

In 1999, we revised our previous modeling of two-degree-of freedom (2-DOF) store trajectories discussed in [1,2]* using substantial further developments of modeling provided in [3,4] and emphasizing coupling with store rigid body dynamics and stability. Details of this study are presented in [5] (a preprint of which is in the last section of this report). We analyzed the dynamic equations for different phases of the separation process using small perturbation theory. This allowed us to simplify the trajectory equations and integrate them in explicit analytical forms for different typical cases associated with body motion inside and outside the cavity. In addition, the eigenvalue structure provides insight into the important parameters for stability in the store-cavity context.

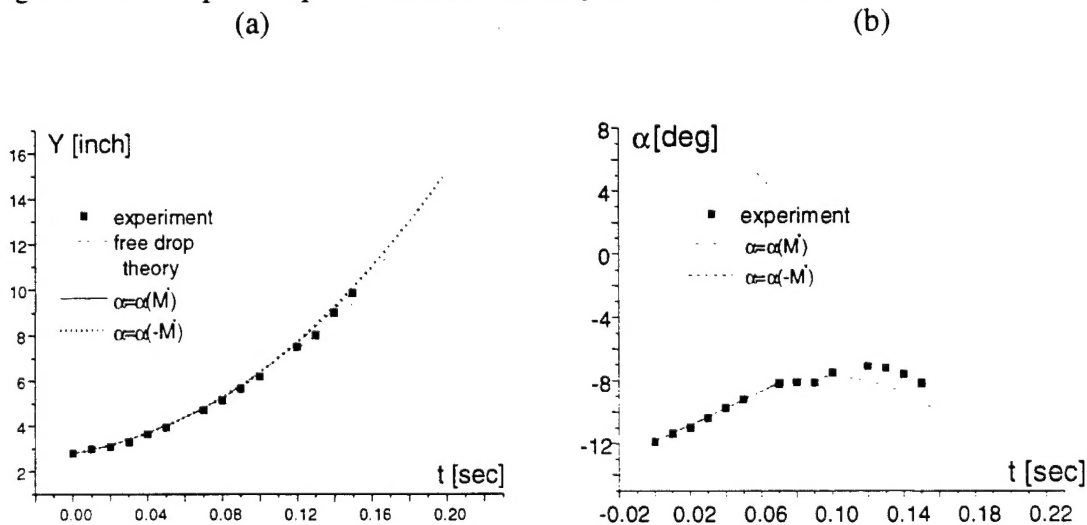


Fig.1 Bifurcation phenomenon of the pitch angle for separation from subsonic rectangular cavity; a) – CG trajectory, b) – pitch angle; Model B4N2, $U_{\infty} = 62.1$ m/s, $Y_0 = 2.8$ inch, $\alpha_0 = -11.9^\circ$, $V_0 = 15$ inch/s, $\omega_0 = 52.86$ deg/s.

Furthermore, the analytical solutions provide explicit dependencies of the body trajectory on the flow and body characteristics. These dependencies help in extracting lumped parameters and gaining insight into the physics of the separation process. They are consistent with the tests we carried out in the IIT subsonic wind tunnel. Our comparisons with IIT data are shown in Fig. 1. For a major portion of the data, the calculations are in good agreement with experiment. Moreover, the theory is able to capture nuances of the body pitching observed experimentally. These results confirm our theoretical model. However, in some cases the body separation is affected by more complex flow phenomena that are not captured by our model. The discrepancy seems to be due to the slip surface displacement induced by the shear-layer instability and/or self-excited oscillations of the

* In this section, reference, equation and figure numbers are local to it.

cavity flow. These effects can lead to a pitching moment phase jump from 0 to 180 degrees when the body crosses the shear layer. The jump may trigger quick transition from one pitch-angle trajectory to another for the body motion outside the cavity (see Fig. 1b). This interpretation is consistent with the experimental data and suggests that two substantially different pitch trajectories exist for approximately the same initial conditions. Since we are dealing with nonlinear dynamic equations, the body trajectory may have a **bifurcation point** associated with shear-layer crossing. Although this transitional phase is relatively short, its aerodynamics determines the selection between possible trajectories outside the cavity. Further theoretical and experimental studies will help to establish and clarify the bifurcation mechanism.

In 2000-2001, we emphasized external and cavity store separations into a *transonic* outer flow. New elements in the effort were:

- Extension of our previous analysis to the transonic regime
- Analysis of separation from cavities of finite span
- Modeling of the drag force components and study 3-DOF trajectory with a breakdown among friction, base, drag due to lift and wave drag

We analyzed separation of a body of revolution from a deep rectangular cavity. The separation process was subdivided into three phases: (Phase 1): the body moves inside the cavity; (Phase 2): the body crosses the shear layer, separating the cavity flow from external stream; and (Phase 3): body is totally outside the cavity. We showed that for many practical applications the relations

$$\delta = \frac{\hat{a}_0}{\hat{l}_0} \ll 1, \quad \frac{\hat{V}_r}{\delta U_\infty} = \varepsilon \leq O(1), \quad \alpha = \frac{\hat{\alpha}}{\delta} = O(1), \quad \delta^2 \text{Re} \gg 1, \quad (1a)$$

$$\frac{\hat{\delta}_s}{\hat{a}_0} \ll 1, \quad \frac{\hat{\delta}_s U_\infty}{\hat{L}_0 \hat{V}_r} \ll 1, \quad d_0 = \frac{\hat{D}_0}{\hat{a}_0} \gg 1, \quad H_0 = \frac{\hat{H}_0}{\hat{a}_0} \gg 1, \quad (1b)$$

are fulfilled.

Here \hat{l}_0 and \hat{a}_0 are body length and its maximum radius respectively; \hat{V}_r is characteristic vertical body speed; $\hat{\alpha}$ is angle of attack; U_∞ is freestream velocity; \hat{L}_0 , \hat{H}_0 and \hat{D}_0 are cavity length, height and half-width; $\hat{\delta}_s$ is shear-layer thickness. $\text{Re} = \rho_\infty U_\infty \hat{l}_0 / \mu_\infty$ is the Reynolds number.

Due to the inequalities (1a) we can describe the flow over the body using slender body theory (*cf.* [6]). According to the inequalities (1b) we can treat the shear layer as a free slip surface, neglect the flow inside the empty cavity and consider the cavity wall effect as a small perturbation. Within this framework, solutions for the flow potential were found separately in the inner and outer asymptotic regions using transonic small disturbance theory.

Apparently, the strongest interaction occurs when the body crosses the shear layer. The latter was treated as a slip surface that is schematically shown in Fig. 2. In this separation phase, the slip surface displacement is unknown *a priori*, and interacts with the solution.

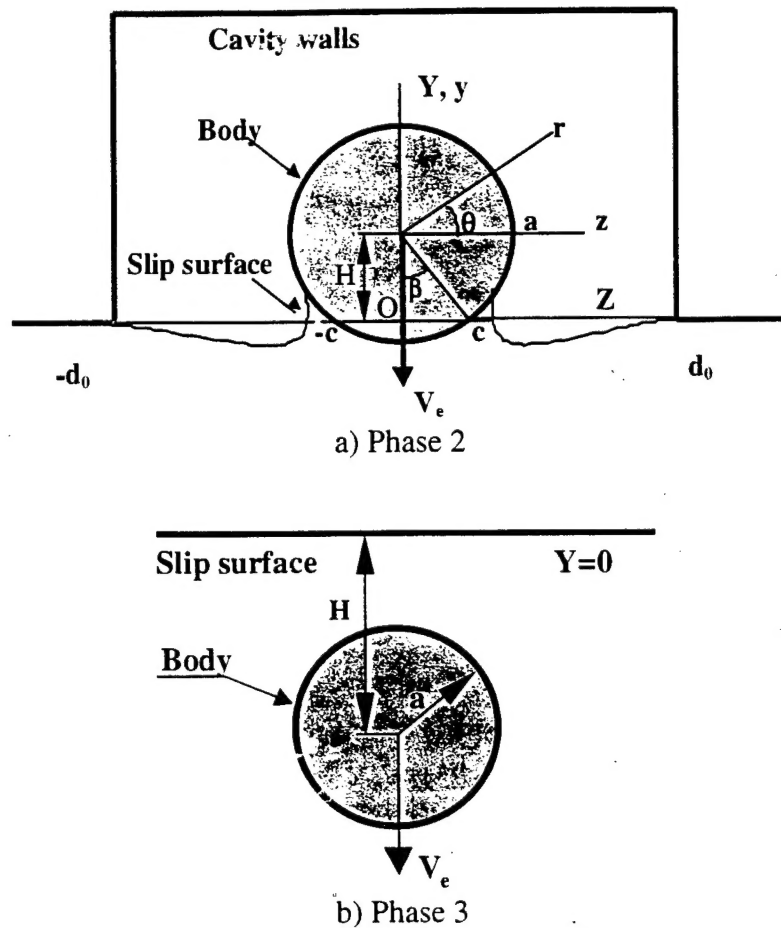


Fig. 2 Cross-sectional views of body crossing shear layer.

The scaling of variables is similar to slender body theory as detailed in [5]. In the dominant approximation, the near-field flow potentials inside the cavity and in the stream (Φ and Φ^+ respectively) are solutions of the two-dimensional Laplace equation in cross-sectional planes with the following boundary conditions:

On the body surface:

$$\begin{aligned} Y = Y_b(X, \theta, t) &= H(X, t) + a(x) \sin \theta, \quad H = Y_o(t) - \alpha(t)X, \\ Y > Y_f: \quad v_n^+ &= V_e^+ \sin \theta; \quad V_e^+(X, t) = V_o(t) - \omega(t)X, \end{aligned} \quad (2a)$$

$$Y < Y_f : v_n = a_x + V_e \sin \theta, V_e(X, t) = \varepsilon V_e^-(X, t) - \alpha(t). \quad (2b)$$

On the slip surface:

$$Y_f = \mu F(X, Z, t), \\ \varepsilon v_f^+ = \mu(F_t + \varepsilon w_f^+ F_z), \quad v_f = \mu(F_t + F_x + w_f F_z), \quad p_f = p_f^-. \quad (3)$$

Pressures below and above the slip surface, p and p^+ respectively, are determined from the unsteady Bernoulli equation, *i.e.*

$$p = \frac{\hat{p} - p_\infty}{\delta^2 \rho_\infty U_\infty^2} = -\left[\Phi_t + u + \frac{1}{2}(w^2 + v^2)\right], \quad p^+ = \frac{\hat{p}^+ - p_\infty}{\delta^2 \rho_\infty U_\infty^2} = -\varepsilon\left[\Phi_t^+ + \frac{\varepsilon}{2}(w^{+2} + v^{+2})\right]. \quad (4)$$

On the cavity walls, the normal component of the flow velocity vanishes.

In the most general case, when all perturbations are of the order of $O(\varepsilon)$, we obtain

$$\varepsilon \ll 1, \quad \mu = \varepsilon; \quad a_x = \varepsilon a_{1x}, \quad \alpha = \varepsilon \alpha_1, \quad V_e = \varepsilon V_{e1} = \varepsilon(V_e^+ - \alpha_1), \quad (5a)$$

$$F = F_0 + \varepsilon F_1, \quad \Phi^+ = \phi_0^+ + \varepsilon \phi_1^+ + O(\varepsilon^2), \quad \Phi = \varepsilon \phi_0 + \varepsilon^2 \phi_1 + O(\varepsilon^3), \quad (5b)$$

$$p = -\varepsilon\left\{\phi_{0t} + \phi_{0x} + \varepsilon\left[\phi_{1t} + \phi_{1x} + \frac{1}{2}(v_0^2 + w_0^2)\right]\right\} + O(\varepsilon^3), \quad (5c)$$

$$p^+ = -\varepsilon\left\{\phi_{0t}^+ + \varepsilon\left[\phi_{1t}^+ + \frac{1}{2}(v_0^{+2} + w_0^{+2})\right]\right\} + O(\varepsilon^3). \quad (5d)$$

In the first order approximation, the boundary conditions on the body surface are similar to Eqs. (2). Conditions (3) on the slip surface can be shifted to the plane $Y = 0$ and expressed as

$$Y = 0: \quad v_{0f}^+ = F_{0t}, \quad v_{0f} = F_{0t} + F_{0x}, \quad w_{0t} + w_{0x} = w_{0t}^+. \quad (6)$$

We analyzed the two unit problems shown schematically in Figures 2a and 2b. Problem 1: Body crosses the shear layer; and Problem 2: Body drops below the slip surface. To solve Problem 1 we applied the conformal mapping of the upper half-plane (cavity region) and the lower half-plane (stream region) (ζ -plane) on the flat plate exterior (σ -plane) and obtained the complex-conjugate velocities using the Keldysh-Sedov integrals

$$W_0(\sigma; X, t) = \frac{1}{\pi i \sqrt{\sigma^2 - b^2}} \frac{\partial \sigma}{\partial \zeta} \left[i \int_{-b}^b \frac{\sqrt{b^2 - s^2} v_{0n}(s) ds}{(s - \sigma)l(s)} - \int_f \frac{\sqrt{s^2 - b^2} w_{0f}(s) ds}{(s - \sigma)l(s)} \right], \quad (7a)$$

$$W_0^+(\sigma; X, t) = \frac{1}{\pi i \sqrt{\sigma^2 - b^2}} \frac{\partial \sigma}{\partial \zeta} \left[i \int_{-b^-}^{b^+} \frac{\sqrt{b^2 - s^2} v_{0n}^+(s) ds}{(s - \sigma) l(s)} + \int_f \frac{\sqrt{s^2 - b^2} w_{0f}^+(s) ds}{(s - \sigma) l(s)} \right]. \quad (7b)$$

Here b and b^- are flat plate semi-spans in the σ -plane, $l(s)$ is mapping metric; the second integrals are calculated along the slip surface located in the intervals $(-\infty, -b)$, $(-\infty, -b^-)$ and (b, ∞) , (b^+, ∞) . Using the Cauchy integral and Eqs. (6), we expressed the transverse flow velocities on the slip surface in terms of the slip-surface shape

$$w_{0f}^+ = -\frac{I_{0f}^+ - I_b^+}{\pi}, \quad w_{0f}^- = \frac{I_{0f}^- + I_b^-}{\pi}, \quad (8a)$$

$$I_{0f}^+(X, Z, t) = \int_f \frac{F_{0f}(Z') dZ'}{Z' - Z}, \quad I_{0f}^-(X, Z, t) = \int_f \frac{F_{0f}(Z') + F_{0X}(Z')}{Z' - Z} dZ', \quad (8b)$$

$$I_b(X, Z, t) = -\frac{2a(H - F)}{(H - F)^2 + Z^2} \left\{ \beta a_x - \frac{V_e \beta a(H - F)}{2[(H - F)^2 + Z^2]} + \sum_{n=1}^{\infty} \left[\frac{a(H - F)}{(H - F)^2 + Z^2} \right]^n \sum_{k=0}^{\left[\frac{n+1}{2} \right]} (-1)^k C_{n+1}^{2k} \left(\frac{Z}{H - F} \right)^{2k} \int_0^\beta w_\theta(\xi) \sin(n\xi) d\xi \right\}. \quad (8c)$$

$$I_b^+(X, Z, t) = -V_e^+(\pi - \beta) \left[\frac{a(H - F)}{(H - F)^2 + Z^2} \right]^2 + 2 \sum_{n=1}^{\infty} \left[\frac{a(H - F)}{(H - F)^2 + Z^2} \right]^{n+1} \sum_{k=0}^{\left[\frac{n+1}{2} \right]} (-1)^k C_{n+1}^{2k} \left(\frac{Z}{H - F} \right)^{2k} \int_\beta^\pi w_\theta^+(\xi) \sin(n\xi) d\xi. \quad (8d)$$

where the angle β is shown in Fig. 2a and $n = 1 - \beta/\pi$. From these relations we derived the Poisson equation for the slip-surface shape F_0

$$\frac{\partial^2 F_0}{\partial \tau^2} + \frac{\partial^2 F_0}{\partial \lambda^2} = -\frac{1}{\pi^2} \int_{-\infty}^{\infty} \frac{[I_{bl}(\lambda, s, \tau) + I_{bX}(\lambda, s, \tau)] ds}{s - Z}, \quad (9)$$

where $\tau \equiv t - X$. This equation contains interesting physics. According to slender body theory, the inner asymptotic solution is harmonic in each crossflow plane. However, the slip surface displacement does not *explicitly* depend only on the streamwise coordinate X and time t , but has an *implicit global interaction* with the solution. This may lead to new physical effects that will be studied in our research. We showed that the problem (as well as the more complicated nonlinear problem for moderate and large displacements of the slip surface) can be solved by simple iterations. This provides a good launching pad for further studies of the body-shear layer interaction. An understanding of these interactions is critical to current experiments on time-averaged shear layer undulations in acoustically controlled and uncontrolled modes and their consequences for safe store

release. Our work will complement PIV and DNS investigations of these phenomena and help establishing the proper control laws for mitigation of adverse consequences of the acoustic damping schemes such as spanwise pulsating jets.

Relevant to Eq. (9) in our first cut modeling for the body trajectory, we assumed the shear layer displacement $F_0 = 0$ and obtained analytical solutions for the near field and expressed the lift force and pitching moment in explicit forms for all three phases of the separation process. We also analyzed the far-field flow and its parametric dependencies at transonic speeds. We found that the scaling for the outer asymptotic region is expressed as

$$X = \frac{\hat{X}}{\hat{l}_0}, \quad \tilde{Y} = \frac{\hat{Y}\mu_1}{\hat{l}_0}, \quad \tilde{Z} = \frac{\hat{Z}\mu_1}{\hat{l}_0}, \quad T = \frac{\hat{t}}{\hat{t}_0}, \quad r = \frac{\hat{r}\mu_1}{\hat{l}_0}, \quad \hat{\Phi} = l_0 U_\infty [X + \varepsilon_1 \varphi(X, \tilde{Y}, \tilde{Z}, t)], \quad (10)$$

where ε_1 results from matching of the outer and inner solutions, μ_1 is associated with the outer-region scale, and \hat{t}_0 is characteristic time scale. The equation for the outer flow-field potential is

$$\delta^2 [K - (\gamma + 1)\varphi_X - (\gamma - 1)S\varphi_T] \varphi_{XX} + \mu^2 (\varphi_{\tilde{Y}\tilde{Y}} + \varphi_{\tilde{Z}\tilde{Z}}) - 2S\varphi_{XT} - S^2 \varphi_{TT} = 0, \quad (11)$$

where $K \equiv \frac{1 - M^2}{\delta^2}$ and $S = \hat{l}_0 / (\hat{t}_0 U_\infty)$ is the Strouhal number. We showed that for practical ranges of S , the outer flow is quasi-steady and is governed by the steady axisymmetric form of the axisymmetric Karman-Guderley equation (in a cylindrical coordinate system)

$$[K - (\gamma + 1)\varphi_X] \varphi_{XX} + \frac{1}{r} (r\varphi_r)_r = 0, \quad (12)$$

with the asymptotic boundary condition

$$r \rightarrow 0: \varepsilon_1 r \varphi_r = \delta^2 \frac{Q_e(X, T/S)}{2\pi}. \quad (13)$$

Here the source strength Q_e is determined from matching with the near-field solution and is expressed in the compact analytical form

$$\text{For Phase 2: } Q_e(X, t) = \frac{2a^2(x) \sin \pi n}{nd} \left[4a_x e_0(n) - \pi V_e (1 + 2n^2) \frac{\sin \pi n}{6n} \right], \quad (14)$$

$$\text{For Phase 3: } Q_e(X, t) = \frac{4\pi a(a_x H - aB_{-2})}{\sqrt{H^2 + d_0^2}}. \quad (15)$$

A numerical solution of the problem (12), (13) was used to predict the transonic wave drag using our slender body transonic small disturbance code. The theoretical model in

[7] for the base drag and the empirical model [8] for the friction drag has also been incorporated in our prediction of the drag. Besides the quasi-steadiness, examination of a practical distinguished limit reveals that the outer flow is dominantly axisymmetric during early separation for which re-contact is important. Both of these properties provide a substantial simplification of the outer transonic problem to make it tractable on a PC desktop or laptop.

Our ongoing parametric studies of external and internal store separation from a rectangular cavity into a transonic flow indicate that the theoretical model captures trajectory bifurcations, re-contact and ricochet. Figure 3 shows an example of external store separation into a Mach 0.999 freestream. If the initial vertical speed is zero (red lines and symbols), the body moves up and hits the wall (re-contact). At relatively small initial vertical velocity ($V_0 = -0.5$ m/s), the separation is smooth and re-contact is avoided. This shows that *external store separation can be controlled by the release mechanism*. It also confirms our conjecture about the IIT tests that repeatability can be enhanced by close control of the release mechanism. Studies such as these can be useful in designing ejection units and thrust motors for stage separation. They not only can be useful to determine the amount of thrust and weight required for these units but they also indicate how we can effectively correct an adverse re-contact situation with a relatively small impulse.

Figure 4 shows trajectories of the center of gravity (CG) for external separation from a flat wall (left plot) and separation from cavity (right plot) into a Mach 0.999 stream. The blue lines with circles are trajectories at identical release conditions (ejection velocity $V_0 = -20$ inch/s). Comparing these trajectories we conclude that *the shear layer increases the lift, pushing the body back into the cavity (ricochet)*. It is also seen that at near-critical conditions of re-contact (external separation) and ricochet (cavity separation), the store trajectory is sensitive to the initial conditions associated with store release. This is consistent with our previous subsonic experiments at IIT. Figure 5 shows that *a variation of the initial angle of attack causes dramatic changes of the CG trajectory*.

The impact of this work will be:

- Enhanced insight into the mechanisms of store and stage interference with the parent vehicle and shear layer.
- Models that can be used to design control systems and determine control laws for safe store release and staging.
- Rapid turnaround PC desktop models for quick assessments and certification.

Future research will study more geometric realism in the simulations, investigate physics of wave interactions with shear layers and between multiple bodies and develop matching techniques for the local flow problem near the weapons bay with the complete airplane flow field.

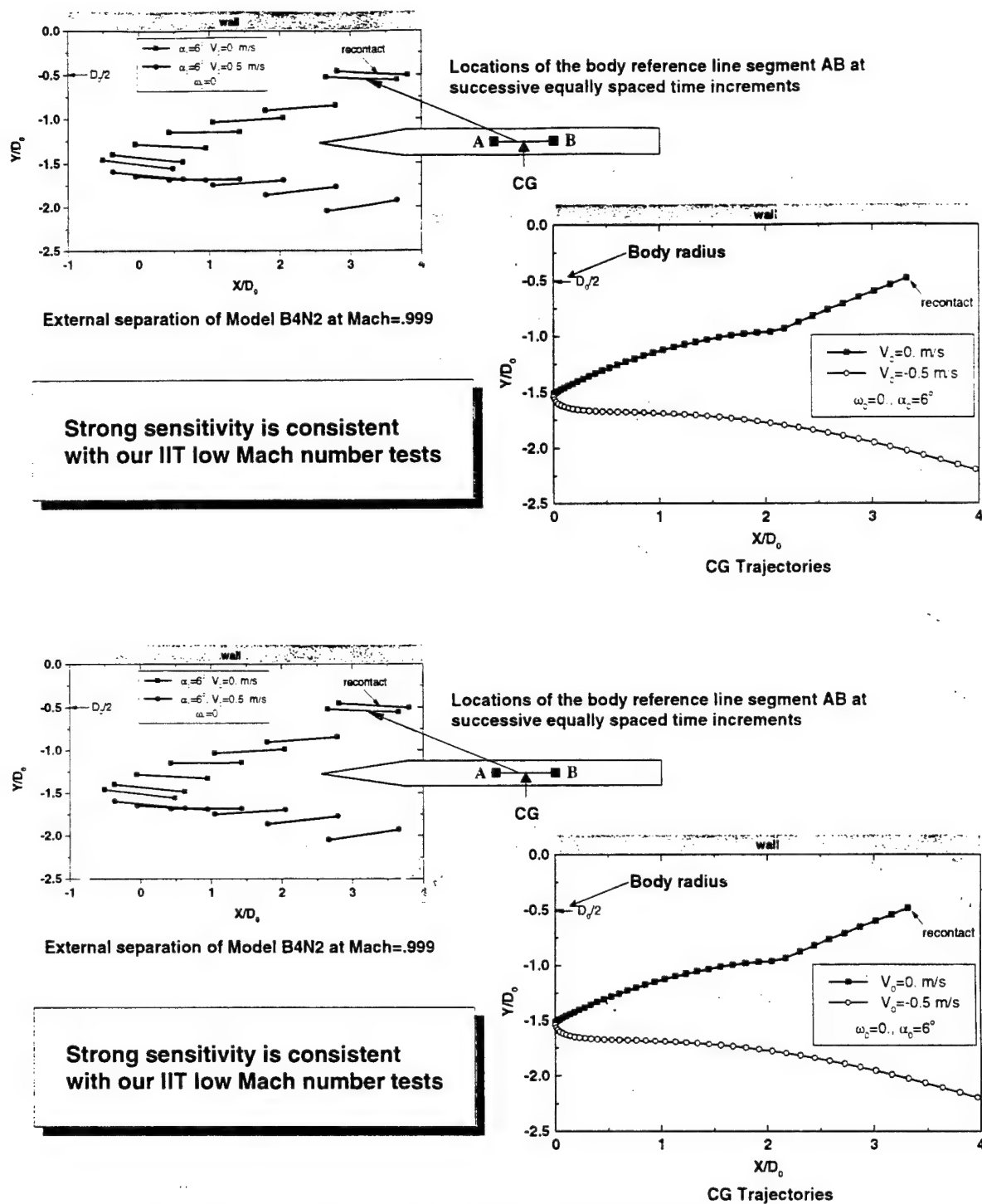
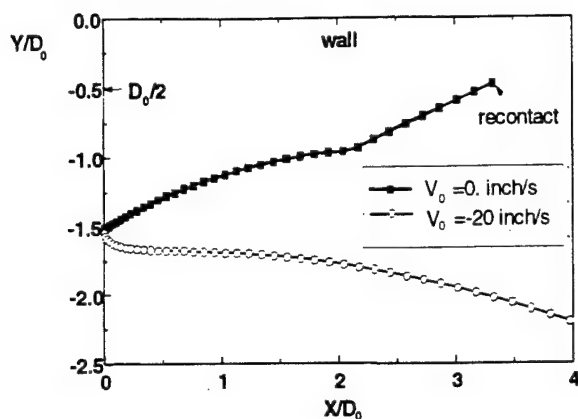
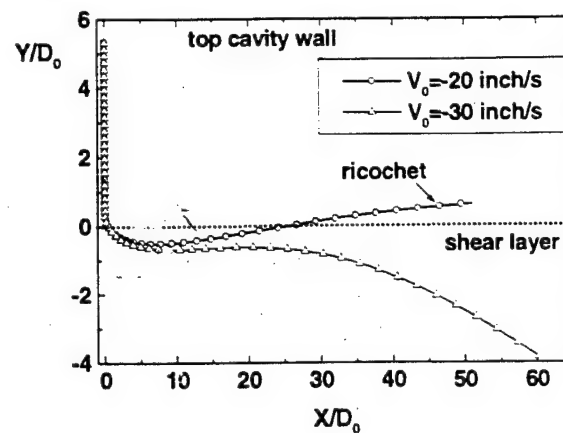


Fig. 3 External store separation into a transonic free stream.

External separation



Separation from cavity



Body of shape B4N2: $M=0.999$, $\alpha_0=6^\circ$, $\omega_0=0$

Fig. 4 CG trajectories for external (left plot) and cavity (right plot) separations; $M = 0.999$, $\omega_0 = 0$, $\alpha_0 = 6^\circ$.

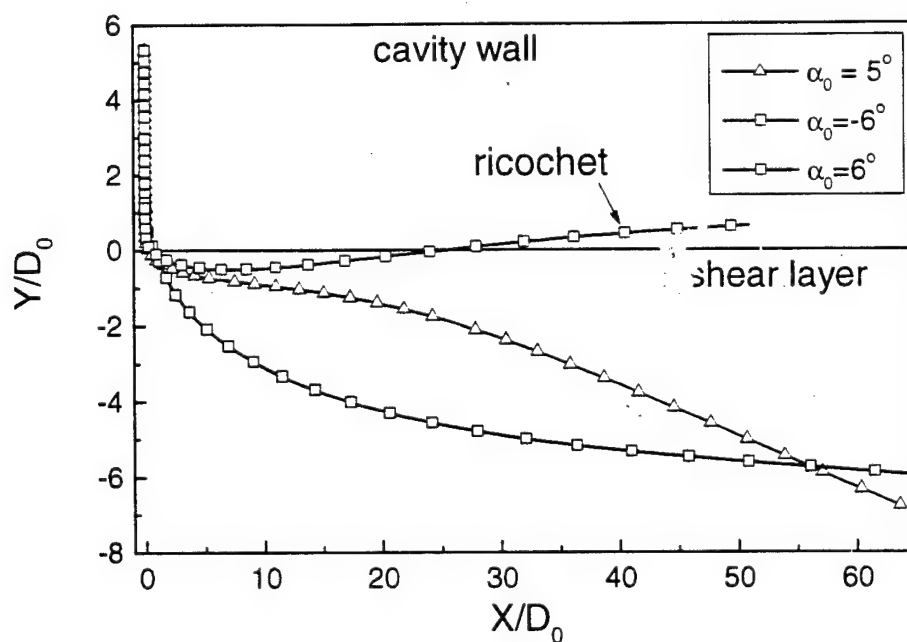


Fig. 5 CG trajectories for separation from cavity at various initial angles of attack α_0 ; $M = 0.999$, $\omega_0 = 0$, $V_0 = -20$ inch/s, body of shape B4N2.

Personnel

N. Malmuth, V.I.Shalaev, and A.V. Fedorov

References

1. Malmuth, N.D., Fedorov, A.V., Shalaev, V., Cole, J., Khokhlov, A., Hites, M., and Williams, D., "Problems in High Speed Flow Prediction Relevant to Control." AIAA Paper No. 98-2695, 2nd AIAA Theoretical Fluid Dynamics Meeting, June 15-18, 1998, Albuquerque, NM.
2. Malmuth, N., Fedorov, A., Shalaev, V., Cole, J., Hites, M., and Williams, D. "Desktop Aerodynamic Models for Store Separation from Weapons Bay Cavities and Related Vortical Processes," Vortex Flow at High Angle Attack, AVT Symposium, Paper 37, Loen, Norway, May 7-11, 2001.
3. Malmuth, N.D., Shalaev, V.I., Fedorov, A.V. "Combined Asymptotics and Numerical Methods for Store Interactions," Technical Report of Contract CF49620-96-C-0004, AFOSR/NM, October 1998 (available in Defense Technical Information Center, stient.dtic.mil).
4. Malmuth, N., Hites, M., and Williams, D., "Photographic Investigation of the Dynamics of an Ogive Model near a Cavity at Subsonic Mach Numbers." Final Report. Fluid Dynamics Research Center Illinois Institute of Technology, January 18, 1998.
5. Shalaev, V.I., Fedorov, A.V., and Malmuth, N.D., "Dynamics of Slender Bodies Separating from Rectangular Cavities." AIAA Paper No. 2001-2996, 31 AIAA Fluid Dynamics Conference and Exhibit, 11-14 June 2001, *AIAA Journal* **40** 3, March 2002, *in press*.
6. Cole, J. D. *Perturbation Methods in Applied Mathematics*. Waltham, Massachusetts, 1968.
7. Chow, W.L., "Base Pressure of a Projectile Within the Transonic Flight Regime," *AIAA J.*, **23**, No. 3, pp. 388-395, 1985.
8. Schlichting, G., *Boundary Layer Theory*, McGraw-Hill, New York, 1968.

Publications

Published

- P1. A. Fedorov and N. Malmuth, A. Rasheed and H. Hornung "Stabilization of Hypersonic Boundary Layers by Porous Coatings," *AIAA J.* **39** April 2001, pp. 605-610.
- P2. A. Rasheed, H. Hornung, A. Fedorov and N. Malmuth, "Experiments on Passive Hypersonic Boundary Layer Control Using a Porous Surface," AIAA Paper 2001-0274, January 2001.

- P3. N. Malmuth, J. Cole, A. Fedorov, V. Shalaev, M. Hites and D. Williams, "PC Desktop Aerodynamic Models for Store Separation from Weapons Bay Cavities and Related Vortical Processes," AVT-RTO Symposium, *Advanced Flow Management and High Angle of Attack Military Vehicles*, Loen, Norway, 7-10 May 2001.
- P4. Shalaev, V.I., Fedorov, A.V., and Malmuth, N.D., "Dynamics of Slender Bodies Separating from Rectangular Cavities," AIAA Paper No. 2001-2996, 31 AIAA Fluid Dynamics Conference and Exhibit, 11-14 June 2001, AIAA Journal 40 3, March 2002, in press.
- P5. V. Soloviev, A. Konchakov, V. Krivtsov, and N. Malmuth "Simulation of the Spatial Distribution of Air Ionization by an Electron Beam," AIAA 32nd Plasmadynamics and Lasers Conference and 4th Weakly Ionized Gases Workshop, AIAA paper 2001-3089, 11-14 June 2001, Anaheim, California.
- P6. V. Soloviev, V. Krivtsov, A. Konchakov and N. Malmuth, "Simulation of Supersonic Body Drag Reduction Produced By Forebody Filamentary Plasmas," AIAA 32nd Plasmadynamics and Lasers Conference and 4th Weakly Ionized Gases Workshop, AIAA paper 2001-2727, 11-14 June 2001, Anaheim, California.
- P7. N. Ardelyan, V. Bychkov, K. Kosmachevskii, S. Chuvashov and N. Malmuth, "Modeling of Plasmas in Electron Beams and Plasma Jets for Aerodynamic Applications, AIAA 32nd Plasmadynamics and Lasers Conference and 4th Weakly Ionized Gases Workshop, AIAA Paper, 2001-3101, 11-14 June 2001, Anaheim, California.
- P8. N. Malmuth, V. Fomin, A. Maslov, *et al*, "Influence of a Counterflow Plasma Jet on Supersonic Blunt Body Pressures," *AIAA Journal*, **40** 6, June, 2002, in press.

Submitted

- P9. J. Cole and N. Malmuth, "Wave Drag Due to Lift for Transonic Airplanes," *SIAM J. of Appl. Math.*

Details of Analytical Studies

Abstract

Aerodynamic and dynamic problems relevant to separation of a thin body of revolution from rectangular cavities into subsonic and transonic flows are considered. In the dominant approximation, the shear layer separating cavity flow from outer flow is approximated by a slip surface and the flow is described by slender body theory. The separation process is subdivided into three phases: body inside the cavity (Phase 1), body crosses the shear layer (Phase 2), and body outside the cavity in the outer stream (Phase 3). Herein, models for inner (near field) and outer (far field) asymptotic regions are provided for all phases of the body motion. Also, analytical and numerical solutions of the flow and trajectory equations are discussed and compared with experiments.

In Part 1, the general problem for the inner asymptotic region is formulated and analyzed. In order to capture basic features, the case of small perturbations is considered in detail. A Poisson equation is derived for the slip surface displacement induced by the body. The flow problem is reduced to two coupled linear integrodifferential equations for the complex flow velocity and the slip surface displacement. For Phase 2, the solution of this system is singular at the body and slip surface line of intersection. For finite perturbations, a system of nonlinear integrodifferential equations is derived for the inner asymptotic region. It is shown that this system can be solved using an iteration procedure.

In Part 2, the first iteration relevant to zero distortions of the slip surface is considered. Explicit solutions of the governing equations are obtained and analytical expressions for the lift force and pitching moment are derived for all phases of the separation process. It is shown that a singularity arising in Phase 2 at the body and slip surface intersection line is integrable and does not contribute to the aerodynamic forces. Therefore, the solution can be treated as a dominant approximation of the general problem and can be used for the body trajectory analysis.

In Part 3, the two-degree-of-freedom trajectory equations for the center of gravity and pitch angle are analyzed using the results of Part 2. Asymptotic solutions of these equations for Phases 1 and 3 give explicit dependencies of the trajectory on the governing parameters. The analytical results of Part 3 dramatically simplify body trajectory calculations. A robust computational code is developed for quick turn-around predictions of the center of gravity and pitch angle trajectories for all phases of separation. The code is verified by comparisons with the IIT experimental data obtained for subsonic store separations. In many cases, the calculations are in a good agreement with the data. It is shown that a unusual behavior of the pitch angle in Phase 3 is associated with the trajectory bifurcation. Parametric studies of the trajectory dependencies on the initial conditions, flow parameters and body characteristics are presented.

In Part 4, the outer limits of the inner solutions for Phases 2 and 3 are investigated including terms up to the third-order approximation. It is shown that for an infinite span cavity, the outer limit of the dominant solution corresponds to the flow induced by a dipole distribution along the body axis, while the source term arises only in the third-order approximation. A general form of the inner solution for a finite-span cavity is obtained. In this case, the far flowfield is induced by the source distribution whose intensity is proportional to the ratio of the body thickness to the cavity span. The outer asymptotic problem is formulated and analyzed. Explicit inner solutions are used to formulate matching conditions for the transonic outer region. Different regimes of outer

unsteady flows are classified. The drag force components associated with the transonic wave drag, cross-flow, friction drag and base drag are analyzed. These items are the basis for analytical results that are used to develop a computer code to solve the trajectory equations. The obtained theoretical results are used to analyze three-degree-of-freedom body dynamics for separation into subsonic and transonic freestreams. Examples of the external and cavity store separations are discussed including critical cases of recontact and ricochet.

Table of Contents

Abstract	ii
Table of Contents	iv
List of Figures.....	vii
Nomenclature.....	x
Introduction.....	xiii
Part 1. Flow Field in the Inner Asymptotic Region.....	1
1.1 Introduction.....	1
1.2 Problem formulation.....	1
1.3 Asymptotic theory for small flow perturbations.....	4
1.3.1 Body moves in the cavity or in the stream (Phases 1 and 3).....	7
1.3.2 Body crosses the slip surface (Phase 2).....	12
1.4 Analysis of the slip-surface effect for finite perturbations.....	15
1.5 Discussion and conclusions.....	21
1.6 Illustrations.....	24
Appendix A.....	29
Part 2. Analytical Solutions of the First Order Approximation.....	34
2.1 Introduction	34
2.2 Unit problems for body dropping inside and outside the cavity (Phases 1 and 3).....	35
2.2.1 Solutions obtained by the multipole expansion method.....	36
2.2.2 Lift force and pitching moment calculations.....	39
2.3 Unit problem for body crossing the slip surface (Phase2).....	42
2.3.1 Solution of the flow equations.....	42
2.3.2 Lift force and pitching moment.....	44
2.4 Cross-checking of the theory.....	51
2.5 Discussion and conclusions.....	52
2.6 Illustrations.....	54
Appendix B. Analytical evaluation of improper integrals.....	55
Appendix C. Analytical and numerical investigations of integrals.....	60

Part 3. Dynamics of Slender Bodies Separating from Rectangular Cavities.....	66
3.1 Introduction and problem formulation.....	66
3.2 Phase 1: body inside cavity.....	67
3.3 Phase 3: body outside cavity.....	70
3.3.1 Eigenvalues λ_1 and λ_2 are complex.....	72
3.3.2 Eigenvalues λ_1 and λ_2 are real.....	73
3.4 Results and discussion.....	74
3.4.1 Experimental data.....	74
3.4.2 Comparison with experiment.....	75
3.4.3 Parametric studies.....	76
3.5 Conclusions.....	76
3.6 Illustrations.....	78
Part 4. Investigations of the outer limits of the inner solutions.....	87
4.1 Introduction.....	87
4.2 Outer expansion of the dominant inner solution.....	88
4.3 Separation from a finite-span cavity into a transonic stream:	
General form and outer limits of the inner solution for Phase 2.....	91
4.4 Separation from a finite-span cavity into transonic stream:	
General form and outer limits of inner solutions for Phase 3.....	94
4.5 Outer limits of higher order approximations.....	96
4.6 Outer asymptotic expansion for the flow potential.....	102
4.6.1 Matching conditions.....	103
4.6.2 Classification of unsteady solutions in the outer asymptotic region.....	104
4.7 Analysis of drag components.....	107
4.7.1 Friction drag.....	108
4.7.2 Base drag.....	108
4.7.3 Transonic wave drag.....	109
4.7.4 Cross-flow drag.....	109
4.8 Solution of 3-DOF trajectory equations.....	113
4.9 Analysis of store separation from cavities and walls to a transonic stream.....	113

4.9.1 External separation.....	113
4.9.2 Store separation from cavities.....	116
4.10 Summary and conclusions.....	118
4.11 Illustrations.....	121
Summary.....	146
References.....	151

List of Figures

Figure	Title	Page
1.1	Flow scheme and coordinate systems: side view	24
1.2	Flow scheme and coordinate systems: back view	24
1.3	Cross-section flow scheme for Phase 1: the body in the cavity	25
1.4	Flow schemes for unit problems (1a) and (2a) in Phase 1	25
1.5	Flow scheme for Phase 3	26
1.6	Flow scheme and transformed plane for the unit problem (2b)	26
1.7	Different body disposition with respect to the slip surface in Phase 2	27
1.8	Cross-section flow scheme for Phase 2; the contour of integration and the transformed plane	27
1.9	Curvilinear coordinates on slip surface	28
2.1	Cross-section scheme for the reflection method for Phase 1 and 3	54
2.2	Plots of special functions	54
3.1	Schematic of store separation: a) - side view; b) - back view	78
3.2	Models for free drop tests in the IIT wind tunnel.	79
3.3	Model B4N2; λ_1 m/s, $Y_0 = 1.42$ inch., $\alpha_0 = 0^\circ$, $V_0 = 8$ inch./s, $\omega_0 = 9$ deg/s	80
3.4	Model B4N2; $U_\infty = 41.3$ m/s, $Y_0 = 2.4$ inch., $\alpha_0 = 9.6^\circ$, $V_0 = 2$ inch./s, $\omega_0 = -80$ deg./s	80
3.5	Model B1N1; $U_\infty = 62.7$ m/s, $Y_0 = 2.72$ inch./s, $\alpha_0 = -11.8^\circ$, $V_0 = 9$ inch./s, $\omega_0 = 75$ deg./s	81
3.6	Model B1N1; $U_\infty = 40.8$ m/s, $Y_0 = 2.65$ inch., $\alpha_0 = -7.8^\circ$, $V_0 = 15$ inch./s, $\omega_0 = 80$ deg./s.	81
3.7	Model B4N2; $U_\infty = 40.6$ m/s, $Y_0 = 2.65$ in., $\alpha_0 = -9.2^\circ$, $V_0 = 15$ in/s, $\omega_0 = 70.8$ deg./s	82
3.8	Model B5N5; $U_\infty = 62.5$ m/s, $Y_0 = 3.85$ in., $\alpha_0 = 2.4^\circ$, $V_0 = 19$ in/s, $\omega_0 = 140$ deg./s	82
3.9	Model B4N2; $U_\infty = 62.3$ m/s, $Y_0 = 2.33$ in., $\alpha_0 = 9.5^\circ$, $V_0 = 6$ in/s	83
3.10	Model B4N2; $U_\infty = 62.1$ m/s, $Y_0 = 2.8$ inch., $\alpha_0 = -11.9^\circ$,	83

	$V_0 = 15 \text{ inch./s}$, $\omega_0 = 52.86 \text{ deg./s}$	
3.11	Model B4N2; $U_\infty = 62.3 \text{ m/s}$, $Y_0 = 1.42 \text{ in.}$, $\alpha_0 = 0^\circ$, $\omega_0 = 8 \text{ deg./s}$	84
3.12	Effect of the free stream velocity on the body trajectory; Model B4N2; $Y_0 = 1.42 \text{ inch}$, $\alpha_0 = 0^\circ$, $V_0 = 8 \text{ inch./s}$, $\omega_0 = 8 \text{ deg./s}$	84
3.13	Influence of the initial angular speed on the body trajectory; Model B4N2; $U_\infty = 62.3 \text{ m/s}$, $Y_0 = 1.42 \text{ inch.}$, $\alpha_0 = 0^\circ$, $V_0 = 8 \text{ inch./s}$	85
3.14	Influence of the initial pitch angle on the body trajectory; Model B4N2; $U_\infty = 62.3 \text{ m/s}$, $Y_0 = 1.42 \text{ inch.}$, $V_0 = 8 \text{ inch./s}$, $\omega_0 = 8 \text{ deg./s}$	85
3.15	Trajectories of different models; $U_\infty = 62.3 \text{ m/s}$, $Y_0 = 1.42 \text{ inch.}$, $\alpha_0 = 0^\circ$, $V_0 = 8 \text{ inch./s}$, $\omega_0 = 8 \text{ deg./s}$	86
4.1	Cross-flow scheme in Phase 2 (body passes slip surface)	121
4.2	Cross-flow scheme in the transformed plane	121
4.3	Cross-flow scheme in Phase 3: body is outside the cavity	122
4.4	Two circles moving in unbounded stream and integration contour	122
4.5	Typical body locations with respect to the slip surface; the body nose is in outer stream.	123
4.6	Typical body locations with respect to the slip surface; the body tail is in outer stream	123
4.7	Typical area distributions of the effective body in Phase 2 and 3. Initial conditions: $Y_0 = 1 \text{ in}$, $V_0 = 10 \text{ ft/s}$, $\omega_0 = 200 \text{ deg/s}$, $\alpha_0 = 0^\circ$	124
4.8	Ogive-cylinder base pressure as a function of Mach number	124
4.9	Wave drag scaling for bodies of B4N2 type	125
4.10	Components of the cross-flow drag	125
4.11	Trajectory parameters of B4N2 body for the initial conditions: $Y_0 = -0.975 \text{ inch}$, $V_0 = -9.144 \text{ m/s}$, $\alpha_0 = -3.3^\circ$, $\omega_0 = -200 \text{ deg/s}$.	126
4.12	Histories of drag components for B4N2 body for the initial conditions: $Y_0 = -0.975 \text{ inch}$, $V_0 = -9.144 \text{ m/s}$, $\alpha_0 = -3.3^\circ$, $\omega_0 = -200 \text{ deg/s}$.	127
4.13	Trajectories of the body axis and center of gravity for the initial conditions: $\omega_0 = 0$, $Y_0 = -1.95 \text{ inch}$; $\alpha_0 = 6^\circ$.	128
4.14	Pitch angle history for the initial conditions: $\omega_0 = 0$, $Y_0 = -1.95 \text{ in.}$, $\alpha_0 = 6^\circ$.	129
4.15	Locations of the body axis at various initial angles of attack; $\omega_0 = 0$, $Y_0 = -1.95 \text{ inch}$, and $V_0 = 0$.	130

4.16	CG trajectories for the initial pitch angles $\alpha_0 = 0^\circ, 6^\circ$, $\omega_0 = 0$, $Y_0 = -1.95$ inch, and $V_0 = 0$.	131
4.17	Pitch angle history for the initial conditions: $\omega_0 = 0$, $Y_0 = -1.95$ inch, and $V_0 = 0$.	132
4.18	Center of gravity evolution for bodies of different radii.; $M = 0.999$, $V_0 = -9.144$ m/s, $\alpha_0 = 3.3^\circ$, $\omega_0 = 200$ deg/s	133
4.19	The body thickness effect on store trajectory characteristics; $M = 0.999$, $V_0 = -9.144$ m/s, $\alpha_0 = 3.3^\circ$, $\omega_0 = 200$ deg/s	133
4.20	Histories of drag components for bodies of various thickness; $M = 0.999$, $V_0 = -9.144$ m/s, $\alpha_0 = 3.3^\circ$, $\omega_0 = 200$ deg/s	134
4.21	CG trajectory parameters for the bodies of various thickness	135
4.22	Pitch angle histories for bodies of various thickness	136
4.23	Vertical speed for bodies of various thickness	136
4.24	Centerline trajectories for different bodies	137
4.25	Histories of drag components for bodies of different diameters	138
4.26	Time histories of vertical CG coordinate at $V_0 = 20$ and 30 in/s	139
4.27	CG trajectories at $V_0 = 20$ and 30 in/s	139
4.28	Pitch angle evolution at $V_0 = 20$ and 30 in/s	140
4.29	Evolution of CG vertical speed at $V_0 = 20$ and 30 in/s	140
4.30	Centerline trajectories at $V_0 = 20$ and 30 in/s	141
4.31	Evolution of drag components	142
4.32	CG vertical coordinate histories at various initial angles of attack	143
4.33	CG trajectories at various initial angles of attack: $Y_0 = 1$ in, $V_0 = 20$ in/s, $\omega_0 = 0$ deg/s.	143
4.34	Pitch angle histories at various initial angles of attack; $Y_0 = 1$ in, $V_0 = 20$ in/s, $\omega_0 = 0$ deg/s.	144
4.35	CG vertical speed histories at various initial angles of attack; $Y_0 = 1$ in, $V_0 = 20$ in/s, $\omega_0 = 0$ deg/s.	144
4.36	Histories of drag components at $\alpha = 5^\circ$ and $\alpha = -6^\circ$; $Y_0 = 1$ in, $V_0 = 20$ in/s, $\omega_0 = 0$ deg/s.	145

Nomenclature

\hat{a}_0	maximum body radius
$a = \frac{\hat{a}}{\hat{a}_0}$	local body radius
$A_0(X, t)$	function accounting for the outer flow effect on the body aerodynamics, Eq. (4.1.1a)
A_b	cross-sectional area of actual body
A_{eff}	cross-sectional area of the equivalent body of revolution
$c = \sqrt{H^2 - a^2}$	
$c_g = \frac{g\hat{l}_0}{\delta U_\infty^2}$	gravity force coefficient
$c_l = \frac{\rho_\infty \hat{l}_0^3 \delta^2}{m}$	lift force coefficient
$c_m = \frac{\rho_\infty \hat{l}_0^5 \delta^2}{I}$	pitching moment coefficient
$C_D = \frac{\hat{D}}{\rho_\infty U_\infty^2 \pi \delta^2 \hat{l}_0^2}$	total drag coefficient
C_{DF}	friction drag coefficient, Eq. (4.6.2a)
C_{DB}	base drag coefficient, Eq. (4.6.4a)
C_{DW}	wave drag coefficient, Eq. (4.6.5)
C_{DP}	cross-flow drag coefficient, Eq. (4.6.6a)
D_0	dipole intensity in Eq. (4.1.4b), and body diameter in Section 4.9
$d_0 = \frac{\hat{d}_0}{\hat{a}_0}$	cavity half span
$F(X, Z, t)$	slip surface shape; $Y_f = \mu F(X, Z, t)$
g	gravity acceleration
$H(X, t)$	vertical distance from body axis to slip surface, Eq. (1.1.7a)
H_0	cavity depth
I	moment of inertia
\hat{l}_0	body length
$K = (1 - M^2) / \delta^2$	transonic similarity parameter
$L = \frac{\hat{L}}{\rho_\infty U_\infty^2 \delta^2 \hat{l}_0^2}$	lift force
$M = \frac{\hat{M}}{\rho_\infty U_\infty^2 \delta^2 \hat{l}_0^2}$	pitching moment

$n(X, t) = \frac{\pi - \beta}{\pi}$	normalized angle; Eq. (1.2.17a)
$p = \frac{\hat{p} - p_\infty}{\delta^2 \rho_\infty U_\infty^2}$	pressure in the inner region
\tilde{p}	pressure in the outer region, Eq. (4.5.9c)
$q(X, t) = \frac{a(X)}{2H(X, t)}$	inverse vertical distance; $q \leq 1/2$
$q_1(x, t) = 0.5a/(H_0 - H)$	
Q_{eff}	effective source intensity, Eq. (4.2.7b)
$r = \frac{\hat{r}}{\hat{a}_0}$	polar radius in the inner region, Eq. (1.1.2a)
$\tilde{r} = \frac{\hat{r}\mu}{\hat{l}_0}$	polar radius in the outer region, Eq. (4.5.9a)
$Re = \frac{\rho_\infty U_\infty \hat{l}_0}{\mu_\infty}$	Reynolds number
$S = \frac{\hat{l}_0}{\hat{l}_0 U_\infty}$	Strouhal number
$t = \frac{\hat{U}_\infty \hat{t}}{\hat{l}_0}$	time
u, v, w	flow velocity components
$W = w - iv$	complex conjugate velocity
$V_e = V_o - \alpha x - \alpha$	effective cross-section speed
V_o	speed of center of gravity
$X = \frac{\hat{X}}{\hat{l}_0}, Y = \frac{\hat{Y}}{\hat{a}_0}, Z = \frac{\hat{Z}}{\hat{a}_0}$	coordinates attached to cavity
$x = \frac{\hat{x}}{\hat{l}_0}, y = \frac{\hat{y}}{\hat{a}_0}, z = \frac{\hat{z}}{\hat{a}_0}$	coordinates attached to body
Y_o	vertical coordinate of the center of gravity
$x_0(t)$	body nose coordinate, Eq. (1.1.10a)
$x_e(t)$	body base coordinate, Eq. (1.1.10a)
<i>Greek letters</i>	
$\alpha = \frac{\bar{\alpha}}{\delta}$	pitch angle
$\beta(X, t) = \arccos(H/a)$	angle between the body cross-section and OZ -axis at their intersection point (see Fig. 1.8a)

$\delta = \frac{\hat{a}_0}{\hat{l}_0}$	half of body thickness ratio
$\varepsilon = a_0 / d_0$	ratio of the body radius to the cavity half span
$\omega = \frac{\delta U_\infty \hat{\omega}}{\hat{l}_0}$	pitch angular speed
$\Pi = \Phi + i\Psi$	complex flow potential
Φ	flow potential
Ψ	stream function
θ	polar angle
$\vartheta = \pi/2 + \theta$	
$\zeta = Z + iY$	
ρ	density

Subscripts

∞	free stream
o	center of gravity
f	slip surface
b	body surface

Superscripts

\wedge	dimensional values
$+$	values above shear-layer
\sim	dimensionless functions in outer region

Introduction

The store separation problem has important practical applications. Its diverse aspects have been intensively investigated. Engineering, semi-empirical, computational and experimental approaches are illustrated in [1-4]. Most studies have been concerned with external separation at subsonic or supersonic speeds. Relatively less attention has been given to separation from cavities, especially at transonic speeds. This is because the problem is very complicated due to the large number of parameters governing the flow structure and the vast variety of physical phenomena involved in the separation process.

Our objectives in the research to be described in this document are to fill this gap by identifying the first-order physics, solve unit problems related to modeling the basic mechanisms and develop fast and robust methods for predicting store trajectories. Key thrusts are to divide the separation process into component phases, formulate unit problems for each phase and solve these problems using a combination of asymptotic and numerical methods. *In contrast to ad-hoc approaches, these give systematic approximation schemes modeling store separation processes that easily couple with rigid-body dynamics for desktop PC "design" codes that rapidly predict store trajectories. They also improve our understanding of the physics, parametric limits and trends.*

Matched asymptotics suggest that a component of the *global* problem of interaction of the separating with the entire airplane flow field, is the *local* problem of separation of a body of revolution from a rectangular cavity into an external subsonic or transonic flow of uniform freestream speed. In this physical system, we divide the separation process into three phases that will hereinafter be denoted Phases 1-3. In Phase 1, the body moves inside the cavity, whereas in Phase 2 the body crosses the shear layer separating the cavity flow from external stream. In Phase 3 the body is totally outside the cavity and moves in the external stream. We assume that the body is thin, the vertical flow velocity and angles of attack $\hat{\alpha}$ are small, so that the following relations hold

$$\delta = \frac{\hat{a}_0}{\hat{l}_0} \ll 1, \quad \frac{\hat{V}_r}{\delta U_\infty} = \varepsilon \leq O(1), \quad \alpha = \frac{\hat{\alpha}}{\delta} = O(1), \quad (1)$$

where \hat{l}_0 and \hat{a}_0 are respectively the body length and its maximum radius, \hat{V}_r is the characteristic vertical component (plunge) speed and δU_∞ is the scale of the vertical velocity perturbations in the external freestream of velocity U_∞ .

The body-shear layer interaction is an important component of the store separation process, especially, in Phase 2. This interaction depends on the ratio of shear-layer thickness $\hat{\delta}_s$ to body radius \hat{a}_0 . For many practical applications, the following relations hold

$$\frac{\hat{\delta}_s}{\hat{a}_0} \ll 1, \quad \delta^2 \text{Re} \gg 1, \quad \text{Re} = \frac{\rho_\infty U_\infty \hat{L}_0}{\mu_\infty}, \quad (2)$$

where Re is Reynolds number; ρ_∞ and μ_∞ are freestream density and viscosity. According to the first inequality of (2) the shear layer can be treated as a free slip surface with a tangential velocity jump and continuous normal velocity, pressure and the density across itself. The second inequality of (2) allows us to neglect viscous effects and use potential flow theory for regions well outside of the shear layer. If the shear layer thickness is small compared to the body thickness, it is reasonable to assume the potential flow approximation will provide a good approximation of the aerodynamic forces. We consider deep cavities of the length-to-height ratio $\hat{L}_0 / \hat{H}_0 < 6$. In this case, the outer flow weakly penetrates into the cavity; *i.e.*, flow velocities inside the cavity can be neglected because of the relations

$$\frac{\hat{v}_c}{\hat{V}_r} \sim \frac{\hat{\delta}_s}{\varepsilon \delta \hat{L}_0} \ll 1, \quad (3)$$

Within this framework, the flow over the body can be described by slender body theory [5-7]. The aerodynamic forces in this theory are controlled primarily by a cross flow "inner region" close to the body. Parts 1 and 2 of this report emphasize this inner asymptotic region. It covers a distance from the body axis of the order of the body radius. Following Refs. [16, 17, 19-21] we formulate the problem in Section 1.1. In the dominant approximation, the near-field solution has a similar form for both subsonic and transonic freestreams. It is governed by two-dimensional Laplace equations in the crossflow plane approximately perpendicular to the freestream direction. The relevant crossflow boundary value problems allow us to use the well-developed theory of analytical functions [8-15] but with a new twist associated with the presence of the slip surface approximating the temporal mean position of the a thin shear layer. From the inner solution we can calculate the lift force and pitching moment acting on the body and analyze two degree-of-freedom body dynamics restricted to vertical motion and pitching. These can be extended to more general motions involving roll and yaw motions with generalizations of our techniques.

Even with these simplifications however, it is difficult to obtain explicit solutions due to the complex geometry of the flow boundaries. To facilitate analysis we note that for many applications, the relative cavity height and half-width, \hat{D}_0 , are much larger than the body radius; *i.e.*

$$d_0 = \frac{\hat{D}_0}{\hat{a}_0} \gg 1, \quad H_0 = \frac{\hat{H}_0}{\hat{a}_0} \gg 1. \quad (4)$$

This allows the cavity wall effect to be treated as a small perturbation. From this approximation, it is possible to isolate the wall-body and slip surface-body interactions and treat them as separate component sub-problems whose solutions can be superimposed to provide the complete flow.

The slip surface-body interaction is the most difficult component problem because the shape of the free boundary is not known *a priori* and should be determined as a part of the solution since it strongly and nonlinearly interacts with it. This is a challenging problem even for current CFD modeling and many methods are in development to solve it. Since our goal is to develop transparent models of the physics as well as rapid turnaround methods, we use a simplification of the boundary value problem which is described in Section 1.3, using small perturbations that avoids large scale computation. Using the theory of analytical functions [8-15], we formulate a new approach and derive the slip-surface shape from a Poisson equation, with the right-hand side being an explicit function of the transverse coordinates and trajectory parameters. The problem is reduced to two singular linear integrodifferential equations for the slip-surface shape and the complex flow velocity. These equations include integrals of Cauchy type along the body cross-section contour and can be solved numerically by simple iterations. In Phase 2, this solution is singular at the body and slip surface line of intersection. We do not analyze this singularity since it is integrated and its contribution to the aerodynamics is negligible within the approximations considered here. Using the asymptotic results, in Section 1.4 we reformulate the general problem for the body-slip surface interaction and reduce it to a system of nonlinear singular integrodifferential equations that can be solved by simple iterations. Our new approach reduces the boundary value problem for the crossflow to boundary data quadratures, dramatically simplifying the solution procedure.

In Part 2, we consider the first iteration and find analytical expressions for the flow potential in all three phases of the body motion [17, 19-21] neglecting the slip-surface deformation. In Section 2.2, we obtain solutions in the form of rapidly converging series for Phases 1 and 3. The method of solution is based on the theory of Ref. [9] with new terms associated with three-dimensional effects. In Section 2.3, a conformal mapping is applied to obtain the solution for Phase 2. This solution differs from known results such as [15] by new terms related with three-dimensional flow effects. For all phases, we derive simple analytical expressions for the lift force and pitching moment acting on the body. These results are cross-checked by comparison with known analytical solutions [15, 24]

In Part 3 we analyze 2-DOF trajectory equations for vertical center of gravity translation and pitching rotation [20,21]. In Sections 3.2 and 3.3, approximate analytical solutions of the trajectory equations are obtained for Phases 1 and 3. A numerical code predicting the trajectory through the three phases is developed. In Section 3.4, the code is verified by comparisons with subsonic wind tunnel experiments [18]. Results of parametric studies are also presented.

In Part 4, we analyze the outer asymptotic problem. In Section 4.2, we investigate far field asymptotics of the inner solutions obtained in Part 2 for store separation from a flat plate and from an infinite-span cavity. In the former case, an equivalence rule similar to

[25-29] is formulated. For the latter, the far field corresponds to a dipole distribution along the body axis. In Section 4.3, a general form of the inner solution for Phase 2 is obtained for store separation from a finite-span cavity and its outer limit is studied. In Section 4.4, similar results are obtained for Phase 3. Higher order approximations of the inner solutions are discussed in Section 4.5. In Section 4.6, we formulate matching conditions and determine a general form of the outer solution. In contrast to the usual slender body theory [6], different time scales inherent in the problem considered generate a variety of unsteady regimes for the outer transonic flow. We identify these regimes in dependence of the relationship between the Strouhal number and flow perturbation scale. It is shown that the quasi-steady outer flow approximation is adequate in order to accurately calculate transonic wave drag. In Section 4.7, we analyze different drag components including the wave drag, pressure drag, viscous drag and base drag. In Section 4.8, the numerical method for solving the 3-DOF trajectory equations is discussed. From this method, we develop numerical codes predicting 3-DOF trajectories for store separations from a flat wall (external separations) or from a rectangular cavity. In Sections 4.9, numerical examples for external separations and separations from cavities are presented and discussed. They show that the theoretical model can simulate such complex phenomena as re-contact and ricocheting.

Part 1. Flow Field in the Inner Asymptotic Region

1.1 Introduction

Within the framework of slender body theory [5-7] the flow field is subdivided into two asymptotic regions. The inner region is located over the body surface and has a length scale of the order of the body radius. In this region, Laplace's equation for the flow potential and the unsteady form of Bernoulli's equation for the pressure describe both subsonic and transonic flows. Hereinafter we formulate the problem for the inner asymptotic region and discuss the governing equations emphasizing the most difficult problem associated with the slip surface motion. We have not found a rational and rigorous method for prediction of the slip surface motion for three-dimensional compressible flow in the literature. This is a challenging problem even for current CFD and a variety of numerical schemes were developed to solve it. Existing approximate methods are based on the results of Wagner [11], who analyzed incompressible two-dimensional flows for body submerging into liquids and gliding/planing. However, these methods do not account for compressibility and three-dimensional aspects considered herein. Moreover, we are dealing with the shear-layer interactions that are quite different from those occurring in hydrodynamic problems relevant to air-liquid interfaces. The theoretical model of Wagner [11] does not allow us to treat a combination of unsteady and three-dimensional effects that are important in store separation problems. Accordingly, the equations for the shear-layer dynamics obtained in this report are substantially different from those of Wagner [11].

In Section 1.2 we formulate the inner asymptotic problem in the dominant approximation. In Section 1.3 we use small perturbation theory to identify basic physical properties of the flow and find an appropriate form of the general solution for unsteady flows with a slip surface boundary. In Section 1.4, as an extension of the results obtained in Section 1.3, we derive a nonlinear system of equations for the case of finite flow perturbations. We show that this system can be solved using an iteration procedure. A short discussion of the result obtained in Part 1 and basic conclusions are presented in Section 1.5.

1.2 Problem formulation

We consider a slender body of revolution released from the top wall of a rectangular cavity at an initial instant $\hat{t} = 0$. The initial angle of attack $\hat{\alpha}_0$, vertical speed \hat{V}_0 and angular speed $\hat{\omega}_0$ are assumed to be small, of the order of $O(\delta)$. The body drops under gravity along the cavity symmetry plane and separates from the cavity into the external flow. At the initial instant, the flow within the cavity is neglected. The cavity interior is separated from external stream by the slip surface bridging the cavity edges. The flow scheme for Phase 2 (body crosses the shear layer) and the coordinate systems are shown in Figures 1.1 and 1.2. The coordinate system $O\hat{X}\hat{Y}\hat{Z}$ is attached to the unperturbed slip surface, as shown in Fig.1.1. Therein, the $O\hat{X}$ -axis is directed along the freestream velocity and $O\hat{Y}$ as well as $O\hat{Z}$ are respectively vertical and spanwise coordinates. The coordinate system $o\hat{x}\hat{y}\hat{z}$ is attached to the body center of gravity (CG) that moves

vertically with the velocity $\hat{V}_o(\hat{t})$. The $o\hat{x}$ -axis is directed along the body symmetry axis and the $o\hat{y}$ and $o\hat{z}$ axes lie in the cross-sectional plane. The direction of $o\hat{z}$ -axis coincides with the direction of $O\hat{Z}$ -axis. The axes $o\hat{x}$ and $o\hat{y}$ are inclined with respect to the axes $O\hat{X}$ and $O\hat{Y}$ at the angle $\hat{\alpha}(\hat{t})$; they rotate around $o\hat{z}$ -axis with the angular speed $\hat{\omega}(\hat{t})$. Along with the Cartesian coordinates we use the polar coordinates, \hat{r} and θ , specified as

$$\hat{z} = \hat{r} \cos \theta, \quad \hat{y} = \hat{r} \sin \theta. \quad (1.1.1)$$

The dimensionless variables for the inner asymptotic region are determined as

$$X = \frac{\hat{X}}{\hat{l}_0}; Y = \frac{\hat{Y}}{\hat{a}_0}; Z = \frac{\hat{Z}}{\hat{a}_0}; x = \frac{\hat{x}}{\hat{l}_0}; y = \frac{\hat{y}}{\hat{a}_0}; z = \frac{\hat{z}}{\hat{a}_0}, \quad (1.1.2a)$$

$$t = \frac{U_\infty \hat{t}}{\hat{l}_0}; \alpha = \frac{\hat{\alpha}}{\delta}; V_o = \frac{\hat{V}_o}{\hat{V}_r}; \omega = \frac{\delta U_\infty \hat{\omega}}{\hat{l}_0}. \quad (1.1.2b)$$

Neglecting terms of $O(\hat{\alpha}^2)$ and assuming that the longitudinal and transverse coordinates of the CG are constant, in particular, $Z_o(t) = X_o(t) = 0$, we obtain the relations

$$X = x, Y = Y_o(t) + y - x\alpha, Z = z, \quad (1.1.3)$$

where $Y_o(t)$ is vertical coordinate of CG.

The flow space consists of the cavity region (above the slip surface) and the external stream region (below the slip surface). In the cavity region, the potential, $\hat{\Phi}^+$, and flow velocities are defined as

$$\hat{\Phi}^+ = \hat{a}_0 \hat{V}_r \Phi^+ = \varepsilon \delta^2 U_\infty \hat{l}_0 \Phi, \quad \hat{\Phi}_t^+ = \varepsilon \delta^2 U_\infty^2 \Phi_t^+, \quad \hat{\Phi}_{\hat{x}}^+ = \varepsilon \delta^2 U_\infty u^+, \quad (1.1.4a)$$

$$\hat{\Phi}_{\hat{y}}^+ = \varepsilon \delta U_\infty v^+, \quad \hat{\Phi}_{\hat{z}}^+ = \varepsilon \delta U_\infty w^+, \quad u^+ = \Phi_x^+, \quad v^+ = \Phi_y^+, \quad w^+ = \Phi_z^+. \quad (1.1.4b)$$

Hereinafter, the superscript “+” denotes flow quantities inside the cavity. The corresponding quantities in the external stream region are expressed as

$$\hat{\Phi} = \hat{l}_0 U_\infty (1 + \delta^2 \Phi), \quad \hat{\Phi}_t = \delta^2 U_\infty^2 \Phi_t, \quad \hat{\Phi}_{\hat{x}} = U_\infty (1 + \delta^2 u), \quad (1.1.5a)$$

$$\hat{\Phi}_{\bar{y}} = \delta U_{\infty} v, \hat{\Phi}_{\bar{z}} = \delta U_{\infty} w, u = \Phi_x, v = \Phi_y, w = \Phi_z. \quad (1.1.5b)$$

The pressures \hat{p} and \hat{p}^+ are determined from the unsteady form of Bernoulli's equation is

$$p^+ = \frac{\hat{p}^+ - p_{\infty}}{\delta^2 \rho_{\infty} U_{\infty}^2} = -\varepsilon \left[\Phi_t^+ + \frac{\varepsilon}{2} (w^{+2} + v^{+2}) \right]. \quad (1.1.6a)$$

$$p = \frac{\hat{p} - p_{\infty}}{\delta^2 \rho_{\infty} U_{\infty}^2} = - \left[\Phi_t + u + \frac{1}{2} (w^2 + v^2) \right]. \quad (1.1.6b)$$

To $O(\delta^2)$, both potentials are harmonic functions in the cross-sectional planes. Accordingly, we can introduce the complex variable ζ , the complex potential $\Pi(\zeta; X, t)$, and the complex conjugate velocity $W(\zeta; X, t)$ as

$$\Pi(\zeta; X, t) = \Phi + i\Psi, \quad W(\zeta, X, t) = \frac{d\Pi}{d\zeta} = w - iv, \quad \zeta = Z + iY,$$

where $\Psi(X, Y, Z, t)$ is the nondimensional stream function. The boundary conditions on the body surface $Y = Y_b$ are expressed in the form

$$Y_b(X, Z, t) = H + a \sin \theta = H \pm \sqrt{a^2 - Z^2}, \quad H(X, t) = Y_o(t) - \alpha(t)X, \quad (1.1.7a)$$

$$r = a, \quad Y_b > Y_f : \quad v_n^+ = \frac{\partial \Phi^+}{\partial r} = V_e^+ \sin \theta; \quad V_e^+(X, t) = \frac{\partial H}{\partial t} = V_o(t) - \omega(t)X, \quad (1.1.7b)$$

$$r = a, \quad Y_b < Y_f : \quad v_n^- = \frac{\partial \Phi}{\partial r} = a_x + V_e \sin \theta, \quad V_e(X, t) = \varepsilon V_e^+(X, t) - \alpha(t), \quad (1.1.7c)$$

where v_n is flow velocity normal to the body surface and $H(X, t)$ is the distance from the body axis to the plane $Y = 0$. In Eq. (1.1.7a), the plus and minus signs respectively correspond to $y > 0$ and $y < 0$. Equations (1.1.7b) and (1.1.7c) correspond to the body surface inside and outside the cavity, respectively; and $V_e^+(X, t)$ and $V_e(X, t)$ are effective velocities of the body cross-section.

The boundary conditions on the slip surface, $Y_f = \mu F(X, Z, t)$, are formulated as

$$\varepsilon v^+(X, \mu F(X, Z, t), Z, t) = \mu (F_t + \varepsilon w_f^+ F_z), \quad (1.1.8a)$$

$$v(X, \mu F(X, Z, t), Z, t) = \mu (F_t + F_x + w_f F_z), \quad (1.1.8b)$$

$$p(X, \mu F(X, Z, t), Z, t) = p^+(X, \mu F(X, Z, t), Z, t), \quad (1.1.8b)$$

where the parameter μ characterizes a scale of the slip-surface perturbation; the subscript f denotes flow parameters on the slip surface.

On the cavity walls, normal velocities are zero and the boundary conditions are expressed as

$$Y = H_0, \quad -d_0 \leq Z \leq d_0 : \frac{\partial \Phi^+}{\partial Y} = 0; \quad Z = \pm d_0, \quad 0 \leq Y \leq H_0 : \frac{\partial \Phi^\pm}{\partial Z} = 0. \quad (1.1.9)$$

The flow velocities on the upstream and downstream walls are of the order of $O(\delta^2)$, and the boundary conditions are not involved in the dominant approximation of slender body theory. In this approximation, the lift force and pitching moment can be determined using the inner asymptotic solution only. Therefore, the CG coordinate, $Y_o(t)$, and speed, $V_o(t)$, as well as the pitch angle, $\alpha(t)$, and the angular speed, $\omega(t)$, are solutions of the dynamic equations

$$\frac{d^2 Y_o}{dt^2} = \frac{dV_o}{dt} = c_l L - c_g, \quad L = \frac{\hat{L}}{\rho_\infty U_\infty^2 \delta^2 \hat{l}_0^2} = - \int_{x_0}^{x_e} \int_0^{2\pi} p'(x, \theta, t) a(x) \sin \theta dx d\theta, \quad (1.1.10a)$$

$$\frac{d^2 \alpha}{dt^2} = \frac{d\omega}{dt} = c_m M, \quad M = \frac{\hat{M}}{\rho_\infty U_\infty^2 \delta^2 \hat{l}_0^2} = - \int_{x_0}^{x_e} \int_0^{2\pi} p'(x, \theta, t) x a(x) \sin \theta dx d\theta, \quad (1.1.10b)$$

$$c_g = \frac{g \hat{l}_0}{\delta U_\infty^2}, \quad c_l = \frac{\rho_\infty \hat{l}_0^3 \delta^2}{m}, \quad c_m = \frac{\rho_\infty \hat{l}_0^5 \delta^2}{I}, \quad p' = \begin{cases} p^+, & Y_b > \mu F \\ p, & Y_b < \mu F \end{cases} \quad (1.1.10c)$$

Here \hat{L} and \hat{M} are respectively lift force and pitching moment; m and I are body mass and moment of inertia; $x_0(t)$ and $x_e(t)$ are body nose tip and base coordinates.

1.3 Asymptotic theory for small flow perturbations

The unknown *a priori* slip surface shape and the nonlinear boundary conditions (1.1.8) are the main obstacles to obtain an explicit solution for the problem formulated in Section 1.2. In order to find analytical solutions and capture basic features of this problem we consider the case of small flow perturbations. Let the body drop with small vertical velocity and angle of attack and its cross-section area is a slow function of the axial coordinate; *i.e.*

$$a_x = \varepsilon_a a_{1x}, \quad \alpha = \varepsilon_\alpha \alpha_1, \quad V_e = \varepsilon(V - \omega X) - \varepsilon_\alpha \alpha_1, \quad V_e^+ = \varepsilon(V - \omega X), \\ \varepsilon_a \ll 1, \quad \varepsilon_\alpha \ll 1, \quad \varepsilon \ll 1.$$

We substitute these relations to the boundary conditions (1.1.7) on the body surface and express them in the form

$$\begin{aligned} r = a, Y_b > Y_f : v_n^+ &= \frac{\partial \Phi^+}{\partial r} = \varepsilon(V - \omega X) \sin \theta, \\ r = a, Y_b < Y_f : v_n &= \frac{\partial \Phi}{\partial r} = \varepsilon_a a_{1x} + \varepsilon(V - \omega X) - \varepsilon_a \alpha_1 \sin \theta \end{aligned}$$

These relations indicate that the flow potentials and slip surface shape can be expanded as

$$\Phi^+ = \varepsilon \phi^+ + \dots, \quad \Phi = \varepsilon \phi + \varepsilon_a \phi_a + \varepsilon_a \phi_a + \dots, \quad \mu F = \varepsilon F_0 + \varepsilon_a F_a + \varepsilon_a F_a + \dots$$

It is possible to consider the distinguished limits

$$\frac{\varepsilon_a}{\varepsilon} \rightarrow 0 \text{ or } \infty, \quad \frac{\varepsilon_a}{\varepsilon} \rightarrow 0 \text{ or } \infty$$

However, our analysis shows that the corresponding problems are not simpler than the general problem for $\varepsilon_a \sim \varepsilon \sim \varepsilon$. Therefore, we assume that

$$\varepsilon_a = \varepsilon_a = \varepsilon \ll 1, \quad (1.2.1a)$$

$$a_x = \varepsilon a_{1x}, \quad \alpha = \varepsilon \alpha_1, \quad V_e = \varepsilon V_{e1}, \quad V_{e1} = \varepsilon(V_{e1}^+ - \alpha_1), \quad V_{e1}^+ = (V - \omega X). \quad (1.2.1b)$$

In this case, we consider the most general problem when all sources of perturbations are of the same order of $O(\varepsilon)$, and all of them are included in the dominant approximation. Different cases for various distinguished limits can be easily treated using the general solution.

Flow perturbations in the cavity and in the external stream are of the same order of $O(\varepsilon)$, and we express the solution in the form of the asymptotic expansions

$$\mu = \varepsilon: F = F_0 + \varepsilon F_1, \quad \Phi^+ = \phi_0^+ + \varepsilon \phi_1^+ + O(\varepsilon^2), \quad \Phi = \varepsilon \phi_0 + \varepsilon^2 \phi_1 + O(\varepsilon^3), \quad (1.2.2a)$$

$$p = -\varepsilon \left\{ \phi_{0r} + \phi_{0x} + \varepsilon \left[\phi_{1r} + \phi_{1x} + \frac{1}{2} (v_0^2 + w_0^2) \right] \right\} + O(\varepsilon^3), \quad (1.2.2b)$$

$$p^+ = -\varepsilon \left\{ \phi_{0r}^+ + \varepsilon \left[\phi_{1r}^+ + \frac{1}{2} (v_0^{+2} + w_0^{+2}) \right] \right\} + O(\varepsilon^3). \quad (1.2.2c)$$

All terms of the potential expansions are governed by the Laplace equation with the boundary conditions on the cavity walls given by Eq. (1.1.9). In the dominant approximation, the boundary conditions (1.1.7) on the body surface are reduced to the form

$$r = a, Y_b > 0: v_{0n}^+ = \frac{\partial \phi_0^-}{\partial r} = V_e^+ \sin \theta, \quad (1.2.3a)$$

$$r = a, Y_b < 0: v_{0n} = \frac{\partial \phi_0}{\partial r} = a_{1x} + (V_e^- - \alpha_1) \sin \theta. \quad (1.2.3b)$$

The boundary conditions (1.1.8) on the slip surface are linearized and shifted to the plane $Y = 0$; they are expressed as

$$Y = 0: v_0^+ = F_{0t}, v_0 = F_{0t} + F_{0X}; \phi_{0t} + \phi_{0X} = \phi_{0t}^+. \quad (1.2.3c)$$

Differentiating the last equation (1.2.3c) with respect to Z we obtain the equation for the tangential flow velocities on the both sides of the slip surface

$$\frac{\partial w_{0f}}{\partial t} + \frac{\partial w_{0f}}{\partial X} = \frac{\partial w_{0f}^+}{\partial t}. \quad (1.2.3d)$$

In the second-order approximation, the boundary conditions (1.1.7) are

$$r = a: \frac{\partial \phi_1^+}{\partial r} = \frac{\partial \phi_1}{\partial r} = 0. \quad (1.2.4a)$$

In order to formulate the boundary conditions on the slip surface in the second-order approximation, we estimate the potential and tangential velocity of the dominant approximation on this surface as

$$\begin{aligned} \phi_0^-(X, \varepsilon F_0, Z, t) &= \phi_0^+(X, 0, Z, t) + \varepsilon F_0 F_{0t}, \quad \phi_0(X, \varepsilon F_0, Z, t) = \phi_0(X, 0, Z, t) + \varepsilon F_0 (F_{0t} + F_{0X}), \\ w_0^+(X, \varepsilon F_0, Z, t) &= \frac{\partial \phi_0^+(X, 0, Z, t)}{\partial Z} + O(\varepsilon), \quad w_0(X, \varepsilon F_0, Z, t) = \frac{\partial \phi_0(X, 0, Z, t)}{\partial Z} + O(\varepsilon). \end{aligned}$$

Substituting these relations to Eqs. (1.2.2), we obtain the boundary conditions of the second order approximation

$$Y = 0: v_{1f}^+ = F_{1t} + w_0^+ F_{0Z}, v_{1f} = F_{1t} + F_{1X} + w_0 F_{0Z}, \quad (1.2.4b)$$

$$\begin{aligned} \frac{\partial \phi_1^+}{\partial t} - \frac{\partial \phi_1}{\partial t} - \frac{\partial \phi_1}{\partial X} &= R_0(X, Z, t) = \\ &= \frac{3}{2} F_{0X} (2F_{0t} + F_{0X}) + F_0 (2F_{0t} + F_{0X})_X + \frac{1}{2} (w_0^2 - w_0^{+2}), \end{aligned} \quad (1.2.4c)$$

$$\frac{\partial w_1^+}{\partial t} - \frac{\partial w_1}{\partial t} - \frac{\partial w_1}{\partial X} = \frac{\partial R_0(X, Z, t)}{\partial Z}. \quad (1.2.4d)$$

In comparison with the dominant approximation, the conditions (1.2.4) include additional terms due to the slip surface displacement and the potential jump through the slip surface.

For Phase 2, when the body crosses the shear layer, the conditions (1.2.3c)-(1.2.3d), (1.2.4b)-(1.2.4d) are applied at $|Z| > c$.

The potentials $\phi_0(X, Y, Z, t)$ and $\phi_1(X, Y, Z, t)$ are solutions of the two-dimensional Laplace equation in the cross-section planes. Therefore, they are determined modulo arbitrary functions of X and t . These functions are multiplied by gauge functions appropriate to matching in the form $\ln(1/\delta)g_0(X, t)$ and $\ln(1/\delta)g_1(X, t)$ in accord with slender body theory [5-7]. They are determined from matching with the outer solution. In our initial consideration of the inner problem, we do not consider these functions.

1.3.1 Body moves in the cavity or in the stream (Phases 1 and 3)

In Phase 1 (body drops inside the cavity), for each cross-section plane the appropriate inner problem involves a circle of radius $a(x)$ dropping with the velocity V_e^+ in a rectangle with its lower boundary being the slip surface (see Fig. 1.3). To simplify the problem we estimate on part of the cavity wall effect by modeling the potential on the slip surface as zero. Then, continuing the flow symmetrically through the boundaries, we reduce the original problem to the problem of flow over a doubly-periodic lattice of circles, which has the analytical solution [9]. From this solution we conclude that the side-wall effect is of the order of $O(d_0^{-2}) \ll 1$. The top-wall effect is proportional to $(H_0 - H)^{-2}$; it is small when the body is near the slip surface. The slip-surface effect decreases as H^{-2} ; it is small when the body is near the top wall. Therefore, we can assume that the influence domains of these effects are weakly coupled, and each effect can be treated separately. This allows us to split the problem into the following unit problems for the complex conjugate velocity $W_0(\zeta; X, t) = w_0 - iv_0$:

- (1a) Find a harmonic function in the lower half-plane $Y < H_0$ that satisfies Eq. (1.2.3a) for the normal velocity on the circle and provides a vanishing imaginary part ($v_0 = 0$) at $Y = 0$ (see Fig. 1.4a)
- (2a) Find a harmonic function in the upper half-plane that satisfies Eq. (1.2.3a) for the normal velocity on the circle and provides a real part, w_0 given by Eqs. (1.2.3c)-(1.2.3d) at $Y = 0$ (see Fig. 1.4b).

Considering Phase 3 (the body moves in the external stream), we can formulate for each cross-section the problem: a circle drops with the velocity V_e from the mixed top boundary consisting of flat walls ($Y = 0, |Z| > d_0$) and free slip surface ($Y = 0, |Z| < d_0$). The flow scheme is shown in Fig. 1.5. Note that the finiteness of the cavity span is important for the far field asymptotic, which will be analyzed in Part 4. We neglect the cavity wall effect near the body (it is estimated as $O[1/(H^2 + d_0^2)] \ll 1$) and formulate the unit problem:

- (2b) Find a harmonic function $W_0(\zeta; X, t)$ in the lower half-plane that satisfies Eq. (1.2.3b) for the normal velocity on the circle and provides the real part w_0 given by Eqs. (1.2.3c)-(1.2.3d) at $Y = 0$.

The solution of the problem (1a) with the uniform boundary condition on the wall is found using the condition of analytical continuation of the complex conjugate velocity $W_0(\bar{\zeta}) = \overline{W_0(\zeta)}$, and the multipole expansion method [9]. It can be expressed in the form of the Laurent series (see Part 2)

$$W_{01}^+(\zeta; X, t) = \sum_{n=0}^{\infty} a^{n+1} \left\{ \frac{A_{-k-1} + iB_{-k-1}}{[\zeta - i(H_0 - H)]^{n+1}} + \frac{A_{-k-1} - iB_{-k-1}}{[\zeta + i(H_0 - H)]^{n+1}} \right\}. \quad (1.2.5)$$

where the functions $A_{-k-1}(X, t)$ and $B_{-k-1}(X, t)$ are found from the boundary conditions (1.2.3a).

The third equation of (1.2.3c) relevant to the slip-surface potential allows the solution $\phi_{0f} = 0$. In this case, the solution of the unit problems (2a) and (2b) can be expressed in a form similar to Eq. (1.2.5) (see Part 2). The boundary conditions (1.2.3c) also allow a nonzero potential on the slip surface. In this case, we cannot find an analytical solution of the problems (2a) and (2b). However, we can simplify these problems by reducing them to integrodifferential equations, which consist of one-dimensional integrals along the cross-sectional body contour only. This can be done using a conformal mapping of the flow regions shown in Fig. 1.4b and Fig. 1.6a with the cuts from the body to infinity into the rectangle in the complex plane $\sigma = \xi + i\eta$ as shown in Fig. 1.6b. The mapping has the form

$$\sigma = \frac{\omega_1}{2\pi i} \ln \frac{|c+H|(\zeta - ic)}{a(\zeta + ic)}, \quad c = \sqrt{H^2 - a^2}, \quad \omega_2 = \frac{2\omega_1}{\pi} \ln \frac{a}{a - |H|}. \quad (1.2.6)$$

In the transformed plane (see Fig. 1.6b), the lower side of rectangle, $(0, 2\omega_1)$, corresponds to the body surface; the upper side, $(i\omega_2 + 2\omega_1)$, corresponds to the slip surface; the left and right sides are the cut edges.

We assume that the tangential velocities on the both sides of the slip surface, $w_{0f}(X, Z, t)$ and $w_{0f}^+(X, Z, t)$, are given. Then, using the formula of Villat [8], we find the complex conjugate velocity in the rectangle by its real part on the upper side and the imaginary part on the lower side. For the unit problem (2b) the solution has the form

$$W_{02}(\sigma) = \frac{1}{\pi i} \frac{\partial \sigma}{\partial \zeta} \left\{ \int_{i\omega_2}^{i\omega_2 + 2\omega_1} G(\sigma, s) w_{0f}(s) ds - i \int_0^{2\omega_1} G(\sigma, s) v_{0n}(s) ds \right\}, \quad (1.2.7a)$$

$$G(\sigma, s) = \frac{\sigma_1(s - \sigma + \omega_1)}{l(s)\sigma_1(\omega_1)\sigma_1(s - \sigma)} \exp[-\eta_1(s - \sigma)] l[\zeta(\xi)] = \left| \frac{\partial \sigma}{\partial \zeta} \right|_{\eta=1}. \quad (1.2.7b)$$

where $\sigma_1(z)$ is Weierstrass sigma-function, and η_1 is its characteristic [12]. A similar formula determines the function $W_{02}^+(\zeta; X, t)$ for the unit problem (2a). In this case, the full solution in the cavity is represented as

$$W_0^+(\zeta; X, t) = W_{01}^+(\zeta; X, t) + W_{02}^+(\zeta; X, t) - W_{00}^+(\zeta; X, t), \quad (1.2.8)$$

where $W_{00}^+(\zeta; X, t)$ is common part of the functions $W_{01}^+(\zeta; X, t)$ and $W_{02}^+(\zeta; X, t)$ that corresponds to the circle dropping in unbounded fluid.

For the unit problems (2a) and (2b), solutions for the lower and upper half-planes, which do not contain the body, are given by the Dirichlet formulas

$$W_0^-(\zeta) = -\frac{1}{\pi i} \int_{-\infty}^{\infty} \frac{w_{0f}(s) ds}{s - \zeta}; \quad W_0^+(\zeta) = \frac{1}{\pi i} \int_{-\infty}^{\infty} \frac{w_{0f}^+(s) ds}{s - \zeta}. \quad (1.2.9)$$

Because the tangential velocities on both sides of the slip surface are not known *a priori*, we should find them along with the slip surface shape as a part of solution. However, Equations (1.2.3) and (1.2.7) are not closed, and we need to derive an additional equation using the relations between the real and imaginary parts of the boundary value of a harmonic function [13]. We represent the complex conjugate velocity by the Cauchy integral along the contour shown in Fig. 1.6a for the problem (2b) or similar contour in the upper half-plane for the problem (2a). Then, using the Sokhotsky-Plemelj relations combined with the boundary condition, we obtain the following equations, which relate the tangential velocities on the slip surface with its shape,

Problem (2a):

$$w_{0f}^-(X, Z, t) = -\frac{I_{0f}^+(X, Z, t) - I_b^+(X, Z, t)}{\pi}, \quad w_{0f}^+(X, Z, t) = \frac{I_{0f}^-(X, Z, t)}{\pi}; \quad (1.2.10a)$$

Problem (2b):

$$w_{0f}^-(X, Z, t) = \frac{I_{0f}^-(X, Z, t) + I_b^-(X, Z, t)}{\pi}, \quad w_{0f}^+(X, Z, t) = -\frac{I_{0f}^+(X, Z, t)}{\pi}. \quad (1.2.10b)$$

Principal values of the Cauchy integrals $I_{0f}^-(X, Z, t)$ and $I_{0f}^+(X, Z, t)$ along the slip surface are expressed as

$$I_{0f}^+(Z) = \int_{-\infty}^{\infty} \frac{F_{0f}(Z') dZ'}{Z' - Z}, I_{0f}(Z) = \int_{-\infty}^{\infty} \frac{F_{0f}(Z') + F_{0X}(Z')}{Z' - Z} dZ'. \quad (1.2.11)$$

Using the flow symmetry and the relations presented in Appendix A, we express the Cauchy integrals $I_b^+(Z)$ and $I_b(Z)$ along the body surface as

$$I_b(X, Z, t) = \operatorname{Re} i \oint_b \frac{w_0(s_b) - i v_0(s_b)}{s_b - Z} ds_b = \frac{2\pi a Z}{H^2 + Z^2} \left\{ a_{x1} + \right. \\ \left. + \frac{aH}{H^2 + Z^2} \left[w_{01} - V_{e1} + \sum_{n=2}^{\infty} w_{0n} \left(\frac{aH}{H^2 + Z^2} \right)^{n-1} \sum_{k=0}^{\left[\frac{n}{2} \right]} (-1)^k C_{n+1}^{2k+1} \left(\frac{Z}{H} \right)^{2k} \right] \right\}, \quad (1.2.12a)$$

$$I_b^+(X, Z, t) = -a \operatorname{Re} \int_0^{2\pi} \frac{w_0^+(s_b) - i v_0^+(s_b)}{s_b - Z} ds_b = \\ = \frac{2\pi a^2 H Z}{(H^2 + Z^2)^2} \left\{ w_{01}^+ - V_{e1}^+ + \sum_{n=2}^{\infty} w_{0n}^+ \left(\frac{aH}{H^2 + Z^2} \right)^{n-1} \sum_{k=0}^{\left[\frac{n}{2} \right]} (-1)^k C_{n+1}^{2k+1} \left(\frac{Z}{H} \right)^{2k} \right\}. \quad (1.2.12b)$$

Here the symbol $\left[\frac{n}{2} \right]$ denote the integer part of the fraction; C_{n+1}^{2k+1} are binomial coefficients; $\vartheta = \pi/2 + \theta$ is polar angle measured from the plane of symmetry as shown in Fig. 1.6a; $w_\theta(X, t, \theta)$ is flow velocity tangential to the body surface and the functions $w_{0n}(X, t)$ are coefficients of its Fourier series

$$w_{0n}(X, t) = \frac{1}{2\pi} \int_0^{2\pi} w_{0\theta}(X, t, \vartheta) \sin(n\vartheta) d\vartheta, \quad (1.2.13a)$$

$$w_{0n}^+(X, t) = \frac{1}{2\pi} \int_0^{2\pi} w_{0\theta}^+(X, t, \vartheta) \sin(n\vartheta) d\vartheta. \quad (1.2.13b)$$

Using the solution (1.2.5) we can represent the functions $w_{0n}(X, t)$ and $w_{0n}^+(X, t)$ in the form

$$w_{01}(X, t) = -\frac{2B_{-2}(X, t) - V_{e1}}{2}, \quad (1.2.13c)$$

$$w_{02n}(X, t) = (-1)^n A_{-2n-1}(X, t), \quad w_{02n+1}(X, t) = (-1)^n B_{-2n-2}(X, t), \quad (1.2.13d)$$

where the functions $A_{-2n-1}(X, t)$ and $B_{-2n-2}(X, t)$ are determined in Section 2.2 of Part 2 in the form of power series of the parameter $q(X, t) = a/(2H) < 1/2$.

Substituting Eqs. (1.2.10)-(1.2.13) into Eq. (1.2.3d) and introducing the new variables $\tau = t - X$, $\lambda = X$, we obtain for the slip-surface shape the integrodifferential equation

$$\int_{-\infty}^{\infty} \left\{ \left(\frac{\partial^2}{\partial t^2} + \frac{\partial^2}{\partial \lambda^2} \right) F_0(\lambda, s, \tau) \right\} \frac{ds}{s - Z} = -P_0(\lambda, Z, \tau), \quad (1.2.14a)$$

where the right hand side is expressed as

$$\text{For Problem (2a):} \quad P_0(\lambda, Z, \tau) = -\frac{\partial I_b^+(X, Z, t)}{\partial t}; \quad (1.2.14b)$$

$$\text{For Problem (2b):} \quad P_0(\lambda, Z, \tau) = \left(\frac{\partial}{\partial t} + \frac{\partial}{\partial X} \right) I_b(X, Z, t). \quad (1.2.14c)$$

Solving the Abel equation (1.2.14a) we obtain the Poisson equation for the function $F_0(X, Z, t)$

$$\frac{\partial^2 F_0}{\partial \tau^2} + \frac{\partial^2 F_0}{\partial \lambda^2} = -2\pi S_0(\lambda, Z, \tau), \quad S_0(\lambda, Z, \tau) = \frac{1}{2\pi^3} \int_{-\infty}^{\infty} \frac{P_0(\lambda, s, \tau) ds}{s - Z}. \quad (1.2.15a)$$

An integral representation of the solution is:

$$F_0(X, Z, t) = \int_{-\infty-X}^{\infty} \int_{-\infty}^{\infty} S_0(X', Z, t') G_P(X, t; X', t') dt' dX', \quad (1.2.15b)$$

$$G_P(X, t; X', t') = \ln \left[2(X - X')^2 + (t - t')^2 - 2(t - t')(X - X') \right]. \quad (1.2.15c)$$

Using the relations given in Appendix A we express the function $S_0(\lambda, Z, \tau)$ as

$$\text{For Problem (2a):} \quad S_0(X, Z, \tau) = \frac{\partial Q_0^+(X, Z, t)}{\partial t}, \quad (1.2.16a)$$

$$Q_0^+ = \frac{2q}{\pi} \left\{ q(w_{01}^+ - V_{e1}^+) \frac{1 - \bar{Z}^2}{(1 + \bar{Z}^2)^2} + \sum_{n=2}^{\infty} \frac{w_{0n}^+ q^n}{n!} \sum_{k=0}^{\left[\frac{n}{2} \right]} (-1)^k C_{n+1}^{2k+1} Q_{nk}(\bar{Z}) \right\}. \quad (1.2.16b)$$

$$\text{For Problem (2b):} \quad S_0(X, Z, \tau) = \left(\frac{\partial}{\partial t} + \frac{\partial}{\partial X} \right) Q_0(X, Z, t), \quad (1.2.16c)$$

$$Q_0 = \frac{2q}{\pi} \left\{ \frac{a_{1X}}{1 + \bar{Z}^2} + q(w_{01} - V_{e1}) \frac{1 - \bar{Z}^2}{(1 + \bar{Z}^2)^2} + \sum_{n=2}^{\infty} \frac{w_{0n} q^n}{n!} \sum_{k=0}^{\left[\frac{n}{2} \right]} (-1)^k C_{n+1}^{2k+1} Q_{nk}(\bar{Z}) \right\}, \quad (1.2.16d)$$

$$Q_{nk}(\bar{Z}) = \sum_{m=0}^k \left\{ (2(k-m)-1)!! (2(n-k+m)-1)!! \bar{Z}^{2m} - \frac{n! \bar{Z}^{2k+2}}{1 + \bar{Z}^2} \left[\sum_{m=0}^n \frac{[2(n-m)-1]!!}{(n-m)!} \left(\frac{2}{1 + \bar{Z}^2} \right)^m + \left(\frac{2}{1 + \bar{Z}^2} \right)^n \right] \right\}. \quad (1.2.16e)$$

where $\bar{Z} = Z/H$. Therefore, we obtained the right hand side of Eq. (1.2.15a) in the form of the power series of the variable q . Note that these power series are rapidly convergent since $q < 1/2$.

To summarize, we have shown that the slip surface shape is given by the Poisson integral (1.2.15) in closed form. Equations (1.2.15) provide explicit coupling of the slip-surface perturbations with the flow velocity on the body surface. Accordingly, the inner asymptotic solution is intrinsically non-local with respect to the streamwise coordinate and time, although it is harmonic in each cross-section plane. This contrasts with classic slender-body theory [5-7] where the non-locality of the inner solution is associated with the function of integration $A_0(X, t)$ correction to the crossflow-harmonic inner dominant terms. The latter is determined from matching of the inner and outer solutions. As contrasted to the non-local behavior due to the shear layer, this “switchback” term (referring to its *low* order in the inner solution that matches a *high* order term in the outer solution) has a “global” dependence reflecting the upstream downstream interaction from the outer solution. This is a needed 3-D refinement of the 2-D crossflow nature of the inner solution near field, reflecting the outer flow physics.

Equations (1.2.6), (1.2.7) and (1.2.15) comprise a closed system of linear integrodifferential equations that can be solved numerically by simple iterations. At the first iteration we assume $\phi_{0f} = \phi_{0f}^+ = 0$ and obtain the solution in the form of series presented in Section 2.2 of Part 2. We calculate the tangential velocity on the body surface, and, then, the slip surface shape and flow velocities on its sides from Eq. (1.2.14) and (1.2.10). After this step, we calculate the contribution of the first integral (1.2.7a) to the tangential velocity $w_\theta(\theta)$ on the body surface and repeat the above procedure in the second iteration. This sequence of calculations is repeated until the required accuracy is achieved. For rough estimates, we can use the first iteration.

1.3.2 Body crosses the slip surface (Phase 2)

For Phase 2 (body crosses the slip surface), with the accuracy discussed in Section 1.2 we can neglect the side and top wall effects. The infinite flat slip surface ($Y_f = 0, |Z| > c(X, t)$) subdivides the body into three parts. Typical cases are shown in Fig. 1.7. These depend on the angle of attack, submergence depth, body, nose position of the body ($X_0 < X < X_1$) and the location of its rear part ($X_2 < X < X_e$) relative to inside or outside the cavity. The solutions for these body portions are obtained with the framework of the unit problems (1a), (2a) and (2b) discussed in Section 1.2. The body part ($X_1 < X < X_2$) is partially submerged: a portion of it is inside the stream ($Y_b < 0$),

and the other portion is inside the cavity ($Y_b > 0$). Boundary conditions on the surface of each portion and on the slip surface are given by Eqs. (1.2.3) and (1.2.13). As in Phases 1 and 3, the boundary conditions allow zero value of the potential on the slip surface, $\phi_{0f} = \phi_{0f}^+ = 0$. In this case, the solutions for the cavity and stream regions are obtained in Section 2.3 of Part 2; they correspond to the first iteration. In the general case, the problem is also reduced to a system of integrodifferential equations using a conformal mapping of the cavity and stream flow regions into the upper and lower half-planes, respectively. The cross-section scheme is presented in Fig. 1.8. The mapping of the stream region to the lower half-plane of the complex variable $\sigma = \xi + i\eta$ is given by the relations

$$\zeta = f^-(\sigma, X, t) = c \frac{R^n(\sigma) + 1}{R^n(\sigma) - 1}; \quad n(X, t) = \frac{\pi - \beta}{\pi}, \quad R(\sigma) = \frac{\sigma + b}{\sigma - b}, \quad (1.2.17a)$$

$$\frac{\partial \sigma}{\partial \zeta} = \frac{(\sigma^2 - b^2)(R^n(\sigma) - 1)^2}{4c^2 R^n(\sigma)}; \quad b = \frac{c}{n}; \quad c = \sqrt{a^2 - H^2} = a \sin \beta, \quad (1.2.17b)$$

where $\beta(X, t)$ is angle between the body cross-section and OZ -axis at their intersection point (see Fig. 1.8a). The submerged body portion ($Y_b < 0$) is transformed to the lower side of the interval $[-b, b]$. The mapping, $\zeta = f^+(\sigma, X, t)$, of the cavity region to the upper half-plane and the upper body portion ($Y_b > 0$) in the upper side of the interval $[-b^+, b^+]$ is given by Eqs. (1.2.9) with a replacement of n by $m = 1 - n$ and of b by $b^+ = c/m$.

For given tangential velocities on the both sides of the slip surface and the normal velocities on the body parts specified by Eqs. (1.2.3a) and (1.2.3b), the complex conjugate velocity can be obtained in the explicit analytical form from the Keldysh-Sedov formula in the transformed plane [8]

$$W_0(\sigma; X, t) = \frac{1}{\pi i \sqrt{\sigma^2 - b^2}} \left(\frac{\partial \zeta}{\partial \sigma} \right)^{-1} \left[i \int_{-b}^b \frac{\sqrt{b^2 - s^2} v_{0n}(s) ds}{(s - \sigma) l(s)} - \int_f \frac{\sqrt{s^2 - b^2} w_{0f}(s) ds}{(s - \sigma) l(s)} \right], \quad (1.2.18a)$$

$$W_0^+(\sigma; X, t) = \frac{1}{\pi i \sqrt{\sigma^2 - b^2}} \left(\frac{\partial \zeta}{\partial \sigma} \right)^{-1} \left[i \int_{-b}^b \frac{\sqrt{b^2 - s^2} v_{0n}^+(s) ds}{(s - \sigma) l(s)} + \int_f \frac{\sqrt{s^2 - b^2} w_{0f}^+(s) ds}{(s - \sigma) l(s)} \right], \quad (1.2.18b)$$

$$\int_f = \int_{-\infty}^{-b} + \int_b^{\infty}, \quad l(s) = \left| \frac{\partial \zeta}{\partial \sigma} \right|_{\eta=0}^{-1}.$$

From Cauchy integrals for the complex conjugate velocity in the cavity and external flow regions, we derive the following relations for the transverse velocities on the upper and lower sides of the slip surface

$$w_{0f}^+(X, Z, t) = -\frac{I_{0f}^+(X, Z, t) - I_b^+(X, Z, t)}{\pi}, \quad (1.2.19a)$$

$$w_{0f}^-(X, Z, t) = \frac{I_{0f}^-(X, Z, t) + I_b^-(X, Z, t)}{\pi}. \quad (1.2.19b)$$

Integrals I_{0f}^+ and I_{0f}^- along the slip surface preserve their forms (1.2.11) provided that the integration path consists of the intervals $(-\infty, c)$ and (c, ∞)

$$I_{0f}^+(Z) = \left(\int_{-\infty}^{-c} + \int_c^{\infty} \right) \frac{F_{0f}(Z') dZ'}{Z' - Z}, \quad I_{0f}^-(Z) = \left(\int_{-\infty}^{-c} + \int_c^{\infty} \right) \frac{F_{0f}(Z') + F_{0X}(Z')}{Z' - Z} dZ'. \quad (1.2.20)$$

In Phase 2, $H = 0$ can occur. In order to avoid a singularity at these points, we express the integrals along the body contours inside the stream and cavity regions in the form

$$\begin{aligned} I_b(X, Z, t) &= \operatorname{Re} i \int_{\zeta_b < F} \frac{w_1(\zeta_b) - i v_1(\zeta_b)}{\zeta_b - Z} d\zeta_b = a \operatorname{Re} \int_{-\beta}^{\beta} \frac{w_{\theta 1}(\vartheta) + i v_{n1}(\vartheta)}{-\beta(H + iZ) \left(1 - \frac{a}{H + iZ} e^{i\vartheta} \right)} d\vartheta = \\ &= \operatorname{Re} i \left\{ \frac{2\beta a a_{1X}}{H + iZ} + \left[\pi w_{01} + V_{e1} \left(\beta + \frac{1}{2} \sin 2\beta \right) \right] \left(\frac{a}{H + iZ} \right)^2 + \pi \sum_{n=2}^{\infty} w_{0n} \left(\frac{a}{H + iZ} \right)^{n+1} \right\}. \end{aligned} \quad (1.2.21a)$$

$$\begin{aligned} I_b^+(X, Z, t) &= a \operatorname{Re} \int_{\beta}^{2\pi-\beta} \frac{[w_{\theta 1}^+(\vartheta) + i v_{n1}^+(\vartheta)] d\vartheta}{(H + iZ) \left(1 - \frac{a}{H + iZ} e^{i\vartheta} \right)} = \\ &= \operatorname{Re} i \left\{ \left[\pi w_{01}^+ - V_{e1}^+ \left(\pi - \beta - \frac{1}{2} \sin 2\beta \right) \right] \left(\frac{a}{H + iZ} \right)^2 + \pi \sum_{n=2}^{\infty} w_{0n}^+ \left(\frac{a}{H + iZ} \right)^{n+1} \right\}, \end{aligned} \quad (1.2.21b)$$

$$w_{0n}(\beta) = \frac{1}{\pi} \int_0^{\beta} w_{\theta}(\vartheta) \sin(n\vartheta) d\vartheta, \quad w_{0n}^+(\beta) = \frac{1}{\pi} \int_{\beta}^{\pi} w_{\theta}^+(\vartheta) \sin(n\vartheta) d\vartheta. \quad (1.2.21c)$$

Equations (1.2.14a) and (1.2.15a) for the slip surface preserve their forms, provided that the function $P_0(X, t, Z)$ is replaced by the expression

$$P_0(X, t, Z) = \frac{\partial I_b}{\partial t} + \frac{\partial I_b}{\partial X} - \frac{\partial I_b^+}{\partial t}. \quad (1.2.22)$$

In Appendix A, the function $S_0(X, t, Z)$ is expressed as

$$2\pi^3 S_0(X, t, Z) = \frac{\partial Q_0}{\partial t} + \frac{\partial Q_0}{\partial X} - \frac{\partial Q_0^+}{\partial t}, \quad (1.2.23a)$$

$$Q_0 = \left(\int_{-\infty}^{-c} + \int_c^{\infty} \right) \frac{I_b(X, t, y) dy}{y - Z} = \frac{2\beta a a_{1X}}{Z^2 + H^2} \left[Z \ln \frac{Z+c}{Z-c} + (\pi - 2\beta)H \right] + \left(\frac{aZ}{Z^2 + H^2} \right)^2 \times$$

$$\times \left[\pi w_{01} - V_{e1} \left(\beta + \frac{\sin 2\beta}{2} \right) \right] \left\{ 2 \frac{H}{Z} \ln \frac{Z+c}{Z-c} + (\pi - 2\beta + 2 \sin^2 \beta) \left[\left(\frac{H}{Z} \right)^2 - 2 \right] + 8 \cos^2 \beta \right\} +$$

$$+ \left(\frac{a}{Z^2 + H^2} \right)^3 \sum_{n=2}^{\infty} w_{0n}(\beta) Q_{0n}(X, Z, t) \left(\frac{a}{Z^2 + H^2} \right)^{n-2}, \quad (1.2.23b)$$

$$Q_0^+ = \left(\int_{-\infty}^{-c} + \int_c^{\infty} \right) \frac{I_b^+(X, t, y) dy}{y - Z} = \left(\frac{aZ}{Z^2 + H^2} \right)^2 \left[\pi w_{01} - V_{e1} \left(\pi - \beta - \frac{\sin 2\beta}{2} \right) \right] \times$$

$$\times \left\{ 2 \frac{H}{Z} \ln \frac{Z+c}{Z-c} + (\pi - 2\beta + 2 \sin^2 \beta) \left[\left(\frac{H}{Z} \right)^2 - 2 \right] + 8 \cos^2 \beta \right\} +$$

$$+ \left(\frac{a}{Z^2 + H^2} \right)^3 \sum_{n=2}^{\infty} w_{0n}(\beta) Q_{0n}(X, Z, t) \left(\frac{a}{Z^2 + H^2} \right)^{n-2}, \quad (1.2.23c)$$

$$Q_{0n}(X, Z, t) = \left\{ \ln \frac{Z+c}{Z-c} + 2 \sum_{m=1}^n \frac{C_n^m \cos m\beta}{ma^m} [(Z+c)^m - (c-Z)^m] \right\} \sum_{k=0}^{\left[\frac{n}{2} \right]} (-1)^k C_{n+1}^{2k+1} H^{n-2k} Z^{2k+1} +$$

$$+ \left\{ \pi - 2\beta + 2 \sum_{m=1}^n \frac{C_n^m \sin m\beta}{ma^m} [(Z+c)^m + (c-Z)^m] \right\} \sum_{k=0}^{\left[\frac{n+1}{2} \right]} (-1)^k C_{n+1}^{2k} H^{n-2k+1} Z^{2k}. \quad (1.2.23d)$$

Thus, as in Phases 1 and 3, the slip-surface shape in Phase 2 is determined by a Poisson integral (2.1.15b) involving an explicit function depending on the trajectory parameters. Analyzing the relations (1.2.23) we conclude that the slip surface shape has a singularity on the line of intersection of the body with the slip surface. This singularity is due to linearization of the equations and boundary conditions. It has also the physical explanation: a vortical surface cannot end on a rigid wall. In order to find a non-singular solution, we need to analyze the inner asymptotic region near the intersection line. A similar situation occurs in the two-dimensional problem of a submerging cylindrical body [11]. The singularity disappears if $c \rightarrow 0$, $\beta \rightarrow 0, \pi$; i.e., the body cross-section is in the cavity or in the stream. In this case, Equations (1.2.21) and (1.2.23) translates to Eqs. (1.2.12) and (1.2.16).

1.4 Analysis of the slip-surface effect for finite perturbations

In this section we analyze the flow equations when the flow perturbations are not small, $\varepsilon = \mu = 1$. We focus on the slip-surface effect since it is the most difficult aspect to

model. As shown in Section 1.2, this effect can be isolated from cavity wall effects. Within the framework of slender body theory, we analyze the following problems in a cross-section plane:

- 1) In Phase 1, the circle of radius $a(x)$ drops in the upper half plane (where fluid is at rest) toward the slip surface
- 2) In Phase 2, the circle crosses the slip surface
- 3) In Phase 3, the circle moves in the external stream away from the slip surface.

Using the asymptotic results of the previous section we describe these unit problems by a system of nonlinear integrodifferential equations, which satisfy all boundary conditions and directly couple the slip surface distortion with the flow over the body surface. This system can be solved numerically by a relatively simple iteration method. The first-step solutions are expressed in analytical forms; they are similar to the dominant approximation discussed in Section 1.2.

We reformulate the boundary conditions (1.1.8) using the curvilinear non-orthogonal coordinate system attached to the slip surface as shown on Fig. 1.9. Here τ is coordinate along the intersection curve of the slip surface and the plane $Z = \text{const}$; n is normal coordinate to this curve; φ is angle between τ -axis and OZ -axis. Using the boundary conditions (1.1.8) we can express the curvilinear components of the fluid velocity vector on the slip surface as

$$u_n^+ = \frac{F_t}{h}, u_n^- = \frac{F_t + F_x}{h}, u_\tau^+ = hw_f^+ + \frac{F_z F_t}{h}, \quad (1.3.1a)$$

$$u_\tau^- = hw_f + \frac{F_z(F_t + F_x)}{h}, h = \sqrt{1 + F_z^2}, \quad (1.3.1b)$$

where u_n and u_τ are normal and tangential velocities on the slip surface; superscripts '+' and '-' stand for its upper and lower sides, respectively. Differentiating (1.1.8) with respect to Z we obtain the equation for the transverse flow velocities on the both sides of the curve slip surface in the form

$$\frac{\partial w_f^+}{\partial t} - \frac{\partial w_f}{\partial t} - \frac{\partial w_f}{\partial X} = w_f w_{fz} + v_f v_{fz} - w_f^+ w_{fz}^+ - v_f^+ v_{fz}^+ = R(X, Z, t). \quad (1.3.2)$$

In order to correlate the boundary potential with the slip-surface shape we represent the complex conjugate velocity in the cavity or stream regions by the Cauchy integral along the contour bounding this region. These contours are similar to those shown in Figs. 1.3, 1.6 and 1.8 for Phases 1, 3 and 2, respectively. From these integrals, using the Sokhotsky-Plemelj relations we derive the following equations for tangential velocities on the slip surface:

For Phase 1:

$$w_f^+(X, Z, t) = -\frac{I_f^+(X, Z, t) - I_b^+(X, Z, t)}{\pi}, \quad w_f(X, Z, t) = \frac{I_f(X, Z, t)}{\pi}; \quad (1.3.3a)$$

For Phase 3:

$$w_f(X, Z, t) = \frac{I_f(X, Z, t) + I_b(X, Z, t)}{\pi}, \quad w_f^+(X, Z, t) = -\frac{I_f^+(X, Z, t)}{\pi}; \quad (1.3.3b)$$

For Phase 2:

$$w_f^+(X, Z, t) = -\frac{I_f^+(X, Z, t) - I_b^+(X, Z, t)}{\pi}, \quad w_f(X, Z, t) = \frac{I_f(X, Z, t) + I_b(X, Z, t)}{\pi}. \quad (1.3.3c)$$

Integrals I_f^+ and I_f along the upper and lower sides of the slip surface are expressed as

For Phase 1:

$$\begin{aligned} I_f^+(X, Z, t) &= \operatorname{Re} i \int_f \frac{w_f^+(\zeta') - i v_f^+(\zeta')}{\zeta' - \zeta} d\zeta' = I_{0f}^+(X, Z, t) + I_{1f}^+(X, Z, t) = \\ &= \int_{-\infty}^{\infty} \frac{F_t(Z') dZ'}{Z' - Z} + \sum_{n=1}^{\infty} (-1)^n \int_{-\infty}^{\infty} \left(\frac{F' - F}{Z' - Z} \right)^{2n-1} \left[u_{\tau}^+(Z') + u_n^+(Z') \frac{F' - F}{Z' - Z} \right] \frac{h(Z') dZ'}{Z' - Z}, \end{aligned} \quad (1.3.4a)$$

For Phase 3:

$$\begin{aligned} I_f(X, Z, t) &= \operatorname{Re} i \int_f \frac{w_f(\zeta') - i v_f(\zeta')}{\zeta' - \zeta} d\zeta' = I_f(X, Z, t) + I_{1f}(X, Z, t) = \\ &= \int_{-\infty}^{\infty} \frac{F_t(Z') + F_x(Z')}{Z' - Z} dZ' + \\ &+ \sum_{n=1}^{\infty} (-1)^n \int_{-\infty}^{\infty} \left(\frac{F' - F}{Z' - Z} \right)^{2n-1} \left[u_{\tau}^-(Z') + u_n^-(Z') \frac{F' - F}{Z' - Z} \right] \frac{h(Z') dZ'}{Z' - Z}. \end{aligned} \quad (1.3.4b)$$

For Phase 2, these integrals have the same form if the integration is carried out in the intervals $(-\infty, -Z_A)$ and (Z_A, ∞) ; the attachment points A are shown in Fig. 1.2. Due to flow symmetry, integrals I_b^+ and I_b along the body surface are expressed as

$$I_b(X, Z, t) = \operatorname{Re} i \oint_b \frac{w(s_b) - i v(s_b)}{s_b - Z} ds_b = \frac{2\pi a Z}{(H - F)^2 + Z^2} \left[a_x + \frac{a(H - F)(w_1 - V_e)}{(H - F)^2 + Z^2} \right] +$$

$$+ \frac{2\pi a Z}{(H-F)^2 + Z^2} \left\{ \sum_{n=2}^{\infty} w_n \left[\frac{a(H-F)}{(H-F)^2 + Z^2} \right]^{n-1} \sum_{k=0}^{\left[\frac{n}{2} \right]} (-1)^k C_{n+1}^{2k+1} \left[\frac{Z}{(H-F)} \right]^{2k} \right\}. \quad (1.3.5a)$$

$$\begin{aligned} I_b^+(X, Z, t) &= -a \operatorname{Re} \int_0^{2\pi} \frac{w^+(s_b) - iv^+(s_b)}{s_b - Z} ds_b = \\ &= \frac{2\pi a^2 (H-F)Z}{[(H-F)^2 + Z^2]^2} \left\{ w_1^+ - V_e^+ + \sum_{n=2}^{\infty} w_n^+ \left[\frac{a(H-F)}{(H-F)^2 + Z^2} \right]^{n-1} \sum_{k=0}^{\left[\frac{n}{2} \right]} (-1)^k C_{n+1}^{2k+1} \left[\frac{Z}{(H-F)} \right]^{2k} \right\}. \end{aligned} \quad (1.3.5b)$$

where the coefficients w_n and w_n^+ are given by Eqs. (1.2.13). For Phases 2, similar to Eqs. (1.2.21), we obtain

$$\begin{aligned} I_b(X, Z, t) &= \operatorname{Re} i \int_{\zeta_b < F} \frac{w(\zeta_b) - iv(\zeta_b)}{\zeta_b - Z} d\zeta_b = a \operatorname{Re} \int_{-\beta_A}^{\beta_A} \frac{w_\theta(\vartheta) + iv_n(\vartheta)}{(H-F+iZ) \left(1 - \frac{a}{H-F+iZ} e^{i\vartheta} \right)} d\vartheta = \\ &= \operatorname{Re} i \left\{ \frac{2\beta_A a a_x}{H-F+iZ} + \left[\pi w_1 + V_e \left(\beta_A + \frac{1}{2} \sin 2\beta_A \right) \right] \left(\frac{a}{H-F+iZ} \right)^2 + \right. \\ &\quad \left. + \pi \sum_{n=2}^{\infty} w_n \left(\frac{a}{H-F+iZ} \right)^{n+1} \right\}, \end{aligned} \quad (1.3.5c)$$

$$\begin{aligned} I_b^-(X, Z, t) &= a \operatorname{Re} \int_{\beta_A}^{2\pi-\beta_A} \frac{[w_\theta^+(\vartheta) + iv_n^+(\vartheta)] d\vartheta}{(H-F+iZ) \left(1 - \frac{a}{H-F+iZ} e^{i\vartheta} \right)} = \\ &= \operatorname{Re} i \left\{ \left[\pi w_1^+ - V_e^+ \left(\pi - \beta_A - \frac{1}{2} \sin 2\beta_A \right) \right] \left(\frac{a}{H-F+iZ} \right)^2 + \pi \sum_{n=2}^{\infty} w_n^+ \left(\frac{a}{H-F+iZ} \right)^{n+1} \right\}, \end{aligned} \quad (1.3.5d)$$

$$w_{0n} = \frac{1}{\pi} \int_0^{\beta_A} w_\theta(\vartheta) \sin(n\vartheta) d\vartheta, \quad w_{0n}^+ = \frac{1}{\pi} \int_{\beta_A}^{\pi} w_\theta^+(\vartheta) \sin(n\vartheta) d\vartheta. \quad (1.3.5e)$$

Substituting these relations into Eq. (1.3.2) we have

For Phase 1:

$$\frac{1}{\pi} \int_{-\infty}^{\infty} \frac{[F_t(Z')h(Z')]_t + [F_\lambda(Z')h(Z')]_\lambda dZ'}{Z' - Z} = \frac{1}{\pi} \left[\frac{\partial I_{1f}}{\partial \lambda} + \frac{\partial I_{1f}^+}{\partial t} - \frac{\partial I_b^+}{\partial t} \right] - R, \quad (1.3.6a)$$

For Phase 3:

$$\frac{1}{\pi} \int_{-\infty}^{\infty} \frac{[F_t(Z')h(Z')]_t + [F_\lambda(Z')h(Z')]_\lambda}{Z' - Z} dZ' = -\frac{1}{\pi} \left[\frac{\partial I_{1f}}{\partial \lambda} + \frac{\partial I_{1f}^+}{\partial t} + \frac{\partial I_b}{\partial \lambda} \right] - R, \quad (1.3.6b)$$

For Phase 2:

$$\begin{aligned} \frac{1}{\pi} \left(\int_{-\infty}^{-Z_A} + \int_{Z_A}^{\infty} \right) \frac{[F_t(Z')h(Z')]_t + [F_\lambda(Z')h(Z')]_\lambda}{Z' - Z} dZ' = \\ = -\frac{1}{\pi} \left[\frac{\partial I_{1f}}{\partial \lambda} + \frac{\partial I_{1f}^+}{\partial t} + \frac{\partial I_b}{\partial \lambda} - \frac{\partial I_b^+}{\partial t} \right] - R. \end{aligned} \quad (1.3.6c)$$

These equations are similar to Eqs. (1.2.14) and (1.2.22) of Section 1.2 besides the presence of additional nonlinear terms. Assuming that the right-hand sides are known, we can solve the Abel equations (1.3.6) and express Eqs. (1.3.6) in the form

$$\begin{aligned} \frac{\partial^2 F}{\partial t^2} + \frac{\partial^2 F}{\partial \lambda^2} + \frac{F_Z(F_t F_{Zt} + F_\lambda F_{Z\lambda})}{h} = -2\pi S(X, Z, t) - \\ - \frac{1}{\pi^2 h} \int_{-\infty}^{\infty} \left[\frac{\partial I_{1f}(\lambda, Z', t)}{\partial \lambda} + \frac{\partial I_{1f}^+(\lambda, Z', t)}{\partial t} + \pi R(\lambda, Z', t) \right] \frac{dZ'}{Z' - Z}. \end{aligned} \quad (1.3.7a)$$

$$\text{For Phase 1:} \quad S(X, Z, t) = -\frac{1}{2\pi^3 h} \int_{-\infty}^{\infty} \frac{\partial I_b^+(\lambda, Z', t)}{\partial t} \frac{dZ'}{Z' - Z}, \quad (1.3.7b)$$

$$\text{For Phase 3:} \quad S(X, Z, t) = \frac{1}{2\pi^3 h} \frac{\partial}{\partial \lambda} \int_{-\infty}^{\infty} \frac{I_b(\lambda, Z', t) dZ'}{Z' - Z}, \quad (1.3.7c)$$

$$\text{For Phase 2:} \quad S(X, Z, t) = \frac{1}{2\pi^3 h} \left(\int_{-\infty}^{-Z_A} + \int_{Z_A}^{\infty} \right) \left[\frac{\partial I_b(\lambda, Z', t)}{\partial \lambda} - \frac{\partial I_b^+(\lambda, Z', t)}{\partial t} \right] \frac{dZ'}{Z' - Z}. \quad (1.3.7d)$$

Equation (1.3.7a) is a nonlinear integrodifferential equation for the slip-surface shape provided that tangential velocities on the slip surface and the body cross-section contour are known. It is similar to the Poisson equation (1.2.15a). The leading operator of the left-hand side of Eq. (1.3.7a) is the Laplace operator. The first term in the right-hand side of Eq. (1.3.7a) provides direct coupling of the slip-surface displacement with the body motion. It is similar to the forcing term in Eq. (1.2.15a), however we cannot calculate it explicitly, since the integrands of Eqs. (1.3.7b)-(1.3.7d) depend on the slip-surface shape. The other terms of Eq. (1.3.7a) represent nonlinear effects of the slip surface motion.

In order to close the problem, we need to obtain an explicit form of the solution for the complex conjugate velocity. To use the Keldysh-Sedov formula we map the slip surface to the plane $Y = 0$. Assuming that the slip surface shape is known we apply the Cisotti formula to conformal mapping of the cavity region or the stream region on a ring in the complex plane $\chi = Z_1 + iY_1$. For Phase 1 and 3, this mapping has the form [10]

$$\zeta(\chi) - iF(X, 0, t) = i \int_0^\chi \frac{e^{im(z)} dz}{(1-z)^2}, \quad m(z) = \frac{1}{2\pi} \int_0^{2\pi} \frac{e^{it} + z}{e^{it} - z} \varphi(t) dt, \quad \varphi(s) = \operatorname{arctg}[F_z(s)]. \quad (1.3.8)$$

The outer boundary of the ring is a circle associated with the slip surface. The inner boundary is not circular and corresponds to the body surface. In order to map this ring to the rectangle of sides $2\omega_1$ and $2i\omega_2$ in the complex plane $\sigma = \xi + i\eta$, we can use the numerical method [14]. The body is transformed to the interval $[0, 2\omega_1]$ of the real axis, and the slip surface is transformed to the parallel interval $[i\omega_2, i\omega_2 + 2\omega_1]$. In the σ -plane, the solution is expressed by the formula of Villat [8] as

$$W(\sigma) = \frac{1}{\pi i} \frac{\partial \sigma}{\partial \zeta} \left\{ \int_{i\omega_2}^{i\omega_2 + 2\omega_1} G(\sigma, s) u_r^-(s) ds - i \int_{i\omega_2}^{i\omega_2 + 2\omega_1} G(\sigma, s) v_n(s) ds \right\}. \quad (1.3.9)$$

For the external regions, which are the stream region for Phase 1 and the cavity region for Phase 3, we have the Neumann problems with the normal velocities on the slip surface given by Eqs. (1.3.1). In these regions, solutions are found using the additional conformal mapping of the ring (1.3.8) exterior to the lower or upper half planes of the complex variable $\sigma_1 = \xi_1 + i\eta_1$

$$\sigma_1 = \frac{1}{2} \left(\chi + \frac{1}{\chi} \right). \quad (1.3.10)$$

In this plane, the body cross-section is not a circle. However, its profile is symmetrical with respect to the η_1 -axis. It is given by the equation $\eta_1 = \tilde{H}(x, t) + \tilde{a}(x, \tilde{\theta}, t) \sin \tilde{\theta}$, where $\tilde{H}(x, t)$ is transformed distance to the body axis, and $\tilde{a}(x, \tilde{\theta}, t)$ is transformed body radius. This equation can be written in the form $\tilde{r} = \tilde{a}(x, \tilde{\theta}, t)$, where \tilde{r} and $\tilde{\theta}$ are attached to the body axis polar coordinates in the transformed plane.

The solutions in the upper and lower half planes (without the body) are expressed as

$$W^+(\sigma_1) = -\frac{1}{\pi} \frac{\partial \sigma_1}{\partial \zeta} \int_{-\infty}^{\infty} \frac{u_n^+(s) ds}{(s - \sigma_1) l_1(s)}. \quad (1.3.11a)$$

$$W(\sigma_1) = \frac{1}{\pi} \frac{\partial \sigma_1}{\partial \zeta} \int_{-\infty}^{\infty} \frac{u_n^-(s) ds}{(s - \sigma_1) l_1(s)}, \quad l_1(s) = \left| \frac{\partial \sigma_1}{\partial \zeta} \right|_{\eta_1=0}. \quad (1.3.11b)$$

Corresponding solutions with the body present can be obtained using the multipole expansion method [9].

Equations (1.3.3)-(1.3.11) comprise a closed system of nonlinear integrodifferential equations that can be solved numerically by iterations. The first step approximation corresponds to a flat slip surface of zero potential. This problem is similar to the dominant approximation problem analyzed in Section 1.2 for small displacements of the slip surface.

In Phase 2, in order to obtain expressions for the complex conjugate velocity, we note that the mappings (1.3.8) and (1.3.10), with the boundary angle defined as

$$\varphi(s) = \begin{cases} \arctg[F_s(X, s, t)], & |s| > c \\ \frac{\pi}{2} + \theta(s), & |s| < c \end{cases},$$

transform the cavity flow region to the upper half plane. The body portion located inside the cavity is transformed to the upper side of the interval $[-b, b]$. The external stream region and the submerged body portion are transformed to the lower half plane and the lower side of the interval $[-b, b]$, respectively. Applying the Keldysh-Sedov formula we can express the complex conjugate velocity in the form

$$W(X, \chi, t) = \frac{1}{\pi i \sqrt{\chi^2 - b^2}} \left(\frac{\partial \zeta}{\partial \chi} \right)^{-1} \left[i \int_{-b}^b \frac{\sqrt{b^2 - s^2} v_n(s) ds}{(s - \chi) l(s)} - \int_f \frac{\sqrt{s^2 - b^2} u_r^-(s) ds}{(s - \chi) l(s)} \right], \quad (1.3.12a)$$

$$W^+(X, \chi, t) = \frac{1}{\pi i \sqrt{\chi^2 - b^2}} \left(\frac{\partial \zeta}{\partial \chi} \right)^{-1} \left[i \int_{-b}^b \frac{\sqrt{b^2 - s^2} v_n(s) ds}{(s - \chi) l(s)} + \int_f \frac{\sqrt{s^2 - b^2} u_r^+(s) ds}{(s - \chi) l(s)} \right], \quad (1.3.12b)$$

$$\int_f = \int_b^\infty - \int_{-\infty}^{-b}, \quad l(s) = \left| \frac{\partial \zeta}{\partial \chi} \right|_{\chi=0}^{-1}.$$

These expressions allow us to calculate the tangential velocity on the body surface and normal velocities on the slip surface. Thus, Equations (1.3.5), (1.3.10) and (1.3.11) form a closed system of integrodifferential equations, which can be solved by iterations. In the first step, the slip surface is specified as $Y = 0, |Z| > c$. This approach substantially simplifies numerical calculations because the flow characteristics are calculated using analytical formulas at each iteration step.

1.5 Discussion and conclusions

This chapter represents a first step of our combined asymptotic and numerical analysis of the store separation problem. We considered separation of the body of revolution from a rectangular cavity into subsonic/transonic stream. Using slender body theory, we formulated the inner asymptotic problem for the near-field region. Solutions of this aerodynamic problem can be coupled with the body dynamic problem to predict two degrees of freedom trajectories including vertical coordinate of CG and pitch angle.

The body separation process is treated as a sequence of the following phases: in Phase 1, body is inside the cavity; in Phase 2, body crosses the shear layer; in Phase 3, body is outside the cavity in free stream. We showed that for many practical cases the cavity side-wall effects can be neglected. This allowed us to decompose the general problem into the unit problems:

- 1) Body drops from a flat wall to fluid at rest (Phase 1) or to the external stream (Phase 3);
- 2) Body crosses the slip surface (Phase 2);
- 3) Body drops toward the slip surface (Phase 1) or away from the slip surface (Phase 3).

The first unit problem can be solved analytically using the multipole expansion method [9]. The second and third problems are more complicated because they include effects of the body interaction with the free slip surface. In order to obtain their analytical solutions and provide insight into the slip surface effect on the near-field flow, we analyzed the case of small slip-surface displacements using asymptotic methods. We show that the slip surface shape is described by a two-dimensional Poisson equation with the time and longitudinal coordinate to be independent variables and transverse coordinate to be as a parameter. This indicates that the inner solution is not local with respect to time and streamwise coordinate, although it is harmonic in the cross-sectional planes. This is intrinsic property of the inner solution for flows with free boundaries, whereas in the classic slender body theory [5-7] the non-locality is associated with the outer-flow region and matching conditions. The forcing term of the Poisson equation directly couples the slip surface displacement with the body motion. This displacement is an explicit function of the trajectory parameters and transverse coordinate. Analysis of the slip-surface equation and a linear integrodifferential equation for the complex velocity is performed using the conformal mapping and Keldysh-Sedov formula. That gives a general form of the inner solution.

Note that for small perturbations, the equation for Phases 1, 2 and 3 are obtained in compact analytical forms accounting for the slip surface displacement. For these equations a relatively simple iteration procedure can be used for calculations of flow characteristics. For Phases 1 and 3, analytical solutions for the slip-surface displacement will be obtained in near future. They can be used in the cases when the body is sufficiently far from the slip surface. The analytical results provide significant simplification in prediction of the slip surface effect on aerodynamic forces and moments acting on the body in all phases of the separation process.

In the general case, when the slip-surface perturbations are not small, we used the results of small perturbation analysis as a launching pad to attack this complicated problem. We derived the nonlinear integrodifferential equation for the slip surface shape, the leading terms of which are similar to those of obtained for small perturbations. An explicit integral representation of the Laplace equation solution for the complex conjugate velocity is obtained using conformal mappings of the flow regions to simple regions such as a ring or a flat plate exterior. Combining this equation with the slip-surface equation

we derived a closed system of equations that can be solved by iterations. In the first iteration step, the slip surface is treated as a flat plane of zero potential, and the near field solution can be expressed in analytical form.

Our analytical solutions are new. Some of them extend the two-dimensional result [11] to three-dimensional flows. Our approach substantially simplifies numerical calculations because flow characteristics are evaluated at each iteration step using explicit analytical formulas.

1.6 Illustrations

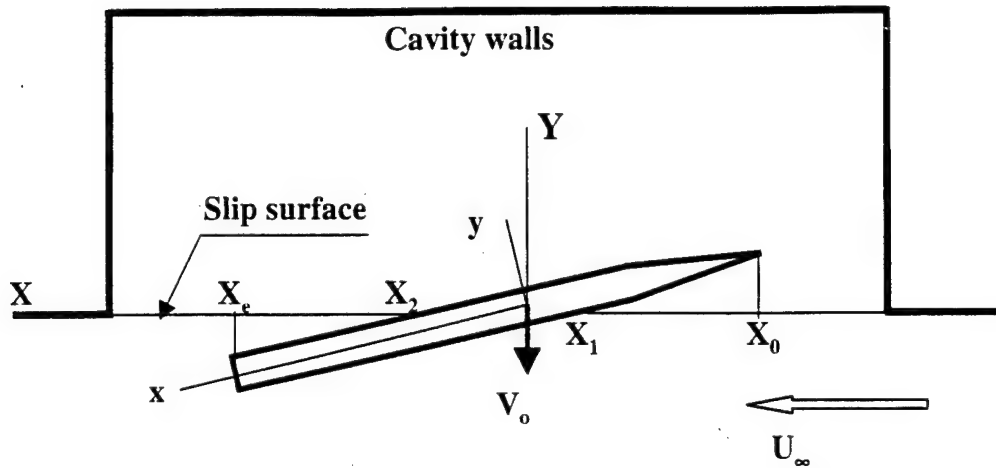


Fig. 1.1 Flow scheme and coordinate systems: side view

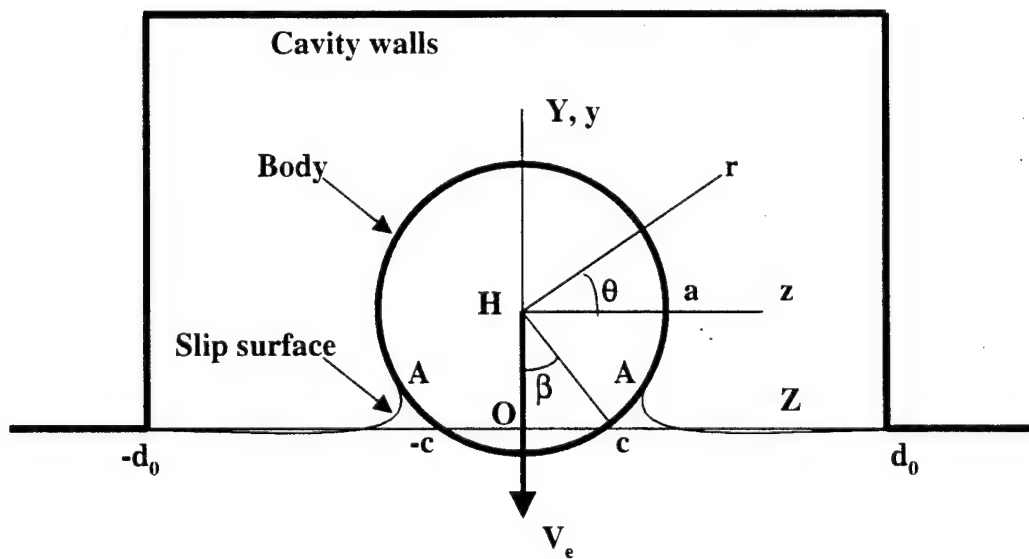


Fig. 1.2 Flow scheme and coordinate systems: back view.

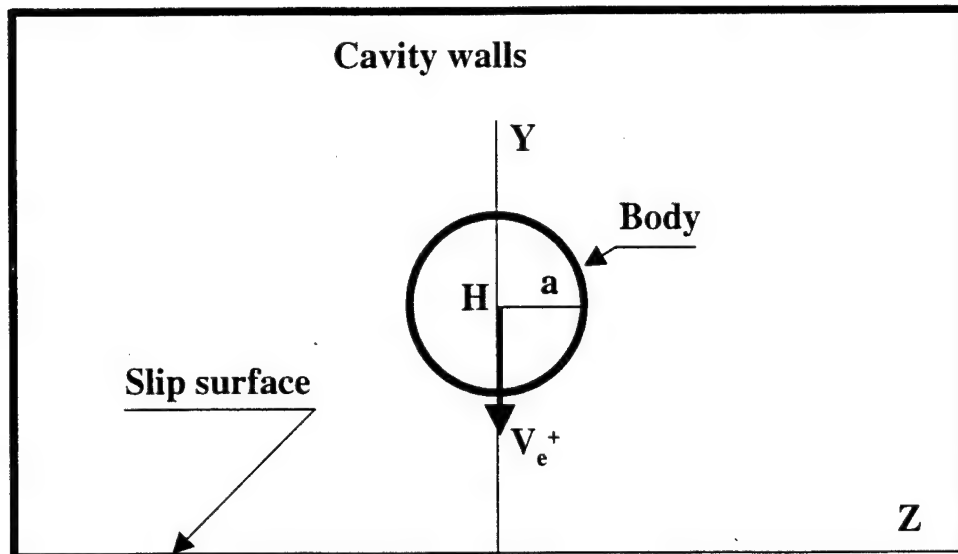


Fig. 1.3 Cross-section flow scheme for Phase 1: the body in the cavity.

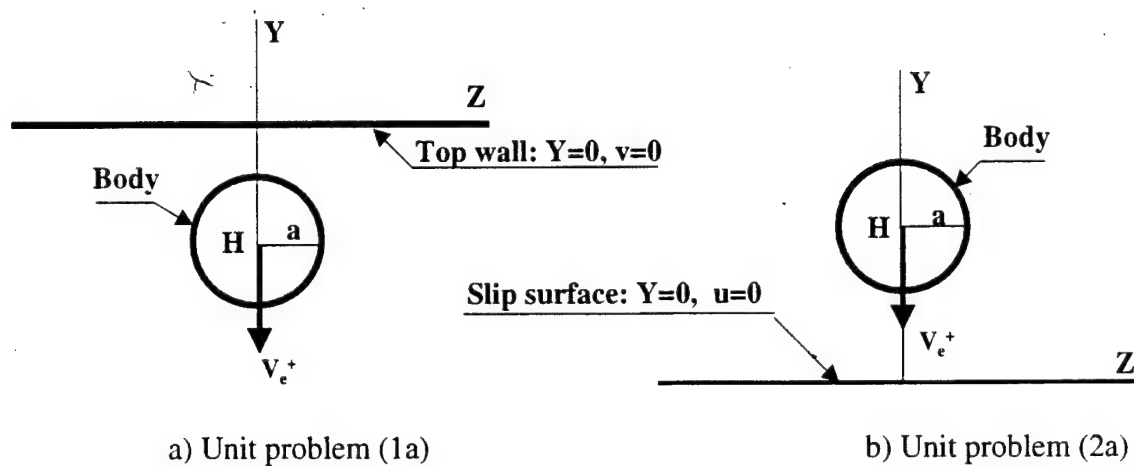


Fig. 1.4 Flow schemes for unit problems (1a) and (2a) in Phase 1.

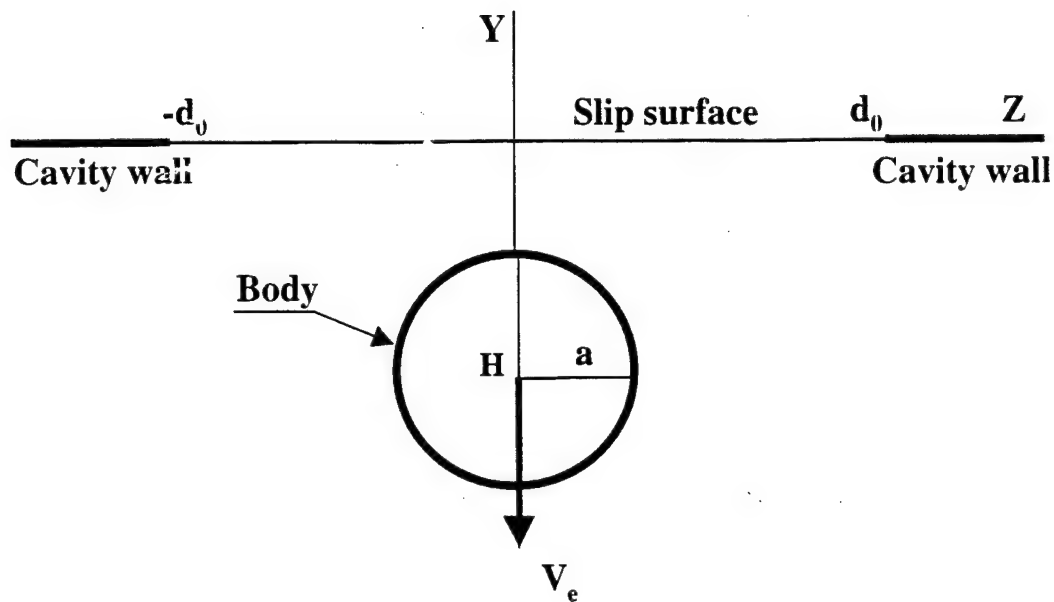


Fig. 1.5 Flow scheme for Phase 3.

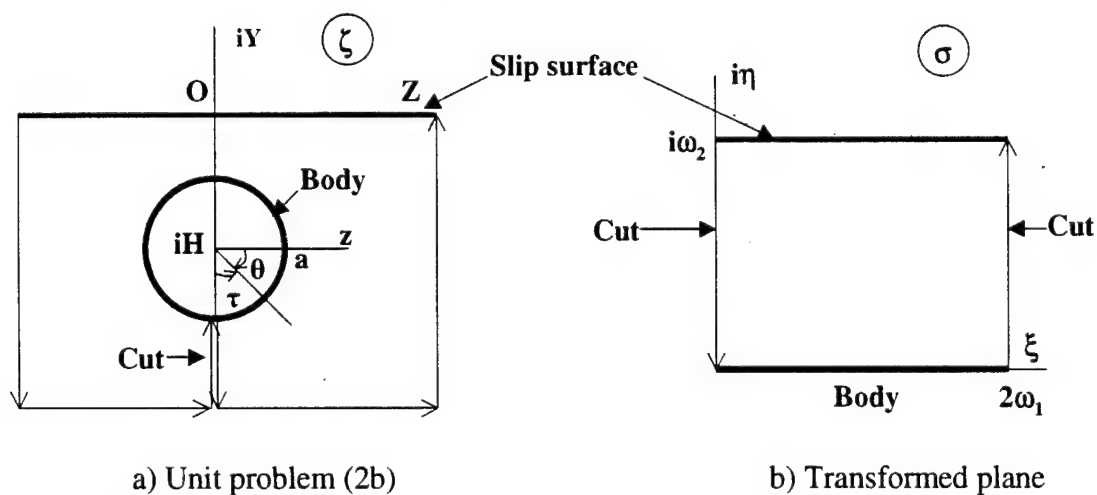


Fig. 1.6 Flow scheme and transformed plane for the unit problem (2b).

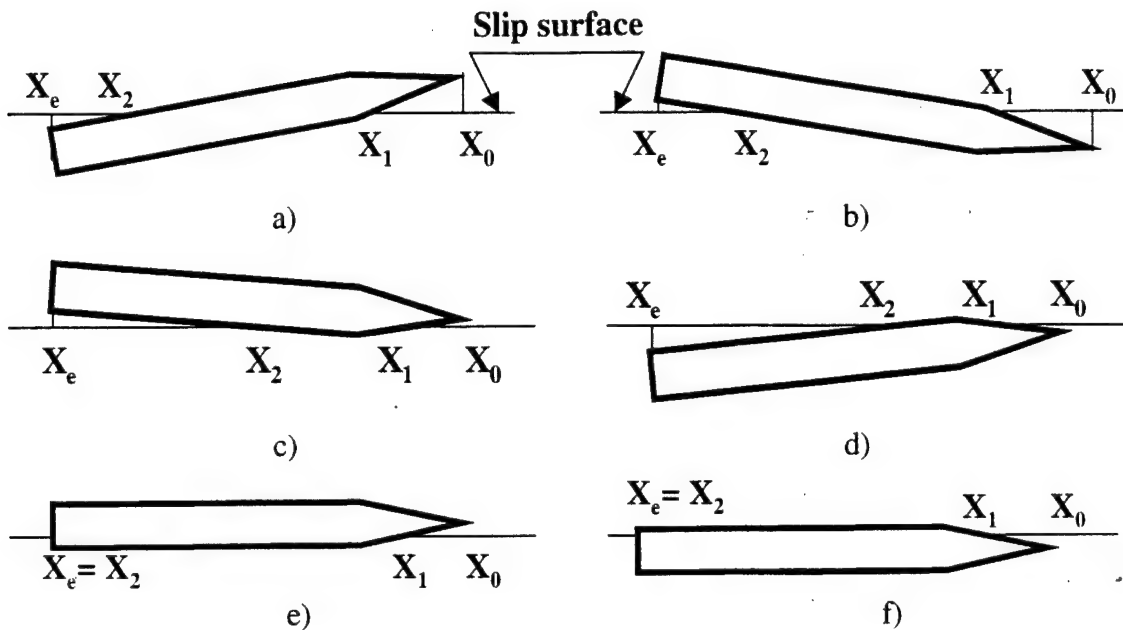


Fig. 1.7 Different body disposition with respect to the slip surface in Phase 2.

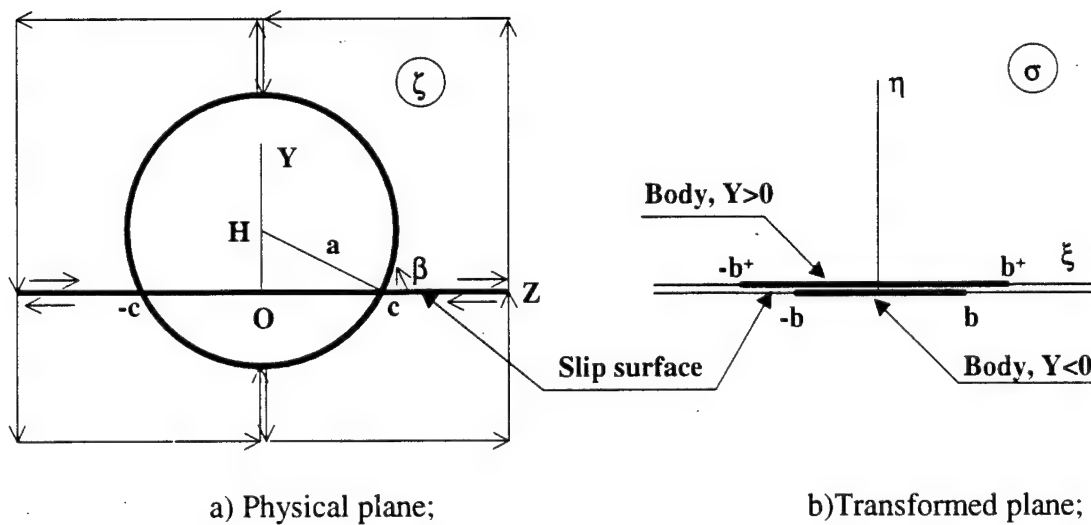


Fig. 1.8 Cross-section flow scheme for Phase 2; the contour of integration and the transformed plane.

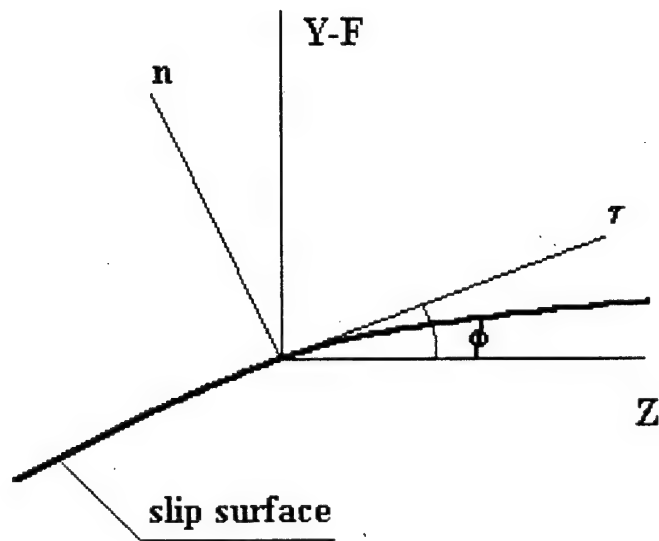


Fig. 1.9 Curvilinear coordinates on slip surface.

Appendix A

Calculation of the integrals I_b and I_b^+

Using the relation $\zeta_b = a \exp(i\theta) = -ia \exp(i\vartheta)$, where $\vartheta = \pi/2 + \theta$ is the polar angle measured from the symmetry plane (see Fig. 1.6a) we represent the Cauchy integrals $I_b^+(Z)$ and $I_b(Z)$ along the body surface as

$$\begin{aligned}
 I_b(X, Z, t) &= \operatorname{Re} i \oint_b \frac{w_0(\zeta_b) - iv_0(\zeta_b)}{s_b - Z} d\zeta_b = a \operatorname{Re} \int_0^{2\pi} \frac{iw_{0\theta}(\vartheta) - v_{0n}(\vartheta)}{iH - Z - ia e^{i\vartheta}} d\vartheta = \\
 &= a \operatorname{Re} \int_0^{2\pi} \frac{w_{0\theta}(\vartheta) + iv_{0n}(\vartheta)}{H + iZ - ae^{i\vartheta}} d\vartheta = a \operatorname{Re} \int_0^{2\pi} \frac{[w_{0\theta}(\vartheta) + iv_{0n}(\vartheta)] d\vartheta}{(H + iZ) \left(1 - \frac{a}{H + iZ} e^{i\vartheta}\right)} = \\
 &= \operatorname{Re} \sum_{n=0}^{\infty} \left(\frac{aH}{H^2 + Z^2} \right)^{n+1} \left(1 - i \frac{Z}{H}\right)^{n+1} \int_0^{2\pi} [w_{0\theta}(\vartheta) + iv_{0n}(\vartheta)] e^{in\vartheta} d\vartheta. \\
 I_b^+(X, Z, t) &= a \operatorname{Re} \int_0^{2\pi} \frac{iw_{0\theta}^+(\tau) - v_{0n}^+(\tau)}{iH - Z - ia e^{i\tau}} d\tau = \\
 &= \operatorname{Re} \sum_{n=0}^{\infty} \left(\frac{aH}{H^2 + Z^2} \right)^{n+1} \left(1 - i \frac{Z}{H}\right)^{n+1} \int_0^{2\pi} [w_{0\theta}^+(\tau) + iv_{0n}^+(\tau)] e^{in\tau} d\tau.
 \end{aligned}$$

Here $w_{0\theta}(\theta)$ is velocity tangential to the body surface. Accounting for symmetry properties of the tangential velocity and the expression (1.2.3b) for the normal velocity, we obtain

$$\begin{aligned}
 \int_0^{2\pi} [w_{0\theta}(\vartheta) + iv_{0n}(\vartheta)] e^{in\vartheta} d\vartheta &= i \int_0^{2\pi} [w_{0\theta}(\vartheta) \sin n\vartheta + v_{0n}(\vartheta) \cos n\vartheta] d\vartheta = 2\pi i (w_{0n} + a_{x1} - V_{e1}), \\
 w_{0n}(X, t) &= \frac{1}{2\pi} \int_0^{2\pi} w_{0\theta}(X, t, \vartheta) \sin(n\vartheta) d\vartheta. \tag{A.1}
 \end{aligned}$$

Using the binomial formula and separating the summation by odd and even indices, we find

$$\left(1 - i \frac{Z}{H}\right)^{n+1} = \sum_{k=0}^{\left[\frac{n+1}{2}\right]} (-1)^k C_{n+1}^{2k} \left(\frac{Z}{H}\right)^{2k} - i \frac{Z}{H} \sum_{k=0}^{\left[\frac{n}{2}\right]} (-1)^k C_{n+1}^{2k+1} \left(\frac{Z}{H}\right)^{2k},$$

where the symbol $\left[\frac{n}{2}\right]$ denote the integer part of the fraction. Accounting for these relations we obtain the expressions

$$I_b = \frac{2\pi aZ}{H^2 + Z^2} \left\{ a_{x1} + \frac{aH}{H^2 + Z^2} \left[w_{01} - V_{e1} + \sum_{n=2}^{\infty} w_{0n} \left(\frac{aH}{H^2 + Z^2} \right)^{n-1} \sum_{k=0}^{\left[\frac{n}{2} \right]} (-1)^k C_{n+1}^{2k+1} \left(\frac{Z}{H} \right)^{2k} \right] \right\}. \quad (\text{A.2a})$$

$$I_b^+ = \frac{2\pi a^2 HZ}{(H^2 + Z^2)^2} \left\{ w_{01}^+ - V_{e1}^+ + \sum_{n=2}^{\infty} w_{0n}^+ \left(\frac{aH}{H^2 + Z^2} \right)^{n-1} \sum_{k=0}^{\left[\frac{n}{2} \right]} (-1)^k C_{n+1}^{2k} \left(\frac{Z}{H} \right)^{2k} \right\}. \quad (\text{A.2b})$$

Calculation of the function $S_0(\lambda, \tau, Z)$

Consider the Cauchy type integral

$$Q_0 = \frac{1}{2\pi^3} \int_{-\infty}^{\infty} \frac{I_b(X, t, Z') dZ'}{Z' - Z} = \frac{a}{\pi^2} \left[a_{1X} I_{0,0} + aH(w_{01} - V_{e1}) I_{0,1} + \sum_{n=2}^{\infty} w_{0n} \sum_{k=0}^{\left[\frac{n}{2} \right]} (-1)^k C_{n+1}^{2k+1} (aH)^{n-2k} I_{k,n} \right], \quad (\text{A.3a})$$

$$I_{0,0} = \int_{-\infty}^{\infty} \frac{Z' dZ'}{(Z' - Z)(H^2 + Z'^2)}, \quad I_{0,1} = \int_{-\infty}^{\infty} \frac{Z' dZ'}{(Z' - Z)(H^2 + Z'^2)^2}, \quad (\text{A.3b})$$

$$I_{k,n} = \int_{-\infty}^{\infty} \frac{Z'^{2k+1} dZ'}{(Z' - Z)(H^2 + Z'^2)^{n+1}}. \quad (\text{A.3c})$$

The principal value of the integral $I_{k,n}$ is expressed as

$$I_{k,n} = \int_{-\infty}^{\infty} \frac{(Z'^{2k+1} - Z^{2k+1}) dZ'}{(Z' - Z)(H^2 + Z'^2)^{n+1}} + Z^{2k+1} \int_{-\infty}^{\infty} \frac{dZ'}{(Z' - Z)(H^2 + Z'^2)^{n+1}} = \sum_{m=0}^k e_m Z^{2m} + Z^{2k+1} I_n$$

The coefficients e_m are calculated using the table integral [19]

$$e_m = \int_{-\infty}^{\infty} \frac{Z'^{2(k-m)} dZ'}{(H^2 + Z'^2)^{n+1}} = \frac{\pi}{H} \frac{[2(k-m)-1]! [2(n-k+m)-1]!}{2^n n! H^{2(n-k+m)}}. \quad (\text{A.4})$$

For the integral I_n , we have the recurrent relation

$$I_n = \int_{-\infty}^{\infty} \frac{dZ'}{(Z' - Z)(H^2 + Z'^2)^{n+1}} = -\frac{Z i_n - I_{n-1}}{H^2 + Z'^2} = -\frac{Z}{H^2 + Z^2} \sum_{m=0}^n \frac{i_{n-m}}{(H^2 + Z^2)^m} + \frac{I_0}{(H^2 + Z^2)^n}.$$

Using the table of integrals [19] we find

$$i_{n-m} = \int_{-\infty}^{\infty} \frac{dZ'}{(H^2 + Z'^2)^{n-m+1}} = \frac{\pi[2(n-m)-1]!!}{2^{n-m} H H^{2(n-m)} (n-m)!}, \quad I_0 = -\frac{\pi Z}{H(H^2 + Z^2)}.$$

Then, we obtain

$$I_n = -\frac{\pi Z}{2^n H H^{2n} (H^2 + Z^2)} \left[\sum_{m=0}^n \frac{2^m [2(n-m)-1]!!}{(n-m)!} \left(\frac{H^2}{H^2 + Z^2} \right)^m + \left(\frac{2H^2}{H^2 + Z^2} \right)^n \right]. \quad (A.5)$$

Thus, the integral is represented as the explicit function of the transverse coordinate Z , vertical location of the body axis $H(X, t)$ and the body radius $a(x)$

$$I_{k,n} = \frac{\pi}{H} \frac{1}{2^n H^{2(n-k)}} \left\{ \sum_{m=0}^k \frac{[2(k-m)-1]!! [2(n-k+m)-1]!!}{n!} \left(\frac{Z^2}{H^2} \right)^m - \frac{Z^{2k+2}}{H^2 + Z^2} \left[\sum_{m=0}^n \frac{2^m [2(n-m)-1]!!}{(n-m)!} \left(\frac{H^2}{H^2 + Z^2} \right)^m + \left(\frac{2H^2}{H^2 + Z^2} \right)^n \right] \right\}. \quad (A.6)$$

The formulas for $I_{0,0}$ and $I_{0,1}$ are obtained by substituting $k=0$, $n=0,1$ to Eq. (A.6)

$$I_{0,0} = \frac{\pi H}{H^2 + Z^2}, \quad I_{0,1} = \frac{\pi(H^2 - Z^2)}{2H(H^2 + Z^2)^2}. \quad (A.7)$$

Now we can find the explicit dependence of the function Q_0 on the variables Z , $H(X, t)$ and $a(x)$. It is expressed in the compact form

$$Q_0 = \frac{2q}{\pi} \left\{ \frac{a_{1X}}{1 + \bar{Z}^2} + q(w_{01} - V_{e1}) \frac{1 - \bar{Z}^2}{(1 + \bar{Z}^2)^2} + \sum_{n=2}^{\infty} \frac{w_{0n} q^n}{n!} \sum_{k=0}^{\left[\frac{n}{2} \right]} (-1)^k C_{n+1}^{2k+1} \times \right. \\ \left. \times \left[\sum_{m=0}^k \frac{[2(k-m)-1]!! [2(n-k+m)-1]!!}{(n-m)!} \bar{Z}^{2m} - \frac{n! \bar{Z}^{2k+2}}{1 + \bar{Z}^2} \left\langle \sum_{m=0}^n \frac{[2(n-m)-1]!!}{(n-m)!} \left(\frac{2}{1 + \bar{Z}^2} \right)^m + \left(\frac{2}{1 + \bar{Z}^2} \right)^n \right\rangle \right] \right\}, \quad (A.8a)$$

$$\bar{Z} = \frac{Z}{H}, \quad q = \frac{a}{2H}. \quad (A.8b)$$

Integrals for the solution of Phase 2

Because the above equations are singular at $H = 0$ we present them in the form

$$I_b(X, Z, t) = \operatorname{Re} i \int_{Y_c < F} \frac{w_1(\zeta_b) - i v_1(\zeta_b)}{\zeta_b - Z} d\zeta_b = a \operatorname{Re} \int_{-\beta}^{\beta} \frac{w_{\theta 1}(\vartheta) + i v_{n 1}(\vartheta)}{(H + iZ) \left(1 - \frac{a}{H + iZ} e^{i\vartheta}\right)} d\vartheta =$$

$$= \operatorname{Re} i \left\{ \frac{2\beta a a_x}{H + iZ} + \left[\pi w_{01} + V_{e1} \left(\beta + \frac{1}{2} \sin 2\beta \right) \right] \left(\frac{a}{H + iZ} \right)^2 + \pi \sum_{n=2}^{\infty} w_{0n} \left(\frac{a}{H + iZ} \right)^{n+1} \right\}. \quad (\text{A.9a})$$

$$I_b^+(X, Z, t) = a \operatorname{Re} \int_{\beta}^{2\pi-\beta} \frac{[w_{\theta 1}^+(\vartheta) + i v_{n 1}^+(\vartheta)] d\vartheta}{(H + iZ) \left(1 - \frac{a}{H + iZ} e^{i\vartheta}\right)} =$$

$$= \operatorname{Re} i \left\{ \left[\pi w_{01}^+ - V_{e1}^+ \left(\pi - \beta - \frac{1}{2} \sin 2\beta \right) \right] \left(\frac{a}{H + iZ} \right)^2 + \pi \sum_{n=2}^{\infty} w_{0n}^+ \left(\frac{a}{H + iZ} \right)^{n+1} \right\}. \quad (\text{A.9b})$$

$$w_{0n} = \frac{1}{\pi} \int_0^{\beta} w_{\theta}(\vartheta) \sin(n\vartheta) d\vartheta, \quad w_{0n}^+ = \frac{1}{\pi} \int_{\beta}^{\pi} w_{\theta}^+(\vartheta) \sin(n\vartheta) d\vartheta. \quad (\text{A.9c})$$

The function Q_0 is expressed as

$$Q_0 = \frac{1}{2\pi^3} \int_{-\infty}^{\infty} \frac{I_b(X, t, y) dy}{y - Z} =$$

$$= -\frac{1}{2\pi^3} \operatorname{Im} \left\{ 2\beta a a_{1X} I_0 + a^2 \left[w_{01} - V_{e1} \left(\beta + \frac{\sin 2\beta}{2} \right) \right] I_1 + \sum_{n=2}^{\infty} w_{0n} a^{n+1} I_n \right\}.$$

The integral I_n , $n = 0, 1, \dots$ is calculated using the table of integrals [22]

$$I_n = \left(\int_c^{\infty} + \int_{-\infty}^{-c} \right) \frac{dy}{(y - Z)(H + iy)^{n+1}} =$$

$$= \left(\frac{H - iZ}{H^2 + Z^2} \right)^{n+1} \left\{ \ln \frac{c - iH}{c - Z} - \ln \frac{c + iH}{c + Z} + \sum_{m=1}^n \frac{C_n^m}{m} \left[\left(\frac{c + Z}{c + iH} \right)^m - \left(\frac{c - Z}{c - iH} \right)^m \right] \right\} =$$

$$= \left\{ \ln \frac{Z + c}{Z - c} + 2 \sum_{m=1}^n \frac{C_n^m \cos m\beta}{m} [(Z + c)^m - (c - Z)^m] - \right.$$

$$\left. - i \left[\pi - 2\beta + 2 \sum_{m=1}^n \frac{C_n^m \sin m\beta}{m} [(Z + c)^m + (c - Z)^m] \right] \right\} \times$$

$$\times \frac{1}{(H^2 + Z^2)^{n+1}} \sum_{k=1}^n (-1)^k H^{n-2k} Z^{2k} (H C_{n+1}^{2k} - i Z C_{n+1}^{2k+1}).$$

The imaginary part of this expression is

$$\begin{aligned}
\operatorname{Im} I_n = & \frac{-1}{(H^2 + Z^2)^{n+1}} \left\{ \ln \frac{Z+c}{Z-c} + \right. \\
& + 2 \sum_{m=1}^n \frac{C_n^m \cos m\beta}{m} [(Z+c)^m - (c-Z)^m] \sum_{k=1}^n (-1)^k C_{n+1}^{2k+1} H^{n-2k} Z^{2k+1} + \\
& \left. + \left\langle \pi - 2\beta + 2 \sum_{m=1}^n \frac{C_n^m \sin m\beta}{m} [(Z+c)^m + (c-Z)^m] \right\rangle \sum_{k=1}^n (-1)^k C_{n+1}^{2k} H^{n-2k+1} Z^{2k} \right\} \quad (\text{A.10})
\end{aligned}$$

At $n = 0, 1$ we obtain

$$\operatorname{Im} I_0 = \frac{-1}{H^2 + Z^2} \left[Z \ln \frac{Z+c}{Z-c} + H(\pi - 2\beta) \right], \quad (\text{A.11a})$$

$$\operatorname{Im} I_1 = \frac{-1}{(H^2 + Z^2)^2} \left[2HZ \ln \frac{Z+c}{Z-c} + (H^2 - 2Z^2)(\pi - 2\beta + 2\sin^2 \beta) + 8Z^2 \cos^2 \beta \right]. \quad (\text{A.11b})$$

Part 2. Analytical Solutions in the First Order Approximation

2.1 Introduction

In Part 1, using slender body theory and the method of small perturbations [5, 6] we analyzed the near-field flows over a thin body of revolution separating from a deep rectangular cavity into subsonic or transonic external streams. The problem formulation, notations and scaling for the inner asymptotic region were provided. Aerodynamic problems relevant to Phase 1 (body is inside the cavity), Phase 2 (body crosses the shear layer) and Phase 3 (body is outside the cavity) were decomposed and simplified. It was shown that in the inner asymptotic region, the cavity side-wall effect can be neglected for all three phases. In this framework, the shear layer separating the cavity interior from external stream is treated as a slip surface with continuous density, pressure and normal velocity across it. The problem of the slip-surface displacement induced by the body motion is challenging. It was isolated from other unit problems and reduced to a system of nonlinear integrodifferential equations for the tangential velocity on the body surface and the slip surface. It was shown that this system can be solved by iterations. In the first step, a plane of zero potential approximates the slip surface and the problem is decomposed into the following unit problems:

1. Thin body of revolution drops from a flat rigid wall:
 - a) to fluid at rest;
 - b) to the stream;
2. Thin body of revolution drops:
 - a) in fluid at rest toward a flat slip surface of zero potential;
 - b) away from a flat slip surface of zero potential in the free stream;
3. Thin body of revolution crosses a flat slip surface of zero potential.

Problems 1a and 2a allow us to find solutions for Phases 1; Problem 3 corresponds to Phase 2; Problem 2b gives the solution for Phase 3; Problem 1b is relevant to external store separation. Using the multipole expansion technique [9], we solve Problems 1, 2 in a Laurent series and obtain coefficients up to the fifth term. This is suitable for explicit calculations of the flow characteristics with appropriate accuracy. To solve Problem 3, we use the method of conformal mapping [8,10,15]. Some terms of the solutions of Problems 1-3 are known, and we use them for cross checking. The other terms, relevant to three-dimensional effects have not been determined elsewhere.

From the solutions of these aerodynamic problems we derive analytical expressions for the lift force and pitching moment acting on the body in all phases of its motion. This allows us to identify key parameters, extract dominant physics effects and develop a robust method giving rapid predictions of body trajectories. In this chapter, we do not discuss the yaw and streamwise components of the body motion. However, our theory can be easily extended to treat these effects. The streamwise component associated with the aerodynamic drag will be analyzed in Part 4.

In Section 2.2, we formulate the unit problems for Phases 1 and 3 and obtain their analytical solutions using the multipole expansion method. We derive explicit dependencies of the lift force and pitching moment on the body trajectory parameters. In Section 2.3, we formulate and solve the unit problems relevant to Phase 2. Then we derive explicit expressions for the cross-sectional lift force components and obtain relations for the total lift force and pitching moment. In Section 2.4, we verify the solutions obtained in previous sections by comparison with known analytical results [15, 16, 24]. In Section 2.5, we conclude the chapter. Appendices B and C include treatment of improper and Cauchy type integrals of relevance to the analysis.

2.2 Unit problems for body dropping inside and outside the cavity (Phases 1 and 3)

We consider here Problems 1a), 1b), 2a) and 2b) in the inner asymptotic region. A combination of solutions of Problems 1a) and 2a) describes Phase 1; Problem 1b) is relevant to external store separation; Problem 2b) corresponds to Phase 3.

Within the framework of slender body theory [5-7], the complex conjugate velocity $W(X, \zeta, t) = w - iv$ is an analytical function of the complex variable $\zeta = Z + iY$ in the cross-section planes. The body cross-section profile is a circle of radius $a(X)$ centered at the point $\zeta = iH(X, t)$. This circle moves with the vertical velocity $V_e(x, t) = V_o(t) - \omega(t)x - \alpha(t)$ in a uniform stream or with the velocity $V_e^+(x, t) = V_o(t) - \omega(t)x$ in fluid at rest (within cavity). Let the wall or slip surface coincide with the plane $Y = 0$. For half planes containing the body, we have the following problem:

- Find an analytical function $W(X, \zeta, t)$ that satisfies Eqs. (1.1.7) for a specified normal velocity on the circle and has zero real (imaginary) part on the slip surface (wall).

The analytical continuation through the wall and the slip surface gives $W(\bar{\zeta}) = \overline{W}(\zeta)$ and $W(\bar{\zeta}) = -\overline{W}(\zeta)$ respectively. Here, the overbar denotes complex conjugation. From these conditions we reduce the half plane problem containing the circle to problems for the full space containing two identical circles located symmetrically with respect to the plane $Y = 0$. The flow scheme in the cross-section plane is shown in Fig. 2.1.

In Part 1, the solutions of these problems are expressed in a general form containing the boundary integrals. This form was derived using a conformal mapping of the flow region to a ring and then to a rectangle. However, since the slip-surface shape is trivial in the first iteration, the method of multipole expansions [9] is more appropriate for the analysis. It allows us to express the solutions in the form of a Laurent series and obtain relatively simple analytical expressions for aerodynamic forces and moments. As contrasted to the problem analyzed in Ref. [9], the considered problems are three-dimensional. This leads to new effects, which has not been previously studied and motivates us to represent details of our analysis as well as discuss the new results.

2.2.1 Solutions obtained by the multipole expansion method

Using the Cauchy formula we obtain the integral equation for the function $W(X, \zeta, t)$ [9]

$$W(X, \zeta, t) = \frac{1}{2i\pi} \int_{|\bar{s}|=a} \frac{W(X, iH + s, t) ds}{\zeta - iH - s} + \frac{1}{2i\pi} \int_{|\bar{s}|=a} \frac{W(-iH + \bar{s}) d\bar{s}}{\zeta + iH - \bar{s}}. \quad (2.1.1)$$

Expanding the kernels into Taylor series, using the analytical continuation and flow symmetry we obtain the solution of this equation and the complex potential in the form of the series

$$W = \sum_{n=0}^{\infty} a^{n+1} \left\{ \frac{C_{-n-1}}{(\zeta - iH)^{n+1}} \pm \frac{\bar{C}_{-n-1}}{(\zeta + iH)^{n+1}} \right\}, \quad (2.1.2a)$$

$$\Pi = A_0(X, t) + aA_{-1}[\ln(\zeta - iH) \pm \ln(\zeta + iH)] - \sum_{n=1}^{\infty} \frac{a^{n+1}}{n} \left[\frac{C_{-n-1}}{(\zeta - iH)^n} \pm \frac{\bar{C}_{-n-1}}{(\zeta + iH)^n} \right], \quad (2.1.2b)$$

$$C_{-n-1} = A_{-n-1} + iB_{-n-1}, \quad A_{-2n} = 0, \quad B_{-2n-1} = 0. \quad (2.1.2c)$$

Here the upper (lower) sign corresponds to the body motion near the wall (slip surface). The function $A_0(X, t)$ is determined from matching of the inner solution (2.1.2) with the outer asymptotic solution. It does not affect the lift force and pitching moment and will be considered in Part 4. Functions $C_{-n-1}(X, t)$ are coefficients in the Laurent series of the complex conjugate velocity at the points $\zeta = iH(X, t)$; $A_{-n-1}(X, t)$ and $B_{-n-1}(X, t)$ are their real and imaginary parts. They are found from the boundary condition on the body surface. For a body dropping into the stream from the wall or slip surface, this condition leads to the infinite system of the linear algebraic equations

$$A_{-1} = a_x, \quad B_{-2} = V_e \pm q \sum_{m=0}^{\infty} (-1)^m q^{2m} (A_{-2m-1} + qB_{-2m-2}), \quad (2.1.3a)$$

$$A_{-2n-1} = \pm \frac{(-1)^n q^{2n}}{(2n-1)!} \sum_{m=0}^{\infty} \frac{(2m+2n-1)!}{2m!} (-1)^m q^{2m} \left(A_{-2m-1} + \frac{2m+2n}{2m+1} qB_{-2m-2} \right), \quad (2.1.3b)$$

$$B_{-2n-2} = \pm \frac{(-1)^n q^{2n+1}}{(2n)!} \sum_{m=0}^{\infty} \frac{(2m+2n)!}{2m!} (-1)^m q^{2m} \left(A_{-2m-1} + \frac{2m+2n+1}{2m+1} qB_{-2m-2} \right). \quad (2.1.3c)$$

Here, $q(X, t) = 0.5a(X)/|H(X, t)| \leq 0.5$. If the body is a cylinder or it drops in fluid at rest (inside the cavity), then $A_{-1} = a_x = 0$ and the other coefficients are determined from a system of algebraic equations similar to (2.1.3). In this case, these equations coincide with the system formulated in Ref. [9].

Note that this approach can be applied to non-circular body cross sections with the coefficients (2.1.3) determined as Fourier series coefficients of the function $v_n(\theta)$. Accordingly, this method can be used to find solutions in the σ_1 -plane defined by Eqs.

(1.3.11). Thus, in every iteration of the general problem considered in Section 1.3, an explicit form of the complex conjugate velocity can be obtained without mapping of the flow region to a rectangle. This leads to significant simplification of the iteration procedure. For practical calculations, we present the approximate solutions of Eqs. (2.1.3) as a power series in the parameter q .

To accuracy $O(q^8)$ (where $q^8 \leq 1/256$) the solution of Problem 1b (for the circle dropping into a stream from a rigid wall) has the coefficients

$$B = V_e [1 + q^2 S_1(q)] + q a_x S_2(q) + O(q^9), \quad (2.1.4a)$$

$$A_{-3} = -q^2 [a_x (1 + 2q^2 + 5q^4 + 14q^6) + 2V_e q (1 + q^2 + 4q^4)] + O(q^9), \quad (2.1.4b)$$

$$S_1(q) = 1 + q^2 + 3q^4 + 8q^6 + O(q^8), \quad S_2(q) = 1 + q^2 + 2q^4 + 5q^6 + O(q^8). \quad (2.1.4c)$$

For a fluid at rest (Problem 1a), the coefficients are given by Eqs. (2.1.4) with $a_x = 0$ and V_e replaced by V_e^+ .

For a circle dropping in a stream from the free surface (Problem 2b) we obtain

$$B = V_e [1 - q^2 S_3(q)] - q a_x S_4(q) + O(q^9), \quad (2.1.5a)$$

$$A_{-3} = q^2 [a_x (1 - 2q^2 - q^4 - 4q^6) + 2q V_e (1 - q^2 + q^4)] + O(q^9), \quad (2.1.5b)$$

$$B_{-4} = q^3 [a_x (1 - 3q^2 - 3q^4) + 3q V_e (1 - q^2 - 3q^4)] + O(q^9), \quad (2.1.5c)$$

$$A_{-5} = -q^4 [a_x (1 - 4q^2 - 6q^4) + 4q V_e (1 - q^2)] + O(q^9), \quad (2.1.5d)$$

$$S_3 = 1 - q^2 - q^4 - 2q^6, \quad S_4(q) = 1 - q^2 - 3q^6. \quad (2.1.5e)$$

When the body drops to the slip surface in a quiescent fluid (Problem 2a), these expressions reduce to

$$B = V_e^+ [1 - q^2 S_5(q)] + O(q^9), \quad S_5(q) = 1 - q^2 - q^4 + O(q^7), \quad (2.1.6a)$$

$$A_{-3} = -2V_e^+ q^3 (1 - q^2 - 2q^4) + O(q^9), \quad B_{-4} = 3V_e^+ q^4 (1 - q^2 - 4q^4) + O(q^9). \quad (2.1.6b)$$

As discussed in Part 1 and for Phase 1 (body drops in the cavity), the complete solution is expressed as a superposition of the two solutions: $W_1^+(X, \zeta, t)$ (corresponding to the body dropping from the top wall) and $(W_2^+(X, \zeta, t) - W_0^+(\zeta; X, t))$ corresponding to the body dropping toward the slip surface. This composite solution is

$$W^+(\zeta; X, t) = W_1^+(\zeta; X, t) + W_2^+(\zeta; X, t) - W_0^+(\zeta; X, t),$$

where W_0^+ is the common part of the both solutions corresponding to the circle motion in the unbounded flow.

In the coordinate system oxy_z attached to the body CG, the pressure and flow potential relevant to Phase 3 are represented as

$$p = -\frac{\partial \Phi}{\partial t} - \frac{\partial \Phi}{\partial x} + V_e \frac{\partial \Phi}{\partial y} - \frac{1}{2} [v^2 + w^2], \quad (2.1.7a)$$

$$\Phi = A_0 + aa_x \ln \frac{r}{a} - \left[(B - V_e)r + \frac{Ba^2}{r} \right] \sin \theta - a \sum_{n=1}^{\infty} \left\{ A_{-2n-1} \left[\left(\frac{r}{a} \right)^{2n} + \left(\frac{a}{r} \right)^{2n} \right] \frac{\cos 2n\theta}{2n} + B_{-2n-2} \left[\left(\frac{r}{a} \right)^{2n+1} + \left(\frac{a}{r} \right)^{2n+1} \right] \frac{\sin(2n+1)\theta}{2n+1} \right\}. \quad (2.1.7b)$$

where r and θ are polar radius and angle in a cross-section plane shown in Fig. 2.1. On the body surface, the potential and its derivatives are given by

$$\Phi = A_0 - (2B - V_e)a \sin(\theta) + \phi, \quad \phi = -2a \sum_{n=1}^{\infty} \left\{ \frac{A_{-2n-1}}{2n} \cos(2n\theta) + \frac{B_{-2n-2}}{2n+1} \sin[(2n+1)\theta] \right\}.$$

$$w_\theta = \frac{1}{a} \frac{\partial \Phi}{\partial \theta} = -(2B - V_e) \cos(\theta) + u_1.$$

$$u_1 = \frac{1}{a} \frac{\partial \phi}{\partial \theta} = 2 \sum_{n=1}^{\infty} \{ A_{-2n-1} \sin(2n\theta) - B_{-2n-2} \cos[(2n+1)\theta] \}.$$

$$\frac{\partial \Phi}{\partial x} = (A_0 + \phi)_x - a_x^2 - \left\{ \frac{[(2B - V_e)a^2]_x}{a} - 2(B - V_e)a_x \right\} \sin \theta.$$

$$\frac{\partial \Phi}{\partial t} = (A_0 + \phi)_t - a(2B - V_e)_t \sin(\theta).$$

Substituting these relations into Eq. (2.1.6), we obtain the pressure on the body surface

$$p = \left\{ a(2B - V_e)_t + \frac{[(2B - V_e)a^2]_x}{a} - 2(B - V_e)a_x \right\} \sin \theta + 2Bu_1 \cos \theta - \frac{u_1^2}{2} + \\ - (A_0 + \phi)_t - (A_0 + \phi)_x + \frac{V_e^2 - a_x^2}{2} - 2B^2 \cos^2 \theta. \quad (2.1.8)$$

For Phase 1, the pressure $p^+(X, r, \theta, t)$ and potential $\Phi^+(X, r, \theta, t)$ are given by (2.1.8) with $A_0 = a_x = \Phi_x^+ = 0$ and V_e replaced by V_e^+ . Then, the pressure on the body surface is determined by the formula

$$p^+ = a(2B - V_e^+)_t \sin \theta + 2Bu_1 \cos \theta - \frac{u_1^2 - V_e^{+2}}{2} - \phi_t - 2B^2 u_1 \cos^2 \theta. \quad (2.1.9)$$

Using the expression for the tangential velocity on the body surface, in the first order approximation we obtain the coefficients w_{0n} in the expansions (1.2.12) or w_n in the relation (1.3.5a) of Part 1. They are expressed as

$$\begin{aligned} w_1(X, t) &= -\frac{2B_{-2}(X, t) - V_e}{2}, \\ w_{2n}(X, t) &= (-1)^n A_{-2n-1}(X, t), \\ w_{2n+1}(X, t) &= (-1)^n B_{-2n-2}(X, t). \end{aligned}$$

Similar relations give the coefficients w_{0n}^+ and w_n^+ .

2.2.2 Lift force and pitching moment calculations

The dimensional forms of the local, $L_x(x, t)$, and total, $L(t)$, lift forces as well as the pitching moment, $M(t)$, are expressed as

$$L_x(x, t) = -a \int_0^{2\pi} p \sin \theta d\theta; \quad L(t) = \int_{x_0}^{x_e} L_x(x, t) dx; \quad M(t) = \int_{x_0}^{x_e} L_x(x, t) x dx$$

Evaluating the pressure from Eqs. (2.1.8) and (2.1.9) we obtain the following expressions for the cross-sectional lift force (in the case of the body dropping inside the stream and in the cavity)

$$\begin{aligned} L_x = -\pi \left\{ \frac{\partial[(2B - V_e)a^2]}{\partial x} + a^2 \frac{\partial(2B - V_e)}{\partial t} - \right. \\ \left. - 2(B - V_e)aa_x + 2BA_{-3}a - 2a \sum_{n=1}^{\infty} (A_{-2n-1} - A_{-2n-3})B_{-2n-2} \right\}, \end{aligned} \quad (2.1.10a)$$

$$L_x^+ = -\pi a \left[a \frac{\partial(2B^+ - V_e^+)}{\partial t} + 2B^+A_{-3} - 2 \sum_{n=1}^{\infty} (A_{-2n-1} - A_{-2n-3})B_{-2n-2} \right]. \quad (2.1.10b)$$

Integrating these equations along the body axis we derive formulas for the lift force and pitching moment. If the body is inside the cavity, then

$$L^+(t) = -\frac{dV_a^+(t)}{dt} + L_1^+(t), \quad M^+(t) = -\frac{d\omega_a^+(t)}{dt} + M_1^+(t), \quad (2.1.11a)$$

$$L_1^+(t) = -2\pi \int_{x_0}^{x_e} \left[B^+A_{-3} - \sum_{n=1}^{\infty} (A_{-2n-1} - A_{-2n-3})B_{-2n-2} \right] a(x) dx, \quad (2.1.11b)$$

$$M_1^+(t) = -2\pi \int_{x_0}^{x_e} \left[B^+A_{-3} - \sum_{n=1}^{\infty} (A_{-2n-1} - A_{-2n-3})B_{-2n-2} \right] a(x) x dx, \quad (2.1.11c)$$

$$V_a^- = \pi \int_{x_0}^{x_e} [2B^+(x,t) - V_e^-(x,t)] a^2(x) dx, \quad \omega_a^- = \pi \int_{x_0}^{x_e} [2B^-(x,t) - V_e^+(x,t)] a^2(x) dx. \quad (2.1.11d)$$

If the body drops inside the stream, then we obtain

$$L^-(t) = -\frac{dV_a^-(t)}{dt} + L_1^-(t), \quad M^-(t) = -\frac{d\omega_a^-(t)}{dt} + M_1^-(t). \quad (2.1.12a)$$

$$L_1^-(t) = -\pi a^2(x_e) [2B(x_e, t) - V_e(x_e, t)] + 2\pi \int_{x_0}^{x_e} \left[(B - V_e) a_x - BA_{-3} + \sum_{n=1}^{\infty} (A_{-2n-1} - A_{-2n-3}) B_{-2n-2} \right] a(x) dx, \quad (2.1.12b)$$

$$M_1^-(t) = V_a^- - \pi a^2(x_e) x_e [2B(x_e, t) - V_e(x_e, t)] + 2\pi \int_{x_0}^{x_e} \left[(B - V_e) a_x - BA_{-3} + \sum_{n=1}^{\infty} (A_{-2n-1} - A_{-2n-3}) B_{-2n-2} \right] a(x) x dx, \quad (2.1.12c)$$

$$V_a^-(t) = \pi \int_{x_0}^{x_e} [2B(x, t) - V_e(x, t)] a^2(x) dx, \quad (2.1.12d)$$

$$\omega_a^-(t) = \pi \int_{x_0}^{x_e} [2B(x, t) - V_e(x, t)] a^2(x) x dx. \quad (2.1.12e)$$

The first terms of the expressions (2.1.11a) and (2.1.12a) for the force and moment are due to the fluid inertia. The first terms of Eqs. (2.1.12b) and (2.1.12c) are associated with the pressure gradient in the stream along the body axis. The integral terms represent the effect of the flow boundary which vanish at great distances from it.

Explicit dependencies of the force and moment on the trajectory parameters are found by substituting into Eqs. (2.1.11)-(2.1.12) the coefficients $P(x, t)$, $A_{-2n-1}(x, t)$ and $B_{-2n-2}(x, t)$ given by Eqs. (2.1.4)-(2.1.6). For Phase 1, when the body drops in the cavity from the top wall $Y = H_0$ to the slip surface $Y = 0$, we use the composite solution. Then, we obtain

$$V_a^+(t) = \alpha_{11} V_o - \alpha_{12} \omega, \quad \omega_a^+(t) = \alpha_{12} V_o - \alpha_{22} \omega, \quad (2.1.13a)$$

$$\alpha_{11} = \pi [g_0 + G_0(t)], \quad \alpha_{12} = \pi [g_1 + G_1(t)], \quad \alpha_{22} = \pi [g_2 + G_2(t)] \quad (2.1.13b)$$

$$g_0 = \int_{x_0}^{x_e} a^2(x) dx, \quad g_1 = \int_{x_0}^{x_e} a^2(x) x dx, \quad g_2 = \int_{x_0}^{x_e} a^2(x) x^2 dx, \quad (2.1.13c)$$

$$G_0 = 2 \int_{x_0}^{x_e} [q_1^2 S_1(q_1) - q^2 S_5(q)] a^2 dx, \quad G_1 = 2 \int_{x_0}^{x_e} [q_1^2 S_1(q_1) - q^2 S_5(q)] a^2 x dx, \quad (2.1.13d)$$

$$G_2 = 2 \int_{x_0}^{x_e} [q_1^2 S_1(q_1) - q^2 S_5(q)] a^2 x^2 dx, \quad q_1 = \frac{a}{2(H_0 - H)}, \quad (2.1.13e)$$

$$B^+ A_{-3} - \sum_{n=1}^{\infty} (A_{-2n-1} - A_{-2n-3}) B_{-2n-2} = -2V_e^{+2} [q_1^3 (1 + 2q_1^2 + 9q_1^4) + q^3 (1 - 2q^2 - 3q^4)]. \quad (2.1.13f)$$

In Phase 3, when the body moves into the stream, we substitute Eqs. (2.1.4), (2.1.5) into Eqs. (2.1.12c) and express the functions $V_a^-(t)$ and $\omega_a^-(t)$ as

$$V_a^-(t) = \alpha_{11}(V_o - \alpha) - \alpha_{12}\omega + \alpha_{10}, \quad \omega_a^-(t) = \alpha_{12}(V_o - \alpha) - \alpha_{22}\omega + \alpha_{20}. \quad (2.1.14)$$

The coefficients of this equation are determined similar to the case of Eqs. (2.1.13). If the body drops from the wall, then

$$\begin{aligned} G_0 &= 2 \int_{x_0}^{x_e} S_1(q) q^2 a^2 dx; \quad G_1 = 2 \int_{x_0}^{x_e} S_1(q) q^2 a^2 x dx; \quad G_2 = 2 \int_{x_0}^{x_e} S_1(q) q^2 a^2 x^2 dx, \\ \alpha_{10} &= 2\pi \int_{x_0}^{x_e} S_2(q) q a^2 a_x dx, \quad \alpha_{20} = 2\pi \int_{x_0}^{x_e} S_2(q) q a^2 a_x x dx, \\ (B - V_e) a_x - B A_{-3} + \sum_{n=1}^{\infty} (A_{-2n-1} - A_{-2n-3}) B_{-2n-2} &= a_x^2 q (1 + 2q^2 + 6q^4 + 19q^6) + \\ &+ 2V_e^2 q^3 (1 + 2q^2 + 9q^4) + V_e a_x q^2 (2 + 6q^2 + 20q^4 + 63q^6) + O(q^9). \end{aligned} \quad (2.1.15)$$

If the body drops from the slip surface, then

$$\begin{aligned} G_0 &= -2 \int_{x_0}^{x_e} S_3(q) q^2 a^2 dx; \quad G_1 = -2 \int_{x_0}^{x_e} S_3(q) q^2 a^2 x dx; \quad G_2 = -2 \int_{x_0}^{x_e} S_3(q) q^2 a^2 x^2 dx, \\ \alpha_{10} &= -2\pi \int_{x_0}^{x_e} S_4(q) q a^2 a_x dx, \quad \alpha_{20} = -2\pi \int_{x_0}^{x_e} S_4(q) q a^2 a_x x dx, \\ (B - V_e) a_x - B A_{-3} + \sum_{n=1}^{\infty} (A_{-2n-1} - A_{-2n-3}) B_{-2n-2} &\approx -q a_x^2 (1 - 2q^2 + 2q^4) - \\ &- 2V_e a_x q^2 (1 - 3q^2 + 2q^6) - 2q^3 V_e^2 (1 - 2q^2 + 6q^4) + O(q^9). \end{aligned} \quad (2.1.16)$$

It is seen that the shear-layer effect is proportional to first power of q for body motion in the stream: *i.e.*, it is stronger than for the body motion inside the cavity. This is due to the three-dimensional effect associated with the axial variation of the body shape ($a_x \neq 0$). These expressions give the explicit dependencies of the lift force and pitching moment on the trajectory parameters, CG speed $V_o(t)$, angular speed $\omega(t)$, angle of attack $\alpha(t)$, and CG vertical coordinate $Y_o(t)$. They allow us to develop a fast numerical algorithm for solving the trajectory equations.

2.3 Unit problem for body crossing the slip surface (Phase 2)

We consider the flow induced by the body crossing the flat slip surface of zero potential. In Phase 2, the slip surface $Y = 0$ divides the body surface into three portions: typical configurations are shown on Fig. 1.7 of Part 1. Depending on the angle of attack and the submerging depth, the nose ($X_0 < X < X_1$) or/and the base portion ($X_2 < X < X_e$) is located in the cavity or/and in the stream: the solutions for these portions are presented in Section 2.2. The third portion ($X_1 < X < X_2$) is partially submerged into the stream. The flow schemes in the cross-section planes are shown in Figs. 1.2 and 1.3 of Part 1. The body surface intersects the slip surface at the line $Z = \pm c(X, t) = \pm a \sin \beta$, where $\beta(X, t) = \arccos(H/a)$ is the angle between the body and slip-surface cross-section contours. The upper portion of the circle moves with the vertical speed $V_e^+(X, t)$ in the fluid at rest; the normal velocity on its boundary is $v_n = V_e^+ \sin \theta$. The lower portion moves with the vertical speed $V_e(X, t)$ in the stream so that the normal velocity on its boundary is $v_n = a_x + V_e \sin \theta$. Thus, in each half plane separately we can formulate the problem:

- Find the complex conjugate velocity $W(X, \zeta, t)$, which provides a specified normal velocity on the corresponding circular arc and has zero real part on $Y = 0$, $|Z| > c$.

In Section 2.3.1 we solve analytically this problem using the conformal mapping method [10] and the Keldysh-Sedov formula [8].

2.3.1 Solution of the flow equations

The solution is obtained from conformal mapping of the upper and lower flow regions. The mapping of the stream region (in the lower half-plane of the complex variable $\sigma = \xi + i\eta$) has the form

$$\zeta = f^-(\sigma, X, t) = c \frac{R^n(\sigma, X, t) + 1}{R^n(\sigma, X, t) - 1}; \quad n(X, t) = \frac{\pi - \beta}{\pi}, \quad R = \frac{\sigma + b}{\sigma - b}, \quad b(X, t) = \frac{c}{n}, \quad (2.2.1a)$$

$$\frac{\partial \sigma}{\partial \zeta} = \frac{(\sigma^2 - b^2)(R^n - 1)^2}{4c^2 R^n}; \quad l(\xi, X, t) = \left| \frac{\partial \sigma}{\partial \zeta} \right|_{\eta=0, |\xi| < b} = \frac{(b^2 - \xi^2)D(\xi, n)}{4c^2 Q^n(\xi, b)}, \quad (2.2.1b)$$

$$Z(\xi)|_{\eta=0} = c \frac{Q^{2n} - 1}{D}, \quad Y(\xi)|_{\eta=0} = -2c \frac{Q^n}{D} \sin \pi n, \quad (2.2.1c)$$

$$D(\xi, n) = Q^{2n} - 2Q^n \cos \pi n + 1, \quad Q^n(\xi, b) = \frac{\xi + b}{\xi - b}. \quad (2.2.1d)$$

In the σ -plane, the submerged circle portion is transformed to the lower side of the interval $[-b, b]$. The mapping $\zeta = f^-(\sigma, X, t)$ of the cavity flow region to the upper half plane and the upper body portion to the upper side of the interval $[-b^+, b^+]$ is obtained by replacing $m = 1 - n$ by n in Eqs. (2.2.1). In the transformed space, the explicit solution is

found using Keldysh-Sedov formula [8]. After integration, the complex conjugate velocity and potential in the stream region are represented as

$$W(\sigma, X, t) = -iV_e \left(1 - \frac{\sigma}{\sqrt{\sigma^2 - b^2}} \frac{\partial \sigma}{\partial \zeta} \right) + \frac{a_x}{i\pi\sqrt{\sigma^2 - b^2}} \frac{\partial \sigma}{\partial \zeta} \int_{-b}^b \frac{\sqrt{b^2 - s^2} ds}{(s - \sigma)l(s)}, \quad (2.2.2a)$$

$$\Pi(\sigma, X, t) = -iV_e \left[\zeta(\sigma) - \sqrt{\sigma^2 - b^2} \right] - \frac{2iaa_x \sqrt{\sigma^2 - b^2}}{\pi} \int_{-b}^b \frac{\psi(s) ds}{\sqrt{b^2 - s^2} (s - \sigma)}, \quad (2.2.2b)$$

$$\psi(s, n) = \operatorname{arctg} \left(\frac{Q^n(s) - 1}{Q^n(s) + 1} \operatorname{ctg} \frac{\pi n}{2} \right).$$

The first terms of Eqs. (2.2.2a), (2.2.2b) are due to the body motion and angle of attack. They are a modification for the flow over a log given in Ref. [15] for slip line boundaries instead of walls obtained by Dr. N. D. Malmuth [16] for the flow over a portion of a circle (see Section 2.4). The second terms arise due to the body shape variation in the streamwise direction. For $n > 1/2$, the flow velocities have a singularity of the type $(\zeta^2 - c^2)^{1/2n-1}$ or $(\sigma^2 - b^2)^{1/2-n}$ at the points where the free surface intersects the body. Since this singularity is integrable, the lift force and pitching moment are not singular. However, local asymptotic analysis near these points is needed for the higher order approximations.

On the body surface, $\eta = -0$, $|\xi| < b$, the flow potential and the tangential velocity are expressed as

$$\Phi(x, \lambda, t) = \Phi_1 + \Phi_2 = V_e \frac{\sin \pi n}{n} \left(\sqrt{1 - \lambda^2} - \frac{2nQ^n(\lambda)}{D(\lambda, n)} \sin \pi n \right) - \frac{2aa_x}{\pi} \sqrt{1 - \lambda^2} E(\lambda, n), \quad (2.2.3a)$$

$$w_\theta(x, \lambda, t) = V_e \left[\frac{Q^{2n}(\lambda) - 1}{D(\lambda, n)} \sin \pi n - \lambda \frac{\sqrt{1 - \lambda^2} D(\lambda, n)}{4n^2 Q^n(\lambda)} \right] + \frac{a_x \sqrt{1 - \lambda^2} I(\lambda, n)}{\pi} \{ 2 - [Q^n(\lambda) + Q^{-n}(\lambda)] \cos \pi n \}, \quad (2.2.3b)$$

$$\lambda = \frac{\xi}{b}, \quad Q(\lambda) = \frac{1 + \lambda}{1 - \lambda}, \quad E(\lambda, n) = \int_{-1}^1 \frac{\psi(s) ds}{\sqrt{1 - s^2} (s - \lambda)}, \quad (2.2.3c)$$

$$I(\lambda, n) = \int_{-1}^1 \frac{Q^n(s) ds}{D(s, n) \sqrt{1 - s^2} (s - \lambda)}, \quad (2.2.3d)$$

where $E(\lambda, n)$ and $I(\lambda, n)$ are the principal values of the integrals and the potential $\Phi_1(x, \lambda, t)$ and $\Phi_2(x, \lambda, t)$ are induced by the circle vertical motion and axial body radius

variation, respectively. Using these functions and Eq. (2.1.6) we obtain the pressure on the body surface

$$p(x, \lambda, t) = -\Phi_t - \Phi_x + \frac{V_e^2}{2} \left[1 - \frac{\lambda^2(1-\lambda^2)D^2(\lambda, n)}{16n^4Q^{2n}(\lambda)} \right] - \frac{a_x^2}{2} \left[1 + \frac{(1-\lambda^2)D^2(\lambda, n)}{\pi^2Q^{2n}(\lambda)} I^2(\lambda, n) \right] + V_e a_x \frac{\lambda(1-\lambda^2)D^2(\lambda, n)}{4n^2\pi Q^{2n}(\lambda)} I(\lambda, n). \quad (2.2.4)$$

Retaining only the first terms $\Phi_1(x, \lambda, t)$ in Eqs. (2.2.2)-(2.2.3) and replacing V_e and n by V_e^+ and $m = 1 - n$ respectively, we obtain the relations for the flow parameters in the cavity region. Thus, the flow potential, tangential velocity and pressure on the upper body portion (inside the cavity) are expressed as

$$\Phi^+(x, \lambda, t) = V_e^+ \frac{\sin \pi m}{m} \left(\sqrt{1-\lambda^2} - \frac{2mQ^m(\lambda)}{D(\lambda, m)} \sin \pi m \right), \quad (2.2.5a)$$

$$w_\theta^+(x, \lambda, t) = V_e^+ \left[\frac{Q^{2m}(\lambda) - 1}{D(\lambda, m)} \sin \pi m - \lambda \frac{\sqrt{1-\lambda^2} D(\lambda, m)}{4m^2 Q^m(\lambda)} \right], \quad (2.2.5b)$$

$$p^+(x, \lambda, t) = -\Phi_t^+ + \frac{V_e^{+2}}{2} \left\{ 1 - \frac{\lambda^2(1-\lambda^2)D^2(\lambda, m)}{16m^4Q^{2m}(\lambda)} \right\}. \quad (2.2.5c)$$

As will be shown in Section 2.3.2 the singularities in Eqs. (2.2.3)-(2.2.5) as $n \rightarrow 0$, $n \rightarrow 1$ and $\lambda \rightarrow \pm 1$ are integrable. Using Eqs. (2.2.3b) and (2.2.5b) we can calculate the coefficients w_{0n} and w_{0n}^+ in Eqs. (1.2.21) and (1.2.23). Because these formulas are rather long we do not present them here.

2.3.2 Lift force and pitching moment

The local lift force $L_x(x, t)$ acting on a cross-section of the partially submerged body portion, $X_1 \leq X \leq X_2$, is determined as

$$\begin{aligned} L_x(x, t) &= \int_{-c}^c p(x, z, t) dz - \int_{-c}^c p^+(x, z, t) dz = \\ &= \int_{-1}^1 \left[p(x, \lambda, t) \frac{\partial f(x, \lambda, t)}{\partial \lambda} - p^+(x, \lambda, t) \frac{\partial f^+(x, \lambda, t)}{\partial \lambda} \right] d\lambda = \\ &= -\frac{\partial(\bar{\Phi} - \bar{\Phi}^+)}{\partial t} - \frac{\partial \bar{\Phi}}{\partial x} + P(x, t), \end{aligned} \quad (2.2.6a)$$

$$P(x, t) = aV_e^2 P_1(x, t) - aa_x^2 P_2(x, t) + aa_x V_e P_{12}(x, t) - V_e^{+2} P^+(x, t). \quad (2.2.6b)$$

Using Eqs. (2.2.1), (2.2.3a) we can express the mean values of potentials. $\overline{\Phi}(x,t) = \overline{\Phi}_1(x,t) + \overline{\Phi}_2(x,t)$ and $\overline{\Phi}^+(x,t)$, as

$$\begin{aligned}\overline{\Phi}_1(x,t) &= \int_{-c}^c \Phi_1(x,z,t) dz = \int_{-b}^b \Phi_1(x,\xi,t) \frac{\partial f(x,\xi,t)}{\partial \xi} d\xi = \\ &= V_e \left[\int_{-c}^c Y_b(z) dz + \int_{-b}^b \sqrt{b^2 - \xi^2} Z_\xi d\xi \right] = -V_e a^2 \left[\pi(1-n) + \frac{1}{2} \sin 2\pi n - \frac{\sin^2 \pi n}{n} I_{10}(n) \right].\end{aligned}$$

Using Eq. (B1.2) given in Appendix B, we obtain

$$\overline{\Phi}_1(x,t) = -V_e a^2 \left[\pi(1-n) + \frac{1}{2} \sin 2\pi n - \frac{\pi(2n^2+1)\sin^2 \pi n}{6n^2} \right].$$

$$n \rightarrow 1: \overline{\Phi}_1(x,t) \approx -2V_e a^2 \pi(1-n), \quad n \rightarrow 0: \overline{\Phi}_1(x,t) \approx -V_e a^2 \pi \left(1 - \frac{\pi^2}{6} \right).$$

Similarly, we find the mean potential for the upper body portion (within the cavity)

$$\begin{aligned}\overline{\Phi}^+(x,t) &= \int_{-b}^b \Phi^+(x,\xi,t) \frac{\partial f^+(x,\xi,t)}{\partial \xi} d\xi = \\ &= -V_e^+ a^2 \left[\pi(1-m) + \frac{1}{2} \sin 2\pi m - \frac{\pi(2m^2+1)\sin^2 \pi m}{6m^2} \right],\end{aligned}\quad (2.2.7a)$$

$$m \rightarrow 1: \overline{\Phi}^+(x,t) \approx -2V_e^+ a^2 \pi(1-m), \quad m \rightarrow 0: \overline{\Phi}^+(x,t) \approx -V_e^+ a^2 \pi \left(1 - \frac{\pi^2}{6} \right). \quad (2.2.7b)$$

The second term of the mean potential is evaluated as

$$\begin{aligned}\overline{\Phi}_2(x,t) &= \int_{-c}^c \Phi_2(x,z,t) dz = \int_{-b}^b \Phi_2(x,\xi,t) \frac{\partial f(x,\xi,t)}{\partial \xi} d\xi = - \int_{-b}^b z(x,\xi,t) \frac{\partial \Phi_2(x,\xi,t)}{\partial \xi} d\xi = \\ &= - \frac{4a^2 a_x n \sin^2(\pi n)}{\pi} E_0(n), \quad E_0(n) = \int_{-1}^1 \frac{Q^n(s) I_1(s,n) ds}{D(s) \sqrt{1-s^2}}.\end{aligned}$$

Integral $I_1(s,n)$ is given by Eqs. (B4.1) and (B4.2) presented in Appendix B

$$I_1(s,n) = \int_{-1}^1 \frac{[Q^{2n}(\lambda) - 1] d\lambda}{D(\lambda) \sqrt{1-\lambda^2} (\lambda-s)} = \frac{\pi}{n} \left[1 - \frac{2n \sin \pi n Q^n(s)}{D(s) \sqrt{1-s^2}} \right].$$

Thus, for the function $E_0(n)$ we obtain the expression

$$E_0(n) = \frac{\pi}{n} [I_0(n) - 2\pi I_{12}(n) \sin \pi l] = \frac{\pi}{n^2 \sin \pi l} \left\{ e_0(n) - \frac{n}{2} [1 + \pi(1-n) \operatorname{ctg} \pi l] \right\}.$$

The integral $I_{12}(n)$ is reduced to a tabulated integral and expressed as (see Appendix B)

$$I_{12}(n) = \int_{-1}^1 \frac{Q^{2n}(s) ds}{D^2(s)(1-s^2)} = \frac{1 + \pi(1-n) \operatorname{ctg} \pi l}{4n \sin^2 \pi l}.$$

The function $e_0(n)$ has the form

$$e_0(n) = n \sin(\pi l) I_0(n) = n \sin(\pi l) \int_{-1}^1 \frac{Q^n(s) ds}{D(s) \sqrt{1-s^2}} = \int_0^1 \frac{\psi(s) s ds}{\sqrt{1-s^2}}.$$

$$n \rightarrow 1: e_0 = \frac{\pi^2(1-n)}{8}, \quad n \rightarrow 0: e_0 = \ln 2 - \frac{\pi^2 n^2}{12}.$$

This form is derived in Appendix C (see Eqs. (C1.1)-(C1.5)) and shown in Fig. 2.2. Accordingly, the mean value of the second potential and its asymptotic behavior can be expressed as

$$\bar{\Phi}_2(x, t) = -4a^2 a_x \frac{\sin \pi l}{n} \left\{ e_0(n) - \frac{n}{2} [1 + \pi(1-n) \operatorname{ctg} \pi l] \right\},$$

$$n \rightarrow 1: \bar{\Phi}_2(x, t) \approx -\frac{1}{2}(1-n)^2 \pi^3 a^2 a_x, \quad n \rightarrow 0: \bar{\Phi}_2(x, t) \approx -2(2 \ln 2 - 1) \pi a^2 a_x.$$

Thus, the mean potential on the wetted surface (outside the cavity) has the form

$$\bar{\Phi}(x, t) = V_e a^2 \left[\pi(1-n) - \frac{1}{2} \sin 2\pi l + \frac{\pi(2n^2 + 1) \sin^2 \pi l}{6n^2} \right] -$$

$$-4a^2 a_x \frac{\sin \pi l}{n} \left\{ e_0(n) - \frac{n}{2} [1 + \pi(1-n) \operatorname{ctg} \pi l] \right\}, \quad (2.2.8a)$$

$$n \rightarrow 1: \bar{\Phi}(x, t) \approx 2V_e a^2 \pi(1-n) - \frac{1}{2}(1-n)^2 \pi^3 a^2 a_x, \quad (2.2.8b)$$

$$n \rightarrow 0: \bar{\Phi}(x, t) \approx V_e a^2 \pi \left(1 + \frac{\pi^2}{6} \right) - 2(2 \ln 2 - 1) \pi a^2 a_x. \quad (2.2.8c)$$

The first nonlinear term of Eq. (2.2.6) is determined by the expression

$$P_1 = \sin \pi l \left[1 - \frac{1}{8n^5} \int_{-1}^1 \frac{\lambda^2 (1-\lambda^2) D^2(\lambda, n)}{Q^{2n}(\lambda)} \frac{\partial z}{\partial \xi} d\lambda \right] =$$

$$= \sin \pi l \left\{ 1 - \frac{1}{8n^3} \int_{-1}^1 [2 - \cos(\pi l) (Q^n(s) + Q^{-n}(s))] s^2 ds \right\}.$$

The latter integral is reduced to the tabulated integral and evaluated in Appendix B (see Eq. (B3.2)). Then, the function $P_1(x, t)$ is expressed as

$$P_1(x, t) = \sin \pi l \left[1 - \frac{1 - \pi l (1 + 2n^2) \operatorname{ctg} \pi l}{6n^3} \right], \quad (2.2.9a)$$

$$n \rightarrow 1: P_1(x, t) \approx -\frac{1}{2}\pi; \quad n \rightarrow 0: P_1(x, t) \approx -\frac{\pi(\pi^2 - 6)}{18}. \quad (2.2.9b)$$

The second nonlinear term of Eq. (2.2.6b) is transformed to the form

$$P_2 = \sin \pi l \left[1 + \frac{1}{\pi^2 n} \int_{-1}^1 \frac{(1 - \lambda^2) D^2(\lambda, n)}{Q^{2n}(\lambda)} I^2(\lambda, n) \frac{\partial z}{\partial \xi} d\lambda \right] = \sin \pi l \left[1 + \frac{2n}{\pi^2} E_1(n) \right]$$

In Appendix C (see Eqs. (C3.1)-(C3.2)), the integral $E_1(n)$ is reduced to the form

$$\begin{aligned} E_1(n) &= \int_{-1}^1 [2 - (Q^n(s) + Q^{-n}(s)) \cos(\pi l)] I^2(s, n) ds = \\ &= \frac{\pi^2}{2n} + \frac{2}{n^4} \left(n^2 \pi^2 \operatorname{ctg}^2(\pi l) \left\{ e_0(n) - \frac{n}{2} [1 + \pi(1 - n) \operatorname{ctg}(\pi l)] \right\} - 2e_{10}(n) \right), \end{aligned}$$

where

$$\begin{aligned} e_{10}(n) &= n^4 \int_{-1}^1 \int_{-1}^1 \frac{Q^n(s) Q^n(t) \ln Q(t) ds dt}{D(s) D(t) \sqrt{1 - s^2} \sqrt{1 - t^2} (t - s)}, \\ n \rightarrow 1: e_{10} &= \frac{\pi^2}{48}, \quad n \rightarrow 0: e_{10} = \frac{1}{4} \left[2 \ln 2 - 1 - \frac{\pi^2 n^2}{6} (3 - 4 \ln 2) \right]. \end{aligned}$$

The function $e_{10}(n)$ is considered in Appendix C (see Eqs. (C4.1)-(C4.2)); its plot is shown in Fig. 2.2. Now, the second nonlinear term is expressed as

$$P_2(x, t) = 2 \sin \pi l \left\{ 1 + 2 \frac{\operatorname{ctg}^2 \pi l}{n} \left[e_0(n) - \frac{n}{2} (1 + \pi(1 - n) \operatorname{ctg} \pi l) \right] - 4 \frac{e_{10}(n)}{\pi^2 n^3} \right\}, \quad (2.2.10a)$$

$$n \rightarrow 1: P_2(1) = \frac{\pi}{2}, \quad n \rightarrow 0: P_2(0) = \frac{3}{2} \pi (3 - 4 \ln 2). \quad (2.2.10b)$$

The third nonlinear term of Eq. (2.2.6b) is

$$P_{12} = \frac{\sin \pi n}{4n^3 \pi} \int_{-1}^1 \frac{\lambda(1-\lambda^2)D^2(\lambda, n)}{Q^{2n}(\lambda)} I(\lambda, n) \frac{\partial z}{\partial \xi} d\lambda = \frac{\sin \pi n}{\pi n} E_2(n)$$

where the function $E_2(n)$ is expressed as (see Eqs. (B5.1)-(B5.3) of Appendix B)

$$\begin{aligned} E_2(n) &= \int_{-1}^1 \left\{ 2 - [Q^n(\lambda) + Q^{-n}(\lambda)] \cos \pi n \right\} I(\lambda, n) \lambda d\lambda = - \int_{-1}^1 \frac{Q^n(s) I_4(s, n) ds}{D(s) \sqrt{1-s^2}} = \\ &= - \frac{1}{n \sin \pi n} \left[4(1 - \pi n \operatorname{ctg} \pi n) e_0(n) - 2e_2(n) + \frac{(2n^2 + 1)}{6} \pi^2 \cos^2 \pi n \right]. \end{aligned}$$

The integral

$$\begin{aligned} I_4(s, n) &= \int_{-1}^1 \frac{\{2 - [Q^n(\lambda) + Q^{-n}(\lambda)] \cos \pi n\} \lambda d\lambda}{\lambda - s} = \\ &= 4(1 - \pi n \operatorname{ctg} \pi n) + s \left\{ \frac{\pi n \cos^2 \pi n}{\sin \pi n} [Q^n(s) - Q^{-n}(s)] - 2 \ln Q(s) \right\} \end{aligned}$$

is given by Eq. (B5.3) of Appendix B. The function

$$\begin{aligned} e_2(n) &= n \sin(\pi n) \int_{-1}^1 \frac{Q^n(s) \ln Q(s) s ds}{D(s) \sqrt{1-s^2}} = \int_0^1 [(2s^2 - 1) \ln Q(s) - 2s] \frac{\psi(s) ds}{\sqrt{1-s^2}}, \\ n \rightarrow 1: e_2 &= \frac{\pi^2(1-n)}{12}, \quad n \rightarrow 0: e_2 = \frac{\pi^2}{12} [1 - 2n^2]. \end{aligned}$$

is considered in Appendix C (see Eqs. (C2.1)-(C2.3)); its plot is shown in Fig. 2.2. Accordingly, the cross-nonlinear term is

$$P_{12}(n) = -\frac{1}{\pi n^2} \left\{ 4[1 - \pi n \operatorname{ctg}(\pi n)] e_0(n) - 2e_2(n) + \frac{2n^2 + 1}{6} \pi^2 \cos^2(\pi n) \right\}, \quad (2.2.11a)$$

$$n \rightarrow 1: P_{12} = -\pi, \quad n \rightarrow 0: P_{12} = -\frac{\pi}{3} \left(4 \ln 2 + 2 - \frac{\pi^2}{2} \right). \quad (2.2.11b)$$

Similar to Eqs. (2.2.9), the later term of Eq. (2.2.6b), which corresponds to the nonlinear pressure component on the body surface inside the cavity, has the form

$$P^+(x, t) = \sin \pi n \left\{ 1 - \frac{1 + \pi n(1 + 2m^2) \operatorname{ctg} \pi n}{6m^3} \right\}, \quad (2.2.12a)$$

$$m \rightarrow 1: P^+(x, t) \approx -\frac{1}{2} \pi, \quad m \rightarrow 0: P^+(x, t) \approx -\frac{\pi(\pi^2 - 6)}{18}. \quad (2.2.12b)$$

Due to the first linear terms of Eq. (2.2.6a) the local lift force is singular at a small submerging depth, when $n \rightarrow 1$. Using the definition of n and Eq. (2.2.8b) we obtain

$$L_x(n \rightarrow 1) \sim -\frac{\partial \bar{\Phi}_1}{\partial t} - \frac{\partial \bar{\Phi}_1}{\partial x} \sim 2V_e a^2 \pi \left(\frac{\partial n}{\partial t} + \frac{\partial n}{\partial x} \right) \sim 2a \frac{V_e(V_e - a_x)}{\pi(1-n)}. \quad (2.2.13)$$

This result is consistent with the two-dimensional theory [11]. However, there is the additional term, which is due to the axial variation of body shape. This singularity leads to impulsive loads at the beginning of the body submergence process. Nevertheless, the body momentum is continuous; it is proportional to the potential $\bar{\Phi}_1 \sim 1 - n$.

The foregoing relations allow us to evaluate the lift force and pitching moment acting on the body in the transitional phase 3, when the body passes through the slip surface. In this phase, the total lift force and pitching moment can be expressed as the superposition of three terms, namely,

$$L(t) = L^+(t) + L^\pm(t) + L^-(t), \quad M(t) = M^+(t) + M^\pm(t) + M^-(t).$$

The terms L^\pm and M^\pm correspond to integration of the local lift (2.2.6) over the interval $[x_1, x_2]$. We can give them in the forms

$$\begin{aligned} L^\pm(t) &= -\frac{dV_a^\pm(t)}{dt} + L_1^\pm(t), \quad M^\pm(t) = -\frac{d\omega_a^\pm(t)}{dt} + M_1^\pm(t), \\ L_1^\pm(t) &= \int_{x_1}^{x_2} P(x, t) dx + (1 - x_{1t}) \bar{\Phi}(x_1, t) + x_{1t} \bar{\Phi}^+(x_1, t) - (1 - x_{2t}) \bar{\Phi}(x_2, t) - x_{2t} \bar{\Phi}^+(x_2, t), \\ M_1^\pm(t) &= \int_{x_1}^{x_2} P(x, t) x dx + \int_{x_1}^{x_2} \bar{\Phi}(x, t) dx + \\ &+ x_1 [(1 - x_{1t}) \bar{\Phi}(x_1, t) + x_{1t} \bar{\Phi}^+(x_1, t)] - x_2 [(1 - x_{2t}) \bar{\Phi}(x_2, t) + x_{2t} \bar{\Phi}^+(x_2, t)], \\ V_a^\pm(t) &= \int_{x_1}^{x_2} [\bar{\Phi}(x, t) - \bar{\Phi}^+(x, t)] dx, \quad \omega_a^\pm(t) = \int_{x_1}^{x_2} [\bar{\Phi}(x, t) - \bar{\Phi}^+(x, t)] x dx. \end{aligned} \quad (2.2.14)$$

The critical points $x_1(t)$, $x_2(t)$ and their speeds are found from the equations

$$\alpha x_k \pm a(x_k) = Y_o(t), \quad x_{kt}(t) \equiv \frac{dx_k(t)}{dt} = \frac{V_o - \alpha x_k}{\alpha \pm a_x(x_k)}, \quad k = 1, 2 \quad (2.2.15)$$

Note that the form of Eqs. (2.2.14) allows us to avoid the singularity (2.2.13) in the critical points on the lowest body generator corresponding to $n = 1$. On the other hand, this singularity is integrable since $1 - n \sim x_k - x$. Explicit dependencies of the lift force

and moment on trajectory parameters can be obtained by substituting the derived above expressions into Eqs. (2.2.14).

The lift force $L^+(t)$ is determined by integrating the local lift force (2.2.10b) over the body portion totally inside the cavity. This term is similar to that given by Eqs. (2.1.11) plus the additional sum accounting for the motion of the critical points. Fig. 1.7 of Part I shows possible locations of the body with respect to the slip surface and the integration intervals. Relevant cases are

- a) Interval $x_1(t) \leq x \leq x_0$, if the body nose ordinate $Y_n(t) > 0$ (see Fig. 1.7a)
- b) Interval $x_2(t) \leq x \leq x_e$, if $Y_n(t) < 0$ and the lowest body-base ordinate $Y_{el}(t) > 0$ (Fig. 1.7b)
- c) Nose interval ($x_1(t) \leq x \leq x_0$) and the base interval ($x_2(t) \leq x \leq x_e$), if $Y_n(t) > 0$ and $Y_{el}(t) > 0$ (Fig. 1.7c).

In the cases shown in Figs. 1.7d and 1.7f, we get $L^+ = M^+ = 0$ because the body nose and tail are in the stream.

The lift force $L^-(t)$ acts on the body portion with its cross-sections being totally in the external stream. Its expression is similar to Eqs. (2.1.12) plus additional terms due to the critical point motion. The totally submerged body part can be located in:

- d) Interval $X_2(t) \leq X \leq X_e$, if $Y_n(t) > 0$ and $Y_{eu}(t) < 0$ (see Fig. 1.7a)
- e) Interval $X_1(t) \leq X \leq X_0$, if $Y_n(t) < 0$ (see Fig. 1.7b)
- f) Intervals $X_1(t) \leq X \leq X_0$ and $X_2(t) \leq X \leq X_e$, if $Y_n(t) < 0$ and $Y_{eu}(t) < 0$ (see Fig. 1.7d)

If the body nose and base are inside the cavity (see Fig. 1.7c) or the body base is partially submerged into external stream (see Fig. 1.7e), then $Y_{el}(t) < 0$ and $Y_{eu}(t) > 0$. For this case, we get $L^- = M^- = 0$.

Extracting the inertia term, we express the total lift force and pitching moment acting on the body in Phase 2 as

$$L(t) = -\frac{dV_a(t)}{dt} + L_1(t), \quad M(t) = -\frac{d\omega_a(t)}{dt} + M_1(t) \quad (2.2.16a)$$

$$L_1(t) = L_1^+(t) + L_1^\pm(t) + L_1^-(t), \quad M_1(t) = M_1^+(t) + M_1^\pm(t) + M_1^-(t), \quad (2.2.16b)$$

$$V_a(t) = V_a^+(t) + V_a^\pm(t) + V_a^-(t), \quad \omega(t) = \omega_a^+(t) + \omega_a^\pm(t) + \omega_a^-(t). \quad (2.2.16c)$$

This form is convenient for numerical solution of the trajectory equations.

2.4 Cross-checks of the theory

Herein we compare our solution given by Eq. (2.2.2) with the solution obtained by Malmuth [16] for a circular cylinder submerging into a freestream with a vertical velocity U . The problem is similar to the problem of the flow over the lens-shaped body considered by Milne Thompson [15] or equivalently, the flow over a log or bump in a solid wall. In contrast, Malmuth considered the same circular segment crossing an infinite span slip line/shear layer in [16]. The former problem is relevant to store separation from a flat wall or portion of a wing or fuselage, where if a cavity is involved, the body lateral dimension is of order of the cavity span. The latter applies to store separation from a cavity bridged by a shear layer in which the cavity span is large compared to the body lateral dimension. This problem is our focus in this section. Its solution is the complex potential

$$\Pi'(\zeta') = \frac{2Uc}{n' \sin(\zeta' / n')}; \zeta = Z + iY = ic \cot \frac{\zeta'}{2}; \frac{\zeta + c}{\zeta - c} = e^{i\zeta'} \quad (2.3.1)$$

In Eqs. (2.3.1), ζ' is complex variable in the bipolar coordinate plane [15], the body intersects the slip surface at the points $(c,0)$ and $(-c,0)$. The part of Eq. (2.2.2) corresponding to Eq. (2.3.1) is expressed as

$$\Pi(\sigma) = iV_e \sqrt{\sigma^2 - b^2}; \sigma = b \frac{S^k + 1}{S^k - 1} = ib \cot \frac{k\zeta}{2}; k = \frac{1}{n}; S = \frac{\zeta + c}{\zeta - c} \quad (2.3.2)$$

The parameters of Eqs. (2.3.1) and (2.3.2) are related by formulas

$$V_e = V_o - \alpha - \alpha x = Us; n' = 2n = 2^{\frac{\pi - \beta}{\pi}}; c = a \sin \beta, \quad (2.3.3)$$

Substituting the expression for σ from the second equation of (2.3.2) to the first formula for the complex potential we obtain

$$\Pi(\zeta') = bV_e \sqrt{1 + \cot^2(k\zeta'/2)} = \frac{bV_e}{\sin(k\zeta'/2)} = \frac{2cV_e}{n' \sin(\zeta' / n')} \equiv \Pi'(\zeta'). \quad (2.3.4)$$

Thus, we prove that solutions (2.3.1) and (2.3.2) are identical. Note that the solution (2.2.2) includes an additional term proportional to $a_x(x)$. This term has no analytical form. Because its integral representation is simpler in the σ -plane we use this plane for calculations of the lift force.

Also note that in the case considered, the classical form of Blasius theorem is strictly not applicable for calculations of the lift force since the solutions above and below the slip surface differ. They are found separately in the relevant upper and lower half-planes. The lift force acting on the upper body portion (inside the cavity) is calculated separately from the lift force acting on the lower portion (outside the cavity). As a result, the expression

for the lift force includes additional terms, which are not included in the classical form of the Blasius theorem. However, generalized forms of this theorem exist such as those given in Milne Thompson [15] that can be further extended to handle the slip line boundaries in our inner problems. This leads to contour integrals that can be evaluated by residue calculus in the upper and lower half planes.

For “external carriage” and separation from a rigid plate, the part of solution proportional to $a_x(x)$ can be expressed in an explicit analytical form that can be exploited for cross checking of our theoretical model. This solution was used in Ref. [24] for calculations of the interaction force between two slender bodies of revolution at zero incidence in a uniform stream. In this case, the flow is modeled by two sources located at the points $\zeta = \pm ic = \pm iH\sqrt{1-(a/H)^2}$, and the complex potential is expressed as

$$\Pi(\zeta) = aa_x [\ln(\zeta - ic) + \ln(\zeta + ic)]. \quad (2.3.5)$$

Expanding the square roots of this expression to the series, we obtain the relation (2.3.5) in the form of series identical to Eq. (2.1.2). We are not aware of an analytical solution in the presence of a slip surface such as this in the literature.

2.5 Discussion and conclusions

In this part, we obtain analytical solutions of dominant approximation problems relevant to separation of a thin body of revolution from a rectangular cavity into a uniform stream. In our approximation, the slip-surface displacement is neglected: *i.e.*, the slip surface is presented as a plane of zero potential. For Phases 1 and 3, we use the multipole expansion method that allows us to derive compact expressions for the pressure on the body surface and the cross-sectional lift force. For Phase 2, the solution is obtained by conformal mapping in the form of a Cauchy type integral that is partially integrated. The local lift force is also represented in explicit form by introducing new special functions which are investigated analytically and numerically.

In Phase 1 (body moves inside the cavity from the top wall to the slip surface), the flow potential and the pressure are expressed by the formulas, which are similar to the known relations derived for two-dimensional flow over a cylinder. In this phase, the full solution is found as a sum of two unit solutions that separately account for the top wall and slip surface effects separately. This approach exploits the fact that the boundary influence decreases rapidly (as the inverse square) with distance.

As contrasted to the two-dimensional problem, solutions for Phases 2 and 3 include new terms relevant to the body shape variation in the axial direction. These terms lead to a qualitatively new behavior of the slip surface and rigid wall effects. For example, in Phase 3 the slip-surface effect is stronger than in Phase 1 because the influence of this boundary decreases only as the inverse distance to the body.

In Phase 2, the flow velocities of the first order approximation are singular at the line of intersection between the slip surface and the body surface. However, these singularities

are integrable. This allows us to calculate the lift force and pitching moment without a detailed analysis of the singular regions. Nevertheless, such an analysis is needed to treat the higher-order approximations. This singularity resembles body nose and wing leading edge stagnation singularities. It does not cause any difficulty in integrating the trajectory equations since the body momentum is a continuous function of the submerging depth that is proportional to the mean potential on the wetted surface.

The results provided here support the development of a computationally non-intense algorithm predicting the body trajectory through all separation phases.

2.6 Illustrations

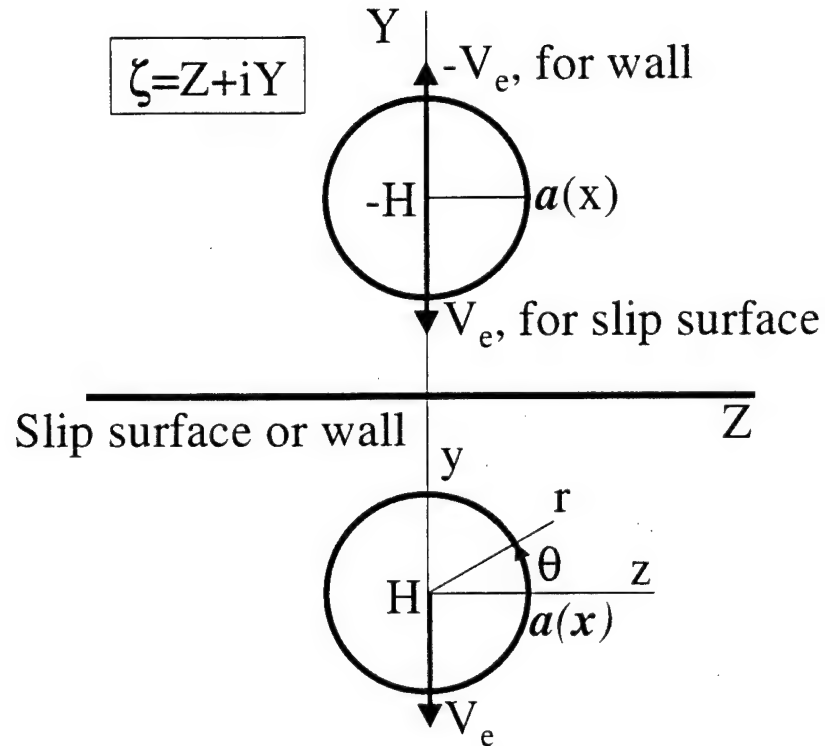


Fig. 2.1 Cross-section scheme for the reflection method for Phases 1 and 3.

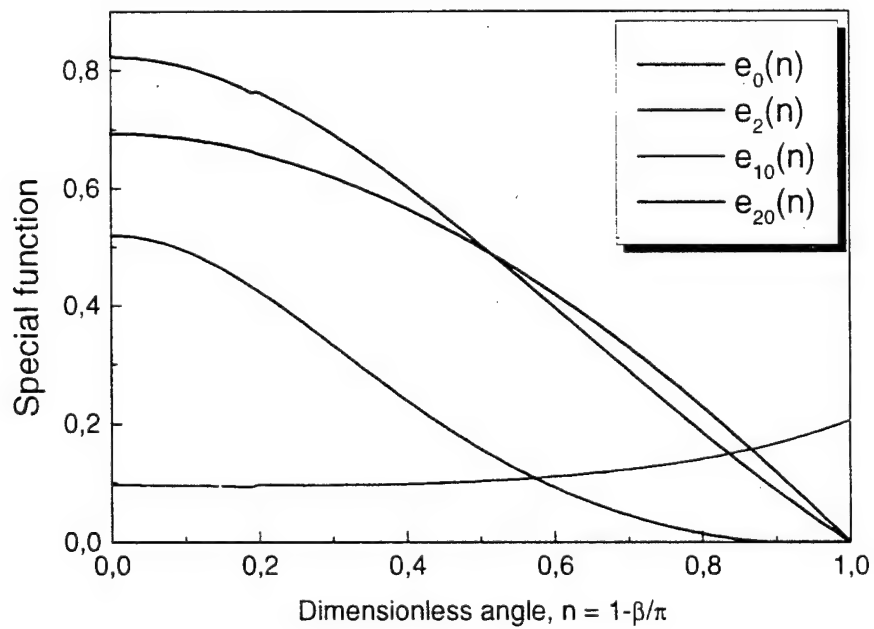


Fig. 2.2 Plots of special functions.

Appendix B. Analytical evaluation of improper integrals

We analyze the integral

$$I_{10}(n) = \int_{-1}^1 \frac{[Q^{2n}(s) - 1]s ds}{D(s)\sqrt{1-s^2}} = 2 \int_{-\infty}^{\infty} \frac{(e^{4nx} - 1)(e^{2x} - 1)e^x dx}{D(x)(1 + e^{2x})^2}, \quad (\text{B1.1a})$$

$$Q = \frac{1+s}{1-s} = e^{2x}, \quad s = \frac{e^{2x} - 1}{e^{2x} + 1}, \quad ds = \frac{4e^{2x} dx}{(e^{2x} + 1)^2}, \quad 1 - s^2 = \frac{4e^{2x}}{(e^{2x} + 1)^2}, \quad (\text{B1.1b})$$

$$D(x) = e^{4nx} - 2e^{2nx} \cos(\pi n) + 1. \quad (\text{B1.1c})$$

Let's consider the following integral along the closed rectangular contour C_1 in the complex plane $z = x + iy$ (see Fig. B1)

$$I = \int_C f(z) dz = i \int_{-\frac{\pi}{2}}^{\frac{\pi}{2}} [f(A + iy) - f(-A + iy)] dy + \int_{-A}^A [f(x - i\frac{\pi}{2}) - f(x + i\frac{\pi}{2})] dx = 2\pi i \text{res}f(0),$$

$$f(z) = \frac{(e^{2nz} + 1)(e^{2z} + 1)e^z}{(e^{2nz} - 1)(e^{2z} - 1)^2}.$$

The integrand has the third order pole at $z = 0$ with the residue

$$\text{res}f(0) = \frac{2n^2 + 1}{12n}.$$

The contour is bounded by the horizontal lines, $y = \pm \frac{\pi}{2}$, and vertical lines $x = \pm A$, $A \rightarrow \infty$. The integrals along the vertical lines vanish as $A \rightarrow \infty$. Along the horizontal lines, we have

$$f(x - i\frac{\pi}{2}) = \frac{ie^x (e^{2x} - 1)(e^{-i\pi n} e^{2nx} + 1)}{(e^{2x} + 1)^2 (e^{-i\pi n} e^{2nx} - 1)}, \quad f(x + i\frac{\pi}{2}) = -\frac{ie^x (e^{2x} - 1)(e^{i\pi n} e^{2nx} + 1)}{(e^{2x} + 1)^2 (e^{i\pi n} e^{2nx} - 1)},$$

$$f(x - i\frac{\pi}{2}) - f(x + i\frac{\pi}{2}) = 2i \frac{e^x (e^{2x} - 1)(e^{4nx} - 1)}{(e^{2x} + 1)^2 D(x)}.$$

Thus the function $I_{10}(n)$ is expressed as

$$I_{10}(n) = \frac{2n^2 + 1}{6n} \pi. \quad (\text{B1.2})$$

Substituting (B1.1b) we analyze the integral

$$\begin{aligned} I_{12}(n) &= \int_{-1}^1 \frac{Q^{2n}(s)ds}{D^2(s)(1-s^2)} = \frac{1}{2} \int_{-\infty}^{\infty} \frac{e^{2nx}dx}{D^2(x)} = \int_0^{\infty} \frac{dx}{(e^{nx} + e^{-nx} + 2\cos(\pi n))^2} = \frac{1}{4n} \int_0^{\infty} \frac{dt}{[ch(t) + \cos(\pi n)]^2} = \\ &= \frac{1}{4n \sin^2(\pi n)} \left[\frac{sh(t)}{ch(t) + \cos(\pi n)} \right]_0^{\infty} + \cos(\pi n) \int_0^{\infty} \frac{dt}{ch(t) + \cos(\pi n)} \quad (\text{B2.1}) \\ m &= 1 - n, \quad t = nx = \ln \left(\frac{1+s}{1-s} \right). \end{aligned}$$

As shown in Ref. [21],

$$\int_0^{\infty} \frac{dt}{ch(t) + \cos(\pi n)} = \frac{2}{\sin(\pi n)} \arctg \left[\tg \left(\frac{\pi n}{2} \right) \th \left(\frac{t}{2} \right) \right]_0^{\infty} = \frac{2}{\sin(\pi n)} \arctg \left[\tg \left(\frac{\pi n}{2} \right) \right] = \frac{\pi(1-n)}{\sin(\pi n)}.$$

Then the function $I_{12}(n)$ is expressed as

$$I_{12}(n) = \frac{1 + \pi(1-n) \operatorname{ctg}(\pi n)}{4n \sin^2(\pi n)}. \quad (\text{B2.2})$$

Consider the integral

$$\begin{aligned} I_{11}(n) &= \int_{-1}^1 [Q^n(s) + Q^{-n}(s)] s^2 ds = \\ &= \int_{-1}^1 [(1+s)^n (1-s)^{-n} + (1+s)^{-n} (1-s)^n - (1+s)^{1+n} (1-s)^{1-n} - (1+s)^{1-n} (1-s)^{1+n}] ds. \quad (\text{B3.1}) \end{aligned}$$

Using the table of integrals [22] and accounting for properties of the Euler gamma-function, we obtain

$$I_{11}(n) = \frac{4}{3} n(1+2n^2) \Gamma(n) \Gamma(1-n) = \frac{4\pi n(1+2n^2)}{3 \sin(\pi n)}. \quad (\text{B3.2})$$

Substituting (B1.1b) we analyze the Cauchy type integral

$$I_1(s, n) = \int_{-1}^1 \frac{[Q^{2n}(\lambda) - 1]d\lambda}{D(\lambda)\sqrt{1-\lambda^2}(\lambda-s)} = \frac{2}{1-s} \int_{-1}^1 \frac{(e^{4nx} - 1)e^x dx}{D(x)[e^{2x} - Q(s)]}. \quad (\text{B4.1})$$

Consider the following integral along the closed contour C_2 in the complex plane $z = x + iy$ (see Fig.B2)

$$\begin{aligned} I = \oint_C f(z)dz &= i \int_{-\frac{\pi}{2}}^{\frac{\pi}{2}} [f(A+iy) - f(-A+iy)]dy + \int_{-A}^A [f(x-i\frac{\pi}{2}) - f(x+i\frac{\pi}{2})]dx + \\ &+ \int_{\pi}^0 f(z_2 + re^{i\varphi})re^{i\varphi}id\varphi + \int_0^{-\pi} f(z_1 + re^{i\varphi})re^{i\varphi}id\varphi = 2\pi i \text{res}f(0). \\ f(z) &= \frac{(e^{2nz} + 1)e^z}{(e^{2nz} - 1)[e^{2z} + Q(s)]}, \end{aligned}$$

The contour is similar to that shown in Fig.B1, while the singular points

$$z_1 = \frac{\ln Q(s) + i\pi}{2}, \quad z_2 = \frac{\ln Q(s) - i\pi}{2},$$

are bypassed along the half-circles of radii $r \rightarrow 0$. The integrand has a simple pole at the point $z = 0$ with the residue

$$\text{res}f(0) = \frac{1-s}{2n}.$$

For the integrals along the half-circles, we have

$$\begin{aligned} f(z_1 + re^{i\varphi}) &= \frac{Q^n(s)e^{i\pi n} + 1}{2ire^{i\varphi}\sqrt{Q(s)}[Q^n(s)e^{i\pi n} - 1]}, \quad f(z_2 + re^{i\varphi}) = -\frac{Q^n(s)e^{-i\pi n} + 1}{2ire^{i\varphi}\sqrt{Q(s)}[Q^n(s)e^{-i\pi n} - 1]}, \\ \int_0^{-\pi} f(z_1 + re^{i\varphi})re^{i\varphi}id\varphi &= -\frac{\pi[Q^n(s)e^{i\pi n} + 1]}{2\sqrt{Q(s)}[Q^n(s)e^{i\pi n} - 1]}, \\ \int_{\pi}^0 f(z_2 + re^{i\varphi})re^{i\varphi}id\varphi &= \frac{\pi[Q^n(s)e^{-i\pi n} + 1]}{2\sqrt{Q(s)}[Q^n(s)e^{-i\pi n} - 1]}, \\ \int_{\pi}^0 f(z_2 + re^{i\varphi})re^{i\varphi}id\varphi + \int_0^{-\pi} f(z_1 + re^{i\varphi})re^{i\varphi}id\varphi &= \frac{2i\pi Q^n(s) \sin \pi n}{D(s, n)\sqrt{Q(s)}}. \end{aligned}$$

Integrals along the vertical contour lines vanish as $A \rightarrow \infty$. Along the horizontal contour lines (except of the end-points $z_{1,2}$) we obtain

$$f(x - i\frac{\pi}{2}) = \frac{ie^x(e^{2n\lambda}e^{-i\pi} + 1)}{(e^{2n\lambda}e^{-i\pi} - 1)[e^{2\lambda} - Q(s)]}, \quad f(x + i\frac{\pi}{2}) = -\frac{ie^x(e^{2n\lambda}e^{i\pi} + 1)}{(e^{2n\lambda}e^{i\pi} - 1)[e^{2\lambda} - Q(s)]},$$

$$f(x - i\frac{\pi}{2}) - f(x + i\frac{\pi}{2}) = \frac{2ie^x(e^{4n\lambda} - 1)}{D(x, n)[e^{2\lambda} - Q(s)]}$$

Then, the function $I_1(s, n)$ is expressed in the form

$$I_1(s, n) = \frac{\pi}{n} \left[1 - \frac{2n \sin(\pi n) Q^n(s)}{D(s) \sqrt{1-s^2}} \right]. \quad (\text{B4.2})$$

We consider a principal value of the Cauchy-type integral

$$I_4(s, n) = \int_{-1}^1 \frac{\{2 - [Q^n(\lambda) + Q^{-n}(\lambda)] \cos(\pi n)\} \lambda d\lambda}{\lambda - s} =$$

$$= \int_{-1}^1 \{2 - [Q^n(\lambda) + Q^{-n}(\lambda)] \cos(\pi n)\} d\lambda + s \int_{-1}^1 \frac{\{2 - [Q^n(\lambda) + Q^{-n}(\lambda)] \cos(\pi n)\} d\lambda}{\lambda - s}. \quad (\text{B5.1})$$

Using the table of integrals [22] and Eq. (B3.2), we get

$$\int_{-1}^1 \frac{Q^n(\lambda) d\lambda}{\lambda - s} = \int_{-1}^1 \frac{(1+\lambda)^n (1-\lambda)^{-n} d\lambda}{\lambda - s} = \frac{\pi}{\sin(\pi n)} [1 - Q^n(s) \cos(\pi n)], \quad (\text{B5.2a})$$

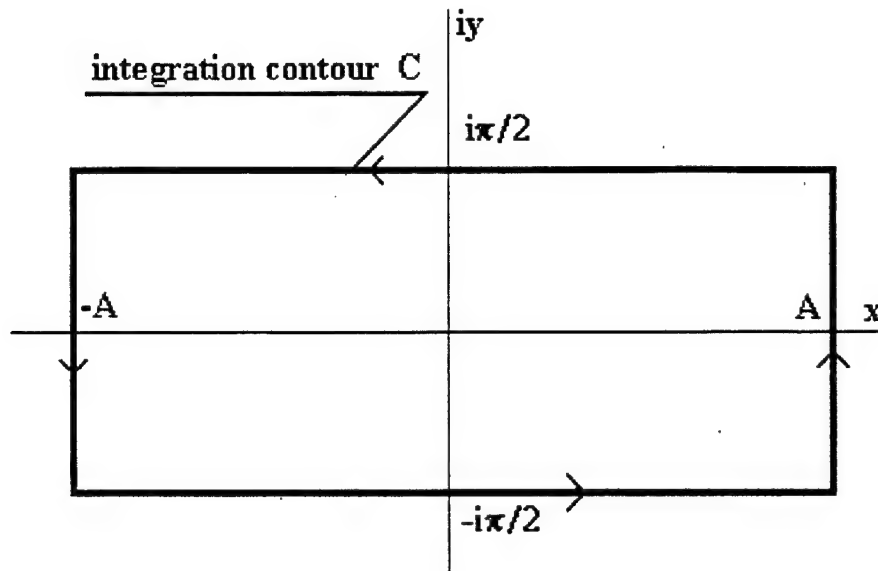
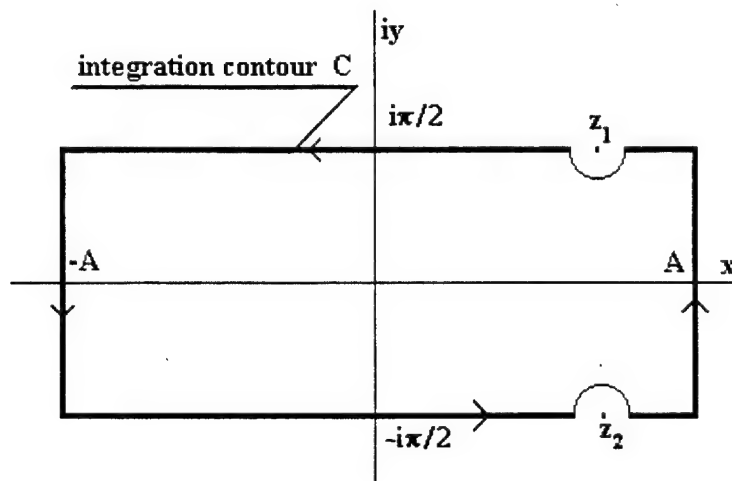
$$\int_{-1}^1 \frac{d\lambda}{\lambda - s} = -\ln Q(s), \quad (\text{B5.2b})$$

$$\int_{-1}^1 \frac{[Q^n(\lambda) + Q^{-n}(\lambda)] d\lambda}{\lambda - s} = -\pi \cot g(\pi n) [Q^n(s) - Q^{-n}(s)], \quad (\text{B5.2c})$$

$$\int_{-1}^1 [Q^n(\lambda) + Q^{-n}(\lambda)] d\lambda = \frac{4\pi n}{\sin(\pi n)}. \quad (\text{B5.2d})$$

Then, the function $I_4(s, n)$ is represented as

$$I_4(s, n) = 4[1 - \pi \cot g(\pi n)] + s \left\{ -2 \ln Q(s) + \frac{\pi \cos^2(\pi n)}{\sin(\pi n)} [Q^n(s) - Q^{-n}(s)] \right\}. \quad (\text{B5.3})$$

Fig.B1 Integration contour C_1 .Fig.B2 Integration contour C_2 .

Appendix C. Analytical and numerical investigations of integrals

Consider the integral

$$I_0(n) = \int_{-1}^1 \frac{Q^n(s) ds}{D(s)\sqrt{1-s^2}} = \frac{1}{2n \sin \pi l} \int_{-1}^1 \frac{\partial \psi(s)}{\partial s} \sqrt{1-s^2} ds = \frac{e_0(n)}{n \sin \pi l}.$$

Integrating by parts we obtain

$$e_0(n) = \int_0^1 \frac{\psi(s) s ds}{\sqrt{1-s^2}}, \quad \psi(s) = \arctg \left[\frac{Q^n(s)-1}{Q^n(s)+1} \operatorname{ctg} \left(\frac{\pi l}{2} \right) \right]. \quad (C1.1)$$

Using the table of integrals [22] we get the following asymptotic expression

$$n \rightarrow 1: I_0(1) = \frac{1}{4} \int_{-1}^1 \sqrt{1-s^2} ds = \frac{\pi}{8}, \quad e_0 \approx \frac{\pi^2(1-n)}{8} \approx 1.2337(1-n). \quad (C1.2)$$

Expanding the integrand to Taylor series versus n we find in the limit $n \rightarrow 0$

$$I_0(n) = n^{-2} \left[i_0 + \frac{n^2}{12} \left(2\pi^2 i_0 - \int_{-1}^1 \frac{ds}{\sqrt{1-s^2}} \right) \right] = n^{-2} \left[i_0 + \frac{\pi^2}{12} (2\pi l_0 - 1) \right].$$

The integral i_0 is reduced to the table integral [22] using the substitution

$$x = \frac{1}{\pi} \ln \frac{1+s}{1-s} = \frac{1}{\pi} \ln Q(s),$$

$$i_0 = \lim_{n \rightarrow 0} n^2 I_0(n) = \int_{-1}^1 \frac{ds}{[\pi^2 + \ln^2 Q(s)] \sqrt{1-s^2}} = \frac{1}{\pi} \int_0^\infty \frac{dx}{(1+x^2) \operatorname{ch}(\frac{\pi}{2})} = \frac{\ln 2}{\pi} \quad (C1.3)$$

Then, we obtain the asymptotic expression

$$n \rightarrow 0: e_0(n) = \ln 2 - \frac{n^2 \pi^2}{12} + O(n^4) \approx 0.693 - 0.8225n^2. \quad (C1.4)$$

To calculate the integral $e_0(n)$ in the range $0 < n < 1$, we remove the singularity at the upper integration limit using the substitution

$$1-s = x^2, \quad Q(x) = \frac{2-x^2}{x^2}, \quad D_1(x) = x^{4n} + (2-x^2)^{2n} - 2x^{2n}(2-x^2)^n \cos \pi l \dots (C1.5)$$

The integral is transformed into the form

$$e_0(n) = 2 \int_0^1 \frac{\psi(x)(1-x^2)dx}{\sqrt{2-x^2}}, \quad \psi(x) = \arctg \left[\frac{(2-x^2)^n - x^{2n}}{(2-x^2)^n + x^{2n}} \operatorname{ctg} \left(\frac{\pi n}{2} \right) \right]$$

and is calculated by the trapezoidal rule.

Consider the integral

$$\begin{aligned} e_2(n) &= n \sin \pi n I_2(n) = 2 \int_0^1 \phi(s) \ln Q(s) s ds = \int_0^1 s \sqrt{1-s^2} \ln Q(s) \frac{\partial \psi(s, n)}{\partial s} ds = \\ &= - \int_0^1 \psi(s, n) \frac{\partial}{\partial s} [s \sqrt{1-s^2} \ln Q(s)] ds = e_3(n) - 2e_0(n), \end{aligned} \quad (\text{C2.1a})$$

$$e_3(n) = \int_0^1 (2s^2 - 1) \psi(s, n) \ln Q(s) \frac{ds}{\sqrt{1-s^2}}. \quad (\text{C2.1b})$$

In the limit $n \rightarrow 1$, we obtain integrating by parts

$$\begin{aligned} I_2(1) &= \frac{1}{4} \int_{-1}^1 \sqrt{1-s^2} \ln Q(s) s ds = \frac{1}{12} \left\{ - (1-s^2)^{3/2} \ln Q(s) \Big|_{-1}^1 + 2 \int_{-1}^1 \sqrt{1-s^2} ds \right\} = \frac{\pi}{12}, \\ e_2(1) &= \frac{\pi^2(1-n)}{12} \approx 0.8225(1-n). \end{aligned} \quad (\text{C2.2})$$

At $n \rightarrow 0$, we find

$$i_2(n) = \lim_{n \rightarrow 0} n^2 I_2(n) = i_{20} + \frac{n^2}{12} [2\pi^2 i_{20} - i_{21}] = \frac{\pi}{12} \left[1 + 2n^2 \left(\frac{\pi^2}{12} - 1 \right) \right].$$

The integral i_{20} is evaluated similar to the case of $I_{10}(n)$ (see Eq. A1.1), and the integral i_{21} is integrated by parts

$$\begin{aligned} i_{21} &= \int_{-1}^1 \frac{\ln Q(s) s ds}{\sqrt{1-s^2}} = - \sqrt{1-s^2} \ln Q(s) \Big|_{-1}^1 + 2 \int_{-1}^1 \frac{ds}{\sqrt{1-s^2}} = 2\pi \\ i_{20} &= \int_{-1}^1 \frac{\ln Q(s) s ds}{[\pi^2 + \ln^2 Q(s)] \sqrt{1-s^2}} = 4 \int_{-1}^1 \frac{x(e^{2x} - 1)e^x dx}{(\pi^2 + 4x^2)(e^{2x} + 1)^2} = \frac{\pi}{12}. \end{aligned}$$

Then, we obtain

$$n \rightarrow 0: e_2(n) = \pi \left(1 - \frac{n^2 \pi^2}{6} \right) i_2(n) = \frac{\pi^2}{12} (1 - 2n^2) \approx 0.8225(1 - 2n^2). \quad (C2.3)$$

To calculate the integral $e_3(n)$ over the segment $0 < n < 1$ we use the substitution (C1.5). Then, integrating by parts we reduce this integral to the form

$$e_3(n) = 2 \int_0^1 \left\{ \ln(2 - x^2) - 2x^2(2 - x^2) \ln Q(x) \right\} \psi(x, n) - \left[x^{2(1-n)} \psi(x, n) - 4n \sin \pi n \frac{(2 - x^2)^n}{D_1(x)} \right] \frac{x^{2n} [\ln(x^2) - 2]}{2 - x^2} \left\} \frac{dx}{\sqrt{2 - x^2}}. \quad (C2.3)$$

The integral (C2.3) is calculated numerically using the trapezoidal rule.

Consider the integral

$$E_1(n) = \int_{-1}^1 f(\lambda, n) I^2(\lambda, n) d\lambda; \quad f(\lambda, n) = [2 - (Q^n(\lambda) + Q^{-n}(\lambda)) \cos(\pi n)]. \quad (C3.1)$$

where $I(s, n)$ is expressed in the form of successive integral

$$I^2(\lambda, n) = \left[\int_{-1}^1 \frac{\phi(s, n) ds}{s - \lambda} \right]^2 = \int_{-1}^1 \frac{\phi(s_1, n) ds_1}{s_1 - \lambda} \int_{-1}^1 \frac{\phi(s_2, n) ds_2}{s_2 - \lambda}, \quad \phi(s, n) = \frac{Q^n(s) ds}{D(s) \sqrt{1 - s^2}}.$$

Then, the integral $E_1(n)$ is transformed into the triple integral. Using the Poincare-Bertrand rule [13] we change the integration sequence and express (C3.1) in the form

$$\begin{aligned} E_1(n) &= \int_{-1}^1 \phi(s_2, n) ds_2 \int_{-1}^1 \frac{f(\lambda, n) d\lambda}{s_2 - \lambda} \int_{-1}^1 \frac{\phi(s_1, n) ds_1}{s_1 - \lambda} = \\ &= \int_{-1}^1 \phi(s_2, n) ds_2 \int_{-1}^1 \phi(s_1, n) E_{11}(s_1, s_2, n) ds_1 + \pi^2 E_0(n), \\ E_0(n) &= \int_{-1}^1 \phi^2(s, n) f(s, n) ds = \int_{-1}^1 \frac{Q^{2n}(s)}{D(s, n)} \{2 - [Q^n(s) + Q^{-n}(s)] \cos(\pi n)\} ds, \\ E_{11}(s_1, s_2, n) &= \frac{1}{s_2 - s_1} \int_{-1}^1 \left(\frac{1}{\lambda - s_2} - \frac{1}{\lambda - s_1} \right) [2 - (Q^n(\lambda) + Q^{-n}(\lambda)) \cos \pi n] d\lambda. \end{aligned}$$

Using Eqs. (B3.2) and (B5.2) of Appendix B we find

$$E_{11}(s_1, s_2, n) = \frac{1}{s_2 - s_1} \{2[\ln Q(s_1) - \ln Q(s_2)] + \frac{\pi \cos^2(\pi n)}{\sin(\pi n)} [Q^n(s_1) - Q^{-n}(s_1) - Q^n(s_2) + Q^{-n}(s_2)]\}.$$

Function $E_0(n)$ is calculated using Eqs. (B2.1)-(B2.2) and expressed in the form

$$E_0(n) = \frac{1}{2n} \int_0^\infty \frac{[1 - \cos(\pi n) ch(t)] dt}{[ch(t) - \cos(\pi n)]^2} = \frac{1}{2n} \left\{ \sin^2(\pi n) \int_0^\infty \frac{dt}{[ch(t) - \cos(\pi n)]^2} - \cos(\pi n) \int_0^\infty \frac{dt}{ch(t) - \cos(\pi n)} \right\} = \frac{1}{2n}.$$

Then, the integral $E_1(n)$ is

$$E_1(n) = \frac{\pi^2}{2n} - 4 \int_{-1}^1 \phi(s) ds \int_{-1}^1 \frac{\phi(t) \ln Q(t) dt}{t - s} + \frac{2\pi \cos^2(\pi n)}{\sin(\pi n)} \int_{-1}^1 \phi(s) I_1(s, n) ds = \frac{\pi^2}{2n} - 4E_{10}(n) + \frac{2\pi \cos^2(\pi n)}{\sin(\pi n)} E_{12}(n),$$

Using Eqs. (B4.2), (C1.1) and (B2.2), we find

$$E_{12}(n) = \frac{\pi}{n} [I_0(n) - 2n \sin(\pi n) I_{12}(n)] = \frac{\pi}{n^2 \sin(\pi n)} \left\{ e_0(n) - \frac{n}{2} [1 + \pi(1-n) \operatorname{ctg}(\pi n)] \right\}.$$

Then, we obtain

$$E_1(n) = \frac{\pi^2}{2n} - 4E_{10}(n) + \frac{2\pi^2}{n^2} \operatorname{ctg}^2(\pi n) \left\{ e_0(n) - \frac{n}{2} [1 + \pi(1-n) \operatorname{ctg}(\pi n)] \right\}. \quad (C3.2)$$

Now, we analyze the double integral

$$e_{10}(n) = n^4 E_{10}(n) = -n^4 \int_{-1}^1 \frac{Q^n(s) \ln Q(s) ds}{D(s, n) \sqrt{1-s^2}} \int_{-1}^1 \frac{Q^n(t) \ln Q(t) dt}{D(t, n) \sqrt{1-t^2} (t-s)}. \quad (C4.1)$$

Its asymptotic value at $n=1$ is

$$e_{10}(1) = -\frac{1}{16} \int_{-1}^1 \ln Q(t) \sqrt{1-t^2} dt \int_{-1}^1 \frac{\sqrt{1-s^2} ds}{s-t} = \frac{\pi}{16} \int_{-1}^1 \ln Q(t) \sqrt{1-t^2} t dt.$$

Integrating by parts we obtain

$$e_{10}(1) = \frac{\pi}{16} \int_{-1}^1 \ln\left(\frac{1+t}{1-t}\right) \sqrt{1-t^2} dt = \frac{\pi}{24} \int_{-1}^1 \sqrt{1-t^2} dt = \frac{\pi^2}{48} \approx 0.2056. \quad (C4.2)$$

At $n = 0$ we have

$$e_{10}(0) = \int_{-1}^1 \frac{i_{14}(t) dt}{[\pi^2 + \ln^2 Q(t)] \sqrt{1-t^2}} = \frac{\pi}{2} (i_0 - 2\pi_1) = \frac{2\ln 2 - 1}{4} \approx 0.09657.$$

The first integral is given by Eq. (C1.3); the second integral is evaluated in a similar way

$$i_1 = \int_{-1}^1 \frac{dt}{(1-t^2)[\ln Q^2(t) + \pi^2]} = \frac{1}{2\pi^3} \int_{-\infty}^{\infty} \frac{dx}{(1+x^2)^2} = \frac{1}{4\pi^2}.$$

In the limit $n \rightarrow 0$, the integral (C4.1) is reduced to the form

$$\begin{aligned} e_{10}(n) &= e_{10}(0) + \frac{n^2}{12} \left\{ 4\pi^2 e_{10}(0) - \int_{-1}^1 \frac{i_{14}(s) ds}{\sqrt{1-s^2}} - \int_{-1}^1 \frac{i_{15}(t) ds}{[\ln^2 Q(s) + \pi^2] \sqrt{1-s^2}} \right\} = \\ &= e_{10}(0) + \frac{n^2 \pi^2}{24} \{ 8e_{10}(0) - 1 \} = \\ &= \frac{1}{4} \left[2\ln 2 - 1 + \frac{n^2 \pi^2}{6} (4\ln 2 - 3) \right] \approx 0.09657 - 0.09352n^2. \end{aligned} \quad (C4.3)$$

The integrals $i_{14}(t)$ and $i_{15}(t)$ are calculated similar to the case of $I_1(s, n)$ (see Eqs. A4.1-A4.2)

$$\begin{aligned} i_{14}(t) &= \int_{-1}^1 \frac{\ln Q(s) ds}{[\pi^2 + \ln^2 Q(s)] \sqrt{1-s^2} (s-t)} = \frac{\pi}{2} \left[1 - \frac{2\pi}{\sqrt{1-t^2} [\ln Q^2(t) + \pi^2]} \right], \\ i_{15}(t) &= \int_{-1}^1 \frac{\ln Q(s) ds}{\sqrt{1-s^2} (s-t)} = \frac{\pi^2}{\sqrt{1-t^2}}. \end{aligned}$$

For $0 < n < 1$, the function $e_{10}(n)$ is evaluated numerically using the substitutions

$$x = (1-s)^{(n+1)/2}, \tau = (1-t)^n, \nu = \frac{2}{n+1}, k = \frac{1}{n}.$$

With these variables the above integrals are transformed into the proper integral

$$e_{10}(n) = 2n^3 \int_0^1 \frac{\sqrt{\tau}(2-\tau^k)^{n-\frac{1}{2}} \ln Q(\tau)}{D_1(\tau, n)} \left[\frac{\sqrt{\tau}(2-\tau^k)^{n-\frac{1}{2}} \ln Q(\tau)}{D_1(\tau, n)} - 2(1-\tau^k)E_r(\tau, n) \right] d\tau. \quad (C4.4)$$

$$E_r(\tau, n) = \nu \int_0^1 \left[\frac{\tau^{\frac{\nu-1}{2}} x^{\frac{\nu}{2}} (2-x^\nu)^{n-\frac{1}{2}}}{D_1(x, n)} - \frac{\sqrt{\tau}(2-\tau^k)^{n-\frac{1}{2}} x^{\nu \frac{1-n}{2}}}{D_1(\tau, n)} \right] \frac{dx}{(\tau^k - x^\nu)(2-\tau^k - x^\nu)}.$$

$$D_1(x, n) = x^{2n\nu} + (2-x^\nu)^{2n} - 2x^{n\nu}(2-x^\nu)^{2n} \cos(\pi n),$$

$$D_1(\tau, n) = (2-\tau^k)^{2n} + \tau^2 - 2\tau(2-\tau^k)^n \cos(\pi n).$$

The integral $e_{10}(n)$ is calculated numerically using the trapezoidal rule.

Consider the integral

$$E_2(n) = \int_{-1}^1 f(\lambda, n) I(\lambda, n) \lambda d\lambda = \int_{-1}^1 \phi(t, n) I_4(t, n) dt. \quad (C5.1)$$

The inner integral $I_4(n)$ is given by Eq. (B5.3). The function $E_2(n)$ is expressed as

$$\begin{aligned} E_2(n) &= 4[1 - \pi \operatorname{ctg}(\pi n)] I_0(n) - 2I_2(n) + \pi \frac{\cos^2(\pi n)}{\sin(\pi n)} I_{10}(n) = \\ &= \frac{1}{n \sin(\pi n)} \left[4[1 - \pi \operatorname{ctg}(\pi n)] e_0(n) - 2e_2(n) + \frac{(2n^2 + 1)}{6} \pi^2 \cos^2(\pi n) \right]. \end{aligned} \quad (C5.2)$$

Its asymptotic behavior is

$$n \rightarrow 1: F_2(n) = \frac{\pi}{2(1-n)}, \quad E_2(0) = -\frac{\pi}{3} \left(\frac{\pi^2}{2} - 4 \ln 2 - 2 \right). \quad (C5.3)$$

Part 3. Dynamics of Slender Bodies Separating from Rectangular Cavities

3.1 Introduction and Problem Formulation

Modeling of store separation from a cavity, even into a subsonic external stream, is very difficult. It is the subject of intensive application of current CFD. The motivation of the work described herein is the need for quick, less computer-intense methods of certifying and assessing the physics of store separation from cavities. Similar rapid evaluation methods are needed for stage and cargo separations. A variety of computational methods are being developed. As contrasted to pure computational modeling, we discuss in this chapter a combined asymptotic and numerical approach based on the theoretical results provided in Parts 1 and 2. The analysis in this chapter neglects slip-surface displacement. A more general case is analyzed in Part 1, where the slip surface is treated as a free boundary. This leads to nonlinear boundary conditions on the slip surface. For the practically important case of small deflections, the boundary conditions can be linearized on the length scale of the cavity. Local flow scales show larger deflections in which an iterative scheme needs to be used to obtain a solution. The non-deflected slip surface corresponds to the initial iterate in such a small-perturbation scheme.

In this chapter, we couple the results for the body aerodynamics, obtained in Parts 1 and 2, with rigid-body dynamics and analyze two degree-of-freedom (2-DOF) vertical and pitching motions induced by aerodynamic and gravity forces during the separation process. The coordinate systems XYZ (attached to the cavity), $oxyz$ (attached to the body center of gravity), (body axes) are shown in Fig. 3.1. The $oxyz$ -frame is inclined with respect to XY -frame at an angle of attack $\alpha(t)$. This frame can rotate around the oz -axis with the angular speed $\omega(t) = d\alpha/dt$. In the wind axes, the center of gravity (CG) coordinates are $X_c = Z_c = 0$ and $Y \equiv Y_c(t)$. We denote $H(X, t) = Y_c - \alpha X$ as the vertical coordinate of the body axis. Using slender body theory [6] scaling, we introduce the nondimensional variables

$$\begin{aligned} X = \frac{\hat{X}}{\hat{l}_0}, \quad Y = \frac{\hat{Y}}{\hat{a}_0}, \quad Z = \frac{\hat{Z}}{\hat{a}_0}, \quad x = \frac{\hat{x}}{\hat{l}_0}, \quad y = \frac{\hat{y}}{\hat{a}_0}, \quad z = \frac{\hat{z}}{\hat{a}_0}, \quad t = \frac{U_\infty \hat{t}}{\hat{l}_0}, \\ \alpha = \frac{\hat{\alpha}}{\delta}, \quad V_c = \frac{\hat{V}_c}{\hat{V}_r}, \quad \omega = \frac{\delta U_\infty \hat{\omega}}{\hat{l}_0}, \end{aligned} \quad (3.1)$$

where the body half thickness ratio, δ , is treated as a small parameter. Crossflow velocities and coordinates are normalized by δU_∞ and \hat{a}_0 respectively. The streamwise and axial coordinates are scaled using \hat{l}_0 and the pressure perturbation, p , is normalized with respect to $\rho_\infty U_\infty^2 \delta^2 \hat{l}_0^2$.

As shown in Ref. [17], the equations for vertical and pitching body motions can be expressed in the form

$$\frac{d(V_c + c_l V_a)}{dt} = c_l L(t) - c_g, \quad \frac{dY_c}{dt} = V_c(t), \quad \frac{d(\omega + c_m \omega_a)}{dt} = c_m M(t), \quad \frac{d\alpha}{dt} = \omega(t), \quad (3.2a)$$

$$V_a(t) = \int_{x_0}^{x_e} \int_0^{2\pi} \Phi(x, \theta, t) a(x) d\theta dx, \quad \omega_a(t) = \int_{x_0}^{x_e} \int_0^{2\pi} \Phi(x, \theta, t) a(x) x d\theta dx, \quad (3.2b)$$

$$c_g = \frac{g \hat{l}_0}{\delta U_\infty^2}, \quad c_l = \frac{\pi \rho_\infty \hat{l}_0^3 \delta^2}{m}, \quad c_m = \frac{\pi \rho_\infty \hat{l}_0^5 \delta^2}{I}, \quad (3.2c)$$

where x_0 and x_e are coordinates of the body nose and base respectively, m and I are the body mass and moment of inertia respectively and Φ is the near field body (inner) flow potential. We consider the initial-value problem for Eqs. (3.2a) assuming that the CG position, angle of attack and body velocity are prescribed at the initial time $t = 0$ as

$$V_c(0) = V_0, \quad \omega(0) = \omega_0, \quad Y_c(0) = Y_0, \quad \alpha(0) = \alpha_0. \quad (3.2d)$$

Note that dV_a/dt and $d\omega_a/dt$ in (3.2a) represent the time derivative of the crossflow potential (incompressible harmonic inner solution) needed for the pressure in the crossflow plane from the unsteady Bernoulli equation. The terms L_1 and M_1 are integrals involving the square of the crossflow speed that also appear in the Bernoulli law for the pressure in the crossflow inner problem. This speed is the square of the crossflow gradient of Φ .

In Section 3.2, analytical solutions of the problem (3.2a)-(3.2d) for Phase 1 are obtained for small lift forces compared to the weight. In Section 3.3, the trajectory equations are analyzed for Phase 3 and are transformed into two decoupled ordinary differential equations with constant coefficients. A stability analysis of their solutions is performed, and behaviors of the pitch angle $\alpha(t)$ and the vertical coordinate $Y_c(t)$ are discussed for typical cases. In Section 3.4, the predictions based on the theoretical model for all three phases (in Eqs. (3.2)) (without the stability linearization) is compared to experimental data of Ref. [18]. Section 3.4 concludes with some parametric trajectory studies. In Section 3.5, conclusions are discussed.

3.2 Phase 1: body inside cavity

The lift force, $L(t)$, and the pitching moment, $M(t)$, acting on the body moving inside the cavity are derived in Ref. [17]. They are expressed as integrals along the body axis, with the integrands expressed as power series in the parameters $q_1(x, t) = 0.5a/(H_0 - H)$ and $q = 0.5a/H$, where H_0 is cavity depth shown in Figs 3.1a and 3.1b. If the body is far from the top cavity wall and the slip surface, then q_1 and q can be treated as small parameters. Neglecting terms of the order of $O(q^3, q_1^3)$ the functions $V_a^+(t)$ and $\omega_a^+(t)$ are

$$V_a^+(t) \equiv \alpha_{11}(t)V_c(t) - \alpha_{12}(t)\omega(t), \quad \omega_a(t) \equiv \alpha_{12}(t)V_c(t) - \alpha_{22}(t)\omega(t), \quad (3.3a)$$

$$\alpha_{11}(t) \equiv \pi[g_0 + G_0(t)], \quad \alpha_{12}(t) \equiv \pi[g_1 + G_1(t)], \quad \alpha_{22}(t) \equiv -\pi[g_2 + G_2(t)], \quad (3.3b)$$

$$g_0 \equiv \int_{x_0}^{x_e} a^2(x) dx, \quad g_1 \equiv \int_{x_0}^{x_e} a^2(x) x dx, \quad g_2 \equiv \int_{x_0}^{x_e} a^2(x) x^2 dx, \quad (3.3c)$$

$$G_0(t) \equiv 2 \int_{x_0}^{x_e} [q_1^2(x, t) - q^2(x, t)] a^2(x) dx, \quad (3.3d)$$

$$G_1(t) \equiv 2 \int_{x_0}^{x_e} [q_1^2(x, t) - q^2(x, t)] a^2(x) x dx, \quad G_2(t) \equiv 2 \int_{x_0}^{x_e} [q_1^2(x, t) - q^2(x, t)] a^2(x) x^2 dx. \quad (3.3e)$$

This transformation helps to express the dynamic equations in a form convenient for further discussion of the body trajectory features. Using Eqs. (3.3a)-(3.3e) the trajectory a first integral of Eqs. (3.2a) is

$$\frac{dY_c}{dt} = -\frac{b_{22}(t)}{\Delta(t)} c_g t + \frac{\Delta_1(t)}{\Delta(t)} V_0 + c_l \pi \omega_0 b_1(t), \quad (3.4a)$$

$$\frac{d\alpha}{dt} = \frac{b_{21}(t)}{\Delta(t)} c_g t + \frac{\Delta_2(t)}{\Delta(t)} \omega_0 + c_m \pi V_0 b_2(t), \quad (3.4b)$$

where

$$b_{11}(t) \equiv 1 + c_l \alpha_{11}(t), \quad b_{12}(t) \equiv c_l \alpha_{12}(t), \quad b_{21}(t) \equiv c_m \alpha_{12}(t), \quad b_{22}(t) \equiv 1 - c_m \alpha_{22}(t),$$

$$\Delta \equiv b_{11}(t)b_{22}(t) + b_{12}(t)b_{21}(t),$$

$$\Delta_1 \equiv b_{11}(0)b_{22}(t) + b_{12}(t)b_{21}(0), \quad \Delta_2 \equiv b_{11}(t)b_{22}(0) + b_{12}(0)b_{21}(t),$$

$$b_1 \equiv \frac{1}{\Delta} \{ (1 - c_m \pi g_2) [G_1(t) - G_1(0)] +$$

$$+ c_m \pi g_1 [G_2(t) - G_2(0)] + c_m \pi [G_1(0)G_2(t) - G_1(t)G_2(0)] \},$$

$$b_2 \equiv \frac{1}{\Delta} \{ (1 + c_l \pi g_0) [G_1(0) - G_1(t)] + c_l \pi g_1 [G_0(t) - G_0(0)] + c_l \pi [G_1(0)G_0(t) - G_1(t)G_0(0)] \}.$$

The first term of Eqs. (3.4a)-(3.4b) models the gravity effect, the second comes from the initial conditions, and the third arises from the boundary and initial conditions. The angular acceleration is proportional to the product of the pitching moment coefficient c_m , the gravity force coefficient c_g and the value $g_1 + G_1(t)$ characterizing the displacement of the center of pressure from the CG. Equations (3.4) can be solved numerically using, for example, the Runge-Kutta method. Note that the slip surface effect and the top wall effect rapidly decrease as the body moves away from these boundaries. Neglecting terms of the order of $O(q^2 + q_1^2)$, which are associated with the boundary effects, the solution of Eqs. (3.4) can be expressed in the explicit analytical form

$$Y_c(t) = Y_0 + V_0 t - \frac{1 - \pi c_m g_2}{2\Delta_0} c_g t^2, \quad \alpha(t) = \alpha_0 + \omega_0 t + \frac{\pi g_1 c_m c_g}{2\Delta_0} t^2, \quad (3.5a)$$

$$\Delta_0 = (1 + c_l \pi g_0)(1 - c_m \pi g_2) + c_l c_m \pi^2 g_1^2. \quad (3.5b)$$

Equations (3.5) show that the CG coordinate, $Y_c(t)$, and the pitch angle, $\alpha(t)$, are parabolic functions of time when the body moves in an unbounded fluid at rest.

Analytical solutions of Eqs. (3.4) can also be obtained when the lift and moment are small compared to the body weight and pitch inertia. This is typical for many practical cases because the coefficients c_l and c_m are proportional to the air density to body density ratio, $\rho_\infty / \rho_b \ll 1$. For a body of uniform density, non-dimensional “ballistic parameters” may be defined to define a “weak” aerodynamic force case. These are

$$c_l = \frac{\rho_\infty}{\rho_b \pi g_0}, \quad c_m = \frac{\rho_\infty}{\rho_b \pi g_2}, \quad \frac{c_l}{c_m} = \frac{g_2}{g_0}. \quad (3.6)$$

Non-dimensional groupings such as these to our knowledge have not been used to evaluate the accuracy of large-scale computer (CFD) store separation simulations. Despite the difficulty associated with gridding, complex geometry and turbulence modeling as well as other uncertainties, surprisingly accurate correlations with flight test and wind tunnel trajectories can in regions of parameter space be obtained with computationally intense numerics. In some cases, pseudo-steady Euler solutions provide surprisingly good answers even when viscous, unsteady and high angle-of-attack vortical and complex shock interactions effects are present. We conjecture that in many of these situations the aerodynamic forces are relatively negligible compared to the rigid body inertial forces. The ballistic parameters provide a means of cataloging and correlating the various scenarios and determining when rougher and approximate simulations as well as coarse grid CFD will have a good chance of giving a fast answer of useful engineering accuracy with low cost and overhead. In fact, it is reasonable to develop a new systematic (asymptotic) approximation scheme for “heavy” bodies in units of non-dimensional parameters such as those in (3.6). This important possible thrust of our research would use the vacuum rigid body solution as the dominant approximation of the aerodynamic coupled trajectory problem. The influence of the aerodynamics would be a linearized second order approximation with simplified mathematics. The discussion that follows is relevant to this idea.

For the experimental conditions in [18], the coefficients c_l and c_m as well as other basic parameters are shown in Tables 1 and 2, where the gravity force coefficient is calculated at the freestream speed $U_\infty = 77.1$ m/s.

If terms linear in c_l and c_m are retained in Eqs. (3.4), the approximate linear and angular trajectories are

$$Y_c = Y_0 + V_0 t - 0.5(1 - \pi c_l g_0) c_g t^2, \quad \alpha = \alpha_0 + \omega_0 t + 0.5 \pi g_1 c_m c_g t^2. \quad (3.7)$$

The CG coordinate and the pitch angle are parabolic functions of time. In the first-order approximation, the vertical motion corresponds to a pure gravity drop. The lift force gives a small negative correction of the CG acceleration similar to the case of a plunging cylinder in the presence of a shear layer considered in Ref. [16]. The analytical expressions (3.7) below are consistent with trends of numerical solutions and experimental data.

Table 1. Physical parameters of models [18]

Model	δ	X_e	g_0	g_1	g_2
B1N1	.31250E-01	.51333E+00	.86206E+00	.68807E-01	.66707E-01
B4N2	.31250E-01	.49500E+00	.86206E+00	.53002E-01	.57596E-01
B5N5	.32609E-01	.62261E+00	.85606E+00	.16423E+00	.12753E+00

Table 2. Aerodynamic and gravity acceleration coefficients for models [18]

Model	c_l	c_m	$c_g U_\infty^2$	c_g
B1N1	.29915E-03	.22204E-02	.95585E+02	.16080E-01
B4N2	.72519E-03	.38857E-02	.95585E+02	.16080E-01
B5N5	.36773E-02	.24684E-01	.87786E+02	.14768E-01

3.3 Phase 3: body outside cavity

If the body is totally outside the cavity and moves into an external free stream, the lift force and pitching moment are again expressed as integrals along the body axis, with the integrands being power series in the parameter $q = 0.5a/H$ (see Section 2.2). These analytical solutions reveal clearly that the slip-surface effect on the body trajectory is proportional to the quantity

$$\int_{x_1}^{x_2} q a^2 a_x dx + \int_{x_1}^{x_2} q^2 a^2 dx \sim \frac{\bar{q}}{3} + \bar{q}^2 g_0 + O(\bar{q}^3 g_0), \quad (3.8)$$

where the bars denote averaging along the body axis. For typical cases, the body shape factor is given by Eq. (3.3c) $g_0 = O(1)$. The average distance parameter is $\bar{q} \leq 0.5$. Its maximum value $\bar{q} = 0.5$ corresponds to contact of the body surface with the slip surface. The maximum values of the first and second terms in Eq. (3.8) are 1/6 and 1/4 respectively. As the body drops, both terms decrease quickly and the slip surface effect vanishes. Thus, dominant terms are associated with the body drop in an unbounded uniform stream. In this case, the equations for the lift force and pitch moment can be reduced to the form

$$L = \pi \left[-g_0 \frac{dV_c}{dt} + g_1 \frac{d\omega}{dt} - (V_c - \alpha) a_e^2 + \omega (g_0 + x_e a_e^2) \right], \quad (3.9a)$$

$$M = \pi \left[-g_1 \frac{dV_c}{dt} + g_2 \frac{d\omega}{dt} + (V_c - \alpha) (g_0 - x_e a_e^2) + \omega x_e^2 a_e^2 \right], \quad (3.9b)$$

where $a_e = a(x_e)$ is the base radius ($a_e = 1$ for cylindrical afterbody). These expressions were derived for bodies with a sharp nose, $\alpha(x_0) = 0$. Substitution of (3.9a) and (3.9b) into the trajectory equations (3.2a) and integration give a linear ODE system (with constant coefficients)

$$\frac{dV_c}{dt} = c_{11}(V_c - \alpha) + c_{12}\omega - c_{10}, \quad \frac{d\omega}{dt} = c_{21}(V_c - \alpha) + c_{22}\omega + c_{20}. \quad (3.10a)$$

$$c_{10} = \frac{1 - c_m \pi g_2}{\Delta_0} c_e, \quad c_{11} = \frac{c_l \pi}{\Delta_0} [c_m \pi g_1 (g_0 - x_e a_e^2) - (1 - c_m \pi g_2) a_e^2], \quad (3.10b)$$

$$c_{20} = \frac{c_m c_e \pi g_1}{\Delta_0}, \quad c_{12} = \frac{c_l \pi}{\Delta_0} [(1 - c_m \pi g_2)(g_0 + x_e a_e^2) + c_m \pi g_1 x_e^2 a_e^2], \quad (3.10c)$$

$$c_{21} = \frac{c_m \pi}{\Delta_0} [(1 + c_l \pi g_0)(g_0 - x_e a_e^2) + c_l \pi g_1 a_e^2], \quad (3.10d)$$

$$c_{22} = \frac{c_m \pi}{\Delta_0} [(1 + c_l \pi g_0) x_e^2 a_e^2 - c_l \pi g_1 (g_0 + x_e a_e^2)], \quad (3.10e)$$

where Δ_0 is given by Eq. (3.5b).

In a manner similar to the nonlinearized 2-DCF equations treated above (after Eqs. (3.2a-c)), we consider the initial-value problem for Eqs. (3.10a) assuming that the body is totally outside the cavity for $t \geq t_0$, and its initial speeds, vertical position and pitch angle are respectively

$$V_c(t_0) = V'_0, \quad \omega(t_0) = \omega'_0, \quad Y_c(t_0) = Y'_0, \quad \alpha(t_0) = \alpha'_0. \quad (3.11)$$

From Eqs. (3.10a), the angular velocity ω and the function $W(t) = V_c(t) - \alpha(t)$ are solutions of the decoupled equations

$$\frac{d^2 W}{dt^2} - 2\gamma \frac{dW}{dt} + \kappa W + c_1 = 0, \quad \frac{d^2 \omega}{dt^2} - 2\gamma \frac{d\omega}{dt} + \kappa \omega + c_2 = 0, \quad (3.12)$$

where the constant coefficients are

$$\gamma = \frac{c_m \pi a_e^2}{2\Delta_0} \left[x_e^2 - \frac{c_l}{c_m} + \pi_l (x_e^2 g_0 - 2x_e g_1 + g_2) \right], \quad (3.13a)$$

$$\kappa = \frac{c_m \pi}{\Delta_0} [g_0 - a_e^2 x_e - c_l \pi a_e^2 (g_0 x_e - g_1)], \quad (3.13b)$$

$$c_1 = \frac{c_m c_g \pi}{\Delta_0} (g_1 - x_e^2 a_e^2), \quad c_2 = \frac{c_m c_g \pi}{\Delta_0} (g_0 - x_e a_e^2). \quad (3.13c)$$

The characteristic (secular) equation for the eigenvalues of the ODE system (3.10a) and its solutions are

$$\lambda^2 - 2\gamma\lambda + \kappa = 0, \quad \lambda_1 = \gamma + i\Omega, \quad \lambda_2 = \gamma - i\Omega, \quad \Omega = \sqrt{\kappa - \gamma^2}. \quad (3.14)$$

Various cases significant for the trajectory stability will now be discussed.

3.3.1 Eigenvalues λ_1 and λ_2 are complex

If λ_1 and λ_2 are complex, the trajectory variables are expressed in the form

$$V_c(t) = V'_0 + \frac{d - c_2 \tau}{\kappa} + e^{\gamma\tau} (A_1 \cos \Omega \tau + A_2 \sin \Omega \tau), \quad (3.15a)$$

$$\omega = -\frac{c_2}{\kappa} + e^{\gamma\tau} (B_1 \cos \Omega \tau + B_2 \sin \Omega \tau), \quad (3.15b)$$

$$Y_c(t) = Y'_0 + \left(V'_0 + \frac{d}{\kappa} \right) \tau - \frac{c_2}{2\kappa} \tau^2 + \frac{e^{\gamma\tau}}{\kappa} [(\gamma A_1 - \Omega A_2) \cos \Omega \tau + (\Omega A_1 + \gamma A_2) \sin \Omega \tau], \quad (3.15c)$$

$$\alpha(t) = \alpha'_0 - \frac{1}{\kappa} \{ c_2 \tau + \gamma B_1 - \Omega B_2 - e^{\gamma\tau} [(\gamma B_1 - \Omega B_2) \cos \Omega \tau + (\Omega B_1 + \gamma B_2) \sin \Omega \tau] \}, \quad (3.15d)$$

where $\tau = t - t_0$ and $d = -\kappa(V'_0 - \alpha'_0) - c_1 - \gamma B_1 + \Omega B_2$. The coefficients A_1 , A_2 , B_1 and B_2 are determined from the initial conditions (3.11) and Eqs. (10a). They are expressed as

$$A_1 = -\frac{d}{\kappa}, \quad A_2 = \frac{c_2}{\Omega \kappa} + \frac{\dot{V}_0 - \gamma A_1}{\Omega}, \quad \dot{V}_0 = \frac{dV(0)}{dt} = c_{11}(V'_0 - \alpha'_0) + c_{12}\omega'_0 - c_{10}, \quad (3.16a)$$

$$B_1 = \omega'_0 + \frac{c_2}{\kappa}, \quad B_2 = \frac{\dot{\omega}_0 - \gamma B_1}{\Omega}, \quad \dot{\omega}_0 = \frac{d\omega(0)}{dt} = c_{21}(V'_0 - \alpha'_0) + c_{22}\omega'_0 + c_{20}. \quad (3.16b)$$

Equations (3.15) indicate that the body motion consists of two components. The first terms of Eqs. (3.15a), (3.15b) correspond to body rotation, with the constant angular speed $-c_2/\kappa$ and a vertical translation with uniform acceleration $-c_2/\kappa$. Also present is a drift with constant velocity $\alpha'_0 - (c_1 + 2\gamma B_1 - \dot{\omega}_0)/\kappa$ that depends on the initial angle of attack and angular velocity. These terms are associated with a non-oscillatory motion,

which we refer to as the “mean state.” The second component corresponds to periodic modulations of this state. These oscillations are neutral for $\gamma = 0$, unstable for positive γ and stable for negative γ . For pointed body tails, $a_e = 0$, Eq. (3.13) specializes to

$$\gamma = 0, \quad \kappa = \Omega^2 = \frac{c_m \pi}{\Delta_0} g_0, \quad c_1 = \frac{c_m c_g \pi}{\Delta_0} g_1, \quad c_2 = \frac{c_m c_g \pi}{\Delta_0} g_0.$$

This case corresponds to neutral oscillations. For heavy bodies with base radius $a_e = 1$ and small ballistic coefficients $c_l \ll 1$, $c_m \ll 1$, we can linearize about c_l and c_m . Equations (3.13) give

$$\gamma = \pi c_m \left(x_e^2 - \frac{c_l}{c_m} \right), \quad \kappa = \Omega^2 = c_m \pi (g_0 - x_e), \quad (3.17a)$$

$$c_1 = \pi c_m c_g (g_1 - x_e^2), \quad c_2 = \pi c_m c_g (g_0 - x_e), \quad d = \pi c_l (\omega_0 + c_g). \quad (3.17b)$$

Equations (3.17) show that oscillations are unstable for $x_e^2 > c_l / c_m$. This case fits the experimental conditions of Ref. [18]. For $x_e^2 \leq c_l / c_m$, oscillations are stable or neutral. In all cases the increment is small $\gamma \sim c_m \sim \Omega^2 \ll 1$.

The expressions for the vertical speed and angular velocity are

$$V_c = V'_0 - c_g \tau + A_1 (e^{\gamma \tau} \cos \Omega \tau - 1) + A_2 e^{\gamma \tau} \sin \Omega \tau, \quad \omega = -c_g + e^{\gamma \tau} (B_1 \cos \Omega \tau + B_2 \sin \Omega \tau).$$

The first equation indicates that the CG oscillates near its mean state associated with a free drop. If the body dynamics is stable, $\gamma < 0$ and the oscillations vanish as $\tau \rightarrow \infty$. Nevertheless, they induce the constant vertical velocity $-A_1 = c_l \pi (\omega'_0 + c_g) / \Omega^2$. The second equation shows that the angular velocity oscillates near its mean level $\bar{\omega} = -c_g$ associated with a free drop.

3.3.2 Eigenvalues λ_1 and λ_2 are real

If $\lambda_1 = \gamma + \nu$ and $\lambda_2 = \gamma - \nu$ ($\nu = \sqrt{\gamma^2 - \kappa}$) are real, then the solution of Eqs. (3.10a) or Eqs. (3.12) is

$$V_c(t) = V'_0 + \frac{d - c_2 \tau}{\kappa} + e^{\gamma \tau} (A_1 \cosh \nu \tau + A_2 \sinh \nu \tau), \quad \omega = -\frac{c_2}{\kappa} + e^{\gamma \tau} (B_1 \cosh \nu \tau + B_2 \sinh \nu \tau), \quad (3.18a)$$

$$Y_c(t) = Y'_0 + \left(V'_0 + \frac{d}{\kappa} \right) \tau - \frac{c_2}{2\kappa} \tau^2 + \frac{e^{\gamma \tau}}{\kappa} [(\gamma A_1 - \nu A_2) \cosh \nu \tau + (\gamma A_2 - \nu A_1) \sinh \nu \tau], \quad (3.18b)$$

$$\alpha(t) = \alpha'_0 - \frac{1}{\kappa} \{ c_2 \tau + \gamma B_1 - \nu B_2 - e^{\gamma \tau} [(\gamma B_1 - \nu B_2) \cosh \nu \tau + (\gamma B_2 - \nu B_1) \sinh \nu \tau] \}, \quad (3.18c)$$

where $d = -\kappa(V'_0 - \alpha'_0) - c_1 - \gamma B_1 + \nu B_2$, and the coefficients are

$$A_1 = -\frac{d}{\kappa}, \quad A_2 = \frac{c_2}{\nu\kappa} + \frac{V'_0 - \gamma A_1}{\nu}, \quad B_1 = \omega'_0 + \frac{c_2}{\kappa}, \quad B_2 = \frac{\dot{\omega}_0 - \gamma B_1}{\nu}. \quad (3.19)$$

Again, the body motion consists of two components. The first component is similar to the previous case. It is associated with a pure gravity drop and can be treated as a basic state. The second component is relevant to an exponential drift from or toward the basic state depending on the signs of the eigenvalues. If $\lambda_1 < 0$ and $\lambda_2 < 0$, then the exponents decay as $\tau \rightarrow \infty$, and the body motion tends exponentially from the initial conditions to the basic state, which includes rotation with constant angular velocity and translation with constant acceleration. If λ_1 and/or λ_2 are positive, then the exponential terms grow with time and the body departs from its basic state (aperiodic divergence). If $\nu = 0$, then the second component of the body motion is governed by the sign of γ .

These analytical solutions and stability characteristics of the body dynamics can be used for fast qualitative estimations of the body trajectory outside the cavity. To our knowledge, these results are new. *With further development and generalization, test engineers and other personnel can use them to rapidly and cost-effectively certify and qualify store arrangements and new configurations.*

3.4 Results and discussion

To calculate the body trajectory, including all phases of the separation process, Eqs. (3.2a) have been integrated numerically using a fourth order Runge-Kutta scheme [23]. We have used this procedure to develop a research code, which includes a module that calculates the lift force and pitching moment for Phases 1, 2 and 3 using the analytical results of Part 2. The accuracy of the predictions can be related to the size of the perturbation parameters and uncertainties in the experimental launch conditions. In the best cases, the accuracy can be as good as a few percent when the aerodynamic forces are small compared to the weight and the characteristic pitch inertia with experimental initial conditions that matched those assumed in the theory. Large excursions can result if large-scale shear layer motions occur and other disturbances evolve in the external flow.

The combined asymptotic and numerical method described provides a means to rapidly calculate body trajectories. One trajectory is normally predicted in less than 1/2 minute using a PC Pentium166. To illustrate this capability, this quick-turnaround-PC oriented tool will be compared to the subsonic experimental data [18] in what follows.

3.4.1 Experimental Data

Drop tests [18] were conducted at the National Diagnostic Wind Tunnel of IIT Fluid Dynamics Research Center in the Mach number range $0.12 < M < 0.23$. The rectangular cavity of 20 inches length, 41 inches width and 4 inches height was mounted on the top wall of the wind tunnel test section. The models were bodies of revolution of radius $\hat{a}_0 = 3/8"$ and nose length $\hat{x}_n = 3.56"$ (see Fig. 3.2). Two models (B1N1 and B4N2)

were ogive-cylinders of 12 inches length. The third model (B5N5) has elliptic nose and total length of 11.5 inches. The heaviest model B1N1 had a mass $m = 111.85$ g, moment of inertia $I = 0.0014 \text{ kg}\times\text{m}^2$ and a CG location $\hat{x}_0 = 6.16''$. For Model B4N2, $m = 46.14$ g, $I = 0.0008 \text{ kg}\times\text{m}^2$, $\hat{x}_0 = 5.94''$. For the lightest model B5N5, $m = 8.72$ g, $I = 0.000015 \text{ kg}\times\text{m}^2$. In these experiments, bodies were dropped from a cavity in the IIT wind tunnel. The models were released by withdrawing pins holding them at their nose and tail.

3.4.2 Comparison with Experiment

Preliminary analysis of the experimental data shows that at the release time, $t_r \approx 0.03$ sec., the initial angular and vertical velocities can be affected by uncontrolled disturbances that may be induced by the release mechanism. Shortly after the release time, the gravity force may increase the pitch rate, if the model ends are not released simultaneously. This motivated identification of the actual initial angular speed $\hat{\omega}_0$ and vertical velocity \hat{V}_a by differentiating the experimental distributions of the pitch angle $\hat{\alpha}(\hat{t})$ and the CG vertical coordinate $\hat{Y}_c(\hat{t})$. This was used to correlate the theory and help isolate as well as understand any discrepancies between theory and the experiments.

The "a" parts of Figs. 3.3-3.10 show comparisons between predicted (solid lines) and experimental (symbols) CG trajectories for all three models. Dashed lines indicate the free-drop trajectories under the gravity force only. As noted above, the lift is small compared to the body weight. Figure 3.3 shows that a free drop in a vacuum is very close to the computational results and the experimental data for moderate angles of attack, especially for the heavier model B1N1. However, the "vacuum" curve diverges from the experimental data, if the body enters into the external stream at relatively large α . This is clearly seen in Figs. 3.4a, 3.8a, and 3.10a. In these cases, the theoretical prediction accounting for aerodynamic loads is in good agreement with the experiment. Moreover, the theoretical model is capable of capturing trajectory nuances shown in Fig. 3.8a.

The "b" parts of Figs. 3.3-3.10 compare predictions (lines) and experimental (symbols) histories of the angle of attack $\alpha(t)$. Figures 3.3b-3.6b show good agreement between theory and the experiment. The agreement is satisfactory only for the cases shown in Figs. 3.7b-3.9b. Rough estimates indicate that the initial growth of α (see Fig. 3.7b) may be associated with an initial pitch impulse generated by the release mechanism under a gravitational couple from the pins. In this case, both the initial angle of attack and angular speed were estimated from the experiments and were used as the initial conditions for our calculations. For the lightest model B5N5 (see Fig. 3.8b), the discrepancy seems to be due to the difference between the actual nose shape (elliptic) and the shape used in our calculations (parabolic ogive). Unfortunately, calculations were not possible for the actual nose because its precise geometry was not available. Note that the nose shape becomes more important at large pitch angles. The divergence of the predicted and experimental curves in Fig. 3.9b seems to be due to the flow inside the cavity, which is presently not included in our modeling. Pitch oscillations observed in Phase 1 (body is totally inside the cavity) clearly indicate the presence of this effect, which may also

explain the substantial difference between the theory and the experiment shown in Fig. 3.10b.

As indicated above, the pitch behavior in Phase 3 (body is outside the cavity) strongly depends on the entry condition, which is a function of the angular velocity, vertical speed and their derivatives. For the case shown in Fig. 3.10b, the shear-layer displacement from its basic state into the cavity may cause a phase jump of the right-hand side term in Eq. (3.2a) from 0 to 180 degrees. Such a jump affects the pitch history outside the cavity. This is illustrated in Fig. 3.10b by the dotted line that was calculated with the opposite sign of the pitching moment. This curve is in a good agreement with the experimental data. On the other hand, experimental curves, shown in Figs. 3.5b, 3.6b and 3.7b for approximately the same initial conditions, have a regular behavior; *i.e.* they are in good agreement with the computations performed without changes of the sign of pitching moment. These findings suggest a bifurcation in the pitch history $\alpha(t)$ when the body enters into the external stream. The trajectory equations allow such a bifurcation, since the aerodynamic forcing terms of Eqs. (3.2a) are nonlinear (quadratic) functions of speeds V and ω . One of two possible trajectories is selected, when the body crosses the shear layer. Therefore, Phase 2 serves as a trigger of the pitch bifurcation. Accurate modeling of this mechanism is important to predict the pitch history and store trajectory in the next phase when the store is outside the cavity. To verify this hypothesis additional theoretical, numerical and experimental studies are needed.

3.4.3 Parametric Studies

Parametric studies of the body trajectory were conducted for different initial conditions, body parameters and freestream speeds. The results are shown in Figs. 3.11-3.15. Variations of the initial vertical velocity cause not only CG acceleration but phase shift of the pitch angle (see Fig. 3.11). In accord with the analytical solution discussed in Section 3.3.1, an increase of the freestream velocity leads to a substantial increase of the mean pitching angle and the pitch oscillation frequency (see Fig. 3.12), while the CG trajectory is changed slightly. Figure 3.13 shows that pitch oscillation amplitude increases and phase shift occurs as the initial angular speed increases. Amplification of the pitch oscillations is stronger in the case of positive ω_0 with the CG trajectory also noticeably affected. The effect of the initial pitch angle is similar to the effect of ω_0 (compare Figs. 3.14 and 3.15). However, the variation of the CG trajectory in this case is smaller.

Trajectory dependencies on the body shape are illustrated in Fig. 3.15. The calculations were performed for three experimental models of Ref. [18] under the same initial conditions. As expected, the highest amplitude and frequency of the body oscillations correspond to the lightest model B5N5. The body trajectories outside the cavity also are consistent with the analytical solution discussed above.

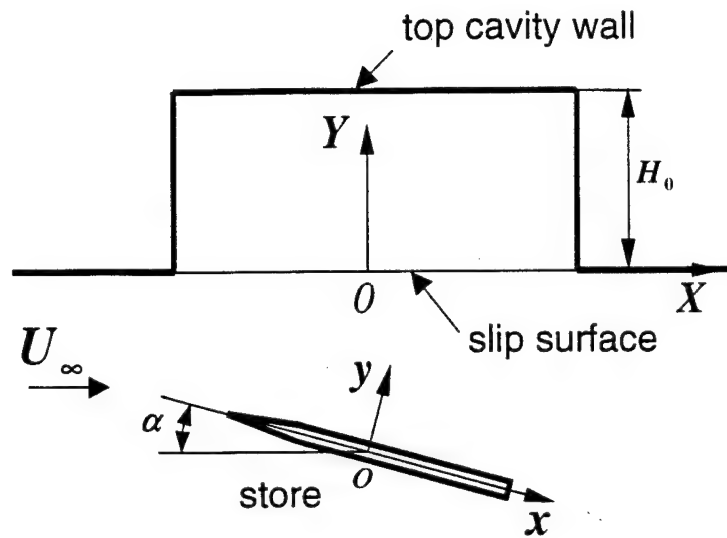
3.5 Conclusions

In this part, we discussed modeling of 2-DOF vertical and pitching motions of thin bodies of revolution separating from a rectangular cavity into external free stream. The problem is analyzed using combined asymptotic and numerical methods. The body dynamic

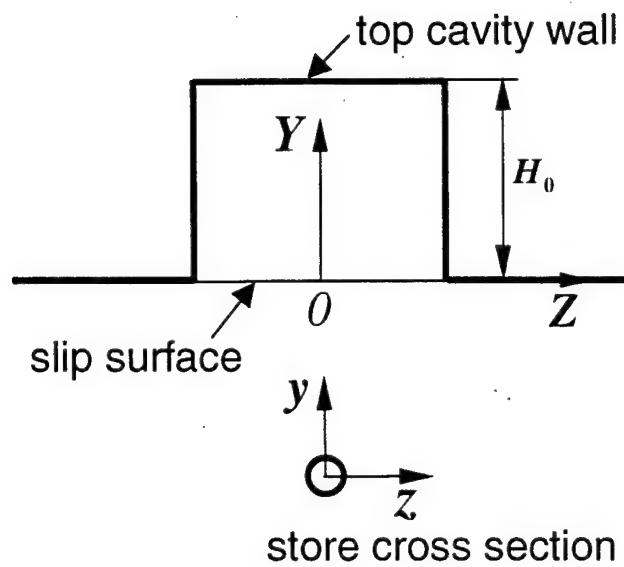
equations include aerodynamic forces and moments, which are predicted using approximate analytical solutions obtained in Part 2 of our previous studies within the framework of the slender body theory. Different phases of the separation process were analyzed using small perturbation theories. This leads to simplifications of the trajectory equations and their integration in closed form for different typical cases associated with Phase 1 (body is inside the cavity) and Phase 3 (body is outside the cavity). These analytical solutions provide explicit dependencies of the body trajectory on the flow and body characteristics, to allow identification of the critical parameters and provide insight into the physics of the separation process.

The numerical code predicting trajectories for all three phases of store separation was validated by comparison with the experiment. For a major portion of the data, the calculations are in good agreement with experiment. Moreover, the theory is able to capture nuances of the body pitching observed experimentally. These results confirm our theoretical model. However, there are cases when the agreement is only satisfactory. The body separation is affected by more complex flow phenomena, which are not captured by our model. One discrepancy seems to be due to the slip surface displacement induced by shear-layer instability and/or self-excited oscillations of the cavity flow. These effects can lead to a pitching moment phase jump from 0 to 180 degrees during Phase 2, when the body crosses the shear layer. The jump may trigger quick transition from one pitch-angle trajectory to another for Phase 3, when the body is outside the cavity. Our calculations showed that this interpretation is consistent with experimental data and indicates the existence of two substantially different pitching trajectories for approximately the same initial conditions. Since nonlinear dynamic equations are involved, the body trajectory may have a bifurcation point associated with Phase 2. Although this transitional phase is relatively short, its aerodynamics may determine the selection between possible trajectories outside the cavity. Further theoretical and experimental studies are needed to establish and clarify the bifurcation mechanism. Our future work will extend this model to transonic speeds. Progress in this direction is discussed in Part 4 of this report.

3.6 Illustrations



a)



b)

Fig. 3.1 Schematic of store separation: a) - side view; b) - back view.

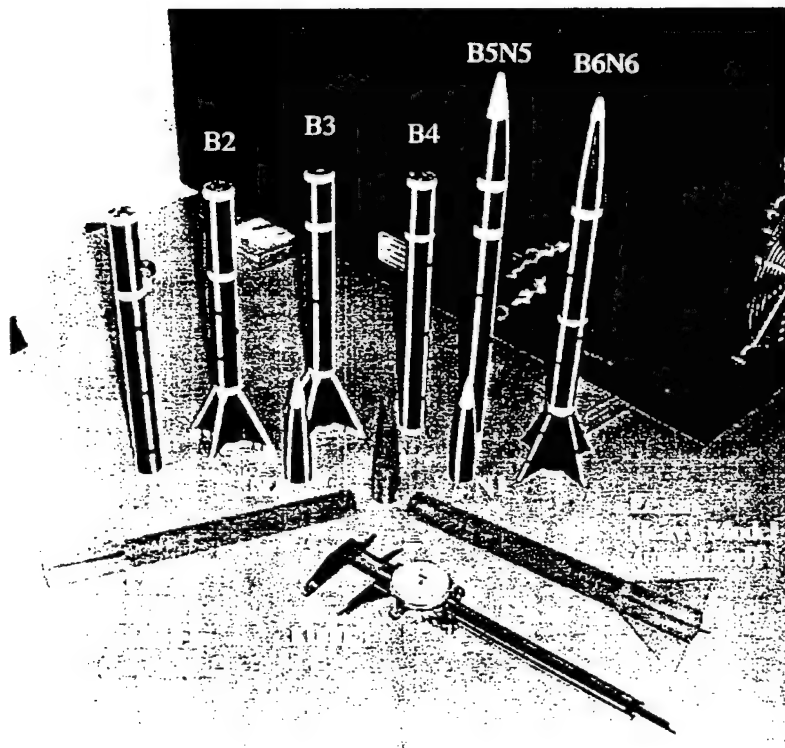
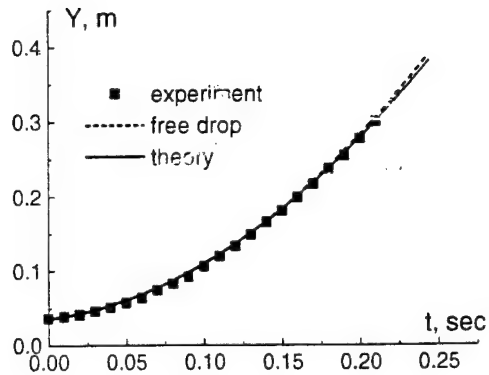
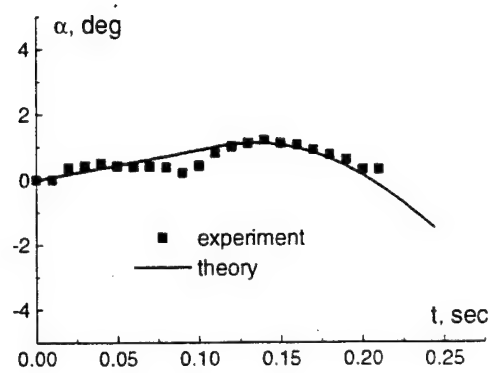


Fig. 3.2 Models for free drop tests in the IIT wind tunnel.

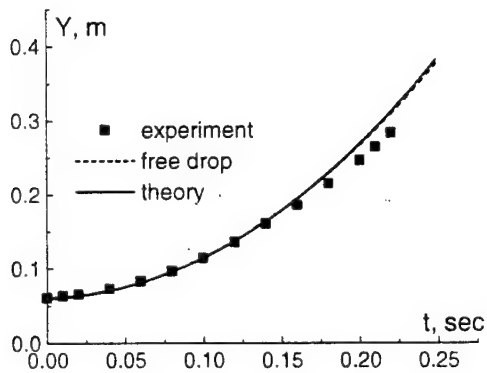


a)

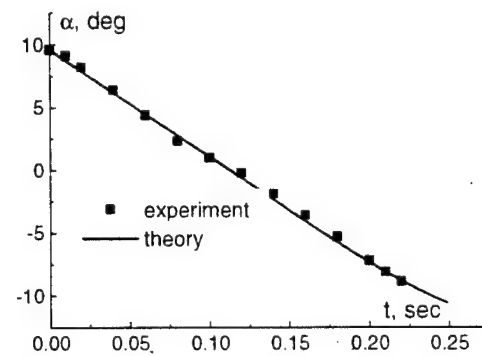


b)

Fig. 3.3 Model B4N2; $U_{\infty} = 62.3$ m/s, $Y_0 = 1.42$ inch., $\alpha_0 = 0^\circ$, $V_0 = 8$ inch/s, $\omega_0 = 9$ deg/s.



a)



b)

Fig. 3.4 Model B4N2: $U_{\infty} = 41.3$ m/s, $Y_0 = 2.4$ inch (0.061 m), $\alpha_0 = 9.6^\circ$,
 $V_0 = 2$ inch/s (0.0508 m/s), $\omega_0 = -80$ deg/s.

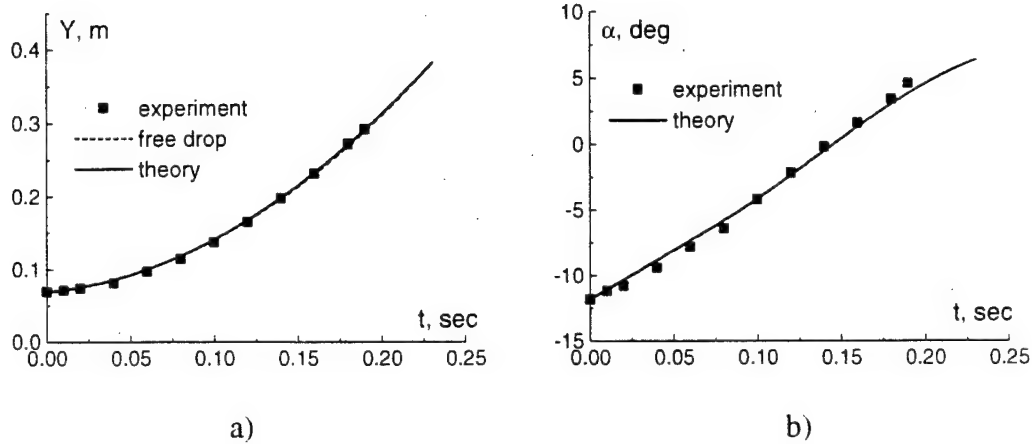


Fig. 3.5 Model B1N1; $U_{\infty} = 62.7$ m/s, $Y_0 = 2.72$ inch (0.0691 m), $\alpha_0 = -11^\circ$, $V_0 = 9$ inch/s (0.2286 m/s), $\omega_0 = 75$ deg/s.

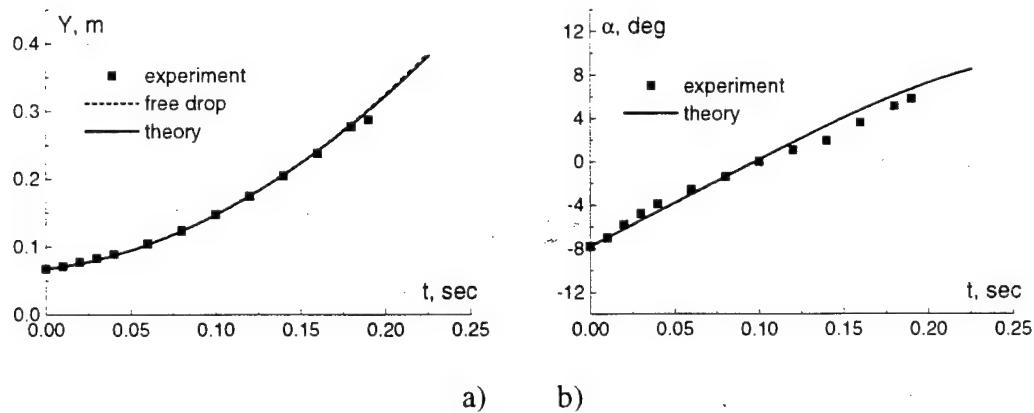
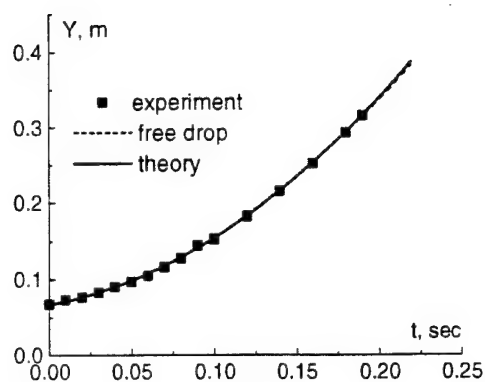
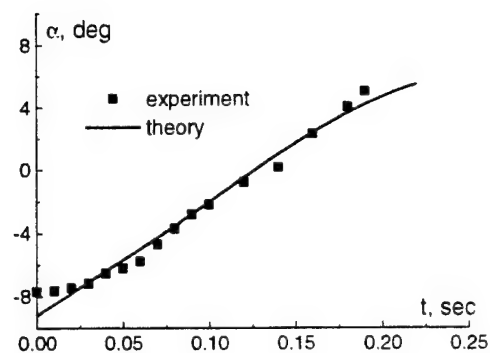


Fig. 3.6 Model B1N1; $U_{\infty} = 40.8$ m/s, $Y_0 = 2.65$ inch (0.0673 m), $\alpha_0 = -7.8^\circ$, $V_0 = 12$ inch/s (0.381 m/s), $\omega_0 = 80$ deg/s.

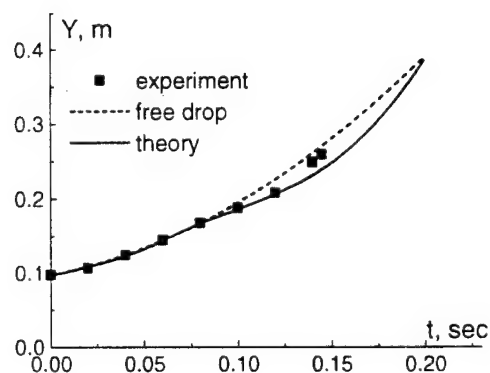


a)

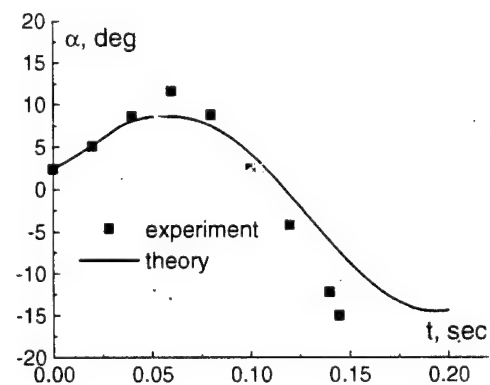


b)

Fig. 3.7 Model B4N2; $U_{\infty} = 40.6$ m/s, $Y_0 = 2.65$ inch (0.0673 m), $\alpha_0 = -9.2^\circ$,
 $V_0 = 15$ inch/s (0.381 m/s), $\omega_0 = 70.8$ deg/s.



a)



b)

Fig. 3.8 Model B5N5; $U_{\infty} = 62.5$ m/s, $Y_0 = 3.85$ inch (0.978 m), $\alpha_0 = 2.4^\circ$,
 $V_0 = 19$ inch/s (0.4826 m/s), $\omega_0 = 140$ deg/s.

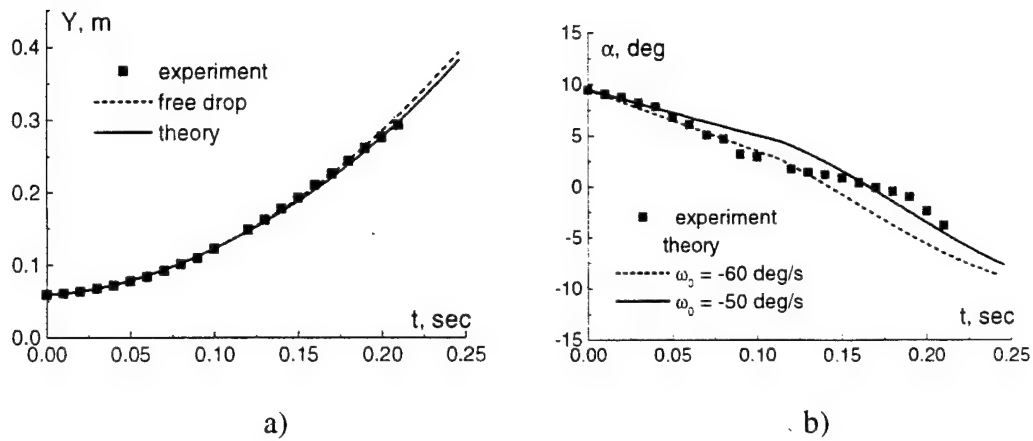


Fig. 3.9 Model B4N2; $U_\infty = 62.3$ m/s, $Y_0 = 2.33$ inch, $\alpha_0 = 9.5^\circ$, $V_0 = 6$ inch/s.

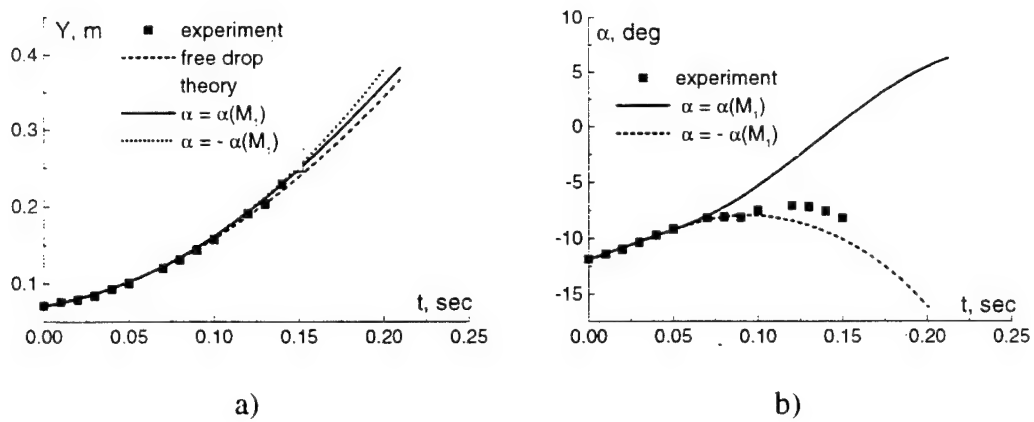


Fig. 3.10 Model B4N2; $U_\infty = 62.1$ m/s, $Y_0 = 2.8$ inch, $\alpha_0 = -11.9^\circ$, $V_0 = 15$ inch/s, $\omega_0 = 52.86$ deg/s.

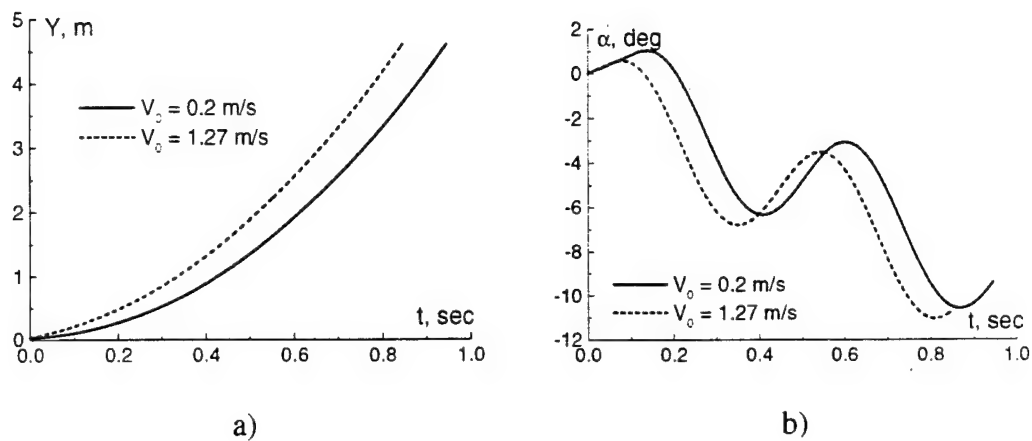


Fig. 3.11 Model B4N2; $U_\infty = 62.3$ m/s, $Y_0 = 1.42$ inch, $\alpha_0 = 0^\circ$, $\omega_0 = 8$ deg/s.
 — $V_0 = 8$ inch/s, - - - $V_0 = 50$ inch/s.

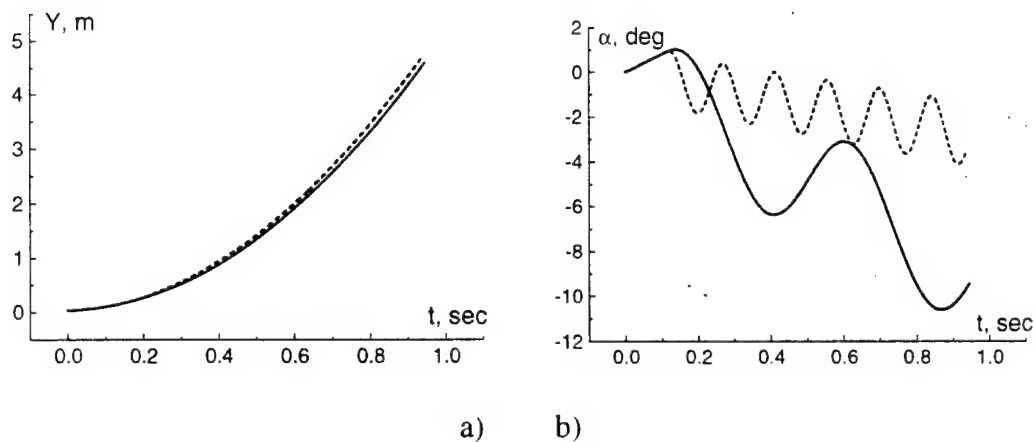


Fig. 3.12 Effect of the free stream velocity on the body trajectory: Model B4N2;
 $Y_0 = 1.42$ inch, $\alpha_0 = 0^\circ$, $V_0 = 8$ inch/s, $\omega_0 = 8$ deg/s. — $U_\infty = 62.3$ m/s,
 - - - $U_\infty = 200$ m/s.

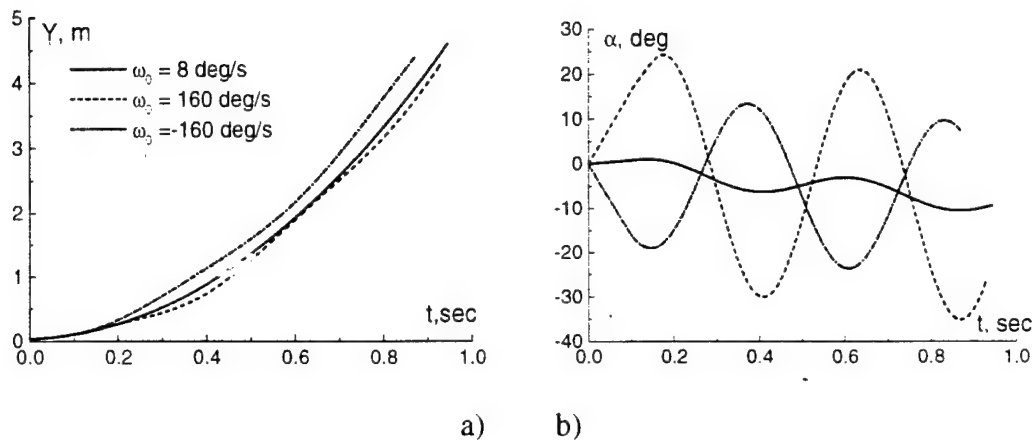


Fig. 3.13 Influence of the initial angular speed on the body trajectory: Model B4N2;
 $U_\infty = 62.3$ m/s; $Y_0 = 1.42$ inch; $\alpha_0 = 0^\circ$; $V_0 = 8$ inch/s.

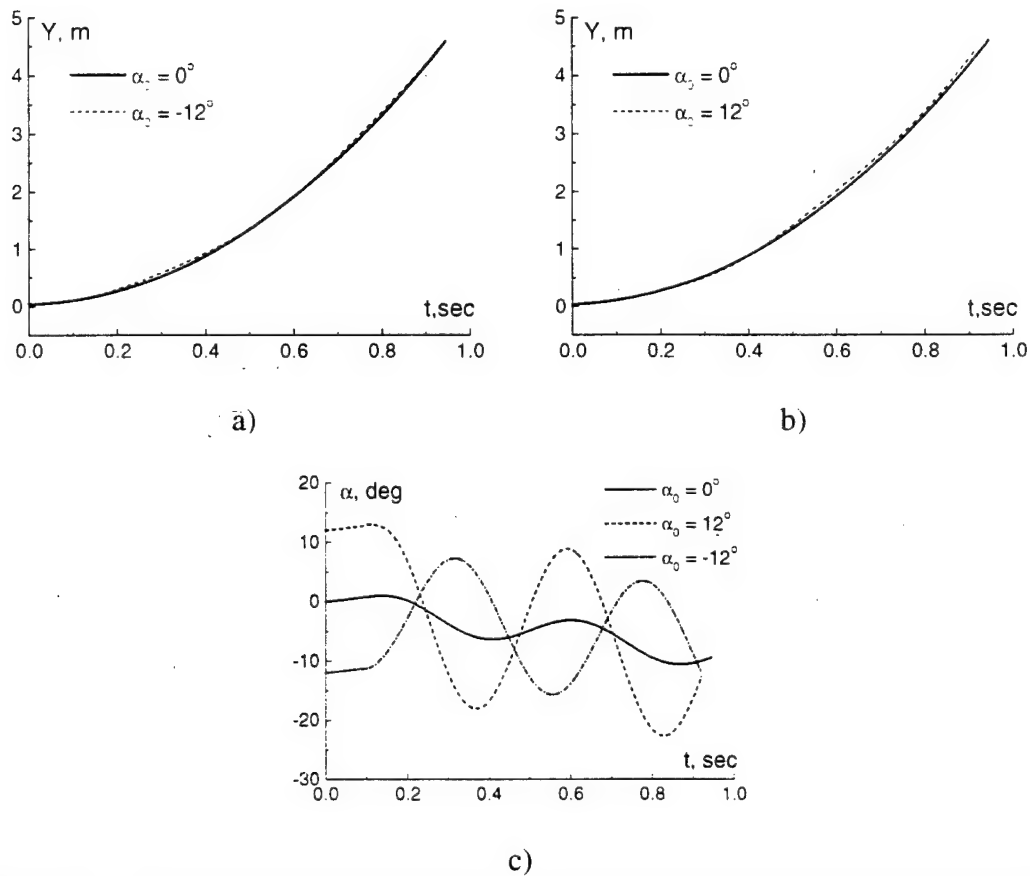


Fig. 3.14 Influence of the initial pitch angle on the body trajectory: Model B4N2;
 $U_\infty = 62.3$ m/s; $Y_0 = 1.42$ inch; $V_0 = 8$ inch/s; $\omega_0 = 8$ deg/s.

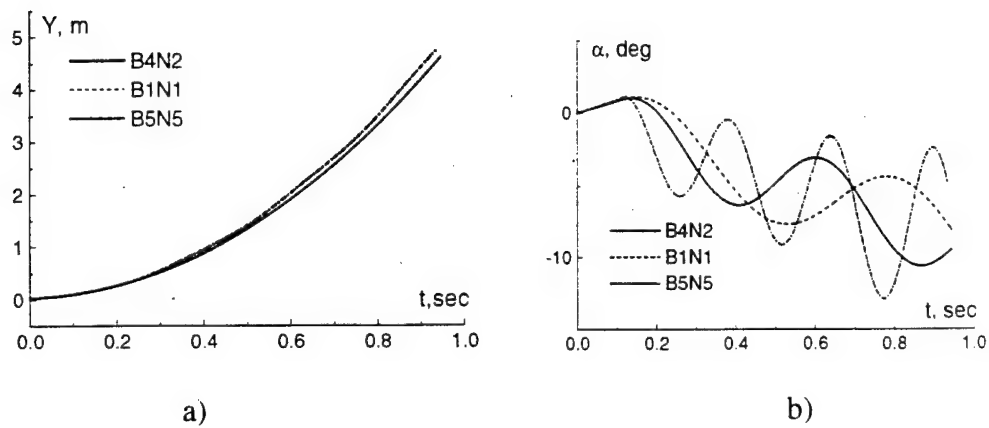


Fig. 3.15 Trajectories of different models; $U_{\infty} = 62.3$ m/s, $Y_0 = 1.42$ inch,
 $\alpha_0 = 0^\circ$, $V_0 = 8$ inch/s, $\omega_0 = 8$ deg/s.

Part 4. Transonic Flow Applications-Investigations of the outer limits of the inner solutions

4.1 Introduction

To calculate the drag force acting on a slender body dropping into an external transonic flow, we need to find the outer asymptotic solution [5, 6]. By matching, this solution is determined from the outer limit of the inner solution. For external store separation from a flat plate, this limit corresponds to the flow induced by sources distributed along the store axis, and the drag can be calculated using the equivalence rule [6.25,26,29]. For other cases, the outer solution is not known. It can be determined from the analysis of the outer limit of the inner solution, *i.e.*, the inner potential $\Phi(X, r, \theta, t)$ needs to be considered for $r \gg H$ for Phases 2 and 3, when the body crosses the shear layer and drops into the external flow.

In Section 4.2, we analyze the limits of the solutions obtained in Part 2 for store separation from a wing or infinite-span cavity. The dominant approximation is not sufficient to calculate the drag force acting on the store. A similar situation was considered in thin wing theory [26-31], where effects of higher-order approximations are taken into account to find the outer transonic solution. Hereinafter, we discuss the higher-order effects associated with a finite cavity span as well as the lift force and the body thickness.

In Sections 4.3 and 4.4, we obtain a general form of the inner solution for store separation from a finite span cavity and analyze its outer limits for Phases 2 and 3. In Section 4.5, we study higher-order effects considering the outer limits of the second- and third-order inner solutions. Cavities with finite and infinite span are discussed. Higher-order approximation unsteady terms are shown to give a dominant order contribution to the far field asymptotics.

In Section 4.6, we match inner and outer asymptotic solutions for transonic flows induced by a store separating from a cavity and wing. For the problem considered, formulation of the matching conditions is not straightforward because of unsteady effects. We identify different regimes for the outer flow field for various relationships between the Strouhal number and the scale of the flow perturbations. Different time scales relevant to the store separation process are identified and discussed.

We assume that short duration processes associated with freestream and body oscillations are averaged over a long -time scale characterizing the outer flow and give a negligibly small contribution to the wave drag. This idea is important relevant to current investigations involving the impact of cavity noise and vibration reduction using spoilers, jets and other devices. Effects of cavity oscillations are on such a short time scale that they or manipulations of them with control devices are averaged out on the trajectory time scale. For store drops, this is a Froude scale. We therefore conjecture that the influence of these rapid oscillations on the trajectory is small and possibly negligible.

Accordingly, we consider the quasi-steady outer solution, which is induced by sources along the body axis that is relevant to the dominant effect for a finite-span cavity.

In Section 4.7, drag force components acting on the body in Phase 2 (the body crosses the shear layer) and Phase 3 (the body drops in the stream) are theoretically modeled. Analytical expressions for the pressure drag are derived using the solutions obtained in Part 2. The friction drag is calculated using a modification of the Schultz-Grunow correlation [32] for axisymmetric flows. The base drag is predicted using results from Ref. [33]. The wave drag modeling is reduced to solving the Karman-Guderley equation over an equivalent body of revolution simulating the store. Analytical formulas and computational examples for the equivalent body shape are provided.

We have developed a computer code to predict 3-DOF store trajectories. As contrasted to the results of Parts 1-3, this module is coupled with a code developed by Dr. N. Malmuth. This is small disturbance solver of the axisymmetric Karman-Guderley equation. It is based on the Murman-Cole successive line overrelaxation (SLOR) approach. It is very rapidly convergent for many practical cases on current-generation (considerably less than 1 GB, 500 MB RAM processors) using a Visual Fortran compiler. A brief description of this code is provided in Section 4.8. Note that the theoretical model developed herein can be extended to 6-DOF trajectories, including yaw and roll.

Parametric studies discussed in Section 4.9 demonstrate the effects of the body thickness and initial (release) conditions on trajectory characteristics. These results are discussed in Section 4.10.

4.2 Outer expansion of the dominant inner solution

For a store moving near a plane surface ($H \sim a$), in accord with the our previous results. (see Section 2.2) the first term of the outer expansion of the inner solution is

$$\Phi|_{r \gg H} \sim A_0(X, t) + 2a(X)a_X(X) \ln(r), \quad (4.2.1a)$$

$$r\Phi_r \sim 2a(X)a_X(X), \quad (4.2.1b)$$

where the function $A_0(X, t)$ accounts for the outer flow effect on the body aerodynamics. The relation (4.2.1b) is treated as an asymptotic boundary condition for the outer problem [6.25.26.29]. In this scheme, the outer expansion corresponds to axisymmetric flow over a body of revolution whose cross-sectional area is twice that of the store cross-sectional area, *i.e.*

$$A_{eff}(x, t) = 2A_b. \quad (4.2.2)$$

From conformal mapping, a similar analysis is relevant to external separation from a fuselage. These results allow us to apply the equivalence rule [6.25.26.29] and calculate the wave drag for external store separation. This is important in extending our predictions of trajectories from 2-DOF to 3-DOF.

To obtain an asymptotic expression for the potential induced by the body motion inside an infinite-span cavity, we use the complex velocity W_0 and the complex potential Π_0 of the dominant approximation (see Section 2.2, Eqs. (2.2.12)). These are

$$W_0(\zeta, X, t) = \frac{\partial \Pi_0}{\partial \zeta} = w - iv = \sum_{n=0}^{\infty} a^{2n+1} \left\{ A_{-2n-1} \left[\frac{1}{(\zeta - iH)^{2n+1}} - \frac{1}{(\zeta + iH)^{2n+1}} \right] + iaB_{-2n-2} \left[\frac{1}{(\zeta - iH)^{2n+2}} + \frac{1}{(\zeta + iH)^{2n+2}} \right] \right\}, \quad (4.2.3a)$$

$$\begin{aligned} \Pi_0(\zeta, X, t) = \Phi + i\Psi &= aa_x \ln \frac{\zeta - iH}{\zeta + iH} - \\ \Pi_0(\zeta, X, t) = \Phi + i\Psi &= aa_x \ln \frac{\zeta - iH}{\zeta + iH} - \\ &+ \frac{iB_{-2n}}{2n-1} \left[\frac{1}{(\zeta - iH)^{2n-1}} + \frac{1}{(\zeta + iH)^{2n-1}} \right] \end{aligned} \quad (4.2.3b)$$

In Section 2.2 of Part 2, the coefficients $A_{-2n-1}(X, t)$ and $B_{-2n-2}(X, t)$ are expressed as convergent series in the parameter $q = a/(2H) < 1/2$. Substituting the relation $\zeta = re^{i\theta} + iH$ into Eq. (4.2.3b) and considering the case $H/r \ll 1$, we can reduce this equation to the form

$$\Pi_0 \approx aa_x \ln \frac{re^{i\theta}}{re^{i\theta} + 2iH} - \frac{2iaB_{-2}e^{-i\theta} \left(1 + i \frac{H}{r} e^{-i\theta} \right)}{r \left(1 + 2i \frac{H}{r} e^{-i\theta} \right)}. \quad (4.2.4a)$$

In the dominant approximation, the potential is therefore expressed as

$$\Phi_0 \approx -\frac{D_0}{r} \sin \theta, \quad D_0(X, t) = 2a(a_x H + B_{-2}). \quad (4.2.4b)$$

Equation (4.2.4b) shows that the outer-flow field has an angular dependence in the cross flow plane; it corresponds to a dipole on the body axis.

From Eq. (4.2.3b), we consider the far field limit appropriate to $a < r \ll H$, $a < r \ll H$; i.e., the case when the body is far from the slip surface. The coefficient B_{-2} is approximated as

$$B_{-2} \approx a \left(V - \alpha - \frac{aa_x}{2H} \right).$$

The dominant terms of the potential (4.2.3b) are

$$\begin{aligned} \Pi_0 &\approx aa_x \left[\ln \frac{re^{i\theta}}{2iH} - \ln \left(1 + \frac{r}{2iH} e^{i\theta} \right) \right] - \frac{ia^2 e^{-i\theta} \left(V - \alpha - \frac{aa_x}{2H} \right)}{r} \approx \\ &\approx aa_x \ln \frac{re^{i\theta}}{2iH} - i(V - \alpha) \frac{a^2}{r} e^{-i\theta} + i \frac{aa_x}{2H} \left(re^{i\theta} + \frac{a^2}{r} e^{-i\theta} \right). \end{aligned}$$

In the dominant approximation, this potential is reduced to the potential of an axisymmetric flow over the body of revolution in an unbounded stream

$$\Phi_0 \approx aa_x \ln \frac{r}{2H} + O\left(\frac{r}{2H}\right). \quad (4.2.5)$$

A similar result can be obtained for the body crossing the shear layer (Phase 2). In this phase, the complex conjugate flow velocity and potential (see Eqs. (2.2.2) of Section 2.3) are

$$\tilde{W}_0 = i(V - \alpha) \left(\frac{\partial \zeta}{\partial \sigma} - \frac{\sigma}{\sqrt{\sigma^2 - b^2}} \right) - \frac{4c^2 a_x}{i\pi \sqrt{\sigma^2 - b^2}} \int_{-b}^b \frac{Q^n(s) ds}{D(s, n) \sqrt{b^2 - s^2} (s - \sigma)}. \quad (4.2.6a)$$

$$\Pi_0 = i(V - \alpha) \left(\zeta - \sqrt{\sigma^2 - b^2} \right) + \frac{2aa_x}{\pi} \sqrt{\sigma^2 - b^2} \int_{-b}^b \frac{\psi(s) ds}{\sqrt{b^2 - s^2} (s - \sigma)}. \quad (4.2.6b)$$

$$\psi = \operatorname{arctg} \left[\frac{(s+b)^n + (s-b)^n}{(s+b)^n - (s-b)^n} \operatorname{ctg} \left(\frac{\pi n}{2} \right) \right]. \quad (4.2.6c)$$

As $\sigma \rightarrow \infty$, the limit of the complex conjugate velocity (4.2.6a) is

$$\tilde{W}_0 = \frac{1 + \frac{b^2}{2\sigma^2}}{i\pi\sigma^2} \int_{-b}^b \frac{\sqrt{b^2 - s^2} v_{nb}(s)}{l(s)} \left(1 + \frac{s}{\sigma} \right) ds. \quad (4.2.7a)$$

and the potential is approximated as

$$\Phi_0 = -\frac{D_0(X, t)}{r} \sin \theta, \quad D_0 = -\frac{1}{\pi} \int_{-b}^b \frac{\sqrt{b^2 - s^2} v_{nb}(s)}{l(s)} ds. \quad (4.2.7b)$$

In the dominant approximation, the potential (4.2.7b) corresponds to the flow induced by a dipole of the strength $D_0(X, t)$. Thus, in the outer limit, the inner solution does not contain a source term for an infinite span cavity. Crossing the shear layer, the body induces a vertical-velocity on the free slip surface (v_f) such that the following integral relation is satisfied

$$\left(\int_{-\infty}^b + \int_b^{+\infty} \right) v_f ds = - \int_{-b}^b v_{nb} ds.$$

Thus, the flow field induced by sources on the body surface and sinks on the shear layer at large distances from the body behaves as a dipole.

4.3 Separation from a finite-span cavity into a transonic external flow: General form and outer limits of the inner solution for Phase 2

For Phase 2, the cross-flow scheme is shown in Fig. 4.1. Notations and dimensionless variables are similar to those introduced in Section 1.2. The inner-flow region includes the cavity region, which is bounded by the slip surface and cavity walls, as well as the free-stream region with the upper boundary consisting of the mixed boundary (the slip surface, $|Z| < d_0$, the flat plates, $|Z| > d_0$) and the submerged body portion. To the accuracy indicated in Section 1.3, we neglect the sidewall effect. In the dominant approximation with respect to the small parameter $\delta \ll 1$, the inner asymptotic solution is described by the two-dimensional Laplace equation in the cross-sectional plane. Here we consider the free-stream region only. We also neglect the slip-surface displacement and treat it as a plane of zero potential. In the cross-sectional plane of the complex variable $\zeta = Z + iY$, the problem for the complex conjugate velocity, $W(\zeta, X, t) = w - iv$, is accordingly formulated as

Find a harmonic function W , which satisfies the conditions:

1. $\text{Im } W = -v = 0$ in the intervals $(-\infty, -d_0)$ and (d_0, ∞)
2. $\text{Re } W = w = 0$ in the intervals $(-d_0, -c)$ and (c, d_0)
3. Velocities v, w are finite at the cavity edges, $Z = d_0, Y = 0$
4. $\text{Im}(e^{-i\theta} W) = -v_n$ on the submerged body surface
5. $W \rightarrow 0$ for $\zeta \rightarrow \infty$

This problem is solved using the conformal mapping (2.2.1) of Section 2.3 (see Part 2) to map the free-stream region to the lower half-plane of the complex variable $\sigma = \xi + i\eta$. In the transformed plane shown in Fig.4.2, the cavity has the semi-span

$$d = b \frac{(1 + \bar{c})^k + (1 - \bar{c})^k}{(1 + \bar{c})^k - (1 - \bar{c})^k}, \quad \bar{c} = \frac{c}{d_0}, \quad k = \frac{1}{n}. \quad (4.3.1)$$

The submerged body portion is the lower side of the flat plate, $Y = -0$, $\xi \leq b$, which moves with the vertical velocity

$$\tilde{v}(\xi, X, t) = v_n / l(\xi) = \frac{1}{l(\xi)} [a_x + V_e \sin \theta], \quad (4.3.2a)$$

$$l(\xi) = \left| \frac{\partial \sigma}{\partial \xi} \right|_{\eta=0} = \frac{(b^2 - \xi^2) D(\xi, n)}{4c^2 Q^n(\xi)}, \quad Q = \frac{b + \xi}{b - \xi}, \quad D = Q^{2n} + 1 - 2Q^n \cos \pi n, \quad (4.3.2b)$$

$$\sin \theta = \frac{Y(\xi) - H}{a(x)} = -2 \frac{Q^n(\xi)}{D(\xi, n)} \sin^2 \pi n + \cos \pi n. \quad (4.3.2c)$$

Here, tilda denotes flow parameters in the σ -plane.

For a finite-span cavity ($d < \infty$), we apply the Keldysh-Sedov formula [8] in the transformed plane and obtain the following expressions for the complex conjugate velocity and complex potential with $\eta < 0$

$$\tilde{W}(\sigma, X, t) = -\frac{1}{\pi} \sqrt{\frac{\sigma^2 - d^2}{\sigma^2 - b^2}} \int_{-b}^b \sqrt{\frac{b^2 - s^2}{d^2 - s^2}} \frac{v_n(s) ds}{(s - \sigma) l(s)}, \quad (4.3.3a)$$

$$W(\sigma, X, t) = \frac{\partial \sigma}{\partial \xi} \tilde{W}; \quad \Pi(\sigma, X, t) = \int \tilde{W} d\sigma. \quad (4.3.3b)$$

Using (4.3.3) we can derive relatively simple explicit expressions for the lift force and pitch moment acting on the body. These expressions have a structure similar to that obtained for an infinite-span cavity in Section 2.3 of Part 2.

Consider the outer limit of the inner solution, $\sigma \rightarrow \infty$, $d = \text{fix}$. From Eqs. (4.3.1) and (4.3.2) we obtain

$$\frac{\partial \xi}{\partial \sigma} = 1 + \frac{(1 - n^2)b^2}{3\sigma^2} + O\left(\frac{b^4}{\sigma^4}\right).$$

Using these expressions, we find from Eq. (4.3.3) that, in the first order approximation, the far field is induced by sources distributed along OX -axis; i. e.

$$W = \frac{Q_{\text{eff}}(X, t)}{2\pi\zeta} \left[1 + O\left(\frac{d^2 + b^2}{\sigma^2}\right) \right], \quad Q_{\text{eff}}(X, t) = \frac{2}{\pi} \int_{-b}^b \sqrt{\frac{b^2 - s^2}{d^2 - s^2}} \frac{v_n(s) ds}{l(s)}. \quad (4.3.4)$$

This relation allows us to match the inner and outer solutions. It also shows that the outer flow is axisymmetric in the dominant approximation.

For relatively wide cavities with $d \gg b$, the complex conjugate velocity (4.3.3a) is expressed as

$$\tilde{W} = -\frac{1}{\pi d} \frac{\sigma^2 - d^2}{\sigma^2 - b^2} \int_{-b}^b \left(1 + \frac{s^2}{2d^2}\right) \frac{b^2 - s^2 v_n(s) ds}{(s - \sigma)l(s)} \approx -\frac{1}{\pi d} \frac{\sigma^2 - d^2}{\sigma^2 - b^2} \int_{-b}^b \frac{b^2 - s^2 v_n(s) ds}{(s - \sigma)l(s)}$$

Substituting the expressions for v_n and l into this equation and integrating we obtain the complex conjugate velocity and complex potential

$$\tilde{W} = \frac{\sqrt{\sigma^2 - d^2}}{d} \left[V_e \left(\frac{\partial \zeta}{\partial \sigma} - \frac{\sigma}{\sqrt{\sigma^2 - b^2}} \right) - \frac{4c^2 a_x I(\sigma, n)}{\pi \sqrt{\sigma^2 - b^2}} \right], \quad (4.3.5a)$$

$$I(\sigma, n) = \int_{-b}^b \frac{Q^n(s) ds}{D(s, n) \sqrt{b^2 - s^2} (s - \sigma)}. \quad (4.3.5b)$$

For the inner region

$$|\sigma| \ll d; \quad \sqrt{\sigma^2 - d^2} = -id \left[1 - \frac{\sigma^2}{2d^2} + \dots \right].$$

the dominant approximation of Eq. (4.3.5) is reduced to ((2.2.2a) for an infinite-span cavity, so that

$$\tilde{W} = -i \left[V_e \left(\frac{\partial \zeta}{\partial \sigma} - \frac{\sigma}{\sqrt{\sigma^2 - b^2}} \right) + \frac{4c^2 a_x I(\sigma, n)}{\pi \sqrt{\sigma^2 - b^2}} \right]. \quad (4.3.6)$$

For the outer limit, $\sigma \rightarrow \infty$, d fixed, we obtain

$$W = \frac{Q_{eff}(X, t)}{2\pi \zeta} \left[1 + O\left(\frac{d^2}{\sigma^2}\right) \right], \quad (4.3.7a)$$

$$Q_{eff}(X, t) = \frac{2a^2(x) \sin \pi n}{nd} \left[4a_x e_0(n) - \pi V_e (1 + 2n^2) \frac{\sin \pi n}{6n} \right], \quad (4.3.7a)$$

where the function $e_0(n)$ is provided in Appendix C of Part 2. Note that the outer limit of the inner solution is proportional to the ratio b/d , whereas the flow parameters in the inner region, as well as the lift force and pitching moment are $O(b^2/d^2)$. Equations (4.3.7) allow us to formulate the matching condition for the outer asymptotic solution in an explicit form.

4.4 Separation from a finite-span cavity into transonic stream: General form and outer limits of inner solutions for Phase 3

For Phase 3, the cross-flow scheme is shown in Fig. 4.3. In this case, the vertical distance from the slip surface to the body axis is $H < -a$; all notations are the same as in Fig. 4.1. We consider the flow in the lower half-plane only. The inner problem for the complex conjugate complex velocity, $W(\zeta, X, t) = w - iv$, is formulated as

Find a harmonic function W satisfying the conditions:

1. $\text{Im} W = -v = 0$ in the intervals $(-\infty, -d_0)$ and (d_0, ∞)
2. $\text{Re} W = w = 0$ in the interval $(-c, c)$
3. the velocities v, w are finite at the cavity edges, $Z = \pm d_0, Y = 0$
4. $\text{Im}(e^{-i\theta} W) = -v_n$ on the body surface, $|\zeta - iH| = a(x)$
5. $W \rightarrow 0$ for $\zeta \rightarrow \infty$

For Phase 3, this problem is more complicated than for Phase 2, since the flow region is doubly connected. The solution method developed in Ref. [8] includes a conformal mapping of the free-stream region to a rectangle. The complex conjugate velocity is expressed by the Keldysh-Sedov formula, including elliptic functions in the integrand (see Section 1.2 of Part 1). However, it is difficult to obtain an analytical solution using this method. We develop another method, which is based on the results of Ref. [9]. It is similar to the method used in Section 2.2 of Part 2. Introduce the analytical function

$$f_1(\zeta, X, t) = \frac{W(\zeta, X, t)}{\sqrt{\zeta^2 - d_0^2}}.$$

Using the symmetry principal for harmonic functions [10], we analytically continue this function to the upper half-plane with the relation

$$f_1(\zeta, X, t) = \frac{W(\zeta, X, t)}{\sqrt{\zeta^2 - d_0^2}} = -\frac{W(\bar{\zeta}, X, t)}{\sqrt{\bar{\zeta}^2 - d_0^2}} = -f_1(\bar{\zeta}, X, t). \quad (4.4.1)$$

From Cauchy's formula, we obtain the integral equation for $W(\zeta)$

$$W(\zeta) = \frac{\zeta^2 - d_0^2}{2i\pi} \left[\int_{t=1} \frac{W(iH+t)dt}{(t+iH)^2 - d_0^2(\zeta - iH - t)} + \int_{t=1} \frac{W(-iH+\bar{t})d\bar{t}}{(t-iH)^2 - d_0^2(\zeta + iH - t)} \right]. \quad (4.4.2)$$

Thus, the problem is reduced to the problem of two circles vertically translating down in an unbounded flow as schematically shown in Fig. 4.4. Using Eq. (4.4.1) and expanding denominators of the integrands as Taylor series, we express Eq. (4.4.2) in the Laurent series

$$\begin{aligned} W(\zeta) &= \frac{\sqrt{\zeta^2 - d_0^2}}{i\sqrt{H^2 + d_0^2}} \sum_{n=0}^{\infty} a^{n+1} \left\{ \frac{C_{-n-1}}{(\zeta - iH)^{n+1}} - \frac{\bar{C}_{-n-1}}{(\zeta + iH)^{n+1}} \right\} = \\ &= \frac{\sqrt{(s + iH)^2 - d_0^2}}{i\sqrt{H^2 + d_0^2}} \sum_{n=0}^{\infty} a^{n+1} \left\{ \frac{C_{-n-1}}{s^{n+1}} - \frac{\bar{C}_{-n-1}}{(s + 2iH)^{n+1}} \right\}, \end{aligned} \quad (4.4.3)$$

where $s = \zeta - iH = re^{i\theta}$. The Laurent coefficients C_{-n-1} and \bar{C}_{-n-1} of the function $f_1(\zeta)$ at the points $\zeta = iH$ and $\zeta = -iH$ are

$$\begin{aligned} C_{-n-1} = A_{-n-1} + iB_{-n-1} &= \frac{1}{2i\pi} \int_{|t|=1} \left[1 - \sum_{k=1}^{\infty} \frac{(2k-1)!!}{2^k k!} \left(\frac{t + 2iH}{H^2 + d_0^2} \right)^k t^k \right] \frac{W(iH + t)t^n dt}{\sqrt{(t + iH)^2 - d_0^2}}, \\ C_{-n-1} &= A_{-n-1} - iB_{-n-1}. \end{aligned}$$

These expressions are derived using the flow symmetry and the boundary conditions on the body surface. The derivation is similar to that described in Section 2.2 of Part 2. In particular, we derive from Eq. (4.4.1)

$$W(\zeta) = W(-\zeta), \quad C_{-n-1} = (-1)^n C_{-n-1}; \quad C_{-2n} = iB_{-2n}; \quad C_{-2n-1} = A_{-2n-1}. \quad (4.4.4)$$

The coefficients $A_{-1} = a_x$, $B_{-2} = V_e + B_0$ are determined by Eqs. (2.1.3) for an infinite span cavity. The finite span cavity effect appears for $n > 1$. Coefficients of these numbers have more complicated form than for an infinite span. They are not provided here since only the two first terms are needed to determine the outer asymptotics.

Consider the outer limit of the inner solution: $r \rightarrow \infty$, d_0 , H fixed. From Eqs. (4.4.3), (4.4.4) we obtain

$$W(s) = \frac{Q_{eff}}{2\pi s} + O\left(\frac{H}{s^2} \frac{1}{H^2 + d_0^2}\right), \quad \frac{\partial A_{eff}}{\partial X} = Q_{eff}(X, t) = \frac{4\pi a(A_{-1}H - aB_{-2})}{\sqrt{H^2 + d_0^2}}. \quad (4.4.5)$$

For the large-span cavity limit, $r \rightarrow \infty$, $d_0 \gg 1$, $H \ll d_0$ we find

$$Q_{eff}(X, t) = \frac{4\pi a(a_x H - aB_{-2})}{d_0} \left[1 - \frac{H^2}{2d_0^2} \right], \quad (4.4.6)$$

The source intensity tends to zero as $d_0 \rightarrow \infty$.

For the other limit, $r \rightarrow \infty$, $H \gg d_0$, the source intensity tends to

$$Q_{eff}(X) = 4\pi a a_x = 2 \frac{dA_b(x)}{dx} = \frac{dA_{eff}(x)}{dx}. \quad (4.4.7)$$

In this case, the cavity effect is negligible and the problem corresponds to a body of cross-sectional area distribution $A_b(x)$ dropping from an infinite flat plate. The effective cross-sectional area is $A_{eff}(x) = 2A_b(x)$.

4.5 Outer limits of higher order approximations

For a zero-thickness wing in an unbounded transonic flow, the outer limit of the first-order inner potential has a dipole form similar to that given by Eqs. (4.2.4b) and (4.2.7b). However, a logarithmic source solution of the second-order approximation is dominant in the far-field region and determines the form of the outer solution [25-29] that couples with this dipole behavior. This source term can give a sizeable wave drag due to lift contribution if $A \equiv \frac{\alpha}{\delta} \rightarrow \infty$, where α is the angle of attack and δ is the thickness ratio.

The lift-induced source strength is proportional to $\ell'(x)\ell''(x)$, where $\ell(x)$ is the lift up to the streamwise station x . This contribution can be of the same order or larger than the wave drag due to thickness. Reference [6], the authoritative source for development of transonic slender body theory based on systematic asymptotic approximation schemes, (particularly, higher order approximations in a lucid, deductive framework) treats the case of $A = O(1)$, in which the wave drag due to thickness dominates the wave drag due to lift. For thin wings, similar asymptotic expansions were considered in [26-29] with α a small parameter. Reference [30] discusses higher order approximations in a subsonic and supersonic flow context.

Our analyses are extending the framework of [6] from a slender body in an infinite flow to one separating from a flat surface or cavity.

The results presented in this section can be regarded as a first step to developing a high-order asymptotic theory for unsteady transonic flows with free boundaries. Within the scope of this report, we restrict our matching considerations to the low order terms. A higher order investigation to be conducted will include the ramifications of the slip surface in the matching scheme and its effect on the intermediate expansions which need to be introduced to avoid the mismatch of the higher inner and outer expansions in slender body theory. This mismatch phenomenon was elucidated in [6]. Accordingly, outer asymptotics of the inner solutions are obtained in Part 2 and Sections 4.3-4.4. Although the focus is on dominant order matching herein, we consider the asymptotics of the second and third order inner solutions for a body of revolution separating from a cavity. We have estimated the order of source terms of the outer solutions using the

approach in [6] for asymptotic matching. This allows us to evaluate the contribution of the higher-order approximations to the inviscid drag force.

Second- and third-order approximations of the inner potential for the body crossing the slip surface can be obtained from the full potential equation with the method of [6]. This equation is

$$(\bar{C}^2 - \bar{U}^2) \frac{\partial^2 \bar{\Phi}}{\partial \bar{X}^2} + (\bar{C}^2 - \bar{v}^2) \frac{\partial^2 \bar{\Phi}}{\partial \bar{Y}^2} + (\bar{C}^2 - \bar{w}^2) \frac{\partial^2 \bar{\Phi}}{\partial \bar{Z}^2} - 2\bar{U} \frac{\partial^2 \bar{\Phi}}{\partial \bar{X} \partial \bar{t}} - \frac{\partial^2 \bar{\Phi}}{\partial \bar{t}^2} - \left(\frac{\partial}{\partial \bar{t}} + \bar{U} \frac{\partial}{\partial \bar{X}} \right) (\bar{v}^2 + \bar{w}^2) - 2\bar{w} \bar{v} \frac{\partial^2 \bar{\Phi}}{\partial \bar{Z} \partial \bar{Y}} = 0, \quad (4.5.1a)$$

$$\bar{U} = \frac{\partial \bar{\Phi}}{\partial \bar{X}}, \quad \bar{v} = \frac{\partial \bar{\Phi}}{\partial \bar{Y}}, \quad \bar{w} = \frac{\partial \bar{\Phi}}{\partial \bar{Z}}, \quad (4.5.1b)$$

$$\bar{C}^2 = \gamma \frac{\bar{p}}{\bar{\rho}}, \quad \frac{\bar{p}}{\bar{\rho}_\infty} = \left(\frac{\bar{p}}{p_\infty} \right)^\gamma, \quad \frac{\bar{U}^2 + \bar{v}^2 + \bar{w}^2}{2} + \frac{\bar{C}^2}{\gamma - 1} = \frac{U_\infty^2}{2} + \frac{c_\infty^2}{\gamma - 1}. \quad (4.5.1c)$$

Here, \bar{C} is the sound speed; $\bar{\rho}$ is fluid density and $\bar{\Phi}(\bar{X}, \bar{Y}, \bar{Z}, \bar{t})$ is the velocity potential. We consider separation from a flat wall to illustrate the asymptotic developments that we have applied preliminarily to finite and infinite-span slip surface cases. For store separation from a flat wall, the appropriate inner asymptotic expansion for the transonic flow potential from [6] is relevant and is

$$\begin{aligned} \bar{\Phi} &= l_0 U_\infty \left\{ X + \delta^2 \log \delta (2S_1(X, t)) + \delta^2 \Phi_1(X, Y, Z, t; K, S) + \right. \\ &\quad \left. \delta^4 \log \delta \Phi_{21}(X, Y, Z, t; K, S) + \delta^4 \Phi_2 + \dots \right\} \\ &\equiv l_0 U_\infty \{ X + \delta^2 \Phi(X, Y, Z, t; S) \}, \end{aligned} \quad (4.5.2a)$$

which is valid in the inner limit

$$Y \equiv \hat{Y} / \delta, \quad Z \equiv \hat{Z} / \delta, \quad K, S \text{ fixed as } \delta \rightarrow 0,$$

where $K \equiv (1 - M_\infty^2) / \delta^2$ is the transonic similarity parameter; $M_\infty = U_\infty / c_\infty$ is the Mach number, $S \equiv l_0 / (U_\infty t_0)$ is the Strouhal number. The appropriateness of (4.5.2a) stems from the fact that for the flat plate the far field looks like that generated from two cylinders (of arbitrary cross section), tangent to each other at the wall whose axes of symmetry are parallel to the freestream. The second cylinder is the reflection of the physical one needed to satisfy the no-flow through boundary conditions on the solid wall. The distance of the cylinders from the wall is negligible in the far field. This gives an equivalent body area that is twice the physical area, as indicated elsewhere in this report. The reflection gives a flow *symmetric* in the direction normal to the flow from a *double source* in the crossflow plane. In contrast, if a slip surface replaces the solid wall, (such as for an infinite span cavity), an *antisymmetric* solution is needed to satisfy the homogeneous Dirichlet condition for the perturbation potential rather than the

homogeneous Neumann one appropriate for the solid wall. Accordingly, the double source far field now becomes nearly a source-sink pair (*dipole*).

A crossflow velocity potential can be defined as

$$\hat{W} = \frac{\partial \hat{\Pi}}{\partial \zeta} = U_{\infty} \delta(w - iv) \equiv U_{\infty} \delta(W_0 + \delta^2 W_2 + \delta^4 W_4), \quad \hat{\Pi} = \bar{\Phi} + i\bar{\Psi}. \quad (4.5.2b)$$

Further the normalized pressure coefficient and sound speed are respectively

$$p = \frac{\bar{p} - p_{\infty}}{\rho_{\infty} U_{\infty}^2 \delta^2} = \frac{1}{\gamma M_{\infty}^2} \left[(M_{\infty}^2 C^2)^{\frac{\gamma}{\gamma-1}} - 1 \right], \quad M_{\infty}^2 = 1 + K\delta^2 + K\delta^4, \quad (4.5.2c)$$

$$C^2 = \frac{\bar{C}^2}{C_{\infty}^2} = \frac{1}{M_{\infty}^2} - \frac{\gamma-1}{2} \delta^2 (2S\Phi_t + 2\Phi_X + w^2 + v^2 + \delta^2 \Phi_X^2). \quad (4.5.2d)$$

As contrasted to the previously used scaling (see Eq. (1.1.2b)), the dimensionless time is defined as $t = \hat{t} / t_0$ (where t_0 is the time scale associated with the flow perturbations). To

$O(\delta^2)$ we express the body surface shape as

$$\begin{aligned} Y_b &= H \pm \sqrt{a^2(X) - Z^2} + \\ &+ \delta^2 \alpha \left[\pm \frac{\alpha}{2} \left(\sqrt{a^2(X) - Z^2} + \frac{Xaa'(X)}{\sqrt{a^2(X) - Z^2}} \right) - aa'(X) - \frac{\alpha^2 X}{3} \right] \\ &= f_0(X, Z, t) + \delta^2 f_1(X, Z, t) + O(\delta^4). \end{aligned} \quad (4.5.3)$$

The potential Φ_0 and the complex conjugate velocity W_0 of the dominant approximation are analyzed in Sections 4.2-4.3. In the polar coordinates r, θ , the potential of the second-order approximation satisfies the Poisson equation [6, 30]

$$\begin{aligned} \frac{1}{r} \frac{\partial}{\partial r} r \frac{\partial \Phi_2}{\partial r} + \frac{1}{r^2} \frac{\partial^2 \Phi_2}{\partial \theta^2} &= S^2 \frac{\partial^2 \Phi_0}{\partial t^2} + 2S \frac{\partial^2 \Phi_0}{\partial X \partial t} + \left(\frac{\partial}{\partial X} + S \frac{\partial}{\partial t} \right) \left[\left(\frac{\partial \Phi_0}{\partial r} \right)^2 + \frac{1}{r^2} \left(\frac{\partial \Phi_0}{\partial \theta} \right)^2 \right] + \\ &+ \left(\frac{\partial \Phi_0}{\partial r} \frac{\partial}{\partial r} + \frac{1}{r^2} \frac{\partial \Phi_0}{\partial \theta} \frac{\partial}{\partial \theta} \right) \left[2 \frac{\partial \Phi_0}{\partial X} + \left(\frac{\partial \Phi_0}{\partial r} \right)^2 + \frac{1}{r^2} \left(\frac{\partial \Phi_0}{\partial \theta} \right)^2 \right]. \end{aligned} \quad (4.5.4)$$

To second-order, the boundary condition for the normal velocity on the body surface is

$$v_{2n} = \frac{f_{1r} + f_{1X} + \varphi_{0X} f_{0X}}{1 + f_{0Z}^2} - \frac{(f_{0r} + f_{0X}) f_{0Z} f_{1Z}}{(1 + f_{0Z}^2)^2}. \quad (4.5.5)$$

On the slip surface and horizontal cavity walls, the boundary conditions are

$$c < |Z| < d_0 : \Phi_2 = 0; \quad |Z| > d : \frac{\partial \Phi_2}{\partial Y} = 0. \quad (4.5.6)$$

In addition, the flow velocities are finite on the cavity edges $Z = \pm d_0$.

The solution of Eq. (4.5.4) is represented as the sum [6,30]

$$\Phi_2 = \Phi_{21} + \Phi_{2p}. \quad (4.5.7)$$

The potential Φ_{21} satisfies Laplace's equation with the boundary conditions (4.5.5), (4.5.6). The solution is obtained using a conformal mapping outside the body in the σ -plane (see Fig. 4.2). This mapping results from a slight modification of Eqs. (2.2.1) (see Part 2) using the asymptotic method developed by Lavrentiev [10]. From the Keldysh-Sedov formula we obtain the complex velocity \tilde{W}_{21} in the σ -plane as

$$\tilde{W}_{21} = -\frac{1}{\pi} \sqrt{\frac{\sigma^2 - d^2}{\sigma^2 - b^2}} \int_{-b}^b \sqrt{\frac{b^2 - s^2}{d^2 - s^2}} \frac{v_{2n}(s) ds}{(s - \sigma)l(s)}, \quad (4.5.8)$$

which is similar to Eq. (4.3.3). Therefore, the asymptotic behavior of the second-order potential Φ_{21} is similar to the asymptotic behavior of the potential Φ_0 . For the finite-span cavity, the asymptotic form of Eq. (4.5.8) as $\sigma \rightarrow \infty$ is determined by the source distribution along the body axis, i.e.,

$$W_{21} \sim \frac{Q_{2eff}}{\sigma}, \quad \Phi_{21} \sim Q_{2eff} \ln r, \quad (4.5.9a)$$

$$Q_{2eff} = \frac{1}{\pi} \int_{-b}^b \sqrt{\frac{b^2 - s^2}{d^2 - s^2}} \frac{v_{2n}(s) ds}{l(s)} \xrightarrow{d \gg b} \frac{b^2}{\pi d} \int_{-1}^1 \sqrt{1 - t^2} \frac{v_{2n}(t) dt}{l(t)}; \quad t = \frac{s}{b}. \quad (4.5.9b)$$

For the infinite-span cavity, the outer limit of the second-order potential Φ_{21} is defined by the dipole distribution on the body axis

$$\Phi_{21} = -\frac{D_{21}(X, t)}{r} \sin \theta, \quad D_{21} = -\frac{1}{\pi} \int_{-b}^b \frac{\sqrt{b^2 - s^2} v_{2n}(s)}{l(s)} ds \quad (4.5.10)$$

The potential Φ_{2p} is a partial solution of the Poisson equation (4.5.4) satisfying the boundary conditions of zero normal velocity on the body surface, $\Phi_{2p} = 0$ on the free surface, and $\partial\Phi_{2p}/\partial Y = 0$ on the horizontal cavity walls. Using the method of Ref. [30], we express the potential Φ_{2p} as

$$\begin{aligned} \Pi_{2p} = & \frac{\bar{\zeta}}{4} \left(S^2 \frac{\partial^2}{\partial t^2} + 2S \frac{\partial^2}{\partial X \partial t} \right) \int \Pi_0(\zeta) d\zeta + \\ & + \frac{1}{2} \Pi_0(\zeta) \left(\frac{\partial \bar{\Pi}_0(\bar{\zeta})}{\partial X} + S \frac{\partial \bar{\Pi}_0(\bar{\zeta})}{\partial t} \right) + \frac{\bar{W}_0(\bar{\zeta})}{4} \int W_0^2(\zeta) d\zeta, \\ \Phi_{2p} = & \text{Re } \Pi_{2p}. \end{aligned} \quad (4.5.11)$$

From Section 4.2 relevant to the infinite-span cavity, the asymptotic behaviors of the complex conjugate velocity and the complex potential are determined by the relations

$$\sigma = \zeta + O(\zeta^{-1}), \quad W_0 = \frac{D_0}{\zeta^2} + O(\zeta^{-3}), \quad \Pi_0 = -\frac{D_0}{\zeta} + O(\zeta^{-2}), \quad \sigma \rightarrow \infty. \quad (4.5.12)$$

Substituting these expansions into Eq. (4.5.11), we find that the third term of this equation is of the order of $O(\zeta^{-5})$ and the second term is of the order of $O(\zeta^{-2})$ as $\zeta \rightarrow \infty$. In the far field, the dominant term of Eq. (4.5.11) has the asymptotic form [30]

$$\Pi_{2p} \sim -\frac{S}{4} (SD_{0tt} + 2D_{0Xt}) \zeta \ln \zeta, \quad (4.5.13a)$$

$$\Phi_{2p} \sim -\frac{S}{4} (SD_{0tt} + 2D_{0Xt}) r [\ln(r) \cos \theta + \theta \sin \theta], \quad (4.5.13b)$$

where the dipole strength $D_0(X, t)$ is determined by Eqs. (4.2.4b) and (4.2.7b). For a finite span cavity, the dominant asymptotic term of the potential Φ_{2p} is determined as

$$\Phi_{2p} \sim \frac{S}{4} \left(S \frac{\partial^2 Q_{eff}}{\partial t^2} + 2 \frac{\partial^2 Q_{eff}}{\partial t \partial X} \right) r^2 (\ln r - 1), \quad (4.5.14)$$

where the source intensity of the first order approximation is determined in Sections 4.3 and 4.4. The potential Φ_{2p} given by the asymptotic expressions (4.5.13) and (4.5.14) is proportional to the Strouhal number. In both cases, the second and third terms of the expansion (4.5.2a) have the same order of magnitude in the region where

$$r \sim \frac{l_0}{S}. \quad (4.5.15)$$

In this region, unsteady asymptotics of the second-order potential can be of the same order of magnitude or dominate the first order asymptotics for the potential. For a finite-span cavity, these asymptotics are axisymmetric, whereas they have an angular dependence for an infinite-span cavity. Note that all terms of the second order approximation (excluding the unsteady terms) obtained in this paragraph are similar to those obtained in Ref. [6]. Then, we can use the theory [6] to formulate the matching conditions and identify an outer solution form in the second-order approximation. Such an analysis will be performed in our future work.

Equations (4.5.9)-(4.5.14) show that the outer limit of the second order approximation does not contain a source term for the case of an infinite span cavity. Then, according to the general theory [6, 26-31], a source term is not contained in the outer asymptotic solution in the second order approximation. This indicates that the second-order solution does not contribute to the inviscid drag. Note that this result is consistent with theory [6], which shows that the source intensity of the second order approximation is directly related to the source intensity of the first-order approximation. Since the first order approximation does not contain a source term for an infinite span cavity, we conclude that such a source term must be zero in the second order approximation.

Using a similar method, we analyze the outer limit of the third-order inner potential for an infinite-span cavity. The equation for this potential is

$$\begin{aligned} \frac{1}{r} \frac{\partial}{\partial r} r \frac{\partial \Phi_3}{\partial r} + \frac{1}{r^2} \frac{\partial^2 \Phi_3}{\partial \theta^2} &= \frac{\gamma+1}{2} \frac{\partial}{\partial X} \left(\frac{\partial \Phi_0}{\partial X} \right)^2 + K \frac{\partial^2 \Phi_0}{\partial X^2} + S^2 \frac{\partial^2 \Phi_2}{\partial t^2} + 2S \frac{\partial^2 \Phi_2}{\partial t \partial X} + \dots \sim \\ &\sim \frac{\gamma+1}{2} \frac{D_{0X} D_{0XX}}{r^2} (1 - \cos 2\theta) + \frac{KD_{0XX}}{r} \sin \theta - S \frac{SD_{21t} + 2D_{21Xt}}{r} \sin \theta - \\ &- \frac{S^2}{4} \left(S^2 \frac{\partial^4 D_0}{\partial t^4} + S \frac{\partial^4 D_0}{\partial t^3 \partial X} + \frac{\partial^4 D_0}{\partial t^2 \partial X^2} \right) r [\ln(r) \cos \theta + \theta \sin \theta] + \dots \end{aligned} \quad (4.5.16)$$

The first two terms on the right hand side of Eq. (4.5.16) are dominant for a steady flow. The last two terms arise due to unsteady effects. Thus, the third-order potential is represented as

$$\begin{aligned} \Phi_3 &= \frac{\gamma+1}{4} D_{0X} D_{0XX} (\Phi_{30}(r) + \Phi_{31}(r) \cos 2\theta) + KD_{0XX} \Phi_{32}(r) \sin \theta - \\ &- \frac{S^2}{4} \left(S^2 \frac{\partial^4 D_0}{\partial t^4} + S \frac{\partial^4 D_0}{\partial t^3 \partial X} + \frac{\partial^4 D_0}{\partial t^2 \partial X^2} \right) [\Phi_{33}(r) \cos \theta + \Phi_{34}(r) \theta \sin \theta] + \dots, \end{aligned} \quad (4.5.17a)$$

$$r \frac{\partial}{\partial r} r \frac{\partial \Phi_{30}}{\partial r} = 2; \quad \Phi_{30} = \ln^2 r, \quad r \frac{\partial}{\partial r} r \frac{\partial \Phi_{31}}{\partial r} - 4\Phi_{31} = -2, \quad (4.5.17b)$$

$$r \frac{\partial}{\partial r} r \frac{\partial \Phi_{32}}{\partial r} - \Phi_{32} = r; \quad r \frac{\partial}{\partial r} r \frac{\partial \Phi_{33}}{\partial r} - \Phi_{33} = r^2 (\ln r + 2), \quad (4.5.17c)$$

$$r \frac{\partial}{\partial r} r \frac{\partial \Phi_{34}}{\partial r} - \Phi_{34} = -r^2. \quad (4.5.17d)$$

Matching using intermediate expansions is discussed in [5.6]. Consistent with the low order matching described herein, the form of the outer solution can be obtained by rewriting the far-field inner asymptotics in outer variables. Using the outer-expansion variable $\tilde{r} = \delta^2 r$, we obtain from Eq. (4.5.15b)

$$\Phi_{30} \sim \left(\ln \frac{\tilde{r}}{\delta^2} \right)^2 = \ln^2 \tilde{r} - 4 \ln \delta \ln \tilde{r} + 4 \ln^2 \delta. \quad (4.5.18)$$

The second term of this relation corresponds to a source term in the outer asymptotic expansion that is $O[\delta^6 \ln \delta]$. This result is consistent with the asymptotic theory [6.26.29] for thin wings and Munk's theorem; *i.e.*, the source intensity and the drag-due-to-lift coefficient are proportional to the square of the lift force. In our case, the lift is $O(\delta^3)$ so that the drag coefficient is proportional to $O(\delta^6 \ln \delta)$.

Due to the third order source type term, this approximation gives a non-zero contribution to the drag. The results of Sections 4.3 and 4.4 indicate that for Phases 2 and the initial stage of Phase 3 the finite span cavity effect is $O(\varepsilon \delta^2 \ln \delta)$ in the far-field asymptotics, where $\varepsilon = a_0 / d_0$. Accordingly, this effect is dominant for $\varepsilon \gg \delta^4$ compared to the drag-due-to-lift component, which is $O(\delta^6 \ln \delta)$. This situation is typical for many practical cases. Its analysis is presented in Section 4.7.

Note that the analysis of this report is restricted by the case of relatively small angles of attack ($\bar{\alpha} \sim \delta$) and vertical body velocities ($\bar{V}_o \sim \delta U_\infty$). For $\bar{\alpha} \gg \delta$ and/or $\bar{V}_o \gg \delta U_\infty$, the drag due to lift may be of the order of (or even larger than) the finite span effect. These cases will be addressed in our future work.

4.6 Outer asymptotic expansion for the flow potential

The complete flow region, which includes the cavity interior, the shear layer and the outer stream (see Fig. 4.5) is subdivided into the outer and inner asymptotic regions. In each region, solutions are expressed as asymptotic expansions with respect to the small parameters

$$\delta = \bar{a}_0 / \bar{l}_0 \rightarrow 0, \quad \varepsilon = \frac{\bar{a}_0}{\bar{d}_0} = \frac{1}{d_0} \rightarrow 0, \quad (4.6.1)$$

where \bar{a}_0 is maximum body radius, \bar{d}_0 is cavity half-span and \bar{l}_0 is body length. From the results of Sections 4.2 – 4.5 we formulate the matching conditions of the inner and outer solutions.

4.6.1 Matching conditions

In the inner asymptotic region, the flow potential is represented as

$$\bar{\Phi}^- = \delta^2 U_\infty \hat{I}_0 [\Phi^+(X, Y, Z, t) + O(\varepsilon^2)], \quad (4.6.2a)$$

$$\bar{\Phi} = \delta^2 U_\infty \hat{I}_0 [\Phi(X, Y, Z, t) + G(X, t) + O(\varepsilon^2)]; \quad G(X, t) \equiv \ln \delta(S_1(X, t)). \quad (4.6.2b)$$

Hereinafter, the superscript “+” denotes flow quantities inside the cavity. The second (switchback) term is added into Eq. (4.6.2b) to match the inner and outer solutions. To $O(\delta^2)$ both potentials are solutions of two-dimensional Laplace equation in the cross-sectional planes. They are determined in Part 2 for an infinite-span cavity and in Sections 4.3 and 4.4 for a finite-span cavity. To dominant order, the pressures \bar{p} and \bar{p}^- are determined from the unsteady Bernoulli equations as

$$p^+ = - \left[\Phi_t^+ + \frac{\varepsilon}{2} (w^{+2} + v^{+2}) \right], \quad (4.6.3a)$$

$$p = - \left[\Phi_t + u + \frac{1}{2} (w^2 + v^2) \right], \quad (4.6.3b)$$

where u, v, w are the flow velocities in the fixed coordinates.

Sections 4.3 – 4.5 show that the finite-span cavity effects are the leading terms of the outer limits of the inner solutions. Therefore, the matching condition of the inner and outer solutions is determined as [6]

$$\bar{r} \frac{\partial \varphi}{\partial \bar{r}} \Big|_{\bar{r} \rightarrow 0} = r \frac{\partial \Phi}{\partial r} \Big|_{r \rightarrow \infty} = \frac{1}{2\pi} \frac{\partial A_{eff}(X, t)}{\partial X}. \quad (4.6.4)$$

Here $A_{eff} = \pi r_{eff}^2$ is the cross-section area of the equivalent body of revolution that is identified in Sections 4.2 – 4.4. The flow potential $\varphi(X, r, \theta, T)$ and the variables for the outer asymptotic region are determined below by Eqs. (4.6.9).

For Phase 2 of separation from a cavity, the effective area of the partially submerged body portion is a function of the dimensionless angle $n(X, t) = 1 - \pi\beta(X, t)$ (see Section 4.3)

$$X_1 \leq x \leq X_2: \quad \frac{\partial A_{eff}(X, t)}{\partial x} = \varepsilon \frac{2a^2(x) \sin \pi n}{n} \left[4a_x e_0(n) - \pi V_c (1 + 2n^2) \frac{\sin \pi n}{6n} \right], \quad (4.6.5)$$

For a fully submerged body portion, the effective area satisfies the equation (see Section 4.4)

$$\frac{\partial A_{eff}(X,t)}{\partial x} = \frac{4\pi a(a_x H - aB)}{H^2 + d^2} \quad (4.6.6)$$

This equation is relevant to Phase 3 (the body is totally outside the cavity) and Phase 2 for the body portions $x \leq X_1$ and $x \geq X_2$. Here $X_1(t)$ and $X_2(t)$ are coordinates of the upstream and downstream critical points, $X_0(t)$ and $X_e(t)$ are coordinates of the body nose and tail respectively. According to Eq. (2.1.3a) of Section 2.1, the function $B(x,t)$ is

$$B(x,t) = \dot{V}_e - q \sum_{k=0}^{\infty} (-1)^k q^{2k} [A_{-2k-1}(x,t) + qB_{-2k-2}(x,t)]; \quad q = \frac{a}{2|H|} \quad (4.6.7)$$

Typical distributions of the effective area are shown in Fig. 4.7 for Phase 2 ($t = 0.03$ s) and Phase 3. In this plot, the abscissa is the CG coordinate \hat{x}/\hat{l}_0 , and the ordinate is the effective cross-sectional area normalized by the maximum body area $A_b = \pi \hat{a}_0^2$. These results were obtained by computations of the 3-DOF trajectory for the body B4N2 at the initial conditions: $Y_0 = 1$ in, $V_0 = 10$ ft/s, $\omega_0 = 200$ deg/s, $\alpha_0 = 0^\circ$. At $t = 0.03$ s, the trajectory parameters are: $Y_0/D = 0.21$, $X_0/D = 0.009$, $\alpha = 6.2^\circ$, $V = -3.2$ m/s, $\omega = 228.3$ deg/s, and $U = 0.024$ m/s. At $t = 0.03$ s, the trajectory parameters are: $Y_0/D = -4.47$, $X_0/D = 28.4$, $\alpha = 5.47^\circ$, $V = -2.19$ m/s, $\omega = -461.3$ deg/s, $U = 1.11$ m/s. The effective body for Phase 2 is thinner than that for Phase 3. In Phase 2, the effective body nose is located at the upstream critical point $X_1 > X_0$. When the body is not far from the cavity ($H \sim O(1) \ll d_0$), Eq. (4.6.6) becomes

$$\frac{\partial A_{eff}}{\partial x} = 4\pi a(a_x H - aB) \left[1 + O\left(\frac{H^2}{d_0^2}\right) \right] \quad (4.6.8a)$$

When the body is far from the cavity ($H \gg d_0$), Eq. (4.6.8a) becomes

$$\frac{dA_{eff}}{dx} = 4\pi a a_x = 2 \frac{dA_b(x)}{dx} \quad (4.6.8b)$$

where $A_b(x)$ is the body cross-section area. This equation coincides with the equation for external separation.

For subsonic and supersonic flows, we can find the function $S_1(X,t)$ using Eqs. (4.6.5)-(4.6.8) and Ward's procedure [7]. Equations (4.6.5)-(4.6.8) allow us to formulate the outer asymptotic problem for transonic flows.

4.6.2 Classification of unsteady solutions in the outer asymptotic region

For analysis of the outer asymptotic region, we introduce the scaling

$$X = \frac{\bar{X}}{\bar{l}_0}; \quad \bar{Y} = \frac{\bar{Y}\mu}{\bar{l}_0}; \quad \bar{Z} = \frac{\bar{Z}\mu}{\bar{l}_0}; \quad T = \frac{\bar{t}}{\bar{l}_0}; \quad \bar{r} = \frac{\bar{r}\mu}{\bar{l}_0}, \quad (4.6.9a)$$

$$\bar{\Phi} = l_0 U_\infty \{X + \delta^2 \varphi(X, \bar{Y}, \bar{Z}, t)\}, \quad (4.6.9b)$$

$$\bar{p} = \frac{\bar{p} - p_\infty}{\rho_\infty U_\infty^2 \delta^2} = \varphi_X + S \varphi_T + O(\delta^2); \quad S = \frac{\bar{l}_0}{\bar{l}_0 U_\infty}. \quad (4.6.9c)$$

where μ is the parameter, which controls the length scale of the outer-region; S is Strouhal number; \bar{l}_0 is a characteristic time scale. Keeping dominant terms of the full potential equation [6] with respect to δ^2 we derive the equation

$$\delta^2 [K' - (\gamma+1)\varphi_X - (\gamma-1)S\varphi_T] \varphi_{XX} + \mu^2 (\varphi_{\bar{Y}\bar{Y}} + \varphi_{\bar{Z}\bar{Z}}) - 2S\varphi_{XT} - S^2 \varphi_{TT} = 0. \quad (4.6.10)$$

Here $K = (1 - M^2)/\delta^2$ is transonic similarity parameter. Equation (4.6.10) depends on the ratio $\bar{S} = S/\delta^2$. We can identify typical forms of this equation as follows.

If $S \ll \delta^2$, $\bar{S} \ll 1$, then, in the dominant approximation, the outer solution is governed by the steady transonic equation

$$\mu = \delta, \quad \bar{p} = -\varphi_X, \quad [K - (\gamma+1)\varphi_X] \varphi_{XX} + \varphi_{\bar{Y}\bar{Y}} + \varphi_{\bar{Z}\bar{Z}} = 0. \quad (4.6.11)$$

If $S = \mu^2 = \delta^2$, $\bar{S} = 1$, so that $\bar{l}_0 = \bar{l}_0/(\delta^2 U_\infty)$, we obtain the usual unsteady transonic equation

$$\bar{p} = -\varphi_X; \quad [K - (\gamma+1)\varphi_X] \varphi_{XX} + (\varphi_{\bar{Y}\bar{Y}} + \varphi_{\bar{Z}\bar{Z}}) - 2\varphi_{XT} = 0. \quad (4.6.12)$$

For faster processes, with Strouhal number $\delta^2 \ll S \ll 1$, we need to introduce an intermediate asymptotic region, where the following linear equations of acoustic type are valid

$$\mu^2 = S, \quad \bar{p} = -\varphi_X, \quad \varphi_{\bar{Y}\bar{Y}} + \varphi_{\bar{Z}\bar{Z}} - 2\varphi_{XT} = O\left(\frac{\delta^2}{S}\right) = 0. \quad (4.6.13)$$

If $S = 1$, so that $\bar{l}_0 = \bar{l}_0/U_\infty$, then the intermediate region has the scale \bar{l}_0 , and the governing equation includes the second derivative of the flow potential with respect to time

$$\mu = 1, \quad \bar{p} = -\varphi_X - \varphi_T, \quad \varphi_{\bar{Y}\bar{Y}} + \varphi_{\bar{Z}\bar{Z}} - 2\varphi_{XT} - \varphi_{TT} = O(\delta^2) = 0. \quad (4.6.14)$$

To determine outer solutions of Eqs. (4.6.12)-(4.6.14) we should investigate properties of the corresponding intermediate solutions. Unsteady perturbations can attenuate passing through the intermediate region. In the outer region, they can be less than steady perturbations, which are of the order of δ^2 or $\delta^2 \ln \delta$. Then, in the first order approximation, the outer solution is steady.

In the problem under consideration, the time scale relevant to the vertical motion under the gravity force is expressed as

$$\bar{t}_0 = \sqrt{\bar{\delta}_0 / g}, \quad S = \frac{\sqrt{\bar{t}_0 g / \delta}}{U_\infty} \quad (4.6.15)$$

This is similar to the conventional Froude time scale. We note that the pitch angle can oscillate. This is typical for a body moving outside the cavity (see Part 3). The time scale associated with these oscillations is determined as

$$t_0 = \frac{2\pi\bar{t}_0}{U_\infty \Omega} = \frac{2\pi\bar{t}_0}{U_\infty} \sqrt{\frac{\rho_b g_z}{\rho_\infty g_0}}, \quad S = \frac{1}{2\pi} \sqrt{\frac{\rho_\infty g_0}{\rho_b g_z}}, \quad (4.6.16)$$

$$g_0 = \int_a^{x_b} a^2(x) dx, \quad g_z = \int_a^{x_b} a^2(x) x^2 dx,$$

where ρ_b is body density.

The presence of several time scales indicates that qualitatively different regimes can arise in the far field region. Their occurrence depends on lumped physical parameters and non-dimensional groupings. We believe that during the long time scale relevant to the outer asymptotic region the short-time effects are averaged out, and their contribution to the wave drag is small [16]. With this interpretation we can neglect the unsteady effects and use Eqs. (4.6.11) to predict the wave drag for transonic separation from a flat wall and cavity. These equations are reduced to the Karman-Guderley axisymmetric form

$$\bar{p} = -\varphi_x \cdot [K - (\gamma+1)\varphi_x] \varphi_{xx} + \frac{1}{\bar{r}} (\bar{r} \varphi_{\bar{r}})_{\bar{r}} = 0, \quad (4.6.17)$$

where φ is the dominant approximation of the outer perturbation potential, which is valid in the outer limit [6]

$$X, \bar{r} \equiv \delta r, K, S \text{ fixed as } \delta \rightarrow 0$$

The second order term in the inner representation of the outer expansion, $g(X, t)$, which is needed to compute surface pressures and wave drag, is determined from solving the Karman-Guderley equation (4.6.17) for φ and taking the limit

$$g(X, t) = \lim_{\tilde{r} \rightarrow 0} \left[\varphi(X, \tilde{r}, t) - \frac{A'_{eff}(X, t)}{2\pi} \ln \tilde{r} \right], \quad (4.6.18)$$

where $A'_{eff} = \partial A_{eff} / \partial X$ is the streamwise derivative of the cross sectional area of the equivalent body. Eqs. (4.6.5)-(4.6.8) show that the expansions ((4.6.2b) and (4.6.9b)) join two different asymptotic expansions valid in two separate asymptotic regions. If the body is near the cavity, $H = O(1) \ll 1/\varepsilon$, then according to Eqs. (4.6.5) and (4.6.8a) the function $G(X, t)$ of the inner expansion (4.6.2b) and the outer potential $\varphi(X, \tilde{r}, t)$ are of the order of ε . If the body is far from the cavity, $H \gg 1/\varepsilon$. Equation (4.6.10b) indicates that $G(X, t)$ and $\varphi(X, \tilde{r}, t)$ are $O(1)$. In the intermediate region, $1 \ll H \ll 1/\varepsilon$, the order of these functions varies from ε to 1. This means that when the body is near the cavity, the nonlinear range of Mach numbers is narrow and the wave drag is ε times smaller than that occurring in classical slender body theory [6,7]. As the store moves away from the cavity, the flow Mach number increases. Note that, in the dominant-order approximation, the inner potential, $\Phi(X, Y, Z, t)$, and the outer potential, $\varphi(X, \tilde{r}, t)$, are governed by different physical effects. The outer solution is induced by sources distributed along the equivalent body axis, whereas the inner solution is induced by multipoles, which do not include source terms.

4.7 Analysis of the drag components

In Phase 2 (when the body crosses the slip surface), the drag force can be represented as the sum of four terms

$$C_D(t) = \frac{\hat{D}}{\rho_\infty U_\infty^2 \pi \delta^2 l_0^2} = C_{DF}(t) + C_{DB}(t) + C_{DW}(t) + C_{DP}(t), \quad (4.7.1a)$$

where $C_{DF}(t)$ is the friction drag coefficient and $C_{DB}(t)$ is the base drag coefficient. The two last terms, the wave drag coefficient $C_{DW}(t)$, and the crossflow drag coefficient $C_{DP}(t)$, result from integrating the streamwise projection of pressure force over the body projected frontal area. Accordingly,

$$C_{DW}(t) + C_{DP}(t) = \delta^2 \int_{x_0}^{x_e} A'(x) dx \int_{-\beta}^{\beta} [p(x, t, \vartheta) - p^+(x, t, \vartheta)] d\vartheta,$$

where $A(x)$ is body cross-section area and $A' = dA/dx$. Substituting the pressures from Eqs. (4.6.3) into this equation and using Eqs. (4.6.2) for the flow potential we obtain

$$C_{DW}(t) + C_{DP}(t) = -2\delta^2 \int_{x_0}^{x_e} \left[\frac{\partial g(x, t)}{\partial t} + \frac{\partial g(x, t)}{\partial x} \right] A'(x) \beta(x, t) dx +$$

$$\begin{aligned}
& -\delta^2 \int_{x_1}^{x_2} A'(x) dx \int_{-\beta}^{\beta} \left[\frac{\partial \Phi(x, t, \vartheta)}{\partial t} + \frac{\partial \Phi(x, t, \vartheta)}{\partial x} - \frac{\partial \Phi^+(x, t, \vartheta)}{\partial t} \right] d\vartheta - \\
& -\delta^2 \int_{x_1}^{x_2} A'(x) dx \int_{-\beta}^{\beta} \left[w^2(x, t, \vartheta) + v^2(x, t, \vartheta) - w^{+2}(x, t, \vartheta) - v^{+2}(x, t, \vartheta) \right] d\vartheta. \quad (4.7.1b)
\end{aligned}$$

where $\beta(x, t)$ is the angle of intersection of the slip surface with the body surface. In Phases 1 or 3, the body is fully in the cavity or in the freestream and $\beta = \pi$. In the right-hand side of this formula, the first term corresponds to the wave drag, and the two other terms relate to the cross-flow drag.

4.7.1 Friction drag

The friction drag coefficient $\hat{C}_{DF}(t)$ is found by integrating the local friction coefficient $c_f(X, Re_x)$ over the body surface; i.e.

$$C_{DF}(t) = \frac{\hat{D}_f}{\rho_\infty U_\infty^2 \pi \delta^2 l_0^2} = \frac{1}{\delta} \int_0^1 k c_f(\bar{X}, Re_x) d\bar{X}, \quad (4.7.2a)$$

$$\bar{X} = X - X_0, \quad Re_x = Re \bar{X} [1 - U(t)], \quad Re = \frac{\rho_\infty U_\infty l_0}{\mu_\infty}, \quad (4.7.2b)$$

where $U(t)$ is horizontal body speed; ρ_∞ , μ_∞ and U_∞ are density, viscosity and speed of the freestream. The coefficient k is indicative of the friction drag being appreciable only on the body portion submerged in the flow external to the cavity. The two typical cases of the body location with respect to the slip surface are shown in Figs. 4.5 and 4.6. For a partially submerged body portion, ($X_1 \leq X \leq X_2$) $k = \beta/\pi$; for the totally submerged portion $k = 1$; for the body portion totally inside the cavity (the nose part, $X_0 \leq X \leq X_1$, in Fig. 4.6) $k = 0$. Because c_f is a weak function of the Mach number at transonic speeds, we use the Schultz-Grunow correlation for the incompressible turbulent boundary layer on a flat plate and its modification for axisymmetric flows [32]. Accordingly,

$$c_f(X, Re_x) = \bar{c}_f(Re_x) \left[\int_0^{\bar{X}} a^{-7/6}(x) dx \right]^{6/7}, \quad \bar{c}_f(Re_x) = 0.37 (\lg Re_x)^{-2.584}. \quad (4.7.3)$$

4.7.2 Base drag

The base drag coefficient $C_{DB}(t)$ is found by integrating the pressure difference, $\bar{p}_b - p_\infty$, over the body base. It is expressed as a function of the Mach number [33]

$$C_{DB}(M) = \frac{\hat{D}_b}{\rho_\infty U_\infty^2 \pi \delta^2 l_0^2} = \frac{a_r^2}{\gamma M^2} [1 - p_b(M)], \quad (4.7.4a)$$

where $M = M_\infty[1 - U(t)]$; a_e is base radius, and $p_b(M) = \hat{p}_b / p_\infty$ is the non-dimensional base pressure. Ref. [33] showed that (4.7.4a) is in good agreement with experimental data for ogive-cylinder bodies. The function $p_b(M)$ is shown in Fig. 4.8. For external separation, the base drag can be expressed as a function of the equivalent body thickness δ and the transonic similarity parameter K ; *i.e.*

$$C_{DB}(M, \delta) = 2\delta^2 C_{D0}(K), \quad (4.7.4b)$$

where $C_{D0}(K)$ is a universal function for thickness-ratio-scaled, affinely-related bodies. A plot of this function for an ogive-cylinder of B4N2 profile specified in Ref. [18] is shown in Fig. 4.9. In Phase 2, the slip surface leads to new physical effects. If the body base is not fully submerged into the external flow, as shown in Fig. 4.5a, then the base pressure $p_b(M) = 1$ is due to the boundary condition on the slip surface. Accordingly, the base drag coefficient is $C_{DB} = 0$. If the body base is fully submerged in the external flow, as shown in Fig. 4.5b, then the base drag is calculated using Eq. (4.7.4).

4.7.3 Transonic wave drag

The wave drag coefficient $C_{DW}(t, M)$ is due to sources distributed along the equivalent body axis. As an illustration for separation from a flat plate, it is

$$C_{DW}(t) = -2\delta^2 \int_{x_3}^{x_2} \left[\frac{\partial g(x, t)}{\partial t} + \frac{\partial g(x, t)}{\partial x} \right] A'(x) dx, \quad (4.7.5)$$

The term "wave drag" indicates that the integral (4.7.5) is equivalent to the integral of the total pressure jumps along the shock wave system [6]. Since the body is moving, the wave drag depends on time, as indicated by the derivatives of g in the integrand of (4.7.5). Also, the end conditions and our inclusion of the base drag in the force accounting negates the need for extra terms indicated in [6], which is applicable for the steady flow over a transonic body in the presence of a flat plate. We examine the class of store separations in which the Strouhal number is such that a pseudo-steady approximation can be used at each time step. Accordingly, the function $C_{DW}(t, M)$ was calculated at these steps with the steady transonic code of N. Malmuth. This code solves the Karman-Guderley equation (4.6.17) for the outer flow potential with the asymptotic boundary condition given by Eqs. (4.6.9b), (4.6.5) and (4.6.6). From numerical studies discussed in Section 4.9, its value monotonically grows as the body moves away from the cavity. This behavior is confirmed by the numerical calculations discussed in Section 4.9.

4.7.4 Cross-flow drag

The cross-flow drag coefficient $C_{DP}(t)$ results from integrating the pressure component relevant to the inner potential $\Phi(X, Y, Z, t)$ (without the term $g(X, t)$ given by Eq. (4.6.2b)) over the body surface. It is expressed by the second and third terms of Eq. (4.7.1b).

We subdivide the body into the three parts: the first part is partially submerged into the outer stream; the second is totally submerged; the third is inside the cavity. Accordingly, the cross-flow drag coefficient can be expressed as a sum of three terms

$$C_{DP}(t) = \frac{\bar{D}_p}{\rho_\infty U_\infty^2 \pi \delta^2 l_0^2} = \delta^2 \int_x^{x_p} c_x(x, t) a(x) a_x(x) dx = \delta^2 (C_{DP1} + C_{DP2} + C_{DP3}), \quad (4.7.6a)$$

$$c_x(x, t) = c_{x1}(x, t) + c_{x2}(x, t) + c_{x3}(x, t) = \int_{-\beta}^{\beta} [p(x, t, \vartheta) - p^-(x, t, \vartheta)] d\vartheta + \\ + \int_0^{2\pi} p(x, t, \vartheta) d\vartheta + \int_0^{2\pi} p^-(x, t, \vartheta) d\vartheta, \quad (4.7.6b)$$

$$C_{DP1}(t) = \int_{x_1}^{x_2} c_{x1}(x, t) A'(x) dx; C_{DP2}(t) = \int_{x_0, x_2}^{x_1, x_p} c_{x2}(x, t) A'(x) dx; C_{DP3}(t) = \int_{x_0, x_2}^{x_1, x_p} c_{x3}(x, t) A'(x) dx, \quad (4.7.6c)$$

where c_x is local cross-flow drag coefficient. The first term of Eq. (4.7.6b), $c_{x1}(x, t)$, corresponds to the partially submerged body portion located in the interval $X_1 < X < X_2$ (see Fig. 4.5b). The second term of Eq. (4.7.6b), $c_{x2}(x, t)$, corresponds to the submerged body portions: it is located in the interval $X_0 \leq X \leq X_1$ for the case shown in Fig. 4.5 and in the interval $X_2 \leq X \leq X_p$ for the case shown in Fig. 4.6. The third component is the cross-flow drag of the body part being inside the cavity. These drag components are expressed in an explicit analytical form that simplifies numerical calculations.

Consider the partially submerged body part. On the body surface, $\eta = -0, |\xi| < b$, the inner potential and the tangential velocity are given by Eqs. (2.2.3) of Section 2.3

$$\Phi(x, \lambda, t) = \Phi_1 + \Phi_2 = \\ = V_e \frac{\sin \pi n}{n} \left(\sqrt{1 - \lambda^2} - \frac{2nQ^n(\lambda)}{D(\lambda, n)} \sin \pi n \right) - \frac{2aa_x}{\pi} \sqrt{1 - \lambda^2} E(\lambda, n), \quad (4.7.7a)$$

$$w_\theta(x, \lambda, t) = V_e \left[\frac{Q^{2n}(\lambda) - 1}{D(\lambda, n)} \sin \pi n - \lambda \frac{\sqrt{1 - \lambda^2} D(\lambda, n)}{4n^2 Q^n(\lambda)} \right] + \\ + \frac{a_x \sqrt{1 - \lambda^2} I(\lambda, n)}{\pi} \{ 2 - [Q^n(\lambda) + Q^{-n}(\lambda)] \cos \pi n \}. \quad (4.7.7b)$$

The potentials $\Phi_1(x, \lambda, t)$ and $\Phi_2(x, \lambda, t)$ are induced by the vertical body motion and axial variations of the body radius, respectively. Using these functions and Eq. (4.6.3) we express the pressure on the body surface by Eq. (2.2.4) of Section 2.3

$$p(x, \lambda, t) = -\Phi_t - \Phi_x + \frac{V_e^2}{2} \left[1 - \frac{\lambda^2(1-\lambda^2)D^2(\lambda, n)}{16n^4 Q^{2n}(\lambda)} \right] - \frac{a_x^2}{2} \left[1 + \frac{(1-\lambda^2)D^2(\lambda, n)}{\pi^2 Q^{2n}(\lambda)} I^2(\lambda, n) \right] + V_e a_x \frac{\lambda(1-\lambda^2)D^2(\lambda, n)}{4n^2 \pi Q^{2n}(\lambda)} I(\lambda, n). \quad (4.7.8)$$

The local cross-flow drag coefficient relevant to the partially submerged body cross section is expressed as

$$c_{x1} = -\left(\frac{\partial}{\partial t} + \frac{\partial}{\partial x} \right) a \tilde{\Phi}(x, t) + V_e^2 N_1(x, t) + a_x^2 N_2(x, t) + V_e a_x N_{12}(x, t). \quad (4.7.9)$$

The average value of the potential over the cross-sectional body contour, $\tilde{\Phi}(x, t)$, is represented in the form

$$\tilde{\Phi} = \int_{-b}^b \Phi(X, \xi, t) \frac{\partial Z}{\partial \xi} d\xi = a_x \tilde{\Phi}_1(n) - V_e \tilde{\Phi}_0(n), \quad (4.7.10a)$$

$$\tilde{\Phi}_0(n) = 4 \frac{\sin \pi n}{n} \left\{ e_0(n) - \frac{n}{2} [1 + \pi(1-n) \operatorname{ctg} \pi n] \right\}, \quad (4.7.10b)$$

$$\tilde{\Phi}_0(0) = 4\pi \left(\ln 2 - \frac{1}{2} \right); \quad \tilde{\Phi}_0(1) = 0, \quad (4.7.10c)$$

$$\tilde{\Phi}_1(n) = 4 \frac{\sin \pi n}{n} e_{20}(n); \quad \tilde{\Phi}_1(0) = 4\pi e_{20}(0); \quad \tilde{\Phi}_1(1) = 0. \quad (4.7.10d)$$

The special function $e_{20}(n)$ is expressed by the double improper Cauchy integral given in Appendix C of Part 2; its plot is shown in Fig. 2.2. The second term of Eq. (4.7.8) is expressed as

$$N_1(n) = -\frac{1}{2} \int_{-b}^b \left[1 - \frac{\lambda^2(1-\lambda^2)D^2(\lambda, n)}{16n^4 Q^{2n}(\lambda)} \right] \frac{\partial Z}{\partial \xi} d\xi = \frac{\pi}{6n^2} \left(1 + 2n^2 - \frac{\sin 2\pi n}{2\pi n} \right) - \pi(1-n), \quad (4.7.11a)$$

$$N_1(1) = \frac{\pi}{2}; \quad N_1(0) = \frac{\pi}{3} \left(\frac{\pi^2}{3} - 2 \right). \quad (4.7.11b)$$

The third term of Eq. (4.7.8) is

$$N_2(n) = \frac{1}{2} \int_{-b}^b \left[1 + \frac{(1-\lambda^2)D^2(\lambda, n)}{\pi^2 Q^{2n}(\lambda)} I^2(\lambda, n) \right] \frac{\partial Z}{\partial \xi} d\xi = \quad (4.7.12a)$$

$$= \pi(2-n) + \frac{4 \cos \pi l}{n \sin \pi l} \left\{ e_0(n) - 2 \left(\frac{\sin \pi l}{\pi l} \right)^2 e_{10}(n) - \frac{n}{2} [1 + \pi(1-n) \operatorname{ctg} \pi l] \right\}, \quad (4.7.12b)$$

$$N_2(1) = \frac{\pi}{2}; N_2(0) = \frac{8\pi}{3}. \quad (4.7.12c)$$

The function $e_{10}(n)$ is given in Appendix C of Part 2; its plot is shown in Fig. 2.2. The fourth term of Eq. (4.7.8) is expressed as

$$N_{12}(n) = - \int_{-b}^b \frac{\lambda(1-\lambda^2) D^2(\lambda, n)}{4n^2 \pi Q^{2n}(\lambda)} I(\lambda, n) \frac{\partial Z}{\partial \xi} d\xi = \quad (4.7.13a)$$

$$= 4 \left(1 - \cos \pi l \frac{\sin \pi l}{\pi l} \right) \frac{e_0(n)}{n \sin \pi l} + \frac{\cos \pi l}{\pi l^2} \left[2e_2(n) - \frac{\pi^2(1+2n^2)}{6} \right], \quad (4.7.13b)$$

$$N_{12}(1) = \pi; N_{12}(0) = \frac{2\pi}{3} (4 \ln 2 - 1). \quad (4.7.13c)$$

The function $e_2(n)$ is given in Appendix C of Part 2; its plot is shown in Fig. 2.2. The functions $\tilde{\Phi}_0(n)$, $\tilde{\Phi}_1(n)$, $N_1(n)$, $N_2(n)$, $N_{12}(n)$ are shown in Fig. 4.10.

Using the results of Section 2.2, we express the local cross-flow drag coefficient relevant to the submerged body portions (the interval $X_0 \leq X \leq X_1$ in Fig. 4.5a and the interval $X_2 \leq X \leq X_c$ in Fig. 4.6a) in the form

$$c_{x2} = a_x^2 + 2B^2 - V_{c'}^2 + 2 \sum_{n=1}^{\infty} (A_{-2n-1}^2 + B_{-2n-2}^2). \quad (4.7.14)$$

Note that this expression is valid for Phase 3. A similar relation is obtained for the cross-flow drag associated with the body part located inside the cavity.

To integrate a singularity in the trajectory equations, which occurs at the beginning of Phase 2, we express the cross-flow drag component, C_{DP1} , given by Eq. (4.7.6c), as a decomposition of the two terms

$$C_{DP1}(t) = \delta^2 [C_{DP1a}(t) + C_{DP1b}(t)] \quad (4.7.15a)$$

$$C_{DP1a}(t) = \frac{d}{dt} \int_{x_1}^{x_2} \tilde{\Phi}(x, t) a(x) a'(x) dx, \quad (4.7.15b)$$

$$C_{DP1b}(t) = m[1 - U(t)] \tilde{\Phi}(x_c, t) a(x_c) a'(x_c) - \int_{x_1}^{x_2} \tilde{\Phi}(x, t) \frac{d[a(x) a'(x)]}{dx} dx +$$

$$+ \int_{x_1}^{x_2} [V_r^2 N_1 + a'^2 N_2 - V_r a' N_{12}] a(x) a'(x) dx. \quad (4.7.15c)$$

Here the first (unsteady) term C_{DP1a} is singular, whereas the second term is regular: $m=1$ if the body base is partially submerged into the stream, and $m=0$ in the other cases. Similar relations are obtained for the partially submerged body part located inside the cavity.

4.8 Solution of 3-DOF trajectory equations

The 3-DOF trajectory equations are written as

$$\frac{dV}{dt} = c_l L(t) - c_g, \quad \frac{d\omega}{dt} = c_m M_p(t), \quad \frac{dU}{dt} = c_i C_D(t). \quad (4.8.1a)$$

$$c_g = \frac{\bar{g} \bar{l}_0}{\delta U_\infty^2}, \quad c_l = \frac{\pi \rho_\infty \bar{l}_0^3 \delta^2}{\bar{m}}, \quad c_m = \frac{\pi \rho_\infty \bar{l}_0^5 \delta^2}{\bar{I}}. \quad (4.8.1b)$$

where \bar{m} and \bar{I} are body mass and moment of inertia, respectively; the lift force $L(t)$ and the pitching moment $M_p(t)$ are provided in Part 2. To integrate these equations we developed a numerical code using a fourth-order Runge-Kutta scheme for the two first equations of (4.8.1a). The most extensive computations are associated with the wave drag, which requires solution of the Karman-Guderley equation. To reduce the run time, the Adams fourth-order explicit method is used to solve the third equation of (4.8.3.1a). Our FORTRAN code consists of the following three components:

- *Function.for* contains auxiliary functions that are used to calculate the lift and drag components.
- *Wdrag.for* contains the program AFTB2 of N. Malmuth for solving the Karman-Guderley equations. As contrasted to the original version of AFTB2, the initial data are specified via COMMON-blocks.
- *Traj3d1.for* contains the main program TRAJC3D with auxiliary subroutines. It provides calculations of the lift and drag forces as well as the pitching moment in three distinct phases of the body separation.

Note that for external separations the computational algorithm is essentially simplified because there is no intricate Phase 3, in which the body crosses the slip surface.

4.9 Analysis of store separation from cavities and walls to a transonic stream

In this section, we analyze effects of the initial conditions and the body thickness on the store trajectory. In our calculations, we use the ogive-cylinder body B4N2 tested in the subsonic wind-tunnel experiments [18]. Physical properties of this body are described in Part 3. In Section 4.9.1, we study external separation from a flat wall that generically simulates a wing. In Section 4.9.2, we discuss separation from a transonic cavity.

4.9.1 External separation

We consider external separation from a flat wall that simulates a fuselage or wing. Calculations were performed for the ogive-cylinder body B4N2, which was tested in the subsonic wind-tunnel experiments of IIT [18]. In our calculations, the freestream Mach number is $M_\infty = 0.999$ and the Reynolds number based on the body length and freestream parameters is $Re = 6.4782755 \cdot 10^6$. The initial location and horizontal velocity of the body CG are $X_0 = U_0 = 0$.

To estimate magnitudes of different drag components, we discuss the numerical results provided in Figs. 4.11 and 4.12. Calculations were conducted at the initial conditions: $Y_0 = -0.975$ inch, $V_0 = -9.144$ m/s, $\alpha_0 = -3.3^\circ$, $\omega_0 = -200$ deg/s. Figure 4.11a shows the CG trajectory $Y/D_0 = f(X/D_0)$, where D_0 is the body diameter; Figure 4.11b shows the pitch angle time history, $\alpha(t)$; Figures 4.12a and 4.12b show histories of the drag components.

Fig. 4.12b shows that the wave drag is larger than the pressure drag in the initial phase of trajectory. However, it decreases rapidly with body deceleration. Comparing the drag components shown in Figs. 4.12a and 4.12b we conclude that the base drag is larger than the wave and pressure drags. The dominant drag component is the friction drag, because the wave, pressure and base drag coefficients are proportional to δ^4 ; whereas the friction drag coefficient is proportional to δ (in the cases under consideration $\delta = 0.03125$ is small). Note that such a hierarchy of drag components is consistent with the calculations of Ref. [25].

Figures 4.13-4.14 illustrate effects of the initial vertical velocity on the body trajectory and pitching angle. Figure 4.13a shows locations of the body axis at various equally spaced times, and Figure 4.13b shows the CG trajectory. For an initial vertical velocity $V_0 = 0$, the body moves toward the wall and finally re-contacts it. For $V_0 = 0.5$ m/s, the body separates from the wall monotonically. This example shows that there is a critical initial vertical velocity, below which the body is not able to separate from the wall. Figures 4.14a and 4.14b show histories of the pitch angle for these two regimes. It is seen that the pitch angle oscillates with weakly growing amplitude; this oscillatory behavior is qualitatively consistent with the experiments [18, 34].

Figures 4.15-4.17 illustrate effects of the initial pitch angle on the body trajectory at the release conditions: $\omega_0 = 0$, $Y_0 = -1.95$ inch, and $V_0 = 0$. Figures 4.15a and 4.15b show locations of the body axis at various times for the initial pitch angles $\alpha_0 = 0^\circ$, $\alpha_0 = 6^\circ$, and $\alpha_0 = -6^\circ$. Figure 4.16 shows the CG trajectory. At $\alpha_0 = 6^\circ$, body re-contact is observed. For $\alpha_0 = 0^\circ$, the body slowly separates from the wall. For $\alpha_0 = -6^\circ$, the lift force causes a more rapid departure. Similar to the case shown in Figs. 4.13-4.14, there is a critical pitch angle above which the body does not separate from the wall. The results in Fig. 4.16 show that the initial pitch angle $\alpha_0 = 6^\circ$ is close to this critical value and the

vertical coordinate of the center of inertia behaves non-monotonically. The pitch angle histories shown in Figs. 4.17a and 4.17b are similar to the case discussed in the previous paragraph. Note that the initial pitch angle effect is similar to the initial vertical velocity effect and is consistent with the concept of the equivalent body velocity introduced in Section 1.2. According to this concept the initial pitch angular velocity behaves similarly to the initial pitch angle and vertical velocity.

The effect of initial condition on the body trajectory illustrated by Figs. 4.13 – 4.17 indicates that external store separations can be effectively controlled by the release mechanism. It also confirms our IIT tests [18] conjecture that the repeatability could be enhanced by close control of the release mechanism. These results may be useful in designing ejection units and thrust motors for stage separation. They allow for evaluation of thrust and weight required for these units, and indicate how to avoid adverse re-contact with a relatively small impulse.

In Figs. 4.18-4.20, calculations for different body thickness are shown. The calculations were conducted for the initial conditions: $M = 0.999$, $V_0 = -9.144 \text{ m/s}$, $\alpha_0 = 3.3^\circ$, $\omega_0 = 200 \text{ deg/s}$ for the B4N2 body of the diameters $D = D_0 = 3/8 \text{ inch}$, $D = 2D_0$ and $D = 3D_0$. The time variations of CG horizontal (Fig. 4.18a) and vertical (Fig. 4.18b) coordinates, CG trajectory (Fig. 4.19a) and the pitch angle history (Fig. 4.19b) show that the body thickness causes noticeable changes in the trajectory characteristics. Because of increasing lift force, dropping time grows with body diameter, approximately as $\sim D^2$ (see Figures 4.18a and 4.19b). As shown in Fig. 4.18a and 4.19a, due to this effect, the thicker bodies penetrate downward longer distances in the horizontal direction, although the total drag varies weakly (see Fig. 4.20).

Histories of the drag components are shown in Fig. 4.20a for the thinnest body and in Fig. 4.20b for the thickest body. Since the body thickness is small, the pressure drag is also small. The base drag is proportional to the base area so that its coefficient D_b is a weak function of the body thickness. The value of D_b is consistent with Chow's [33] results that were scaled with the transonic similarity rule. For such slender bodies, the turbulent friction drag may be dominant. This example shows that prediction and control of the friction drag (including transition and turbulence modeling) may be important for store separation modeling and control. In this regard, the issues of transition and turbulence modeling should also be addressed carefully.

For the body shape and release conditions considered, the wave drag is a very small fraction of the total drag. The transonic drag effect is localized in narrow ranges of t and x even at relatively large δ because of a rapid deceleration of the body. Even for the body of $3D_0$ diameter, the wave drag is very small everywhere, with the exception of a short initial "impulsive" phase (approximately 2 ms) where its value is about 1/2 the total drag. A relatively small effect on the x trajectory of this almost "delta function" drag impulse is due to the fact that the larger wave drag is localized to near sonic Mach numbers. Accordingly, the impulse quickly decelerates the body to the lower transonic Mach

number where the wave drag is insignificant. These conclusions could be changed for different parametric conditions and cases where the axial deceleration of the body is relatively small (for example, in the case of re-contact). *However, the deeper significance of these results is that they hint at an opportunity to economize the use of large-scale codes and even to interpolate and extrapolate from them as well as to interpret their results. Also, these results suggest how simple theoretical mathematical fluid dynamic models can give insight into the importance of the various flow mechanisms.*

Two critical parameters that affect the generality of these observations are the transonic similarity parameter K and the Strouhal number S . In addition, the possibility of throats between the store and the parent body could create sonic choked flow situations. The lift and moment curves show a much larger influence of δ , since the lift force scales quadratically with the increased base area. The frequency of this weakly divergent phugoid pitch oscillation of this finless shape increases with body thickness ratio.

4.9.2 Store separation from cavities

In this section, we discuss parametric calculations, which illustrate dependencies of body trajectories on the initial conditions and body geometry for transonic separation from cavities. As in Section 4.9.1, the main physical characteristics correspond to the body B4N2. All calculations are conducted at the freestream Mach number 0.999. The more complex physical conditions inherent in this type of separation lead to store ricochet dynamics.

Figures 4.21 - 4.25 demonstrate the body thickness effect on the trajectory characteristics. Three bodies of diameters $D = D_0 = 3/8$ inch, $D = 2D_0$, and $D = 3D_0$ are considered. The initial (release) conditions are shown in the figures. In these calculations, we varied the body diameter at fixed body length. The dimensionless cavity width d_0 is also varied inversely proportional to D .

Figure 4.21 illustrates the body thickness effect on time histories of the vertical CG coordinate. In Figs. 4.22, the CG trajectories are shown in X - Y space. The pitch angle and the vertical speed temporal variations are shown in Fig. 4.23 and 4.24. It is seen that the body dynamics strongly depend on the thickness ratio. For $D=D_0$, the body separates from the cavity in a relatively short time period. For $D=2D_0$, the body is almost stopped near the parent body for a long time (until the pitch angle is negative). The total vertical displacement is only about $4D$. During this phase the body drifts downstream and removes in the horizontal direction from the initial state at $X \sim 70D_0$ which is larger than four body lengths.

The average pitch angle and the pitch oscillation frequency also strongly depend on the thickness ratio. The frequency increases approximately proportional to the thickness ratio. For $D=3D_0$, ricochet is observed. The body returns to the cavity with a relatively small downstream displacement. The pitch angle monotonically grows with small oscillations since the pitching moment is too small to overcome pitching due to the initial angular speed.

Figure 4.24 illustrates centerline trajectories for bodies of different diameters. It is seen that the body of $D=3D_0$ returns to the cavity. The body of $D=2D_0$ remains near the parent body for a relatively long time. During this time, it is projected downward from the cavity, with pitch angle decreasing. The $D=D_0$ body enters the external stream almost immediately, and its trajectory only weakly depends on the parent body.

Figures 4.25a – 4.25c show time histories of different drag components for the bodies of $D=D_0$, $D=2D_0$ and $D=3D_0$, respectively. In Phase 2, the wave drag is less than the other components since the effective area is relatively small. By neglecting the wave drag of this phase we can substantially reduce the computational time. In Phase 3, the wave drag is of the order of (or even larger than) the other drag components for the body of $D=2D_0$. The pressure drag has a peak at the exit from the shear layer (the end of Phase 2) since all its components have maximum at $n = 0$, based on the analytical expressions provided in Section 4.7.4. The base drag jumps to a finite value or to zero, when the body base is submerged into the outer stream or is returned to the cavity. In Phase 2, the friction drag monotonically grows, with the wetted area increasing. As seen in the plots for the body of $D=D_0$, all drags tend to their asymptotic values in Phase 3. For the body of $D=2D_0$, the time period is too short to achieve this asymptotic behavior. The body of $D=2D_0$ crosses the shear layer during this time period. It moves downstream, and its pitch angle decreases to a negative value. The base drag history shows that the body base returns into the cavity in the time interval 0.05 - 0.06 s when the pitch angle becomes negative. Then the body begins to separate from the cavity. The body of $D=3D_0$ does not separate. It returns to the cavity with increasing pitch angle.

The second series of calculations are shown in Figs. 4.26 – 4.31 to illustrate the initial vertical speed effect on the body trajectories. Calculations were made at $\alpha_0 = 6^\circ$, $\omega_0 = 0 \text{ deg/s}$, $Y_0 = 1 \text{ inch}$ and the two near-critical values of the initial vertical speed: $V_0 = 20 \text{ in/s}$, 30 in/s . The plots of CG histories (Fig. 4.26), CG trajectories (Fig. 4.27), and centerline time histories (Fig. 4.30) at $V_0 = 20 \text{ m/s}$ indicate that the body ricochets from the freestream and re-contacts the parent body back of the cavity. When the body enters into the shear layer, the pitch angle grows slightly (see Fig. 4.28) due to body inertia. Due to a negative pitching moment, it then decreases with a small angular speed. This trend is too weak to decrease the pitch angle to its critical value (at which the separation becomes possible). For $V_0 = 30 \text{ m/s}$, the body stays near the shear layer for a long time period and penetrates downward a long distance. In this case, the negative angular speed is high enough to decrease the pitch angle below its critical value, and the body separates from the cavity. Figure 4.29 shows that in both cases the vertical CG speed grows to a positive value. For $V_0 = 30 \text{ m/s}$, the gravity force is strong enough to cause the store departure from the cavity, whereas for $V_0 = 20 \text{ m/s}$ this force is too small for separation.

Figures 4.31a – 4.31b show the time evolution of the drag components. At $V_0 = 20 \text{ m/s}$, the body is near the shear layer and the wave drag is small. The base and friction drags are dominant components during most of the trajectory. The pressure drag is important in the final phase of the trajectory. At $V_0 = 30 \text{ m/s}$, the pressure drag peaks occur when the body enters the freestream. We infer that the base drag evolution causes the body to

return to the shear layer. At this time, the pressure drag reaches a minimum and then grows to its maximum value when the body base exits from the shear layer again. As the wetted area decreases, the friction drag decreases. In this case, the wave drag is smaller than the other components.

Figures 4.32-4.37 illustrate the initial pitch angle effect on the trajectory behavior. The calculations were performed at $Y_0 = 1$ inch, $V_0 = 20$ inch/s, $\omega_0 = 0$. The trajectory characteristics are very sensitive to the angle α_0 , which may be induced by the release mechanism and aircraft maneuvering at the release instant. The variation $\Delta\alpha_0 = 1^\circ$ leads to a substantial perturbation of the trajectory: at $\alpha_0 = 5^\circ$ the body separates from the cavity, whereas at $\alpha_0 = 6^\circ$ re-contact is observed (see Figs. 4.32 and 4.33).

Near the critical angle, $\alpha_0 = 5^\circ$, the trajectory behavior is similar to that shown in Figs. 4.26-4.30 for the initial speed $V_0 = 30$ in/s. However, the vertical CG speed in this case does not become positive (see Fig. 4.35). Drag component histories (Fig. 4.36a) cause the body base to enter the external flow and then return to the shear layer again, when the angle of attack becomes negative. Then, the body exits to the external flow and drops downward from the shear layer.

The case $\alpha_0 = 6^\circ$ is also shown for comparison. Here, the body quickly crosses the shear layer and separates from the cavity to a large distance. An interesting feature of this regime is observed for vertical oscillations of CG speed in Phase 3 (body outside the cavity). This behavior is consistent with our analysis for the body dropping in an unbounded stream. Figure 4.36b shows that the body moves in the outer freestream for a long time and the drag components approach their asymptotic values. This corresponds to external body separation.

4.10 Summary and conclusions

In this part, we analyzed the outer asymptotic solution and drag force components. Parametric studies of store trajectories are provided including the separation from a wing (external separation) and cavities into a transonic freestream. To determine the matching conditions and identify forms of the outer solutions we consider the outer limit, $r \gg H$, of the inner solutions. For cavities of a large span, our analysis is based on the solutions of the dominant approximation obtained in Part 2. We found a general form of the inner solutions in the case of finite-span cavities and investigate their limits.

Analyzing asymptotics for the inner solutions of the first order approximation we find:

- For external store separation from a wing, the outer limit relates to axisymmetric flow over an equivalent body of revolution of twice the cross-sectional area of the store.
- In Phase 2 and 3 of separations from an infinite-span cavity, the far flow field is three-dimensional and corresponds to a dipole distribution along the body axis.

For separations from a finite-span cavity our analysis shows:

- In the inner asymptotic region, the finite-cavity span effect is second order with respect to the ratio of the body radius to the cavity span. Therefore, it is small for wide cavities.
- The cavity span effect is dominant in the far field asymptotic behavior of the inner solution. This effect determines one type of outer flow.
- The far flow field is induced by sources distributed along the store axis. The source intensity is proportional to the ratio of the body radius to the cavity span.

We analyzed outer limits for the inner solutions in the second- and third order approximations with respect to the small parameter δ^2 and showed that

- In the region $r \sim l_0/S$, unsteady terms of the second-order potential can be of the same order of magnitude (or even dominant) as the dominant terms of the first-order potential. In the case of a finite-span cavity, the far-field asymptotics are axisymmetric. In the case of the infinite-span cavity, they are three-dimensional.
- For unsteady flows, a thin structure of the far field can be rather complicated and depend on the relationship between the Strouhal number and the body radius.
- If unsteady effects are small, then the higher-order asymptotics have the form of potential induced by sources (in the case of a finite-span cavity) or by dipoles (in the case of an infinite-span cavity).
- For infinite-span cavities, the source term is $O(\delta^6 \ln \delta)$ in the far field. It is negligibly small compared with the source term for finite-span cavities, which is $O(a_0/d_0)\delta^2 \ln \delta$.

Using the asymptotic theory [6] and the results of Parts 2 and 4, we formulated the matching conditions for the inner and outer solutions in the case of a body of revolution separating from a cavity into the outer transonic freestream. For Phases 2 and 3, quasi-steady regimes are discussed in detail. In these cases, the outer flow corresponds to transonic flow over an equivalent body of revolution. We obtain explicit functional forms of the equivalent body as functions of time and the dimensionless cross-section area. The latter continuously grows with time from a small value of the order of ε (in Phase 2) to $O(1)$ in Phase 3. Typical examples of the equivalent body shape are provided.

Analyzing the flow equations in the outer asymptotic region we identified typical flow regimes relevant to different ratios $\bar{S} = S/\delta^2$, where S is the Strouhal number and δ^2 is characteristic scale of flow perturbations. For unsteady problems, we established the presence of the intermediate asymptotic region governed by the linear equations of acoustics. A detailed study of this regime is needed to identify solutions relevant to the

nonlinear transonic case. A thin "boundary layer" structure of the outer asymptotic region is exhibited due to disparate time scales inherent in the separation process.

We believe that for many practical applications, the transonic wave drag can be evaluated in the framework of the quasi-steady regime, since short-time effects are averaged out over the long-time scale relevant to the outer transonic expansion, and their contribution to the wave drag force can be neglected. Our analysis shows that the wave drag monotonically increases during transition from Phase 2 to Phase 3 (as the body moves away from the slip surface). Its value grows from $O(\epsilon\delta^+)$ to $O(\delta^+)$.

The base and friction drags were evaluated using known theoretical results and empirical correlations. The wave drag was calculated by integrating the outer pressure along the equivalent body axis. For Phases 2 and 3, the pressure drag was expressed in closed form using the inner pressure distribution on the body surface obtained in Part 2. We calculated different components of this drag and discussed their behavior.

Using the results of Parts 2 and 4 we developed a FORTRAN code that couples the solver of the trajectory equations with the transonic code of Malmuth for the Karman-Guderley equation. The computational package allows for prediction of 3-DOF trajectories for transonic store separations.

Our parametric studies of 3-DOF body trajectories indicate that the body motion may be rather complicated, including such phenomena as ricochet and/or re-contact. The body trajectory is very sensitive to release conditions: for example, initial vertical speed and pitch angle. When critical initial pitch angles and vertical speeds are exceeded, ricochet/re-contact is possible.

We have shown that stores can easily separate from flat walls. Here, re-contact occurs only at small initial speeds. Our studies also indicate that a body thickness variation (from D_0 to $3D_0$) does not lead to the re-contact.

In contrast, store separation dynamics is more complicated from a cavity. Above the initial critical pitch angle or below the critical initial vertical speed, the body does not cross the slip surface and returns to the cavity. With increasing horizontal displacement and pitch angle, collision with the upstream and downstream cavity walls is possible. Near the critical conditions, the body can remain at a small distance from the shear layer for a long time period. It also may partially return to the cavity interior. If the horizontal displacement during this time period is larger than the cavity length, contact with the upstream cavity wall is possible; otherwise, the store slowly separates.

Our calculations indicate that store separation can be controlled effectively by the release mechanism. Our modeling can help design ejection units and thrust motors for stage separation. It allows for evaluation of thrust and weight required for these units, and indicates how to avoid adverse re-contact with a relatively small impulse.

4.11 Illustrations

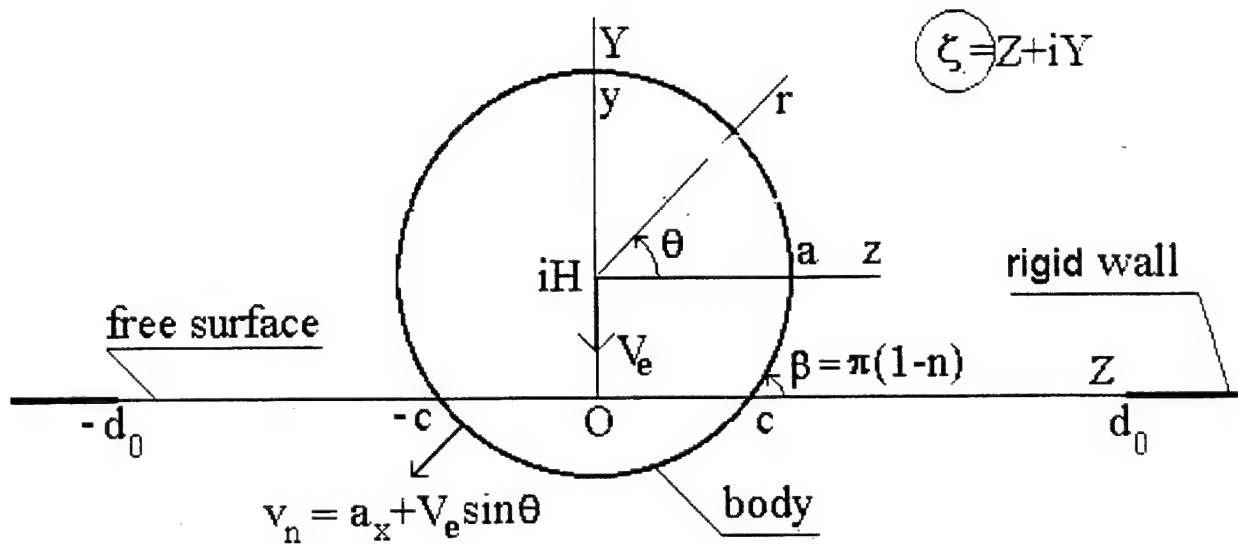


Fig. 4.1 Cross-flow scheme in Phase 2 (body passes slip surface).

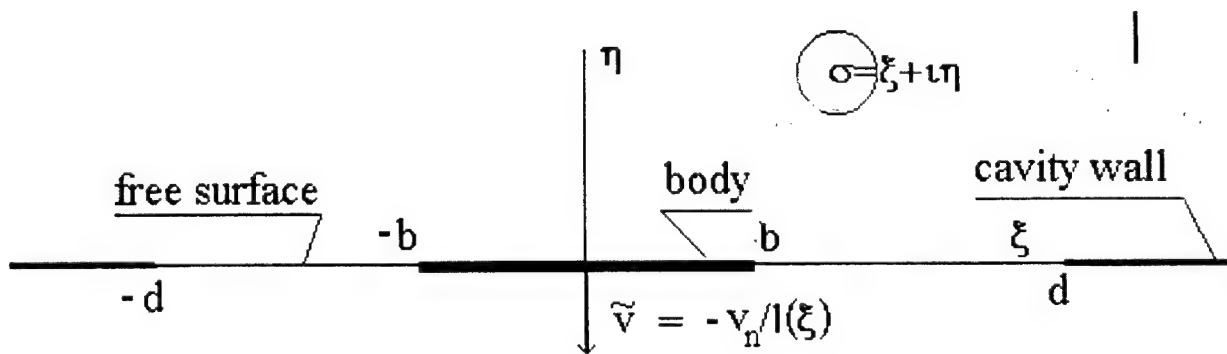


Fig. 4.2 Cross-flow scheme in the transformed plane.

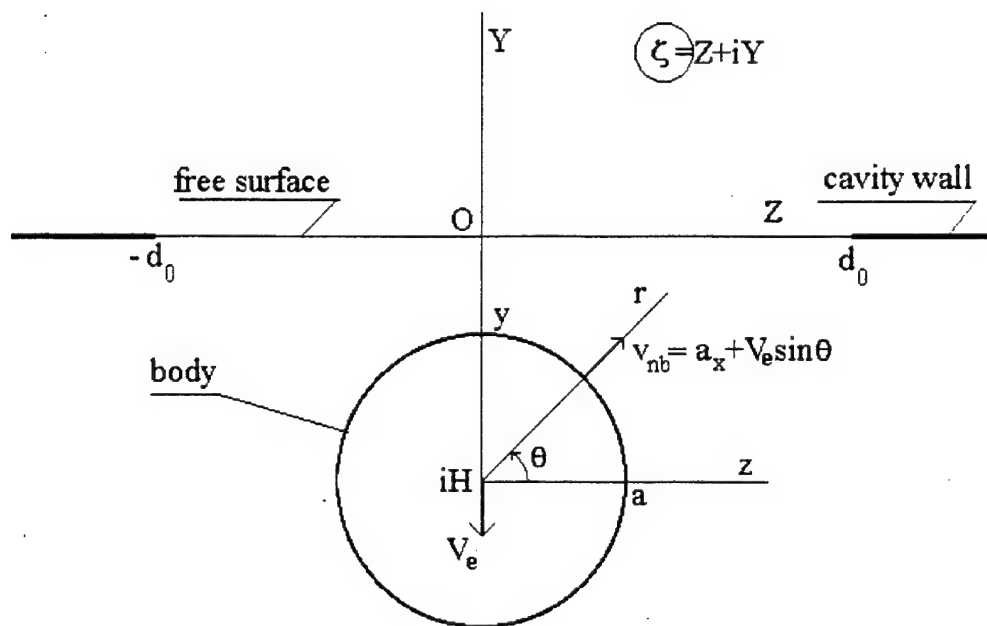


Fig. 4.3 Cross-flow scheme in Phase 3: body is outside the cavity.

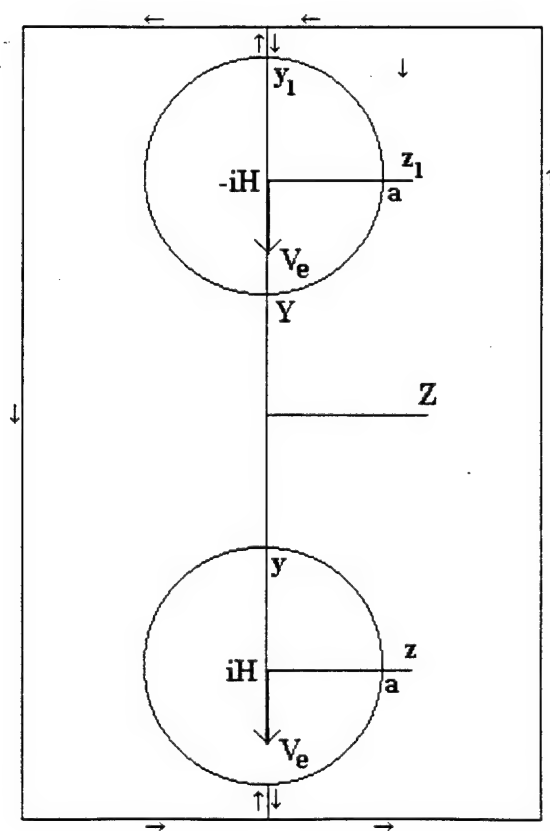


Fig. 4.4 Two circles moving in unbounded stream and integration contour.

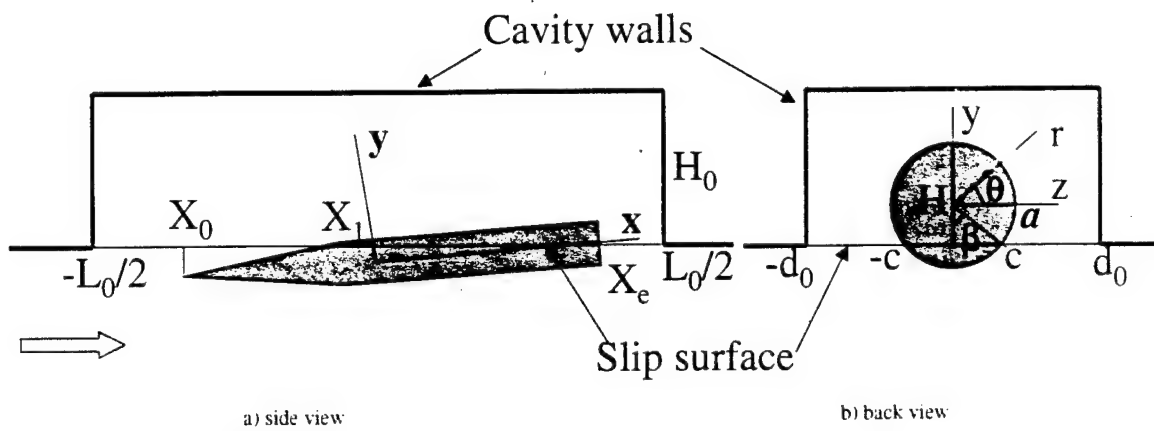


Fig. 4.5 Typical body locations with respect to the slip surface: the body nose is in outer stream.

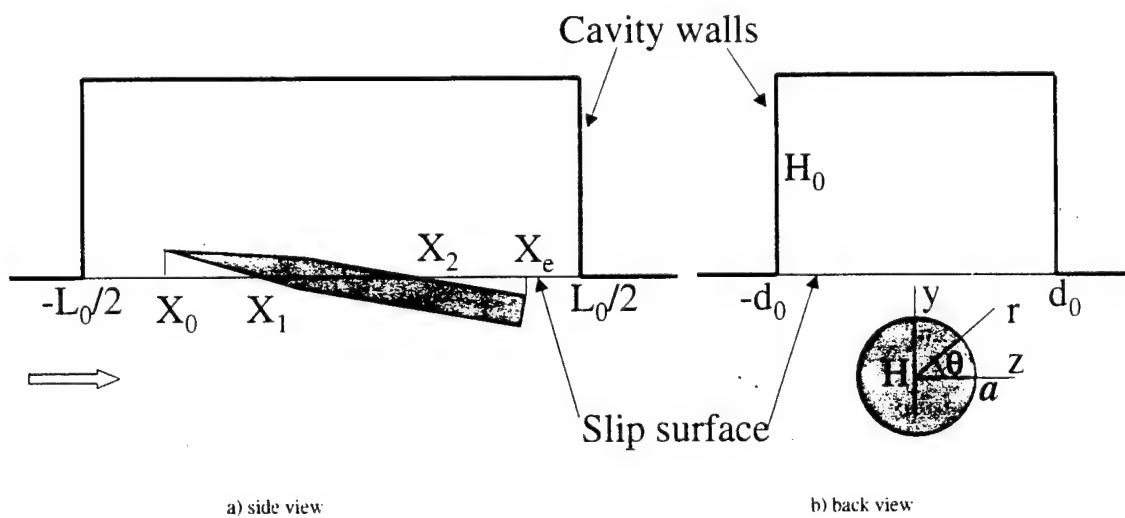


Fig. 4.6 Typical body locations with respect to the slip surface: the body tail is in outer stream.

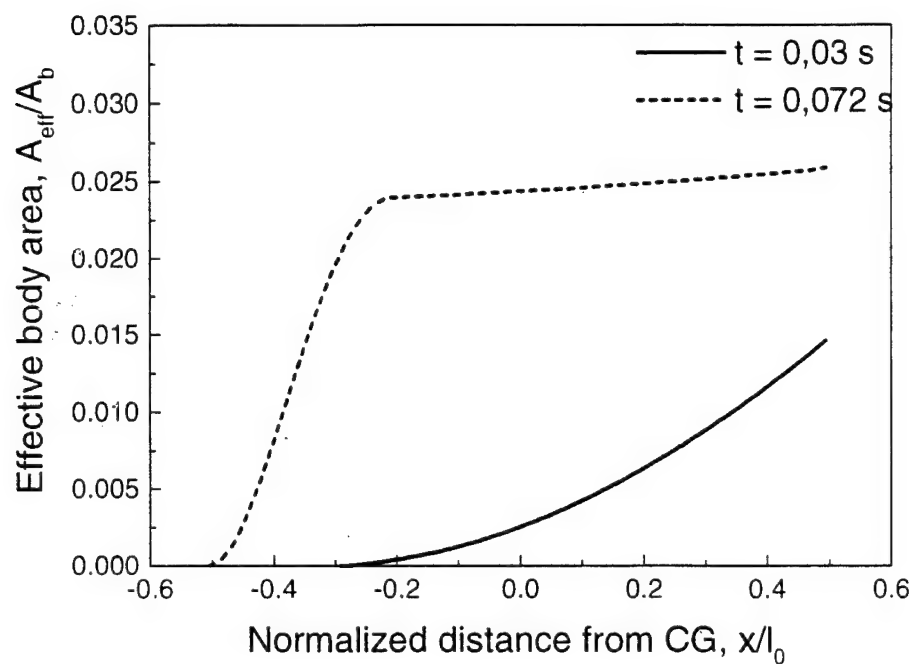


Fig. 4.7 Typical area distributions of the effective body in Phases 2 and 3.
Initial conditions: $Y_0 = 1$ in, $V_0 = 10$ ft/s, $\omega_0 = 200$ deg/s, $\alpha_0 = 0^\circ$.

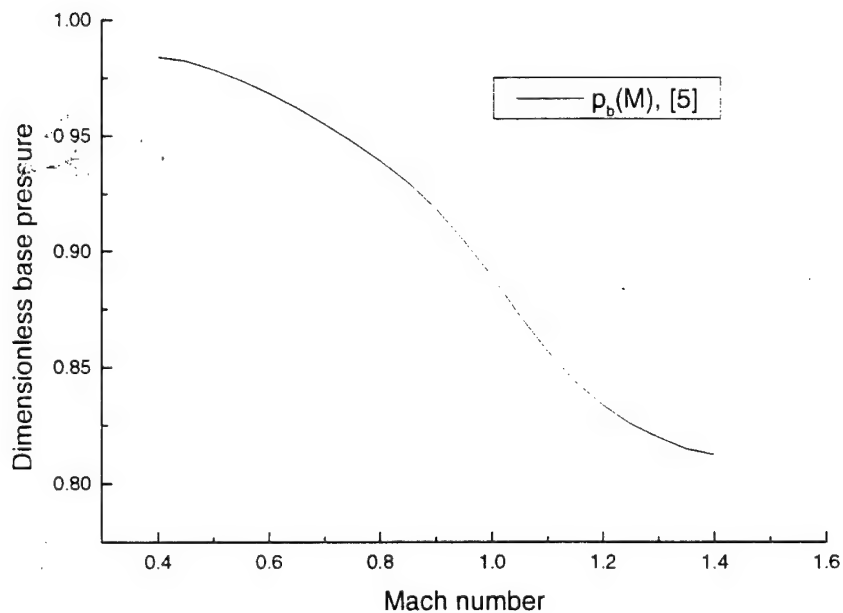


Fig. 4.8 Ogive-cylinder base pressure as a function of Mach number.

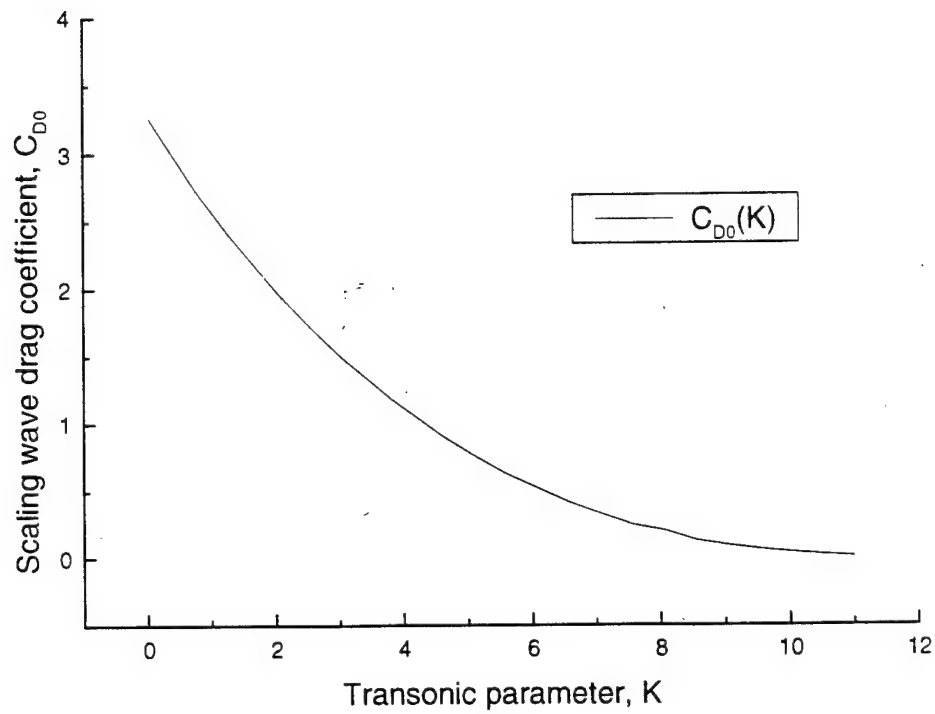


Fig. 4.9 Wave drag scaling for bodies of the B4N2 type.

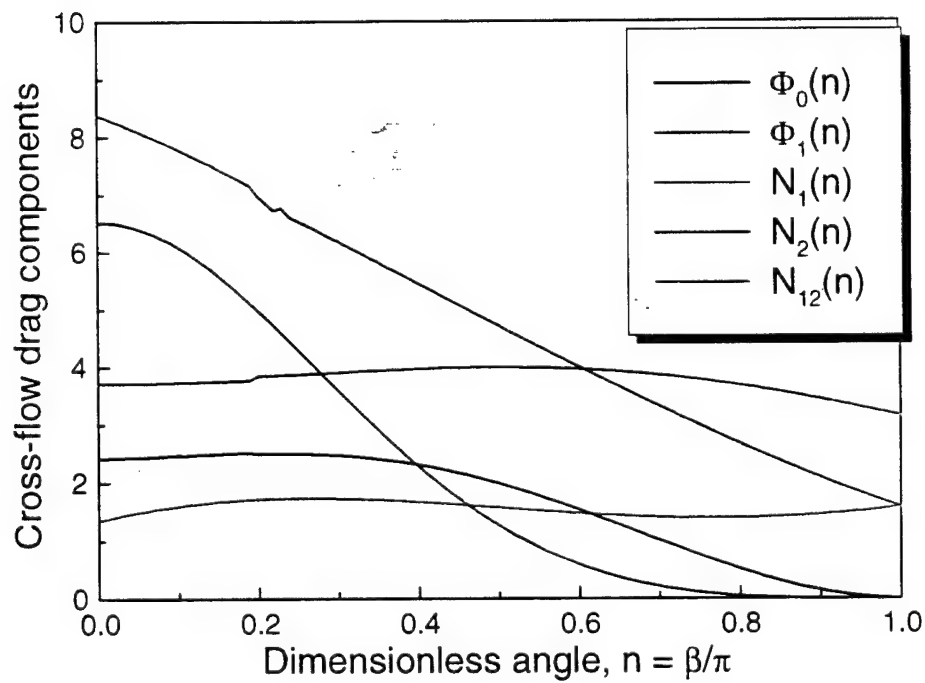
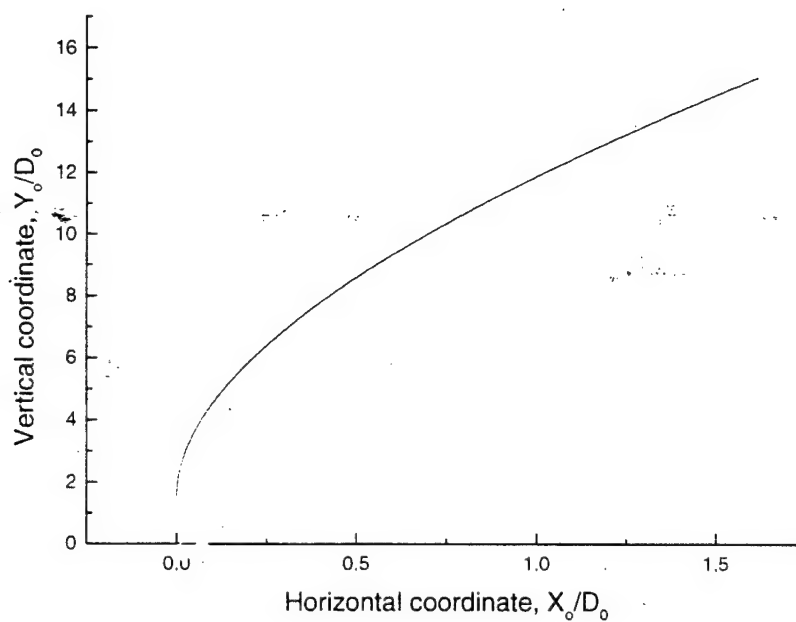
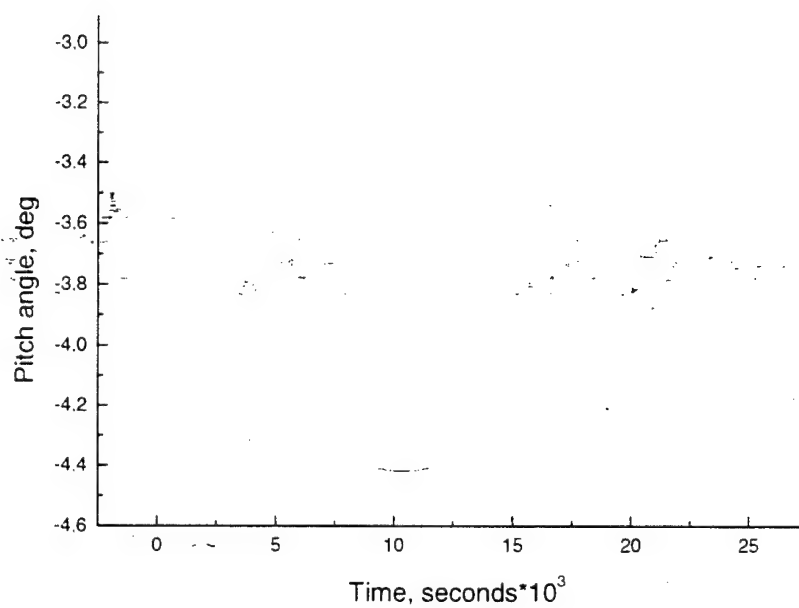


Fig. 4.10 Components of the cross-flow drag.

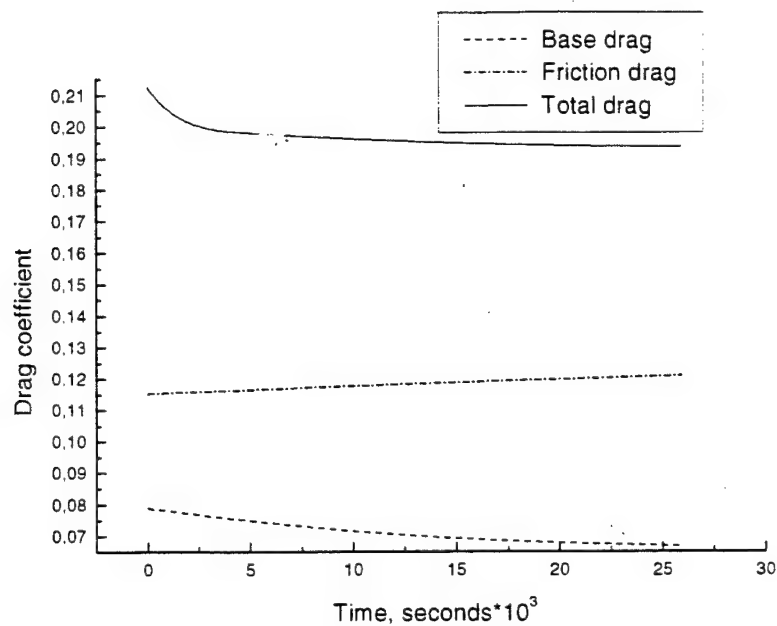


a) CG trajectory

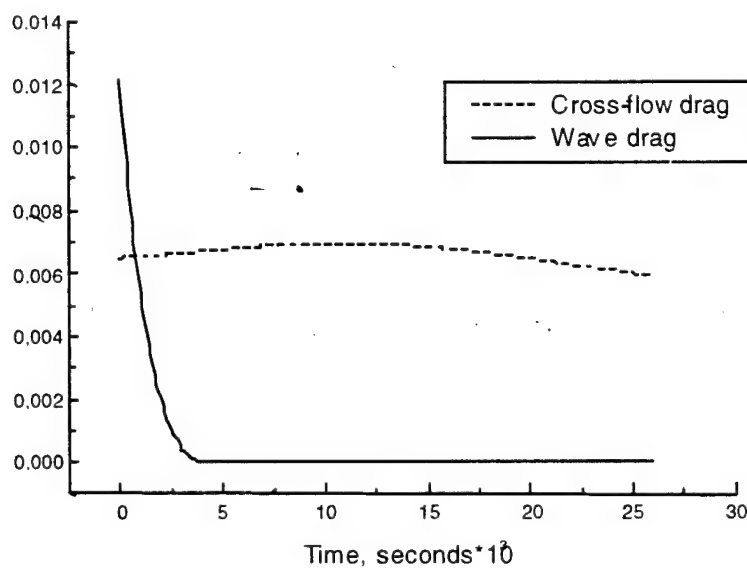


b) Pitch angle history

Fig. 4.11 Trajectory parameters of B4N2 body for the initial conditions: $Y_0 = -0.975$ inch, $V_0 = -9.144$ m/s, $\alpha_0 = -3.3^\circ$, $\omega_0 = -200$ deg/s.

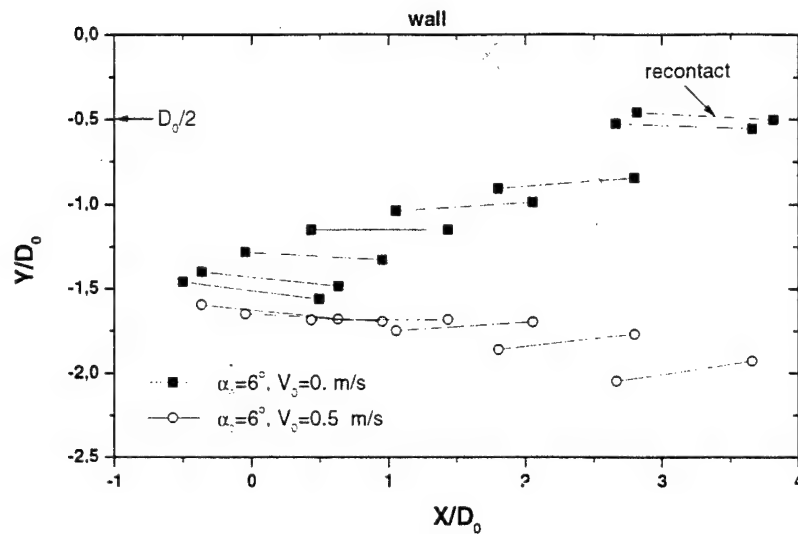


a) Total, friction and base drags

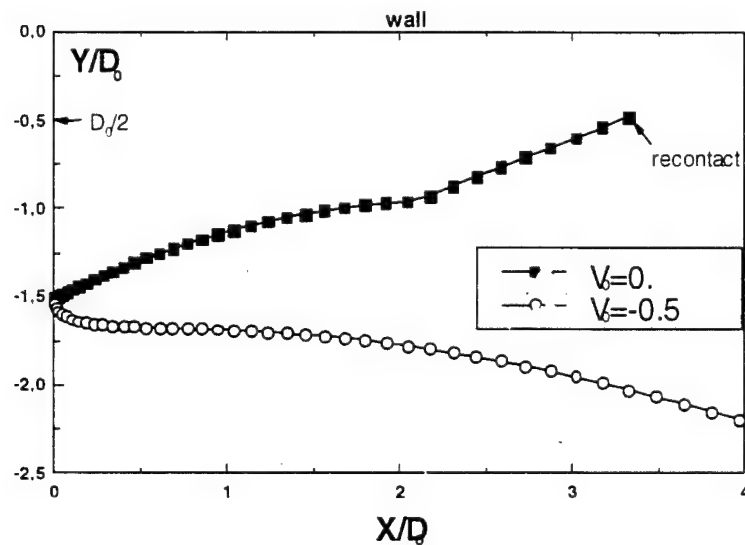


b) Cross-flow and wave drags

Fig. 4.12 Histories of drag components for B4N2 body for the initial conditions:
 $Y_0 = -0.975$ inch, $V_0 = -9.144$ m/s, $\alpha_0 = -3.3^\circ$, $\omega_0 = -200$ deg/s.

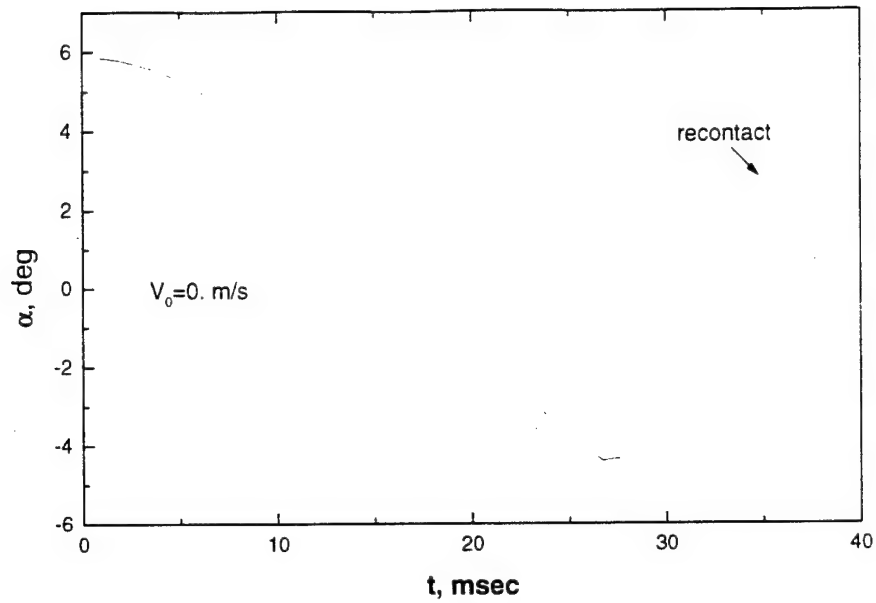


a) Locations of the body axis at various initial vertical speeds

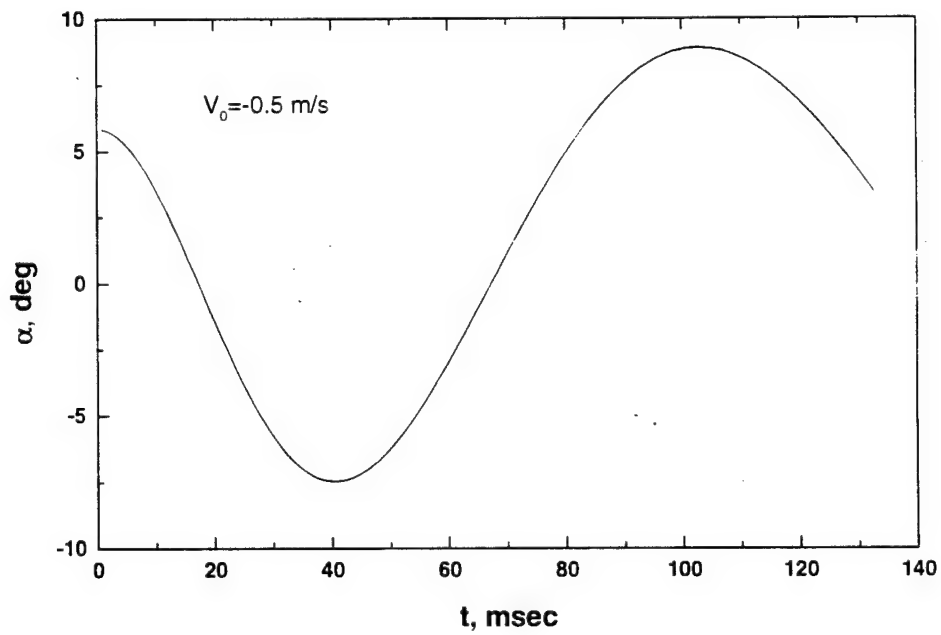


b) Trajectory of center of inertia

Fig. 4.13 Trajectories of the body axis and center of gravity for the initial conditions:
 $\omega_0 = 0$, $Y_0 = -1.95$ inch; $\alpha_0 = 6^\circ$.



a) $V_0 = 0 \text{ m/s}$.



b) $V_0 = 0.5 \text{ m/s}$

Fig. 4.14 Pitch angle history for the initial conditions: $\omega_0 = 0$, $Y_0 = -1.95 \text{ inch}$; $\alpha_0 = 6^\circ$.

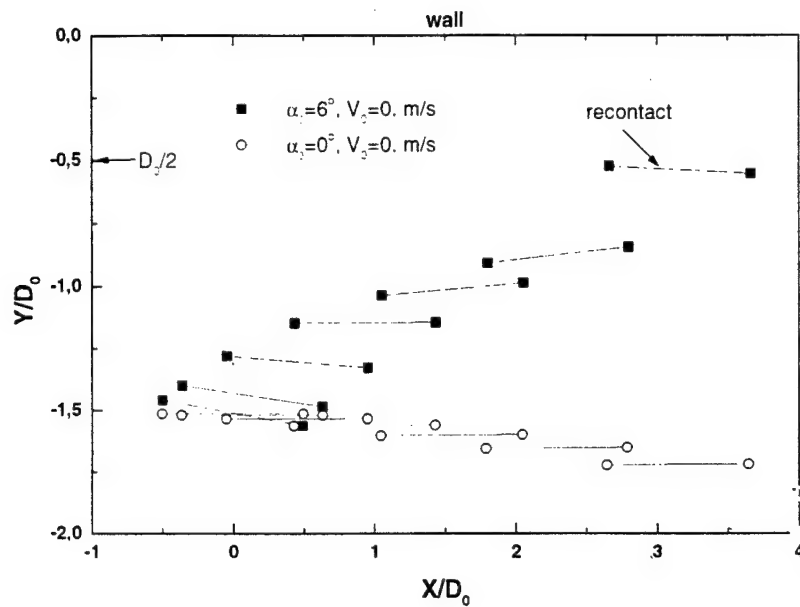
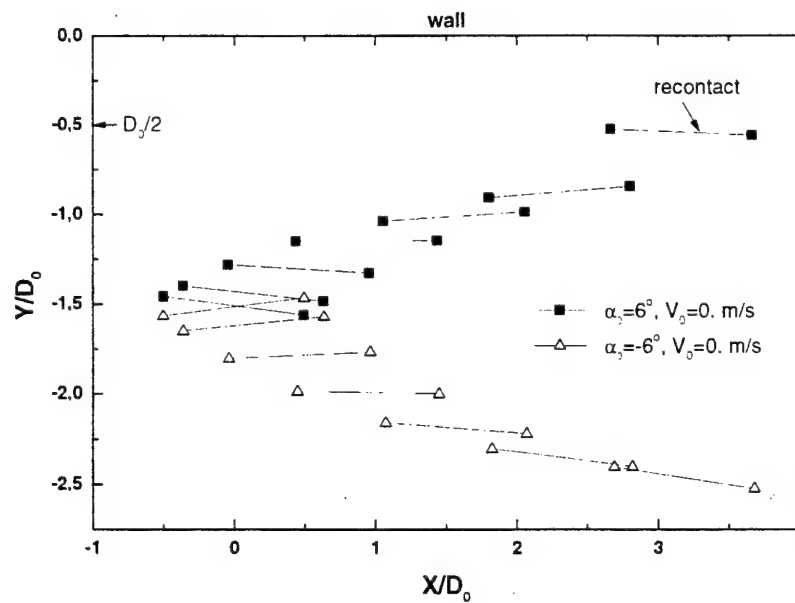
a) $\alpha_0 = 0^\circ, 6^\circ$ b) $\alpha_0 = 6^\circ, -6^\circ$

Fig. 4.15 Locations of the body axis at various initial angles of attack: $\omega_0 = 0$, $Y_0 = -1.95$ inch, and $V_0 = 0$.

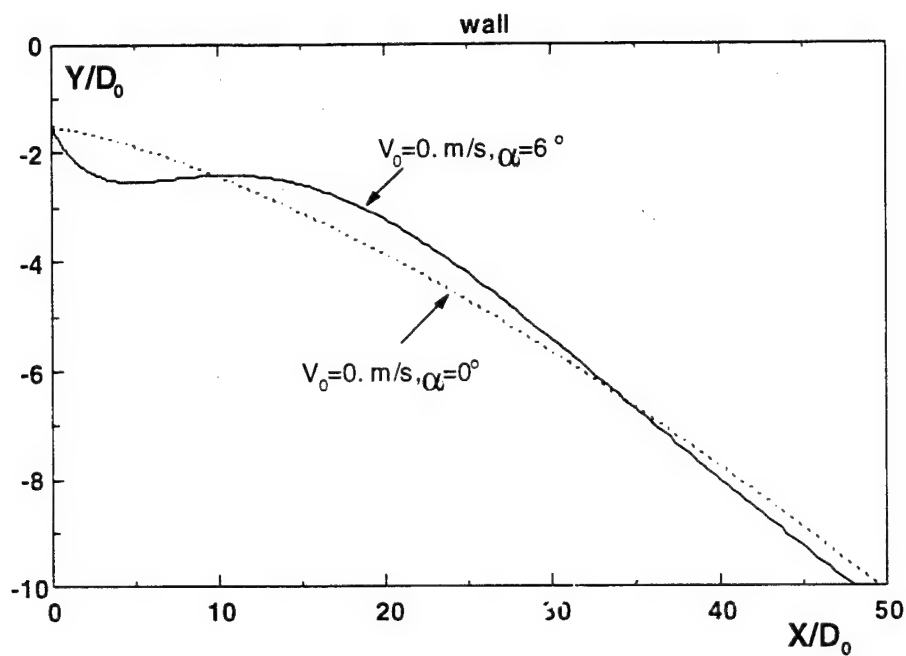
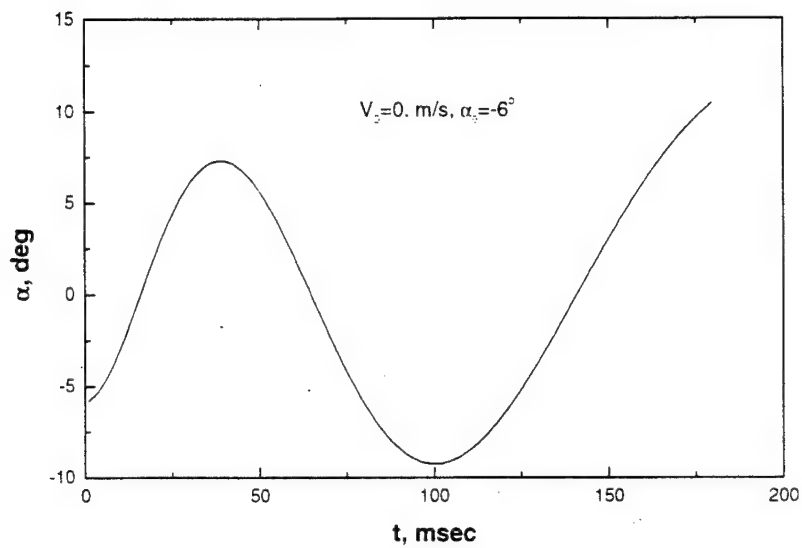
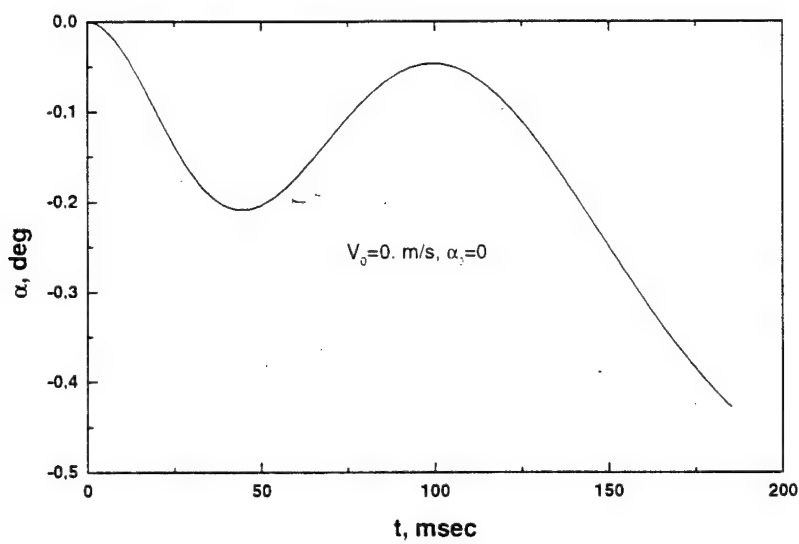


Fig. 4.16 CG trajectories for the initial pitch angles $\alpha_0 = 0^\circ, 6^\circ$; $\omega_0 = 0$, $Y_0 = -1.95$ inch, and $V_0 = 0$.

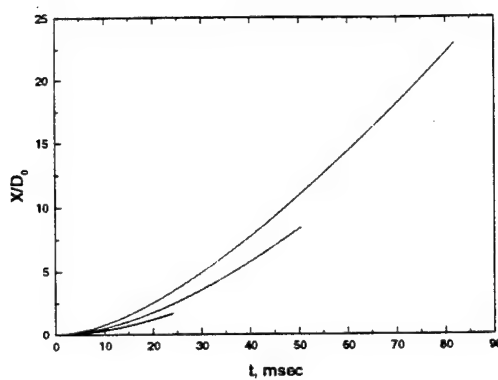


a) $\alpha_0 = -6^\circ$

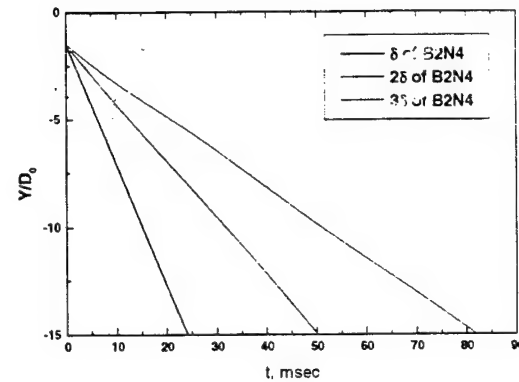


b) $\alpha_0 = 0^\circ$

Fig. 4.17 Pitch angle history for the initial conditions: $\omega_0 = 0$, $Y_0 = -1.95$ inch, and $V_0 = 0$.

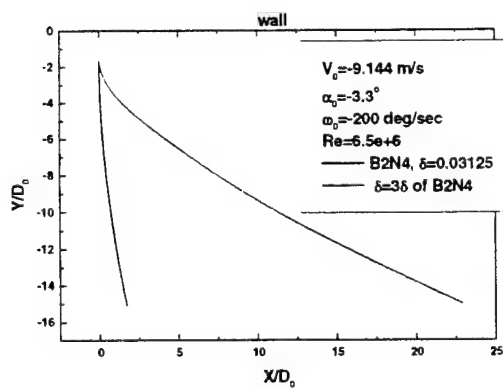


a) Horizontal evolution of the CG;

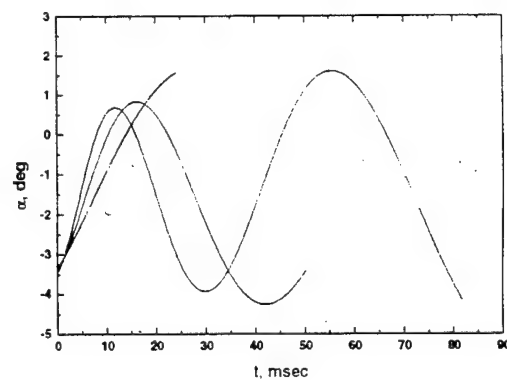


b) Vertical evolution of the CG;

Fig. 4.18 Center of gravity evolution for bodies of different radii: $M = 0.999$,
 $V_0 = -9.144 \text{ m/s}$, $\alpha_0 = 3.3^\circ$, $\omega_0 = 200 \text{ deg/s}$.



c) CG trajectories;



d) Pitch angle histories

Fig. 4.19 Body thickness effect on store trajectory characteristics: $M = 0.999$,
 $V_0 = -9.144 \text{ m/s}$, $\alpha_0 = 3.3^\circ$, $\omega_0 = 200 \text{ deg/s}$.

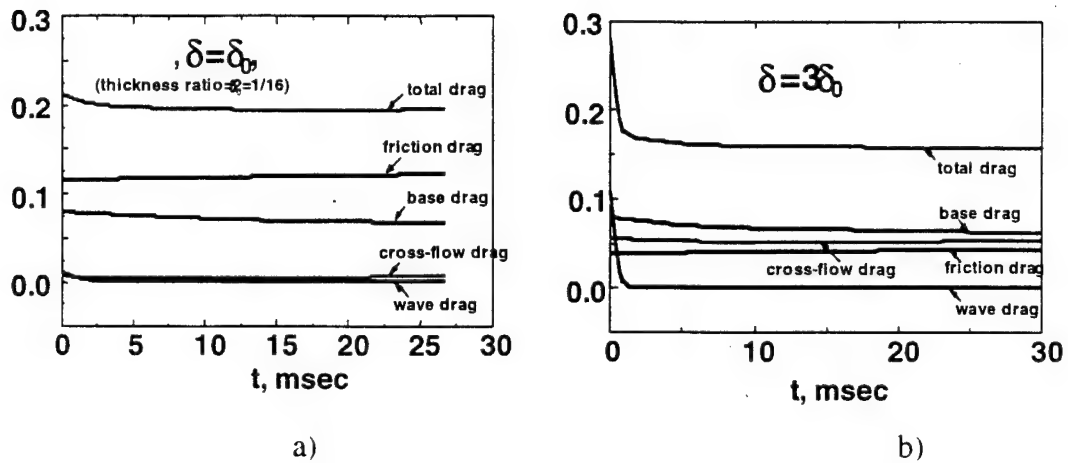
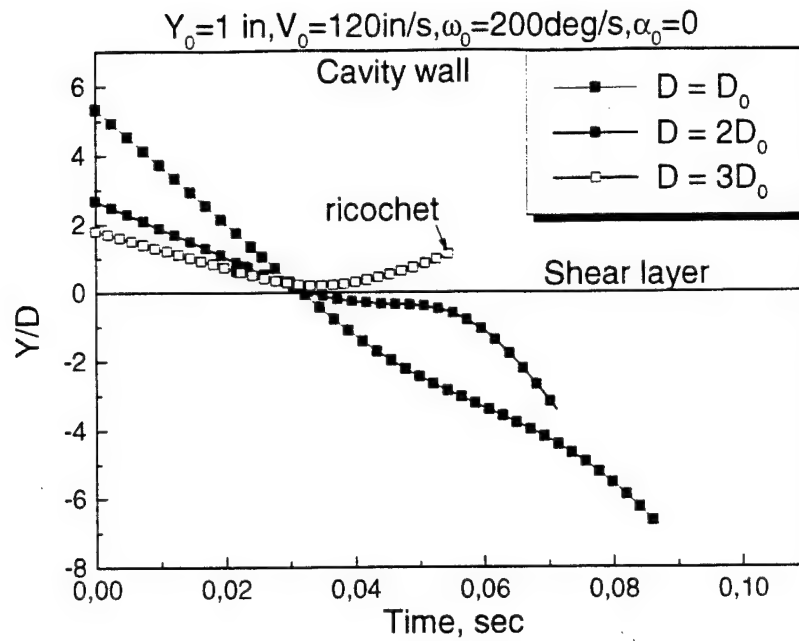
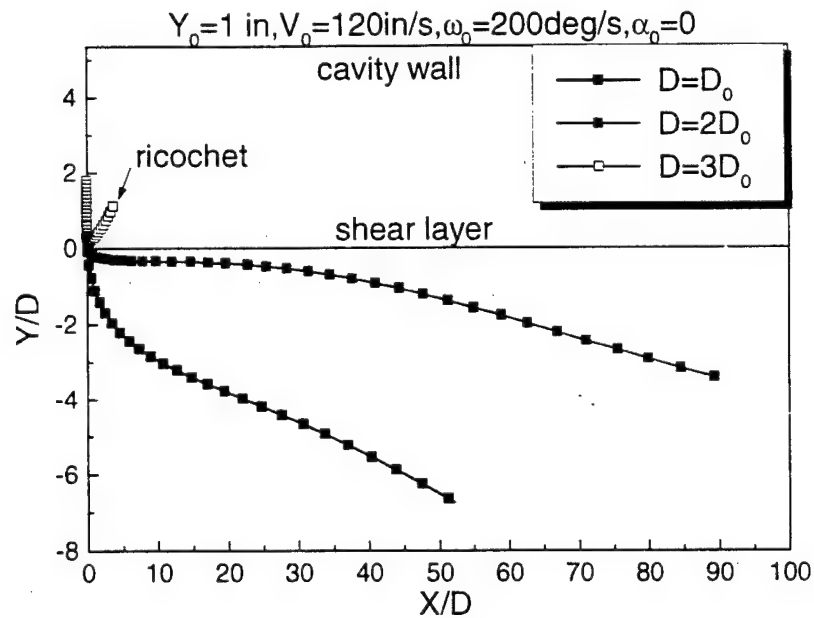


Fig. 4.20 Histories of drag components for bodies of various thickness; $M = 0.999$,
 $V_0 = -9.144$ m/s, $\alpha_0 = 3.3^\circ$, $\omega_0 = 200$ deg/s.



a) Time histories of the vertical CG coordinate



b) Trajectories of CG

Fig. 4.21 CG trajectory parameters for the bodies of various thickness.

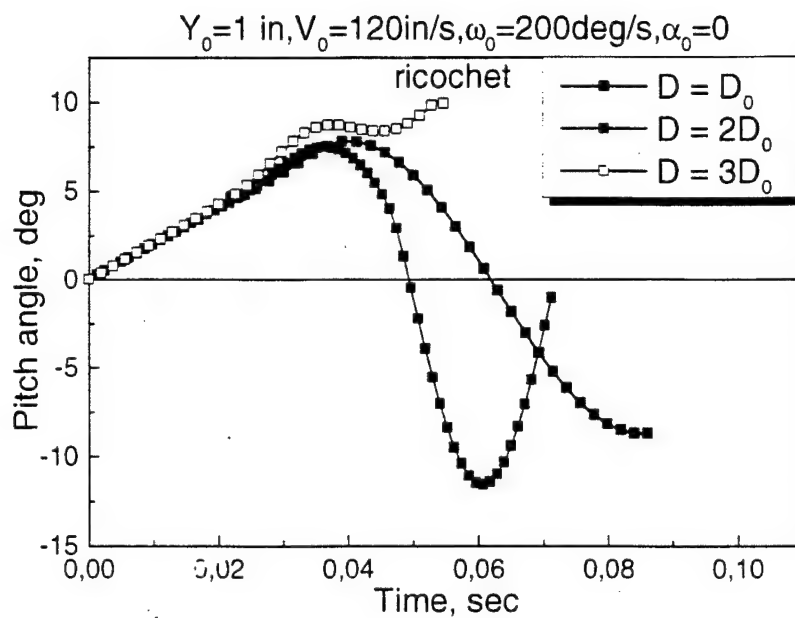


Fig. 4.22 Pitch angle histories for bodies of various thickness.

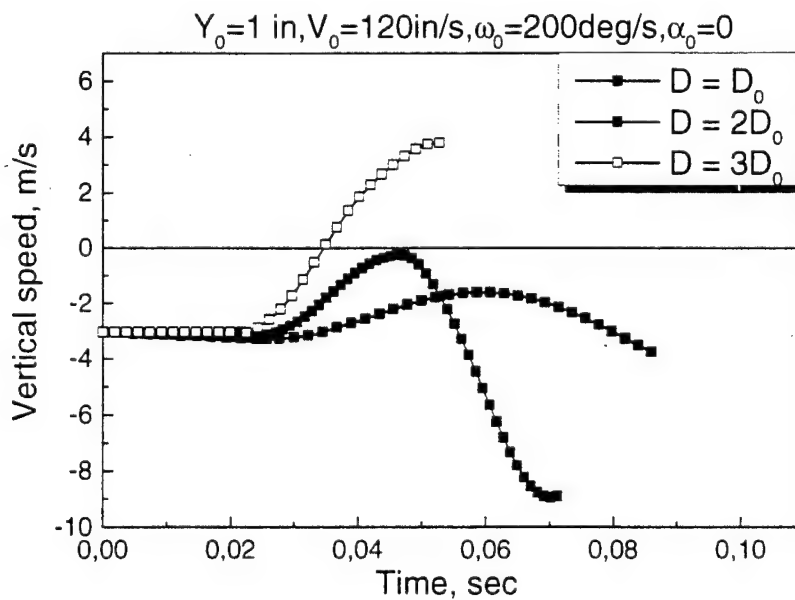


Fig. 4.23 Vertical speed for bodies of various thicknesses.

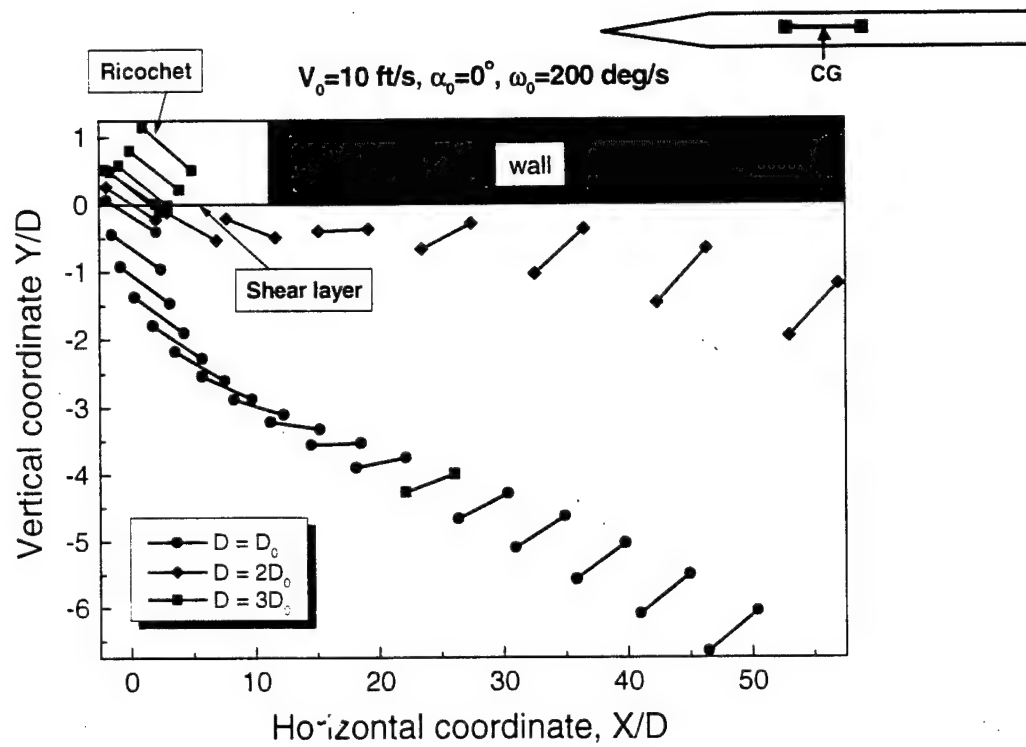


Fig. 4.24 Centerline trajectories for different bodies.

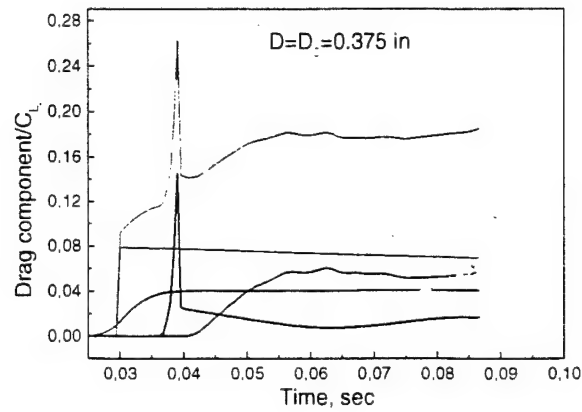
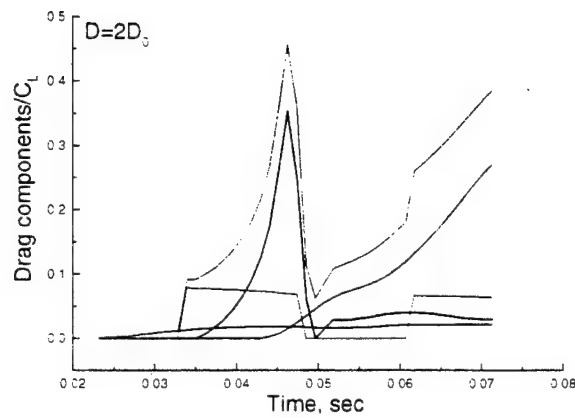
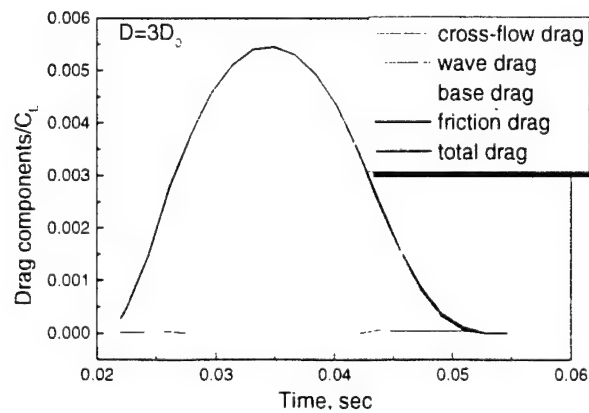
a) $D = D_0$ b) $D = 2D_0$ c) $D = 3D_0$

Fig. 4.25 Histories of drag components for bodies of different diameters.

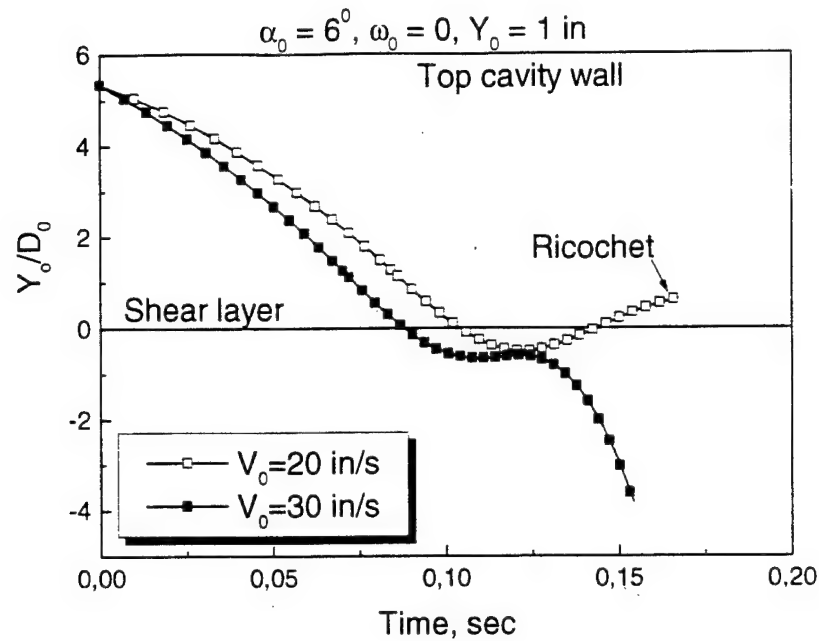


Fig. 4.26 Time histories of vertical CG coordinate at $V_0 = 20$ and 30 inch/s .

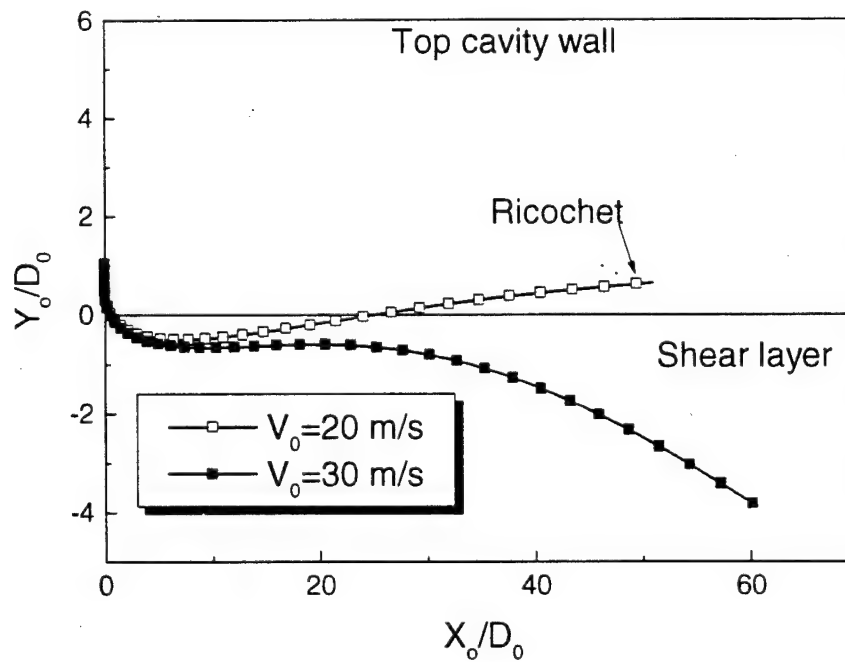


Fig. 4.27 CG trajectories at $V_0 = 20$ and 30 inch/s .

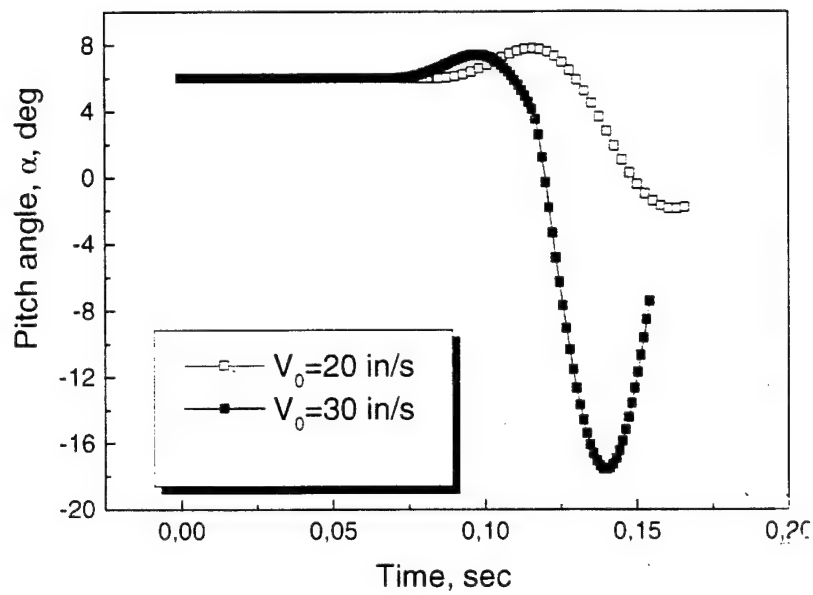


Fig. 4.28 Pitch angle evolution at $V_0 = 20$ and 30 inch/s.

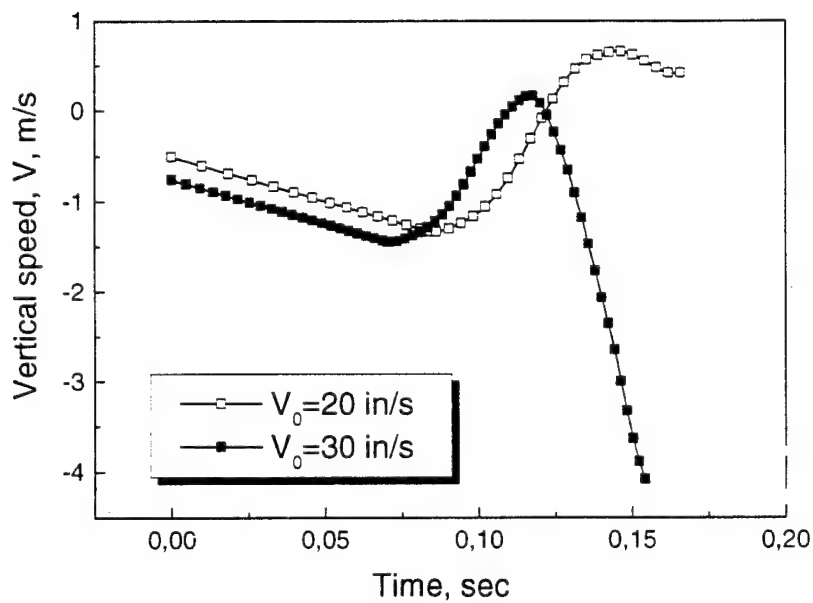


Fig. 4.29 Evolution of CG vertical speed at $V_0 = 20$ and 30 inch/s.

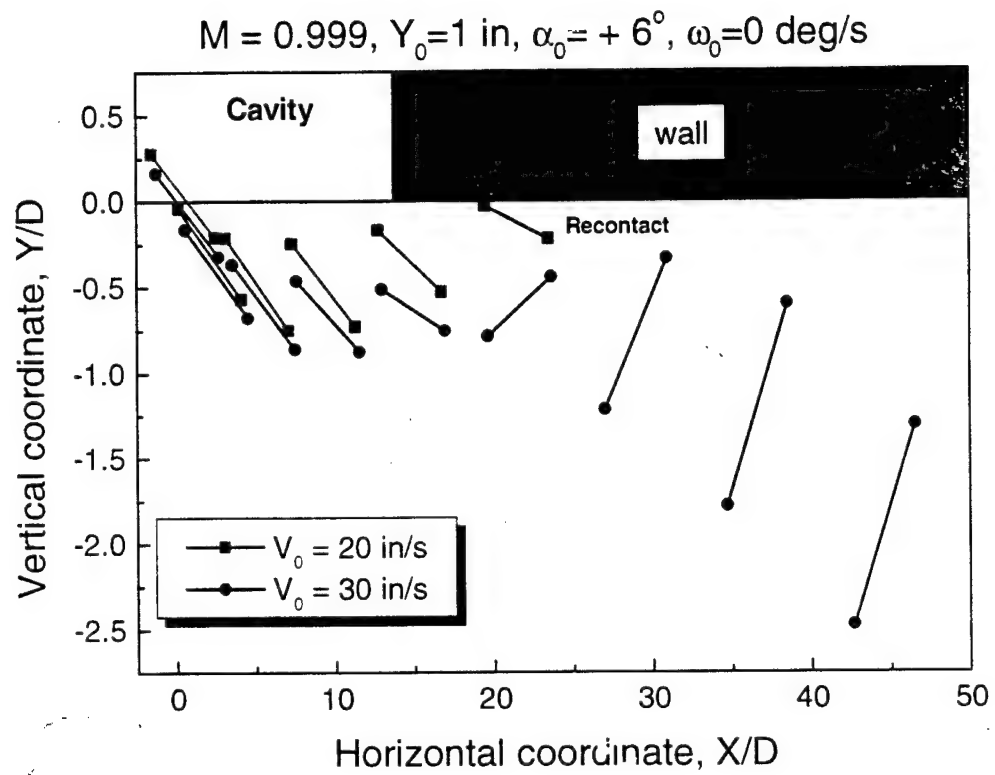


Fig. 4.30 Centerline trajectories at $V_0 = 20$ and 30 inch/s .

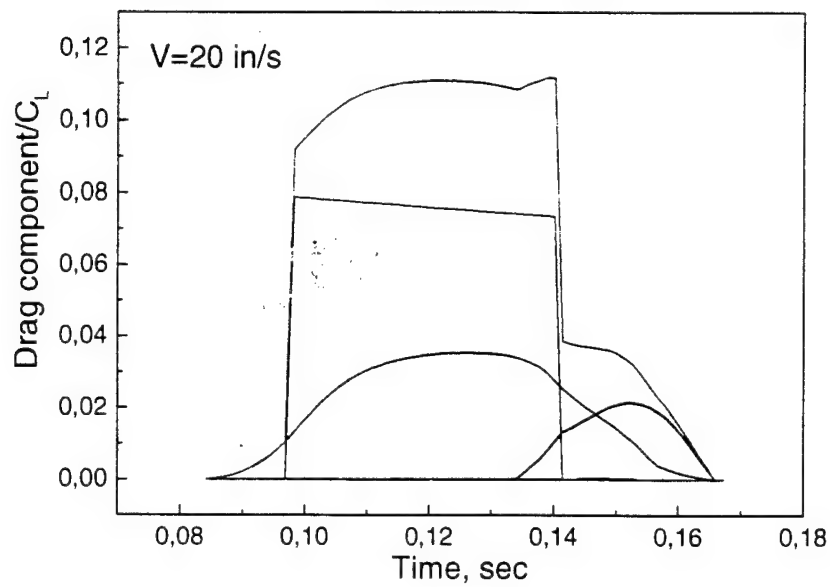
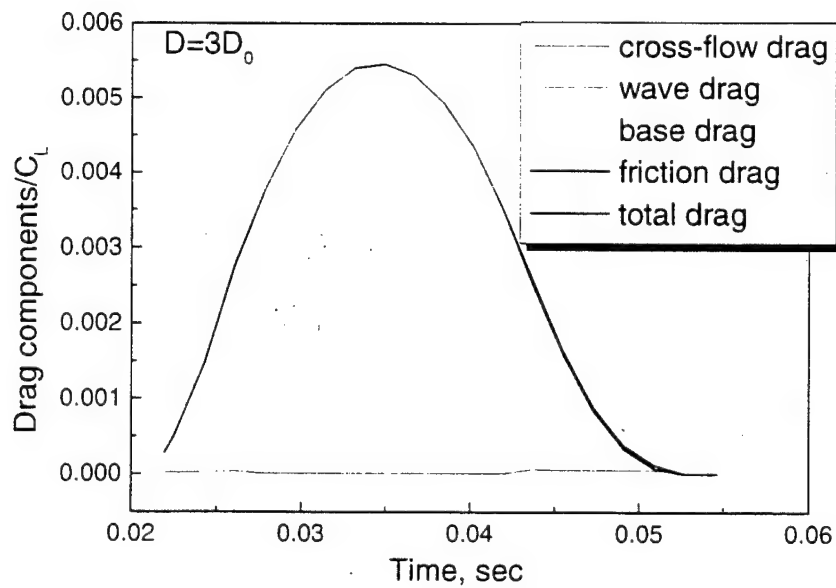
a) $V_0 = 20$ m/sb) $V_0 = 30$ m/s

Fig. 4.31 Evolution of drag components.

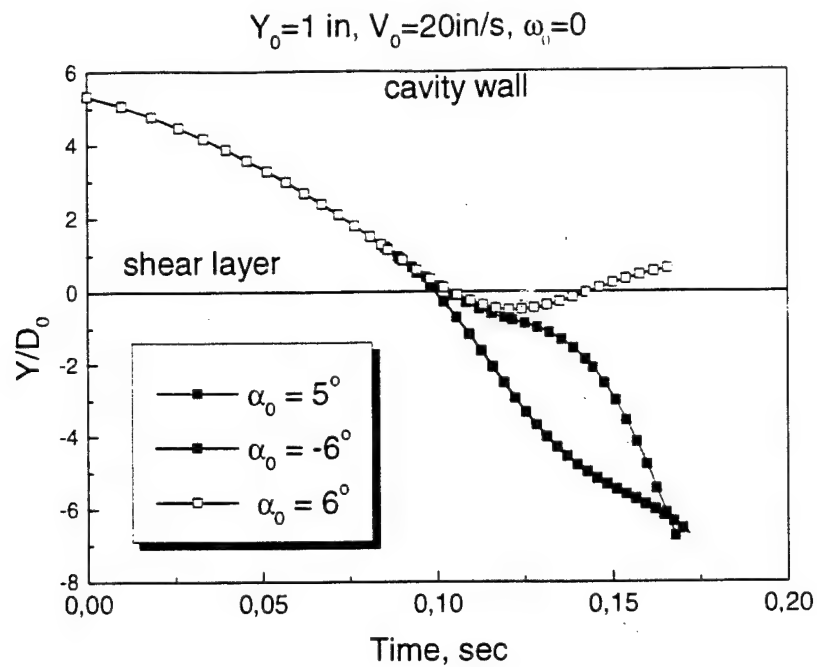


Fig. 4.32 CG vertical coordinate histories at various initial angles of attack.

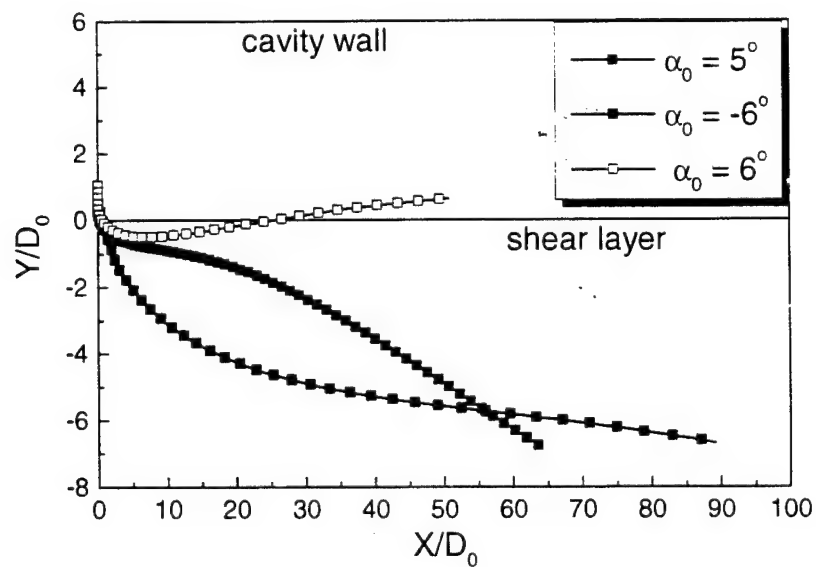


Fig. 4.33 CG trajectories at various initial angles of attack; $Y_0 = 1 \text{ inch, } V_0 = 20 \text{ inch/s, } \omega_0 = 0$.

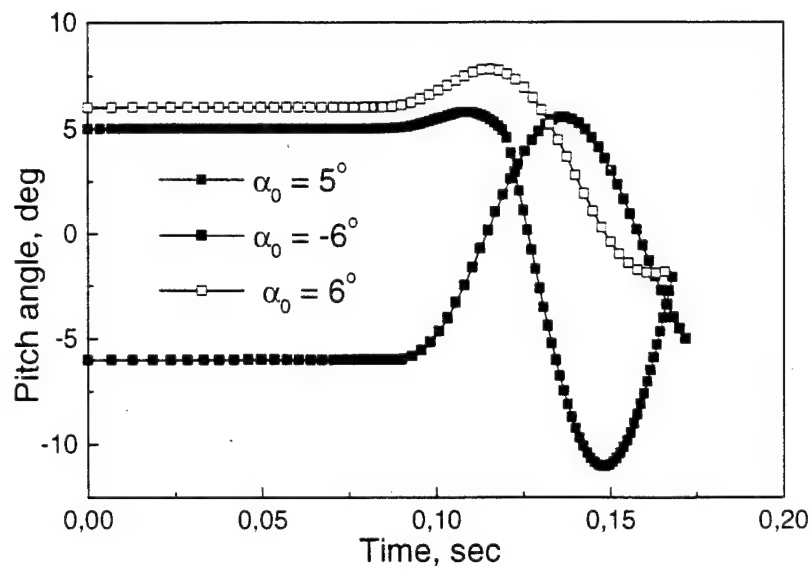


Fig. 4.34 Pitch angle histories at various initial angles of attack: $Y_0 = 1$ inch.
 $V_0 = 20$ inch/s. $\omega_0 = 0$.

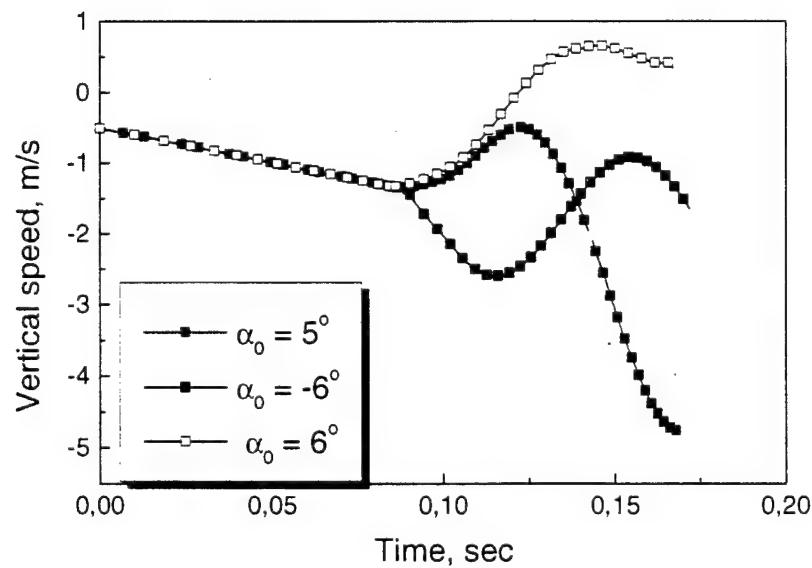


Fig. 4.35 CG vertical speed histories at various initial angles of attack: $Y_0 = 1$ inch.
 $V_0 = 20$ inch/s. $\omega_0 = 0$.

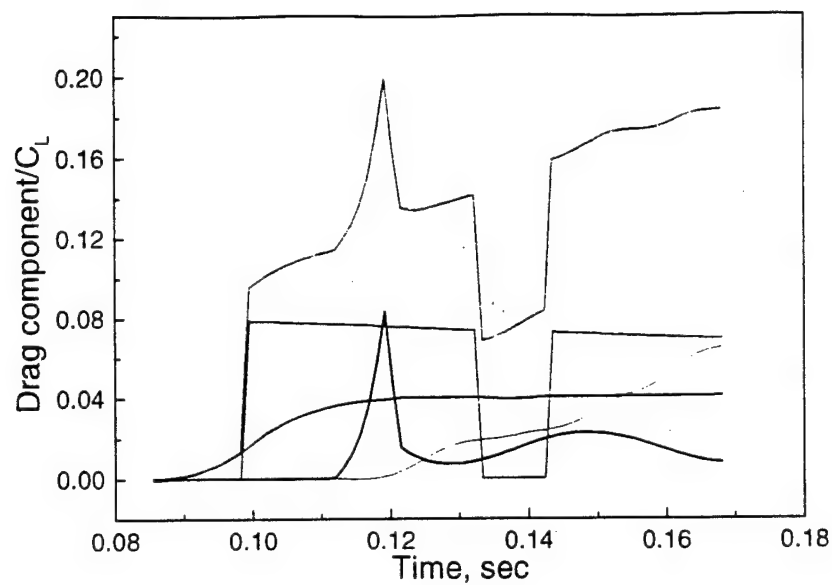
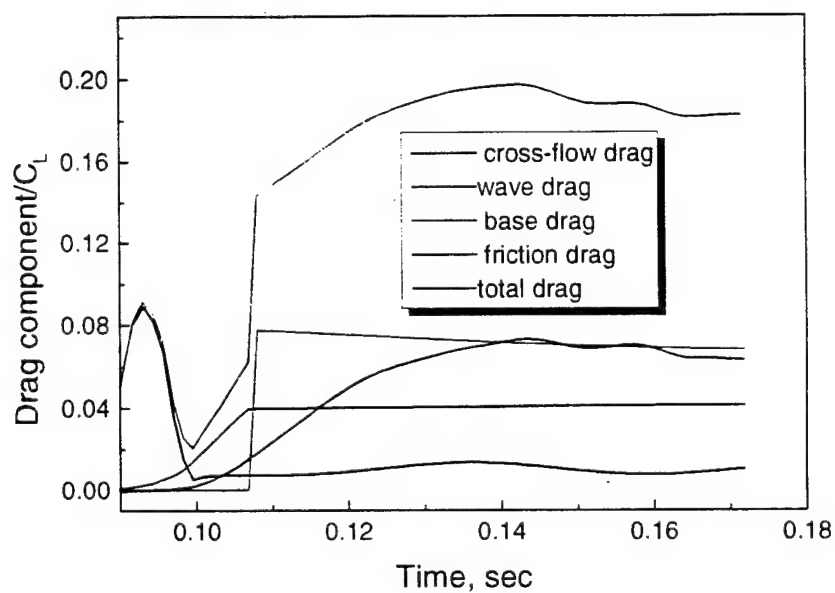
a) $\alpha = 5^\circ$ b) $\alpha = -6^\circ$

Fig. 4.36 Histories of drag components at $\alpha = 5^\circ$ and $\alpha = -6^\circ$; $Y_0 = 1$ inch, $V_0 = 20$ inch/s, $\omega_0 = 0$.

Summary

This report considers aerodynamic and dynamic problems associated with separation of slender bodies of revolution from rectangular cavities into subsonic/transonic stream. Analyses of the aerodynamic problems are based on slender body theory. The inner and outer asymptotic flow regions were analyzed using combined analytical and numerical methods. Asymptotic analyses allowed us to highlight lumped parameters controlling the separation process and split the problem into a series of simpler unit tasks that were solved analytically for a majority of practical cases. The analytical results substantially simplify solving the store dynamic equations. They were used to develop fast and robust numerical codes to predict 2-DOF and 3-DOF store trajectories. The computational package was verified by comparisons with the subsonic wind tunnel experiments of IIT. Parametric studies of store separation into a transonic freestream emphasized critical regimes relevant to store re-contact and ricochet.

In Part 1, we formulated the inner asymptotic problem. The body separation process was treated as a sequence of the three phases: in Phase 1, body is inside the cavity; in Phase 2, body crosses the shear layer; in Phase 3, body is outside the cavity in the outer stream. We showed that for many practical cases the cavity sidewall effects can be neglected. This allowed us to decompose the inner problem into unit problems:

- 1) Body drops from a flat wall to fluid at rest (Phase 1) or to the external stream (Phase 3);
- 2) Body crosses the slip surface (Phase 2);
- 3) Body drops toward the slip surface (Phase 1) or away from the slip surface (Phase 3).

The first problem was solved analytically by rapidly convergent series. The second and third problems are more complicated because they include effects of the body interaction with the free slip surface. To obtain their analytical solutions and provide insight into the slip surface effect on the near-field flow, we analyzed the case of small slip-surface displacements using perturbation theory. In the dominant approximation, we derived a system of linear integrodifferential equations that we solved numerically by an iterative scheme. In the first iteration step therein, the slip surface was treated as a flat plane of zero potential, and the near field solution was expressed analytically. We showed that the slip-surface shape is governed by Poisson equation in the two-dimensional space of streamwise coordinate and time. The forcing term of this equation provides direct coupling of the slip-surface displacement with the body motion. Results of our analyses contrast with those for two-dimensional flows. Our results indicate that, in contrast to classical slender body theory, the inner solution exhibits a global behavior. The nonlinear equations were derived for the general case where the slip-surface perturbations are not small. These analytical studies simplified the modeling of the slip surface effect in determining aerodynamic forces and moments acting on the store in all phases of the separation process.

In Part 2, we obtained analytical solutions of the dominant approximation problems relevant to separation of a thin body of revolution from a rectangular cavity adjacent to a uniform flow. For Phases 1 and 3, we used multipole expansions that allowed us to derive compact expressions for the pressure on the body surface and the cross-sectional lift. For Phase 2, the solution was obtained by conformal mapping and Cauchy integral representations. The local lift force was also expressed in an explicit form with the introduction of new special functions. We investigated their characteristics analytically and numerically. As contrasted to the two-dimensional problem, the solutions for Phases 2 and 3 include new terms relevant to the body shape variation in the axial direction. These terms lead to qualitatively new features of the slip surface and rigid wall effects. For example, in Phase 3 the slip-surface effect is essentially stronger than in Phase 1 because the influence of this boundary decreases inversely with distance from the body. In Phase 2, the flow velocities of the dominant approximation are singular at the line of intersection between the slip surface and the body surface. However, these singularities are integrable. This allows us to calculate the lift force and pitching moment without a detailed analysis of the singular regions. Nevertheless, these singularities should be analyzed in future to treat the higher-order approximations. Our results form a foundation for the development of computationally non-intensive algorithms that predict body trajectories through all separation phases.

In Part 3, 2-DOF dynamics of vertical and pitching motions of thin bodies of revolution separating from a rectangular cavity into an external freestream was discussed. The problem was analyzed using combined asymptotic and numerical methods. Dynamic equations for Phases 1 and 3 were simplified using transonic small perturbation theory and the analytical results of Part 2. This allowed us to integrate them in explicit analytical forms. We showed that in Phase 1, the CG coordinate and pitch angle are very close to parabolic functions of time. In Phase 3, the trajectory parameters oscillate near their mean states, which are, again, almost parabolic functions of time. The analytical solutions allow us to obtain explicit dependencies of the body trajectory parameters on the physical characteristics of the body and freestream. This helps us extract governing parameters and gain insight into the separation process. The results are consistent with the subsonic experiments of IIT [18].

A numerical code predicting the store trajectory for all three phases separation was developed and verified by comparisons with the experimental data [18]. For a majority of the data, the calculations are in good agreement with experiment. Moreover, the theory is able to capture nuances of the trajectory behavior observed experimentally. However, there are cases when the agreement is only satisfactory. In the latter, the body separation is affected by more complex flow phenomena that are not captured by our model. The discrepancy seems to be due to the penetration of the outer flow into the cavity. It indicates that a more complex model is needed for the cavity flow. The slip surface displacement can lead to a pitching moment phase jump from 0 to 180 degrees during Phase 2, when the body crosses the shear layer. The jump may trigger a bifurcation of the pitch-angle history for Phase 3. Our calculations showed that this interpretation is consistent with the experimental data [18] and indicates the existence of two substantially

different pitching trajectories for almost identical initial conditions. Despite the transitional phase 2 being relatively short, its aerodynamics is crucial in identifying one of the two possible trajectories outside the cavity. Further theoretical and experimental studies are needed to establish and clarify the bifurcation mechanism. Our future work will extend this model to transonic speeds.

Our parametric studies show that trajectory parameters, such as the mean state characteristic, oscillation amplitude, frequency and amplification rate depend critically on the body mass, CG location and freestream speed. The trajectory is very sensitive to the initial conditions induced by the release mechanism. Our investigations lead to the conclusion that a satisfactory agreement between theory and experiments is difficult without detailed and accurate release conditions. The latter need to be extracted from analysis of experimental trajectories. Our estimations show that the initial conditions are also influenced by difficult-to-control disturbances such as wind tunnel flow oscillations or/and capture of the model ends by the release mechanism.

In Part 4, we analyzed the outer asymptotic solution and drag force components: parametric studies of store trajectories include the separation from a wing (external separation) and cavities into a transonic freestream. To determine the matching conditions and identify forms of the outer solutions we consider the outer limit, $r \gg H$, of the inner solutions. For cavities of a large span, our analysis is based on the solutions of the dominant approximation obtained in Part 2. We found general forms of the inner solutions in the case of finite-span cavities and investigated their limiting behaviors.

Analyzing asymptotics for the inner solutions of the first order approximation we find:

- In the case of the external store separation from a wing, the outer limit corresponds to the axisymmetric flow over the equivalent body of revolution with the double cross-sectional area of the store.
- In Phase 2 and 3 of separations from an infinite-span cavity, the far flow field is three-dimensional: it corresponds to a dipole distribution along the body axis.

For separations from a finite-span cavity we observed that:

- In the inner asymptotic region, the finite span effect is second order with respect to the ratio of the body radius to the span. Therefore, it is small for wide cavities.
- The cavity span effect is dominant in the far field asymptotic behavior of the inner solution. This effect determines one type of outer flow.
- The far flow field is induced by sources distributed along the store axis. The source intensity is proportional to the ratio of the body radius to the cavity span.

We analyzed outer limits for the inner solutions in the second- and third-order approximations with respect to the small parameter δ^2 and showed that

- In the region $r \sim l_0 / S$, unsteady terms of the second-order potential can be of the same order of magnitude (or even dominant) as the dominant terms of the first-order potential. In the case of a finite-span cavity, the far-field asymptotics are axisymmetric. In the case of infinite-span cavity, they are three-dimensional.
- For unsteady flows, a thin structure of the far field can be rather complicated and depends on the relationship between the Strouhal number and the body radius.
- If unsteady effects are small, then the higher-order asymptotics have the form of a potential induced by sources (in the case of a finite-span cavity) or by dipoles (in the case of an infinite-span cavity).
- For infinite-span cavities, the source term is of the order of $O(\delta^6)$ in the far field. It is negligibly small compared with the source term for finite-span cavities, which is of the order of $O(\delta^2 a_0 / d_0)$.

Using the asymptotic theory and the results of Parts 2 and 4 we formulated the matching conditions for the inner and outer solutions in the case of a body of revolution separating from a cavity into the outer transonic freestream. For Phases 2 and 3, quasi-steady regimes are discussed in detail. In these cases, the outer flow corresponds to transonic flow over an equivalent body of revolution. We obtained explicit forms of the equivalent body as functions of time and the dimensionless cross-section area. The latter continuously grows with time from a small value of the order of ε in Phase 2 to $O(1)$ in Phase 3. Typical examples of the equivalent body shape are presented.

Analyzing the outer asymptotic region we identified different flow regimes depending on the ratio of Strouhal number to the characteristic scale of flow perturbations, $\bar{S} = S / \delta^2$. We conclude that for the unsteady problems considered, an intermediate asymptotic region is possible and would be governed by equations of acoustic type. This region needs to be studied in detail in order to establish a form of the solution for nonlinear transonic regimes. Such a thin structure of the outer asymptotic region is due to different time scales inherent in the separation process.

We believe that for many practical problems, the transonic wave drag can be predicted in the framework of quasi-steady flow. Short-time effects are averaged out over a long time scale relevant to the outer transonic region, and their contribution to the wave drag seems to be small. Our analysis showed that the wave drag increases from $O(\varepsilon \delta^4)$ (in Phase 2) to $O(\delta^4)$ (in Phase 3) as the body moves away from the slip surface.

We derived formulas for the base and friction drags using known theoretical results and empirical correlations. The wave drag is calculated by integrating the outer pressure along the axis of the equivalent body. For Phases 2 and 3, the pressure drag was expressed in analytical form using the inner pressure distribution on the body surface

obtained in Part 2. We calculated different components of the pressure drag and performed their analysis. Using the results of Parts 2 and 4 we developed a FORTRAN code coupling the trajectory equations solver with the code of Malmuth to provide solutions of the Karman-Guderley equation. This package predicts 3-DOF trajectories for transonic store separations.

Numerical results illustrating 3-DOF body dynamics for separations from a wing and cavity in the transonic freestream show that this dynamics can be rather complicated. It includes such phenomena as store ricochet or/and re-contact. The body trajectory is very sensitive to initial "launch" vertical speed or pitch angle. Critical values of these parameters exist. In particular, ricochet/re-contact occur when the initial pitch angle is larger or the vertical speed is smaller than these critical values.

Our studies show that stores can easily separate from flat walls, and re-contact can occur for small initial speeds only. A body thickness variation (from D_0 to $3D_0$) does not lead to the re-contact. The body dynamics is more complicated in the case of the separation from a cavity. Above an initial critical pitch angle or below a critical initial vertical speed, the body does not cross the slip surface and returns to the cavity. With pitch angle increasing or horizontal displacement, contact with the upper or back walls is possible. Near the critical conditions, the body can stay at small heights from the shear layer for a long time period and may partially return to the cavity interior. If the horizontal displacement during this time period is larger than the cavity length, contact with the back cavity wall is possible; otherwise, the store slowly separates.

Our calculations indicate that the store separation can be effectively controlled by the release mechanism. Our modeling can help with the design of ejection units and thrust motors for stage separation. It allows for evaluation of thrust and weight required for these units, and indicates how to avoid an adverse re-contact situation with a relatively small impulse.

References

1. Goodwin, F.K., Dillenius, M.F.E., Nielsen, J.N., "Prediction of Six-Degree-of-Freedom Store Separation Trajectories at Speeds up to the Critical Speed. V.1. Theoretical Methods and Comparison with Experiment," AFFDL-TR-72-83, 1972.
2. Wood, M.E., "Application of Experimental Techniques to Store Release Problems," Proceedings of NEAR Conference on Missile Aerodynamics, Monterey, California, 1988.
3. Schindel, L.H., "Store separation," AGARD-AG-202.
4. Stallings, R.L., "Multiple Body Trajectory Calculations Using the Beggar Code," *J. Aircraft*, 1999, v. 36, No. 5, pp. 802-808.
5. Cole, J.D. *Perturbation Methods in Applied Mathematics*. Waltham, Massachusetts, 1968.
6. Cole, J.D., Cook, L.P. *Transonic Aerodynamics*. Elsevier Science Publisher B.V., 1986.
7. Nielsen, J.N. *Missile Aerodynamics*. McGraw-Hill Company, Inc., New York, 1960.
8. Sedov, L.I. *Two-dimensional Problems of Hydrodynamics and Aerodynamics*. Moscow, Nauka, 1966.
9. Kochin, N.E. "The Influence of the Lattice Step on its Hydrodynamic Characteristics," *J. Appl. Mathematics and Mechanics*, vol. 5, No. 2, 1941.
10. Lavrentiev, M.A., Shabat, B.V. *Methods of the Theory of Complex Variable Functions*. Moscow, Nauka, 1973.
11. Wagner, H. "Uber Stoss- und Gleitfog, H. Uber Stoss- und Gleitfogange an der Oberflache von Flussigkeiten," *ZAMM*, 1932, N 4, pp. 193-215.
12. Whittaker, E.T., and Watson, G.N. *A Course of Modern Analysis*. Cambridge University Press, 1927.
13. Gakhov, F. D. *Boundary-Valued Problems*. Moscow, Nauka, 1958.
14. Kantorovich, L.V., Krylov, V.I., Chernin, K.E. *Tables for Numerical Solutions of Boundary-Valued Problems in Harmonic Function Theory*. Moscow, Mathematical Institute AN USSR, Gostekhizdat, 1956.

15. Milne-Thomson, L.M. *Theoretical Hydrodynamics*. London, Macmillan and Co., LTD, 1960.
16. Malmuth, N.D., Fedorov, A.V., Shalaev, V., Cole, J., Khokhlov, A., Hites, M., and Williams, D., "Problems in High Speed Flow Prediction Relevant to Control." AIAA Paper No. 98-2695, 1998, also unpublished notes and memoranda 1999-2001.
17. Malmuth, N.D., Shalaev, V.I., Fedorov, A.V. "Combined Asymptotics and Numerical Methods for Store Interactions." Technical Report of Contract F49620-96-C-0004, AFOSR/NM, October 1998 (available in Defense Technical Information Center, stient.dtic.mil).
18. Malmuth, N.D., Hites, M., and Williams, D. "Photographic Investigation of the Dynamics of an Ogive Model near a Cavity at Subsonic Mach Numbers." Final Report, Fluid Dynamics Research Center of Illinois Institute of Technology, January, 18, 1998.
19. Malmuth, N.D., Shalaev, V.I., and Fedorov, A.V. "Separation of a Slender Body of Revolution from Rectangular Cavities." Rockwell Science Center, Rep. No. SCNM99-1, 1999.
20. Shalaev, V.I., Fedorov, A.V., and Malmuth N.D. "Dynamics of Slender Bodies Separating from Rectangular Cavities." AIAA Paper, No. 2996, 2001.
21. Shalaev, V.I., Fedorov, A.V., and Malmuth, N.D. "Dynamics of Slender Bodies Separating from Rectangular Cavities." *AIAA J.*, v. 40, No. 3, 2002.
22. Gradshteyn, I.S., and Ryzhik, I. M., *Tables of Integrals, Series, Sums and Products*. Moscow, Nauka, 1970.
23. Korn, G.A., Korn, T.M. *Mathematical Handbook*. McGraw-Hill Book Company, 1968.
24. Yaroshevskii, V.A. "Calculation of Aerodynamic Interference Forces between Two Bodies of Revolution." *Engineering Journal*, 1963, v. 3, No. 3, p. 546 (In Russian). Translation is in *Fluid Dynamics, Soviet Researches*.
25. Malmuth, N.D., Wu, C.C., Cole, J.D., "Slender Body Theory and Optimization Procedures for Transonic Lifting Wing Bodies." *J. of Aircraft*, v. 21, p. 256, 1984.
26. Cheng, H.K., Hafez, M.M., "Transonic Equivalence Rule: a Nonlinear Problem Involving Lift," *J. of Fluid Mechanics*, v. 72, No. 1, 1975.
27. Barnwell, R.W., "Analysis of Transonic Flow about Lifting Wing-Body Configurations." NASA TR, R-440, 1975.
28. Cole, J. and Malmuth, N., "Wave Drag Due to the Lift for Slender Airplanes." NASA Conference Publication 3020, v. 1, p. 293, 1988.

29. Cole, J.D., and Cook, L.P., "Some Problems of Transonic Flow Theory." Symposium Transsonicum III, Eds. Zierep, J., and Oertel, H., IUTAM Symp., Gottingen, May 24-27, 1988; Springer Verlag, Berlin, Heidelberg, 1989, pp. 157-169
30. Lighthill, M.J., "Higher Order Approximations." In: *General Theory of High Speed Aerodynamics*. Ed. by W.R. Sears. Princeton University Press, Sec. E. 1960.
31. Hayes, W.D., "La Seconde Approximation pour les Écoulements Transsonique non Visqueux," *Journal de Mécanique*, v. 5, No. 2, 1966.
32. Schlichting, G., *Boundary Layer Theory*, McGraw-Hill, New York, 1968.
33. Chow, W.L., "Base Pressure of a Projectile Within the Transonic Flight Regime." *AIAA J.*, v. 23, No. 3, pp. 388-395, 1985.
34. Carlson, H.W., Geier, D.J., Lee, J.B., "Comparison and Evaluation of Two Model Techniques Used in predicting Bomb-Release Motions", NACA RM L57J23, December, 1957.

Stabilization of Hypersonic Boundary Layers by Porous Coatings

Alexander V. Fedorov*

Moscow Institute of Physics and Technology, Zhukovski 140160, Russia

Norman D. Malmuth†

Rockwell Science Center, Thousand Oaks, California 91630

and

Adam Rasheed‡ and Hans G. Hornung§

California Institute of Technology, Pasadena, California 91125

A second-mode stability analysis has been performed for a hypersonic boundary layer on a wall covered by a porous coating with equally spaced cylindrical blind microholes. Massive reduction of the second mode amplification is found to be due to the disturbance energy absorption by the porous layer. This stabilization effect was demonstrated by experiments recently conducted on a sharp cone in the T-5 high-enthalpy wind tunnel of the Graduate Aeronautical Laboratories of the California Institute of Technology. Their experimental confirmation of the theoretical predictions underscores the possibility that ultrasonically absorptive porous coatings may be exploited for passive laminar flow control on hypersonic vehicle surfaces.

Nomenclature

A	=	admittance
B	=	thermal admittance
F	=	frequency parameter
h	=	porous layer thickness
n	=	porosity
p	=	pressure perturbation
Pr	=	Prandtl number
Re	=	displacement thickness Reynolds number
Re_τ	=	transition Reynolds number
r	=	pore radius
s	=	pore spacing
T	=	mean flow temperature
t	=	time
U	=	mean flow velocity
u, v, w	=	perturbation velocity components
x, y, z	=	Cartesian coordinates
α, β	=	wavenumber components
γ	=	specific heat ratio
δ^*	=	displacement thickness
θ	=	temperature perturbation
κ	=	thermal conductivity
μ	=	viscosity
ρ	=	mean flow density
σ	=	spatial growth rate
φ	=	wave front angle
ω	=	angular frequency

Subscripts

ad	=	adiabatic
e	=	upper boundary-layer edge
m	=	maximum value
w	=	wall surface

Superscript

*	=	dimensional
---	---	-------------

Introduction

THE ability to stabilize a hypersonic boundary layer and increase its laminar run is of critical importance in the hypersonic vehicle design.¹ Early transition causes significant increases in heat transfer and skin friction. Higher heating requires an increased performance thermal protection system (TPS), active cooling, or trajectory modification. This translates to higher cost and weight of hypersonic vehicles due to increased TPS weight. Moreover, with the low payload mass fraction, even small savings in TPS weight can provide a significant payload increase. Vehicle maintainability and operability are also affected by transition. Robust metallic TPS have temperature limits lower than ceramic TPS. Laminar flow control (LFC) can help meet these more severe constraints. For a streamlined vehicle with large wetted area, viscous drag becomes important. It can be from 10% (fully laminar) to 30% (fully turbulent) of the overall drag.² For optimized hypersonic wave/riders, viscous drag may represent up to 50% of the total drag.³ Vehicle aerodynamics is another area impacted by laminar-turbulent transition. Asymmetry of the transition locus can produce significant yawing moments. Aerodynamic control surfaces and reaction control systems are also affected due to sensitivity of boundary-layer separation to the flow state (laminar or turbulent).

If freestream disturbances and TPS-induced perturbations are small, transition to turbulence is due to amplification of unstable boundary-layer modes.^{1,4} In this case, LFC methods and transition prediction tools are predominantly based on stability theory and experiment.⁵⁻⁸ LFC systems are aimed at slowing down or eliminating amplification of unstable disturbances using passive and/or active control techniques. A third form of flow control is known as reactive control, in which boundary-layer disturbances are canceled by artificially introducing out-of-phase disturbances. Typical passive LFC techniques are pressure gradient and shaping. Active techniques include wall suction and heat transfer. In reactive control methods, periodic suction/blowing, heating/cooling or wall vibrations are used for artificial excitation of counter-phase disturbances.

In hypersonic boundary layers, amplification of the following instability mechanisms may drive the transition process:

1) The first instability mechanism is the first mode associated with Tollmien-Schlichting waves. This instability may be dominant at relatively small local Mach numbers (normally less than 5). This mode is strongly stabilized on cool surfaces. At low wall-temperature ratios, the stabilization effect may be so strong that the first-mode mechanism becomes unimportant.

2) The second mode associated with an inviscid instability present due to a region of supersonic mean flow relative to the disturbance phase velocity⁹ belongs to the family of trapped acoustic modes and becomes the dominant instability in two-dimensional and

Received 11 February 2000; revision received 28 August 2000; accepted for publication 3 October 2000; presented as Paper 2001-0891 at the AIAA 39th Aerospace Sciences Meeting, Reno, NV, 8-11 January 2001. Copyright © 2000 by the authors. Published by the American Institute of Aeronautics and Astronautics, Inc., with permission.

*Associate Professor, Department of Aeromechanics and Flight Engineering. Member AIAA.

†Senior Scientist, Fluid Dynamics. Fellow AIAA.

‡Ph.D. Student, Graduate Aeronautical Laboratories.

§Director, Graduate Aeronautical Laboratories.

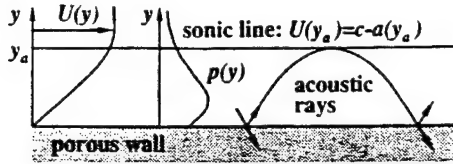


Fig. 1 Acoustic mode in a supersonic boundary layer on semitransparent wall.

quasi-two-dimensional boundary layers at Mach numbers $M > 4$. The existence of the second mode was established by the experiments of Kendall,⁹ Demetriades,¹⁰ Stetson et al.,¹¹ Stetson and Kimmel,¹² and Kimmel et al.¹³ The most amplified second-mode wavelength is approximately twice the boundary-layer thickness, and its phase velocity tends to the boundary-layer edge velocity of mean flow. As a result, the second-mode disturbances are in the ultrasonic frequency band. For example, the most amplified waves observed in the experiment of Stetson et al.¹¹ at Mach 8 correspond to a frequency about 100 kHz. In contrast to the first mode, the second mode is destabilized by cooling.

3) Crossflow vortices are observed in three-dimensional boundary layers on the leading edge of a swept wing, axisymmetric bodies at high angles of attack, etc. This instability is weakly sensitive to wall cooling. It can be effectively stabilized by shaping. For example, two-dimensional shaping of air breathers helps to avoid crossflow instabilities on large acreage regions of the vehicle surface.

4) Görtler vortices play a major role in transition on concave surfaces. Similar to the crossflow instability, their growth rate can be reduced by shaping.

Because severe environmental conditions make it difficult to use active and reactive LFC concepts for hypersonic vehicles, passive LFC techniques are of great interest. Thus, Malmuth et al.¹⁴ proposed a new passive method of second- and higher-mode stabilization. They exploited the hypersonic boundary layer's behavior as an acoustic waveguide, schematically shown in Fig. 1. Therein, acoustic rays are reflected by the wall and turn around near the sonic line: $y = y_a$, $U(y_a) = Re(c) - a(y_a)$, where c is the disturbance phase speed and a is local sound speed. The second, third, and higher boundary-layer modes correspond to the waveguide normal modes. Malmuth et al.¹⁴ assumed that the absorption of acoustic energy by an ultrasonically absorptive coating can stabilize these disturbances. This assumption was examined using stability theory for inviscid disturbances. It was found that an ultrasonically semitransparent wall provides substantial reduction of the second-mode growth rate.

In this paper, we study this stabilization mechanism, including viscous effects and an absorptive skin microstructure. We formulate the eigenvalue problem for viscous disturbances in a hypersonic boundary layer on a wall covered by an ultrasonically absorptive coating of special type, namely, a porous layer with equally spaced cylindrical blind microholes. We obtain the analytical form of boundary conditions on the porous surface and solve the viscous eigenvalue problem numerically. We discuss results of calculations showing the second-mode stabilization on porous surfaces of various pore radii, spacing, and thickness. Then we briefly describe the experimental data of Rasheed et al.¹⁵ that confirm the theoretically based hypersonic boundary-layer stabilization by porous coatings given in this paper. These results were obtained in the T-5 Graduate Aeronautical Laboratories of the California Institute of Technology high-enthalpy wind tunnel on a sharp cone that they detail in Ref. 15. Finally, we conclude the paper with a summary discussion and indicate possible future directions.

Eigenvalue Problem

We consider supersonic boundary-layer flow over a flat plate or sharp cone as schematically shown in Fig. 2. The fluid is a perfect gas with Prandtl number Pr , specific heat ratio γ , and viscosity μ . The coordinates x , y , and z are made nondimensional using the boundary-layer displacement thickness δ^* . In the locally parallel approximation, the mean flow is characterized by the profiles of x -component velocity $U(y)$ and temperature $T(y)$, referenced to the quantities U_e^* and T_e^* at the upper boundary-layer edge. Three-

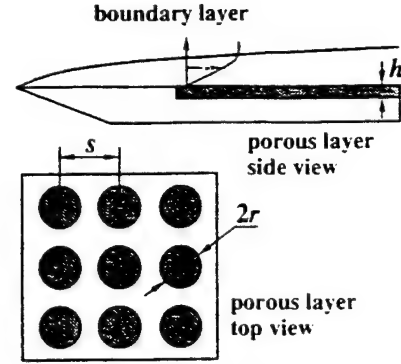


Fig. 2 Schematic of a wall covered by porous layer.

dimensional disturbances are represented in the traveling wave form

$$\tilde{q} = \text{Re}\{q(y) \exp[i(\alpha x + \beta z - \omega t)]\}, \quad \tilde{q} = [\tilde{u}, \tilde{v}, \tilde{w}, \tilde{p}, \tilde{\theta}] \quad (1)$$

where \tilde{u} , \tilde{v} , and \tilde{w} are velocity components; \tilde{p} is the pressure referenced to the double dynamic pressure $\rho_e^* U_e^{*2}$; $\tilde{\theta}$ is the temperature; $\alpha = \alpha^* \delta^*$ and $\beta = \beta^* \delta^*$ are wave number components; and $\omega = \omega^* \delta^* / U_e^*$ is the angular frequency. The system of stability equations that is derived from the full Navier-Stokes equations for a locally parallel compressible boundary layer can be represented in the form¹⁶

$$\frac{dz}{dy} = S \cdot z, \quad z = \left(u, \frac{du}{dy}, v, p, \theta, \frac{d\theta}{dy}, w, \frac{dw}{dy} \right)^T \quad (2)$$

where S is an 8×8 matrix. Its elements are functions of the mean flow profiles, the displacement thickness Reynolds number $Re = \delta^* U_e^* \rho_e^* / \mu_e^*$, and disturbance characteristics ω , α , and β .

We consider a wall covered by a porous layer of the thickness h^* . The pores are equally spaced cylindrical blind holes of radius r^* perpendicular to the wall surface, as schematically shown in Fig. 2. The hole spacing s^* and diameter are assumed to be much less than the boundary-layer displacement thickness δ^* . Because the pore radius is small and interactions between neighboring pores are weak, perturbations of longitudinal and transverse velocity produced by the porous layer are neglected. However, the porous structure is semitransparent relative to the vertical velocity and temperature perturbations. In this case, the wall boundary conditions can be expressed as

$$u(0) = 0, \quad w(0) = 0, \quad v(0) = Ap(0), \quad \theta(0) = Bp(0) \quad (3)$$

where the admittance A and thermal admittance B are complex quantities that depend on properties of the wall material, porosity parameters, mean flow characteristics on the wall surface, and flow perturbation parameters such as a wave frequency and wavelength. These dependencies are derived in the next section. Because boundary-layer modes decay outside the boundary layer, we have

$$u(\infty) = v(\infty) = w(\infty) = \theta(\infty) = 0 \quad (4)$$

The eigenvalue problem (2–4) provides the dispersion relation $F(\alpha, \beta, \omega) = 0$. For temporal stability, the wave number components α and β are real quantities, and ω is a complex eigenvalue. If $\text{Im}(\omega) > 0$, then the disturbance is unstable. For spatial instability in two-dimensional boundary layers, the frequency ω and transverse wave number component β are real, whereas α is a complex eigenvalue. If $\text{Im}(\alpha) < 0$, then the disturbance amplifies downstream with the spatial growth rate $\sigma = -\text{Im}(\alpha)$.

Admittance of Porous Layer

The porous layer is characterized by the porosity n , which is the fraction of the overall volume taken up by the pores. For the pore spacing shown in Fig. 2, the porosity, $n = \pi(r^*/s^*)^2$, can be varied in the range $0 < r^*/s^* < \pi/4$, where the upper limit corresponds to $s^* = 2r^*$. The pore radius and spacing are considered to be much less than the disturbance wavelength, which is of the order of the

boundary-layer displacement thickness. In this case, the porosity is fine enough to avoid disturbing the laminar boundary layer by other mechanisms associated with effective surface roughness. The porous layer thickness h^* is assumed to be much larger than the pore radius r^* , that is, each pore is treated as a long tube.

To obtain the relationship between the admittance A and porous layer parameters, we use the theoretical model developed by Gaponov for subsonic^{17,18} and moderate supersonic speeds.¹⁹ These studies addressed the porosity effect on Tollmien-Schlichting (TS) waves. As contrasted to second-mode waves of acoustic type discussed in this paper, the TS waves over porous walls analyzed by Gaponov are vortical disturbances that become unstable due to viscous mechanisms. For this reason, the second-mode interaction with a porous surface is fundamentally different from that of TS waves. Yet, the results¹⁸ for the disturbance propagation within a porous wall are independent of the nature of the boundary-layer disturbances, for example, second-mode acoustic or TS waves. In particular, they can be used in formulating the porous wall boundary conditions for the vertical velocity of second-mode disturbances considered herein. The thermal admittance B is derived using an explicit coupling between the pressure, temperature, and velocity perturbations within a uniform pore.²⁰

Following the analysis,¹⁸ we apply the theory of sound wave propagation in thin and long tubes (see, for example, Ref. 21). Because $h^* \gg r^*$, the pressure is approximately constant across the pore. In this case, the acoustic field within each pore is characterized by the propagation constant Λ and the characteristic impedance Z_0 . These parameters can be expressed as a function of the series impedance Z and the shunt admittance Y for the tube element of unit length using the transmission line formalism.^{22,23} The series impedance properties of the tube element are associated with the storage of kinetic energy and its dissipation due to viscous losses at the tube wall. The shunt admittance is associated with the potential energy of compression and the thermal energy losses due to the wall heat conductivity. We assume that the mean gas temperature along the tube is constant and equal to the wall surface temperature T_w . Daniels²² and Benade²³ showed that the dimensional series impedance Z^* and shunt admittance Y^* per unit length of a tube with radius r^* are expressed as

$$Z^* = -\frac{i\omega^* \rho_w^*}{\pi r^{*2}} \left[1 - \frac{2}{k_v} \cdot \frac{J_1(k_v)}{J_0(k_v)} \right]^{-1} \quad (5)$$

$$Y^* = -\frac{i\omega^* \pi r^{*2}}{\rho_w^* a_w^{*2}} \left[1 + (\gamma - 1) \cdot \frac{2}{k_t} \cdot \frac{J_1(k_t)}{J_0(k_t)} \right] \quad (6)$$

where, ρ_w^* and a_w^* are mean density and sound speed in a tube. J_0 and J_1 are Bessel functions of the arguments $k_v = r^* \sqrt{i\omega^* \rho_w^* / \mu_w^*}$ and $k_t = k_v \sqrt{Pr}$, which measure the ratio of the tube radius to the viscous boundary-layer thickness and to the thermal boundary-layer thickness on the tube surface, respectively. Using the relation

$$J_0(x) + J_2(x) = 2J_1(x)/x \quad (7)$$

we express Z^* and Y^* in the form

$$Z^* = \frac{i\omega^* \rho_w^*}{\pi r^{*2}} \cdot \frac{J_0(k_v)}{J_2(k_v)} \quad (8)$$

$$Y^* = -\frac{i\omega^* \pi r^{*2}}{\rho_w^* a_w^{*2}} \left[\gamma + (\gamma - 1) \frac{J_2(k_t)}{J_0(k_t)} \right] \quad (9)$$

For the average velocity through the pore, the transmission line is characterized by the impedance $Z_1^* = S^* Z^*$ and shunt admittance $Y_1^* = Y^* / S^*$, where $S^* = \pi r^{*2}$ is pore cross-sectional area. Choosing the boundary-layer displacement thickness and mean flow parameters at the upper boundary-layer edge as reference scales, we have

$$Z_1 \equiv \frac{\pi r^{*2} \delta^*}{\rho_c^* U_c^*} Z^* = \frac{i\omega}{T_w} \frac{J_0(k_v)}{J_2(k_v)}, \quad k_v = r \sqrt{\frac{i\omega \rho_w}{\mu_w}} R \quad (10)$$

$$Y_1 \equiv \frac{\rho_c^* U_c^* \delta^*}{\pi r^{*2}} Y^* = -i\omega M^2 \left[\gamma + (\gamma - 1) \frac{J_2(k_t)}{J_0(k_t)} \right] \quad (11)$$

where $r = r^* / \delta^*$ is nondimensional pore radius. The characteristic impedance Z_0 and the propagation constant Λ are expressed in the form

$$Z_0 = \sqrt{Z_1 / Y_1}, \quad \Lambda = \sqrt{Z_1 Y_1}, \quad \text{Re}(\Lambda) < 0 \quad (12)$$

The coupling between the pressure amplitude p and the average velocity disturbance amplitude \bar{v} at the pore end, $y = -h$, can be expressed as $p(-h) = X \cdot \bar{v}(-h)$, where the impedance X depends on characteristics of the backup structure. If the lower pore end is closed by a solid wall (blind pores), then $\bar{v}(-h) = 0$. In this case, the impedance is $X = \infty$, and the velocity-pressure ratio at the upper end of the pore is

$$\{\bar{v}(0)/p(0)\} = (1/Z_0) \tanh(\Lambda h) \quad (13)$$

Averaging the vertical velocity amplitude at the wall over the surface area, we have $v(0) = n \cdot \bar{v}(0)$. Then the admittance in the boundary conditions (3) is expressed as

$$A = (n/Z_0) \tanh(\Lambda h) \quad (14)$$

If the porous layer is relatively thick ($\Lambda h \rightarrow \infty$), then Eq. (14) is reduced to the form

$$A = -(n/Z_0) \quad (15)$$

Note that the limit $\Lambda h \rightarrow \infty$ leads to Eq. (15) at any finite value of X (i.e., the disturbance at the upper end of each hole does not feel the lower end due to the decay of sound propagating along a tube).

According to the analysis of Stinson and Champoux,²⁰ the pressure disturbance, average temperature disturbance, and average velocity disturbance within a cylindrical pore are coupled as

$$\bar{v}^*(\omega^*) = \frac{1}{i\omega^* \rho_w^*} \frac{dp^*}{dy^*}(\omega^*) \left[1 - \frac{2}{k_v} \frac{J_1(k_v)}{J_0(k_v)} \right] \quad (16)$$

$$\bar{\theta}^*(\omega^*) = \frac{i\omega^* \mu^*}{\kappa_w^*} \left[p^*(\omega^*) \frac{d}{dy^*} (Pr\omega^*) \right] \bar{v}^*(Pr\omega^*) \quad (17)$$

Substituting Eq. (16) into Eq. (17), accounting for Eq. (7), and nondimensionalizing the result, we obtain

$$\bar{\theta} = -(\gamma - 1) M^2 T_w p J_2(k_t) / J_0(k_t) \quad (18)$$

Thus, the thermal admittance in the boundary condition (3) for the temperature disturbance is expressed as

$$B = -n(\gamma - 1) M^2 T_w J_2(k_t) / J_0(k_t) \quad (19)$$

Computational and Parametric Studies

To evaluate the porous layer effect on the second-mode stability, we solve the eigenvalue problem (2-4) numerically using the admittance (14) or its limiting form (15) and the thermal admittance (19). We consider the boundary layer of a perfect gas with Prandtl number $Pr = 0.71$ and specific heat ratio $\gamma = 1.4$. The temperature-viscosity law is specified as $\mu = \mu_0 (T/T_0)^m$ with the exponent $m = 0.75$; the second viscosity is zero. Figure 3 shows the spatial growth rate σ as a function of the Reynolds number Re for two-dimensional unstable waves ($\beta = 0$) of nondimensional frequency $F \equiv \omega^* v_c^* / U_c^{*2} = 2.8 \times 10^{-4}$ in the boundary layer at the Mach number $M = 6$. The wall temperature $T_w = 1.4$ approximately corresponds to the wall temperature ratio $T_w/T_{ad} = 0.2$. Calculations were conducted for a thick porous layer ($\Lambda h \rightarrow \infty$) with the porosity $n = 0.5$ at various values of the nondimensional pore radius $r = r^* / \delta^*$. Note that the porous layer causes massive reduction of the second-mode growth rate. In Figs. 3-6, symbols correspond to the case of zero thermal admittance, $B = 0$. For all cases considered, temperature perturbations on the porous surface weakly affect the disturbance growth rate and can be neglected.

Figure 4 shows that deep pores of fixed radius ($r = 0.03$ at $Re = 2 \times 10^3$) and spacing (porosity $n = 0.5$) strongly stabilize the second-mode waves in a wide frequency band at various Reynolds numbers Re (dashed lines). This example illustrates that it is possible to cause significant reduction of the disturbance growth rate on large surface areas without fine tuning the pore size. As contrasted to

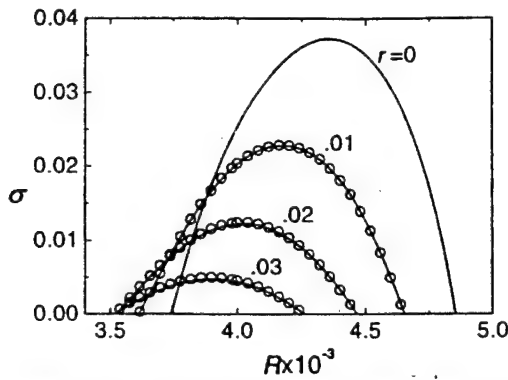


Fig. 3 Growth rate σ as a function of Reynolds number Re at various pore radii r : $M=6$, $T_w=1.4$, $F=2.8 \times 10^{-4}$, $n=0.5$, and $\Lambda h \rightarrow \infty$ (solid lines); symbols indicate zero thermal admittance. (R = Reynolds number in figure.)

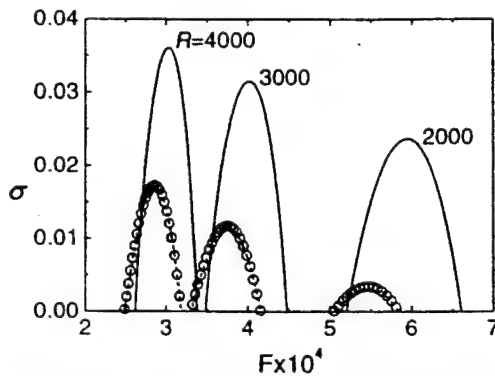


Fig. 4 Growth rate σ as a function of disturbance frequency F at various Reynolds numbers Re : $M=6$, $T_w=1.4$, $n=0.5$, and $\Lambda h \rightarrow \infty$; solid lines $r=0$, dashed lines $r=0.03$ at $Re=2.0 \times 10^3$, symbols indicate zero thermal admittance. (R = Reynolds number in figure.)

reactive flow control techniques, a porous coating provides passive stabilization of the boundary-layer flow regardless the disturbance phase and amplitude distributions in space and time and with no external energy input. Note that the waveguide behavior described earlier in this paper in connection with the instability of the acoustic second mode that is quenched by the ultrasonic absorbing wall concept described herein resembles amplification processes studied by the second author in connection with the stability of hypersonic strong interaction flows.²⁴

Figure 5 shows distributions of the maximum growth rate, $\sigma_m(Re) = \max_{\omega}[\sigma(\omega, Re)]$, at the wall temperatures $T_w = 1.4$, 3.5, and 7.0, that approximately corresponds to the wall temperature ratio $T_w/T_{ad} = 0.2$, 0.5, and 1. The stabilization effect decreases as the wall temperature increases. A strong reduction of the growth rate is observed in the boundary layer on a cool wall (see Fig. 5), a more practical case for hypersonic applications. This trend is consistent with the admittance asymptotic behavior associated with Eqs. (10–12) and (15). For deep pores ($\Lambda h \gg 1$) of relatively small radius ($|k_v| \ll 1$), the admittance A is proportional to $k_v M \sqrt{T_w}$ and decreases with the wall temperature as $T_w^{-m/2}$.

Figure 6 shows the maximum growth rate σ_m as a function of the porosity n for $Re=4 \times 10^3$ and $r=0.03$ for the boundary layer at $M=6$ and $T_w=1.4$. The porous layer of spacing $s=4r$ ($n \approx 0.2$) reduces the growth rate by a factor of 2 compared to the solid wall case $n=0$. Our calculations using the e^N method indicates that this stabilization translates to extending the transition onset point more than three times its value without porosity. In Fig. 7, the second-mode growth rate is shown as a function of the nondimensional porous layer thickness $h=h^*/\delta^*$ at $n=0.4$, $r=0.03$, $Re=4 \times 10^3$, and $F=3 \times 10^{-4}$. The limit $\Lambda h \rightarrow \infty$ is achieved at a relatively small value of $h \approx 0.3$ (pore depth is about five diameters) that is due to strong damping of sound waves in thin pores. There is an optimal thickness, $h \approx 0.12$, at which the porous

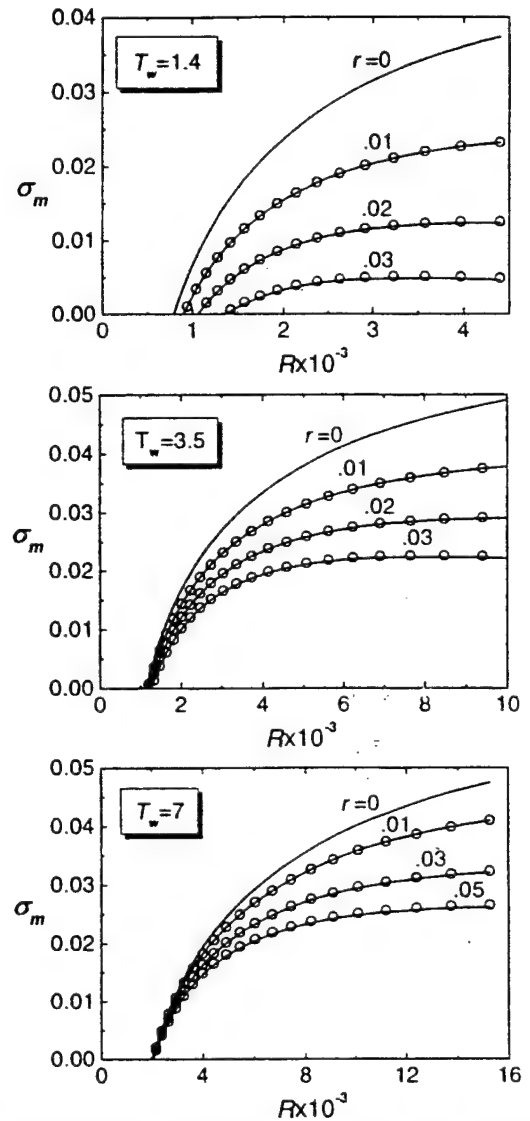


Fig. 5 Distributions of maximum growth rate $\sigma_m(Re)$ at various pore radii r : $M=6$, $n=0.5$, and $\Lambda h \rightarrow \infty$ (—); symbols indicate zero thermal admittance. (R = Reynolds number in figure.)

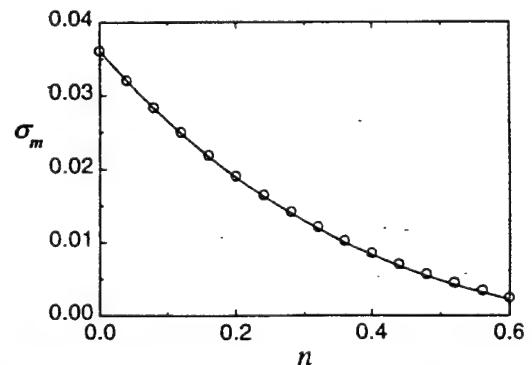


Fig. 6 Maximum growth rate σ_m as a function of porosity n at $Re=4 \times 10^3$: $M=6$, $T_w=1.4$, $r=0.03$, and $\Lambda h \rightarrow \infty$ (—); symbols indicate zero thermal admittance.

wall effect is able to stabilize the disturbance completely. In this case, the disturbance reflected from the pore bottom is in counter phase with the boundary-layer disturbance. However, the optimal thickness strongly depends on the disturbance frequency and the thick porous layer is more robust. Figure 8 illustrates the stabilization effect for three-dimensional waves of the second-mode family. The growth rate is shown as a function of the wave front angle $\varphi = \arctan(\beta_r/\alpha_r)$ at various pore radii. The porous coating causes massive reduction of the disturbance growth rate and substantially

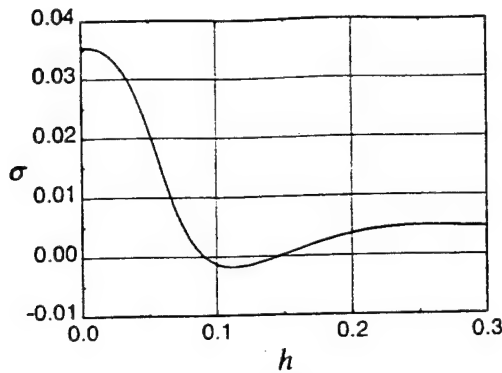


Fig. 7 Growth rate σ as a function of porous layer thickness h at $n = 0.4$, $r = 0.03$, $Re = 4 \times 10^3$, $F = 3 \times 10^{-4}$, $M = 6$, and $T_w = 1.4$ for zero thermal admittance.

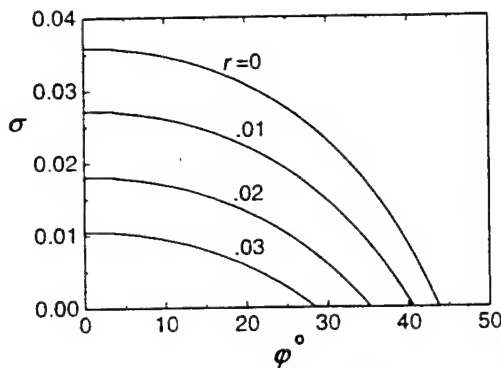


Fig. 8 Growth rate σ as a function of wave front angle ϕ at various pore radii r : $M = 6$, $T_w = 1.4$, $Re = 4287$, $F = 3 \times 10^{-4}$, $n = 0.3$, and $\Delta h \rightarrow \infty$.

decreases the unstable range of wave front angles. These examples show that a relatively thin porous coating can dramatically reduce the second-mode amplification and increase the laminar run if transition is driven by second-mode disturbances.

Experimental Validation of Theory

Rasheed et al.¹⁵ have recently verified the theoretical concept by testing a 5-deg half-angle sharp cone with an ultrasonically absorptive coating in the California Institute of Technology T5 high-enthalpy shock tunnel. The cone was 1 m in length, with half of its surface solid and the other a porous sheet perforated with equally spaced blind cylindrical holes. Porosity parameters were chosen from the preliminary theoretical analysis of Fedorov and Malmuth as well as manufacturing constraints. The average pore radius r^* was $30 \mu\text{m}$, the depth h^* was $500 \mu\text{m}$, and the average spacing s^* was $100 \mu\text{m}$. Figure 9 shows a microphotograph of a portion of the porous surface. For typical runs, the boundary-layer thickness was about 1 mm, and the estimated number of holes per boundary-layer disturbance wavelength was about 20. Static measurements of ultrasound reflectivity of perforated sheet coupons (without flow) showed that the porous coating attenuated the incident ultrasonic signal of 400-kHz frequency by 3.0 dB relative to a solid wall.

The model was instrumented by thermocouples, and the transition onset point was determined from the Stanton number distributions $St(x)$ measured simultaneously on both sides of the model for each run. Nitrogen was selected as the test gas to minimize the chemistry effects, which were not included in the theoretical analysis. Runs were performed for the ranges of the freestream total enthalpy $4.18 \leq H_0 \leq 13.34 \text{ MJ/kg}$ and Mach number $4.59 \leq M_\infty \leq 6.4$. Figure 10 shows a summary plot of the transition onset Reynolds number $Re_{tr} = x_{tr}^* U_\infty^* \rho_\infty^* / \mu_\infty^*$ vs H_0 . The solid squares correspond to transition on the solid wall, and the open circles correspond to transition on the porous surface. The circles with arrows indicate that the boundary layer on the porous surface was

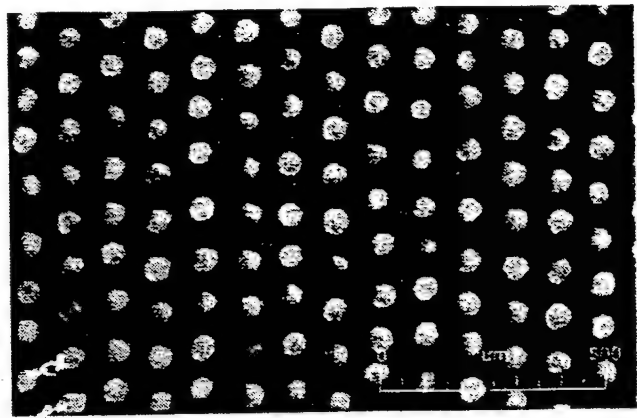


Fig. 9 Microphotograph of porous surface.

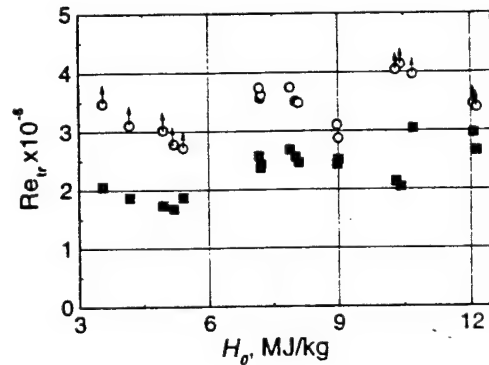


Fig. 10 Transition onset Reynolds number Re_{tr} vs total enthalpy H_0 : \blacksquare , solid wall; \circ , porous wall; and \circ with arrow, boundary layer on porous wall is laminar up to the model base.

laminar up to the model base, that is, the value plotted is not a real data point because the cone was not long enough to measure the transition locus. In all cases, the circles are well above the squares. This indicates that the porous coating always delays transition by a significant amount.

Summary

A second-mode stability analysis has been performed for hypersonic boundary layers over walls covered by porous coatings with equally spaced blind microholes. Absorption of the disturbance energy by porous layers was modeled using the theory of disturbance wave propagation in thin and long tubes. The admittance and thermal admittance coupling the pressure disturbance with the vertical velocity and temperature disturbances on the porous surface are expressed as explicit functions of porosity characteristics. Stability calculations showed that the absorption of disturbance energy by the porous coating provides massive reduction of the second-mode growth rate in a wide range of disturbance frequencies and Reynolds numbers. The flow stabilization is due to vertical velocity perturbations on the porous surface associated with nonzero admittance of porous medium. Temperature perturbations weakly affect the boundary-layer disturbance and can be neglected. This indicates that temperature disturbances play a passive role in the second-mode instability mechanism.

Our conclusions are consistent with the results of Malmuth et al.,¹⁴ obtained from their inviscid stability analysis. The most profound effect is observed on a cool wall that is typical for hypersonic vehicle TPS surfaces. A relatively thin porous coating (of thickness about 30% of the laminar boundary-layer displacement thickness) provides a strong stabilization effect. Such porous coatings can be designed for passive LFC in hypersonic vehicle surfaces. Note that the disturbance absorption should be introduced at the initial phase of transition process, where the unstable disturbance amplitude is about 0.01–0.1% of its level in transitional and turbulent boundary layers. In this phase, additional heating of the porous coating

associated with partial absorption of the disturbance energy is negligibly small compared to the turbulent heating.

The first series of experiments conducted by Rasheed et al.¹⁵ on a sharp cone in the T5 shock tunnel at the Graduate Aeronautical Laboratories at the California Institute of Technology qualitatively confirms the theoretical prediction. Quantitative comparison of the theory with these data is planned for the future. Because the boundary-layer stabilization is due to the disturbance energy extraction mechanism, we believe that similar effects may occur for other types of high-frequency instabilities. Absorptive coatings may also affect the bypass mechanism, which is responsible for transition past TPS roughness elements. These assumptions could be examined by further theoretical modeling and verified by experiments.

Many TPS materials, which can provide efficient absorption of acoustic disturbances, have a random porosity. The interaction of the boundary layer and unstable disturbances with a random porous coating may be different from the case of the regular pore structure discussed earlier. Because of communication between randomly distributed pores, a mean flow may occur inside the coating that leads to a slip effect on the coating surface. Boundary conditions for unstable disturbances may be also affected. These effects will also be addressed in our future studies.

Acknowledgments

Portions of this effort was supported by the Air Force Office of Scientific Research, Air Force Materials Command under Contracts F49620-92-C-0006, F49620-96-C-0004, and F499620-98-1-0353. The U.S. government is authorized to reproduce and distribute reprints for government purposes, notwithstanding any copyright notation thereon. The views and conclusions herein are those of the authors and should not be interpreted as necessarily representing the official policies or endorsements, either expressed, or implied by the Air Force Office of Research or the U.S. government.

References

- ¹Malik, M. R., Zang, T. A., and Bushnell, D. M., "Boundary-Layer Transition in Hypersonic Flows," AIAA Paper 90-5232, 1990.
- ²Reed, H. L., Kimmel, R., Schneider, S., and Arnal, D., "Drag Prediction and Transition in Hypersonic Flow," AIAA Paper 97-1818, June 1997.
- ³Bowcutt, K. G., Anderson, J. D., and Capriotti, D., "Viscous Optimized Hypersonic Waveriders," AIAA Paper 87-0272, 1987.
- ⁴Reshotko, E., "Boundary-Layer Instability, Transition, and Control," AIAA Paper 94-0001, Jan. 1994.
- ⁵Mack, L. M., "Boundary-Layer Stability Theory," *Special Course on Stability and Transition of Laminar Flow*, edited by R. Michel, Rept. 709, AGARD, 1984, pp. 3-1-3-81.
- ⁶Reshotko, E., "Stability Theory as a Guide to the Evaluation of Transition Data," AIAA Journal, Vol. 7, No. 6, 1969, pp. 1086-1091.
- ⁷Malik, M. R., "Prediction and Control of Transition in Supersonic and Hypersonic Boundary Layers," AIAA Journal, Vol. 27, No. 11, 1989, pp. 1487-1493.
- ⁸Malik, M. R., "Stability Theory for Laminar Flow Control Design," *Viscous Drag Reduction in Boundary Layers*, edited by D. M. Bushnell and J. N. Hefner, Vol. 123, Progress in Astronautics and Aeronautics, AIAA, Washington, DC, 1990, pp. 3-46.
- ⁹Kendall, J. M., "Wind-Tunnel Experiments Relating to Supersonic and Hypersonic Boundary-Layer Transition," AIAA Journal, Vol. 13, No. 3, 1975, pp. 290-299.
- ¹⁰Demetriades, A., "Hypersonic Viscous Flow over a Slender Cone, Part III: Laminar Instability and Transition," AIAA Paper 74-535, 1974.
- ¹¹Stetson, K. F., Thompson, E. R., Donaldson, J. C., and Siler, L. G., "Laminar Boundary-Layer Stability Experiments on a Cone at Mach 8, Part 1: Sharp Cone," AIAA Paper 83-1761, 1983.
- ¹²Stetson, K. F., and Kimmel, R. G., "On the Breakdown of a Hypersonic Laminar Boundary Layer," AIAA Paper 93-0896, 1993.
- ¹³Kimmel, R., Demetriades, A., and Donaldson, J., "Space-Time Correlation Measurements in a Hypersonic Transitional Boundary Layer," AIAA Paper 95-2292, 1995.
- ¹⁴Malmuth, N. D., Fedorov, A. V., Shalaev, V., Cole, J., and Khokhlov, A., "Problems in High-Speed Flow Prediction Relevant to Control," AIAA Paper 98-2995, June 1998.
- ¹⁵Rasheed, A., Hornung, H. G., Fedorov, A. V., and Malmuth, N. D., "Experiments on Passive Hypervelocity Boundary-Layer Control Using a Porous Surface," AIAA Paper 2001-0274, Jan. 2001.
- ¹⁶Mack, L. M., "Boundary-Layer Stability Theory," Jet Propulsion Lab., Rept. 900-277, rev. B, California Inst. of Technology, Pasadena, CA, 1969.
- ¹⁷Gaponov, S. A., "Influence of Porous Layer on Boundary-Layer Stability," *Izvestia SO AN SSSR, Seria Tekhnicheskikh Nauk*, Vyp. 1, No. 3, 1971, pp. 21-23 (in Russian).
- ¹⁸Gaponov, S. A., "Influence of Gas Compressibility on Stability of Boundary Layer on Porous Surface at Subsonic Speeds," *Zhurnal Prikladnoi Mekhaniki i Tekhnicheskoi Fiziki*, No. 1, 1975, pp. 121-125 (in Russian).
- ¹⁹Gaponov, S. A., "Stability of Supersonic Boundary Layer on Porous Wall with Heat Conductivity," *Izvestia AN SSSR, Mekhanika Zhidkosti i Gaza*, No. 1, 1977, pp. 41-46 (in Russian).
- ²⁰Stinson, M. R., and Champoux, Y., "Propagation of Sound and the Assignment of Shape Factors in Model Porous Materials Having Simple Pore Geometries," *Journal of the Acoustical Society of America*, Vol. 91, No. 2, 1992, pp. 685-695.
- ²¹Rzhevkin, S. N., *Lectures on Theory of Sound*, Moscow State Univ., Moscow, 1960 (in Russian).
- ²²Daniels, F. B., "On the Propagation of Sound Waves in a Cylindrical Conduit," *Journal of the Acoustical Society of America*, Vol. 22, No. 2, 1950, pp. 563-564.
- ²³Benade, A. H., "On the Propagation of Sound Waves in a Cylindrical Conduit," *Journal of the Acoustical Society of America*, Vol. 44, No. 2, 1968, pp. 616-623.
- ²⁴Malmuth, N., "Stability of the Inviscid Shock Layer in Strong Interaction Flow over a Hypersonic Flat Plate," *Fluid Mechanics and Its Applications*, edited by D. E. Ashpis, T. B. Cieslinski, and R. Hirsch, Kluwer Academic, Boston, 1993, pp. 189-223.

M. Sichel
Associate Editor

Influence of a Counterflow Plasma Jet on Supersonic Blunt-Body Pressures

V. M. Fomin* and A. A. Maslov†

Institute of Theoretical and Applied Mechanics, Novosibirsk, Russia

N. D. Malmuth‡

Rockwell Scientific Company, Thousand Oaks, California 91360

and

V. P. Fomichev,§ A. P. Shashkin,¶ T. A. Korotaeva,** A. N. Shiplyuk,†† and G. A. Pozdnyakov‡‡

Institute of Theoretical and Applied Mechanics, Novosibirsk, XXXXX, Russia

Aerodynamic augmentation in the presence of a thin high-temperature onboard plasma jet directed upstream of a slightly blunted cone was studied experimentally and numerically. The flow around a truncated cone cylinder at zero incidence was considered for Mach numbers $M_\infty = 2.0, 2.5$, and 4.0 . For the first time, computationally validated experimental pressure distributions over the model surface in the presence of the plasma jet were obtained. As in the conventional (nonplasma) counterflow jet, two stable operational regimes of the plasma jet were found. These were a short penetration mode and a long penetration mode (LPM) aerospike into the opposing supersonic freestream. The greatest drag reduction occurred in the moderate LPM regime. LPM strong overblowing reduces the benefits. The experimental pressure results were approximately validated against an Euler computational fluid dynamics simulation, modeling a perfect gas hot jet, counterflowing against a perfect gas supersonic freestream. Plasma effects such as electron pressure, radiation, electric field interactions, Joule heating, and induced vorticity, streamers, and plasmoids have been identified that, if accounted for, may improve the comparison. Procedures for the use of these experimental results have been outlined as a baseline that will be useful in separating fluid dynamic/thermal effects from plasma processes in understanding the physics of onboard plasma jets for aerodynamic augmentation.

Introduction

CONSIDERABLE interest exists today regarding the application of onboard plasma devices (OBPD) to enhance aerodynamic performance of flight vehicles. A number of concepts that have been considered include microwave, electron beams, surface and volume discharges such as coronas, and plasma jets. Both numerical and experimental papers devoted to this problem are exemplified in Refs. 1–5. The effect of a laser optical pulse discharge in a supersonic flow giving a spikelike energy source decreases conical and hemispherical nose drag.⁶ Bodies of revolution with varying bluntness ranging from a sphere to a flat-faced cylinder were considered^{3,4,7} for different methods of modifying the flow such as microwaves, heated wires, or glowing discharges.

Originally, much of the interest was stimulated by the possibility of weakening the vehicle shock system by the interaction of the artificially generated plasma with the shocks system. One of our conjectures is that streamers form that create strong delta-functionlike transverse temperature gradients. By Crocco's theorem, these create intense vorticity that can attenuate the shocks. The origin of the plasma aerodynamic augmentation or flow modification is quite controversial, with one camp believing that the major effects are

due to heating and conventional fluid mechanics, whereas another is convinced that it is all due to plasma physics. Most likely, any benefits are due to a combination of both phenomena. The relative proportion of each is related to the device or scheme used to obtain aerodynamic benefits and the range of parameters considered.

How to create a power source using the minimum possible energy in these devices is not obvious now. Weight and size as well as scaling (including identification of the correct parameters) are key for systems integration and tradeoff comparisons against conventional thrust augmentation schemes for rocket and scramjet propelled vehicles. New databases and modeling are needed to deal with these issues. Thermodynamic analyses are also needed to bound the problem. An example of a simple plasma aerodynamic augmentation device is a counterflow plasma jet. Experimental studies on injection of a cold ordinary gas jet were described in Refs. 8–11. The possibility of decreasing the drag of a blunted body was demonstrated in these studies,^{12–14} including experiments and numerical modeling. This work was extended for hot and, later, plasma jets in Refs. 15 and 16. Available data show that the jet effects substantially depend on the shape of the housing parent body as well as on the jet and freestream flow conditions. However, these data are scattered and do not lead to general conclusions.

Most of the OBPD literature gives information on overall forces and moments without providing pressure distributions. This information is the minimum needed to resolve the aforementioned controversy and is a central theme in this paper, which not only provides this information but also computational fluid dynamics (CFD) validations of perfect gas Euler simulations that can be used to test the hypothesis that, for a range of plasma parameter space, plasma effects such as electron pressure, electric fields, charge separation, plasma radiation, and nonequilibrium and vibrational relaxation are small compared to Joule heating source terms modifying a perfect gas simulation of the plasma jet flow modification. This study examines the conjecture that, if the flow patterns and pressures are approximately similar between experiment and an Euler computational model, conventional gasdynamic processes control the flow. Independent of its origin, heat addition significantly modifies the body flowfield, forming a complex system of compression and expansion waves interacting with bifurcational unsteady flow separations and

Presented as Paper 99-4883 at the AIAA 3rd Weakly Ionized Workshop, Norfolk, VA, 1–4 November 1999; received 11 January 2001; revision received 12 December 2001; accepted for publication 12 December 2001. Copyright © 2002 by the authors. Published by the American Institute of Aeronautics and Astronautics, Inc., with permission. Copies of this paper may be made for personal or internal use, on condition that the copier pay the \$10.00 per-copy fee to the Copyright Clearance Center, Inc., 222 Rosewood Drive, Danvers, MA 01923; include the code 0001-1452/02 \$10.00 in correspondence with the CCC.

* (Job title), (dept.).

† (Job title), (dept.).

‡ (Job title), (dept.). Fellow AIAA.

§ (Job title), (dept.).

¶ (Job title), (dept.).

** (Job title), (dept.).

†† (Job title), (dept.).

‡‡ (Job title), (dept.).

cavities. These bifurcations produce significant changes in the body forces and moments.

Existing onboard plasma jet experimental databases contain no pressure distributions. Furthermore, no adequate theoretical model exists currently. To fill these gaps, experiments and modeling were performed. A description of these studies follows.

Test Facility and Equipment

Performance of counterflow plasma jets in supersonic freestreams was the primary focus of the experimental portion of the investigation. A significant capability was the availability of a long run-time Institute of Theoretical and Applied Mechanics T-325, SB RAS supersonic wind tunnel for the counterflow plasma jet experiments. In this facility, the test section, which is $200 \times 200 \times 600$ mm, provided good views of the flow patterns. The long run times were ideally suited for understanding the flow patterns to be described.

Experiments were performed at Mach numbers $M_\infty = 2.0, 2.5$, and 4.0 , total temperature 300 K, and stagnation pressures 1 – 3 atm, which correspond to unit Reynolds numbers $Re_1 = (13\text{--}40) \times 10^6$ 1/m.

The nonuniformity of the Mach number in the test section did not exceed $\pm 0.8\%$. Pressure and temperature in the settling chamber was measured and kept constant within an accuracy of $\pm 0.5\%$. The test article was a cylinder with a blunted cone forebody. The cone half-angle was $\Theta_c = 30^\circ$, and it was 40 mm in diameter and 200 mm in length. The cone was mounted in the wind-tunnel test section with a strut on one window, so that its forebody could be seen through the test section optical glass. The blunted cone nose was necessary to accommodate a nozzle for the plasma generator and to inject the plasma jet. Figure 1 shows the plasma generator nozzle located in the forebody of the model. A dc plasma generator with a variable length arc and gasdynamic displacement of the anode spot on the anode surface was used in the experiments. The discharge current was 30 – 60 A, voltage was 100 – 200 V, and the characteristic value of the power supply in the gas was 6 kW/g. A (continuous) plasma generator produced a hot jet of nitrogen of temperature 5000 K and gas flow rate 0.7 g/s. The body of the plasma generator was bounded by a water-cooling jacket that permitted long, continuous runs. Current, voltage, gas flow rate, and pressure in a prechamber of the plasma generator were measured in the experiments. The plasma generator operational parameters were adjusted before each T-325 wind-tunnel run. The flow conditions were monitored during the runs.

Standard equipment was used for measurements of current, voltage, and pressure. Precision of measurements of current and voltage was $\pm 0.5\%$ and pressure $\pm 3\%$, respectively.

The plasma generator was attached to a strut that did not affect the measured value of the model drag. The metric part of the model was a thin-walled shell that was attached to a strain-gauge balance located on the extreme downstream end of the casing shield. A strain-gauge registered forces acting only on the thin-walled shell. The forces acting on the plasma generator (including the jet reaction force) were compensated by the strut response that was not measured by the balance.

On the forebody of the model, 10 pressure taps were installed, and 6 were placed on the cylindrical afterbody. Three pressure sensors were located inside the model, between the cone and plasma generator. One was located near the strain-gauge balance.

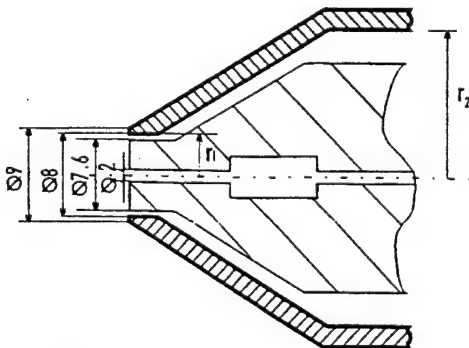


Fig. 1 Plasma generator nozzle, $r_1 = 4$ mm and $r_2 = 17.5$ mm.

The tests included 1) testing of the balance measurement system using a sharp cone model, 2) balance measurements of model drag, 3) pressure measurements on the model surface and inside the model, 4) video filming of the flow pattern with the plasma generator operating, and 5) schlieren pictures of the flow.

Balance and Pressure Measurement Apparatus

The drag force of the model was measured using a strain-gauge, one-component balance with a range of force measurement of 0 – 100 N. The balance was calibrated after each change of the model position in the test section of the T-325 wind tunnel.

The value of the model drag obtained from a strain-gauge balance accounted for the internal pressure in the model using the formula

$$N = B + \int_{r_1}^{r_2} 2\pi r P_{in}(r) dr$$

where B is the force measured by the strain-gauge balance, r_1 is the internal radius of truncation, r_2 is the internal radius of the model forebody (Fig. 1), and $P_{in}(r)$ is the pressure distribution over the internal surface of the forebody.

The pressure distributions on the surface of the model were measured with the taps (diameter 0.7 mm) and strain gauges. These were isolated from the electromagnetic fields of the plasma generator.

Experimental Results

The plasma generator was activated when the desired wind-tunnel flow conditions were established. Plasma generator ignition resulted in a glow enveloping the model and highlighting the flowfield. Two steady flow modes were observed: short jet penetration mode (SPM) into the incoming airflow and long jet penetration mode (LPM). Both modes of flow were observed in the same experiment. The transition from one mode to another was accompanied by transient phenomena, giving different flow patterns. During these transition regimes, a reorganization of the flow structure occurred from one exhibiting a multibarreled jet structure, characteristic of the LPM, to one with one barrel, intrinsic to the SPM. Qualitatively, such phenomena have been previously observed for nonplasma counterflow cold jets embedded in supersonic flows.

Figures 2 show typical schlieren images associated with these experiments exhibiting the aforementioned features. All occur sequentially in one run at nominal, nearly constant wind-tunnel conditions with growing pressure in the plasma generator prechamber. The LPM occurred at the beginning of experiment. Then it transformed itself into the SPM. Following Refs. 8 and 10, the occurrence of the two modes was correlated with the stagnation pressure ratio parameter $P = p_{0j}/p'_{0f}$, where p_{0j} is the total pressure of a plasma jet and p'_{0f} is the total pressure behind normal shock. Figure 2a corresponds to the LPM, where $P = 3.8$. The head bow shock and trailing shocks are obvious. Figure 2c shows the SPM, where $P = 5.0$. An example of a transitional regime, $P = 4.4$, is shown in Fig. 2b. The images of both modes (exposure time ~ 0.01 s) are superimposed in Fig. 2b. A transitional regime exhibiting instability in the zone of interaction of the jet and counterflow was observed in the range $4.1 < P < 4.5$. It is possible to estimate the critical P for which mode transition/bifurcation occurs as approximately 4.3 . This value is slightly higher than that for cold counterflow jets (P critical ~ 3) in similar flow conditions.⁸ The disparity may be related to plasma effects.¹⁷

SPM also appears for $P < 2$. The drag force of the truncated cone model with counterflow plasma jet injection was compared with the value of the drag force of a sharp cone model. Figure 3 shows the values of the drag coefficient of the model $C_D = X/qS$, where X is the drag force of the model, q is the freestream dynamic pressure, and S is the area of model cross section, for various stagnation pressures of the flow p_{0j} , obtained by balance measurements.

Precision of the q_∞ determination was $\pm 0.5\%$. The pressure gauges had a 100 -kPa measurement range, also subject to an error of $\pm 0.5\%$. Total error for C_D was ± 1 – 2% . The maximum error is shown as an 1 bar in Fig. 3 (upper right point). Because the flow under study was unsteady and the model surface was subjected to the high-temperature plasma jet, additional errors could occur due to

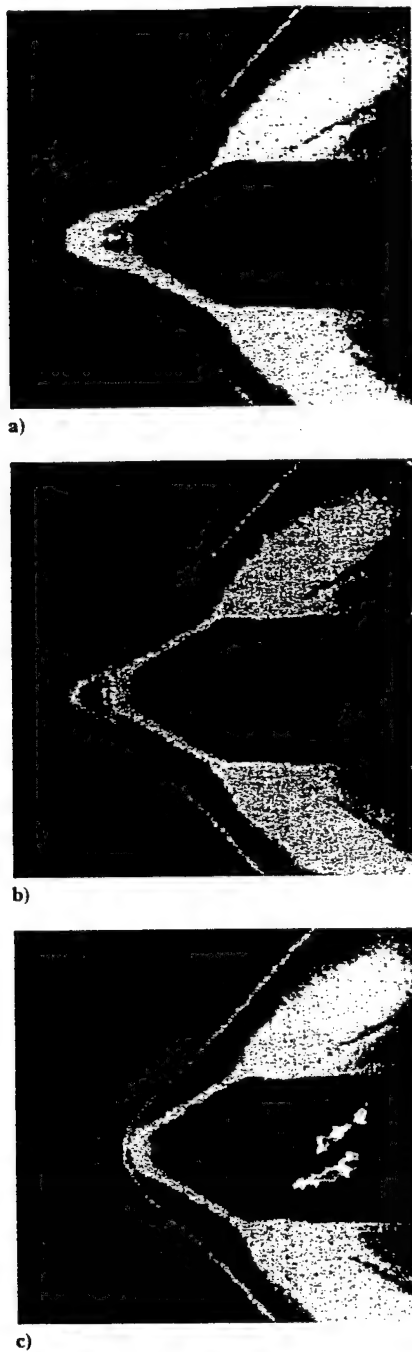


Fig. 2 SPM to LPM transitions.

model erosion. Baseline experiments were carried out with a sharp cone (points 1), blunted cone without a jet (points 2) and with a plasma jet (points 3 and 4) at $M_\infty = 2$.

Surprisingly, the sharp cone has the greatest drag for the investigated range of T-325 freestream pressures. The blunted cone has somewhat less drag. This is due to a suction force on a flat nose, even without the jet.¹⁸ This was not measured in our experiments.

Addition of the plasma jet reduced the drag of the model. The experimental data form two groups of points corresponding to the SPM and the LPM. LPM produced the greatest drag reduction (up to 23%), whereas the drag reduction was not too significant for SPM. For the LPM, the jet penetrates much further into the flow, reducing the effective cone angle/body thickness ratio. Figure 4 shows a plot of the model drag vs the Mach number M_∞ , for $p_{0f} = 100, 200$, and 300 kPa, where 1 refers to a sharp cone, 2 a truncated cone without the jet, and 3 a truncated cone with the jet. The forebody drag was estimated by integration of the measured pressure distributions, accounting for the jet thrust.

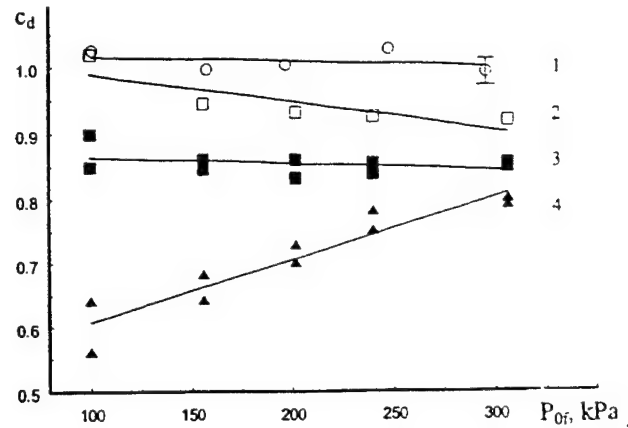


Fig. 3 Cone drag dependence on total pressure P_{0f} : 1, sharp cone; 2, truncated cone without the jet; 3, truncated cone with the plasma jet, SPM, and 4, truncated cone with the plasma jet, LPM.

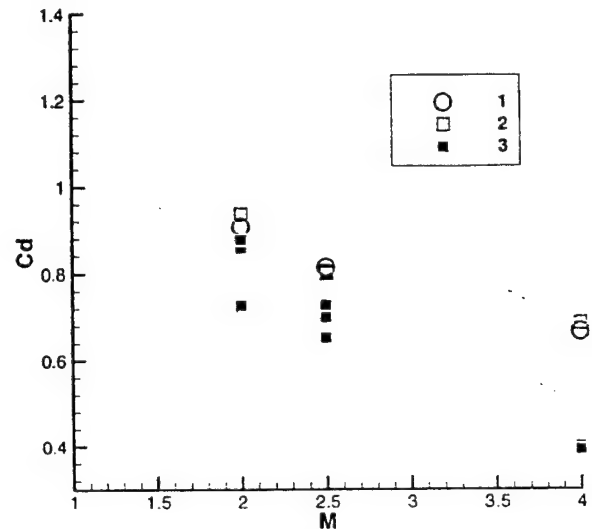


Fig. 4 Model drag dependence on freestream Mach number: 1, sharp cone; 2, truncated cone without the jet; and 3, truncated cone with the plasma jet.

Drag coefficients are plotted vs the freestream total pressure for Mach numbers $M_\infty = 2.0, 2.5$, and 4.0 and for the flow with a jet and without the jet in Fig. 5.

The forces obtained from balance and pressure measurements ($M_\infty = 2.0$) with and without the plasma jet are compared in Fig. 6. It is evident that the integrated surface pressure distribution, accounting for the internal pressure, agrees well with the balance measured forces. This is a mutual validation of our force and pressure measurements.

Computational Studies

As another check of the experiments, a perfect gas model of the flow was implemented computationally. For the comparisons, the governing equations are the inviscid three-dimensional Euler equations for a perfect gas in conservative form. The interaction of the plasma jet with the external flow was modeled by assuming flow variable values such as Mach number and temperature at an internal boundary inside the outer far-field computational domain corresponding to the jet exit boundary. Currently, we are generalizing this model to simulate computationally the interaction of the internal nozzle and external flowfields, including plasma processes.

The gas flow was considered as unsteady with a prescribed initial state. A time-explicit, space-implicit, second-order accurate, central-difference scheme with relaxation smoothing for solving the three-dimensional Euler equations by the finite volume method was used. To obtain a steady-state solution, a time-asymptotic method

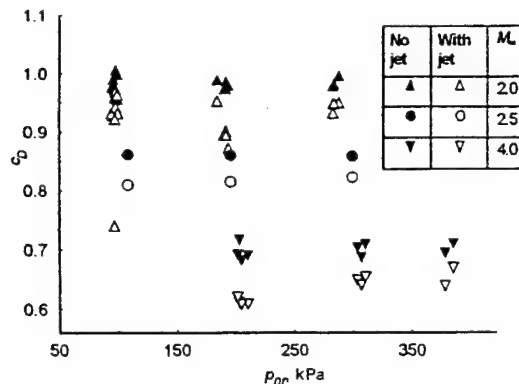


Fig. 5 Drag dependence on total pressure (pressure measurement).

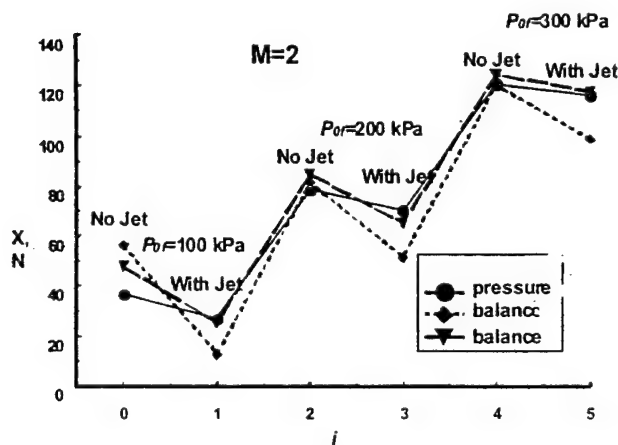


Fig. 6 Drag dependence on total pressure (pressure and balance measurement).

and a shock-capturing weakly nonmonotonic and fully conservative technique was employed. The solutions belong to the class of bounded functions.

For generation of computational grids, the algebraic method of construction of grids¹⁹ was applied. Grid convergence was assessed from calculations on different grids (50×50 , 50×100 , 50×150 , 100×50 , 100×100 , and 150×150) involving varying grid densities on the bodies and in the flow. Global features of the flow solution were preserved on grid refinement but with emergence of subtle local flow details.

Comparison with Experiment

To compare the numerical and experimental data and to analyze the results obtained, a supersonic flow around a truncated cone with a counterflow jet was calculated. The truncated cone parameters were cone half-angle $\Theta_c = 30$ deg, ratio of the midsection diameter d_3 to the front face diameter d_2 of 5:1, and $d_1:d_2 = 1:4$. The freestream conditions were Mach number $M_\infty = 2$, angle of attack $\alpha = 0$ and total temperature $T_{0f} = 283$ K. The Mach number M_{aj} at the jet exit was unity. A specific heat ratio $\gamma = c_p/c_v = 1.4$ was assumed in all calculations. The parameter $P = p_{0j}/p'_{0f}$ was varied in the range 1.15–5. Total temperature in the jet was $T_{0j} = 5000$ K. These parameters were approximately typical of all of the experiments. Both modes (LPM and SPM) were obtained in the calculations.

CFD isotherms of the LPM and the SPM validating those obtained in the experiments are shown in Fig. 7. In Fig. 8, the normalized pressure $C_p = p/2q$, where p is the surface pressure on the model, for $1.7 \leq P \leq 4.5$ is plotted against the dimensionless coordinate X/d_2 , where $d_2 = 9$ mm, for the Mach number $M_\infty = 2$ and $p_{0f} = 1$ atm. Points 1 correspond to a flow regime without a jet and points 2 and 3 with a jet in SPM and LPM, respectively. In Fig. 8, the position of the cone frustum cylinder shoulder is designated by l . The two modes are again evident. In both cases, a significant pressure change due

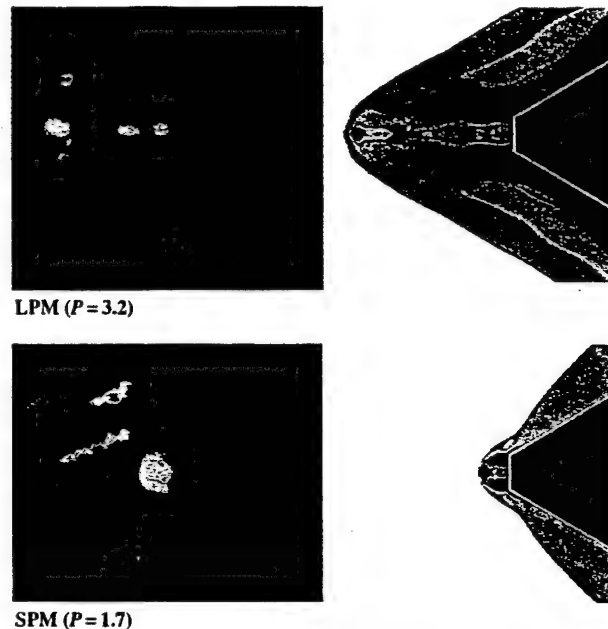


Fig. 7 Photographs and calculated isotherms of flow.

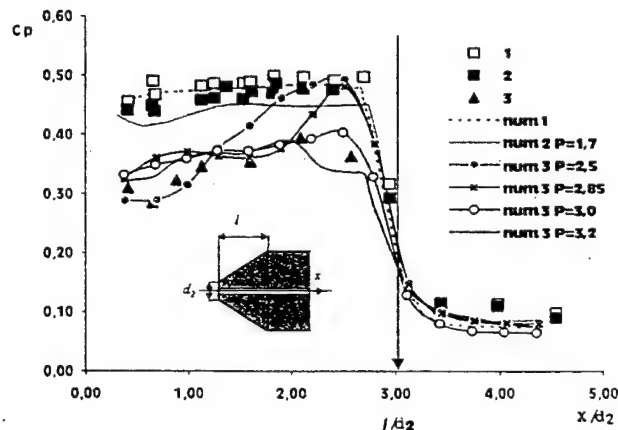


Fig. 8 Pressure distributions over conical and cylindrical surface: 1, truncated cone without a jet and 2 and 3, truncated cone with the plasma jet, SPM and LPM.

to the plasma jet occurs on the model's conical surface. A value of $P = 3.2$ provided the best CFD fit of the lower solid triangle (LPM) experimental points, although a closer estimate for P was 2.4. The value of $P = 1.7$ was used for the upper SPM group. These two cases are shown in Fig. 7. [The parameter P was obtained from experimentally measured pressures in the plasma generator chamber (giving p_{0j}) and the normal shock relations, (giving p'_{0f})].

Uncertainty in estimating P is due to a combination of many factors. These include the time variation of the pressure in the plasma generator, adequacy of assuming choked conditions at the jet exit, heat addition in the nozzle chamber, losses in the conversion of electrical energy into kinetic energy in the nozzle, plasma effects inside and outside the nozzle, and viscous interactions such as shear layers and separations. Separate measurements are needed to assess the plasma generator efficiency. In addition, our earlier mentioned more accurate simulation modeling the coupling of the internal and external flows in the numerics will be used to improve the simulation. Moreover, coupling with plasma chemistry in the high-temperature zones inside the nozzle and the core of the jet needs to be accounted for. Despite the need for such refinements, it is remarkable that the complete pressure distribution is so well reproduced with a reasonable average value for P , even on a relative basis. Absolute levels will require inclusion of plasma effects, examples of which have been cited earlier herein.

Agreement of the perfect gas Euler CFD pressure distributions with the measurements at selective flow conditions such as Mach 2 strongly suggests much of the physics at that Mach number resembles conventional (nonplasma) counterflow jet gasdynamics. The validated pressure distributions such as those obtained in this investigation (for the first time to our knowledge for plasma jets) are more convincing than drag measurements in making this assertion. The proposition that, if pressure distributions of the plasma jet flow are close to the conventional jet flow, plasma effects are insignificant is not axiomatically proven here. However, evidence of the truth of this proposition is the similarity of the observed and computed flow patterns obtained in this study, as shown in the figures. Both indications suggest that this conclusion is at least one, but not a unique, possibility. Mathematically, if the pressure distribution is prescribed in the classical inverse problem of gasdynamics, and if certain side conditions such as closure for an airfoil are also given, a unique solution for the body shape and resulting flowfield is obtained. A similar statement can be conjectured for a body of revolution if a single set of governing equations of motion is used to model the flow. On the other hand, if the form of the equations of motion can be allowed to vary from conventional gasdynamics to real gas plasma gasdynamics, then this conclusion, although plausible, may be challenging to prove. To summarize, coincidence of the pressures for the plasma jet flow with those of a perfect gas jet is a necessary but not sufficient condition to assert that the two flows are equivalent. However, the resemblance of the flow patterns of the computations with those observed makes this conclusion plausible.

Although comparisons of drag between plasma and conventional counterflow jets is less convincing to arrive at such a conclusion, because they contain less information, they are an important check on the pressure measurements and useful to assess the energetic efficiency of possible drag reductions with plasma counterflow jets. These observations are major findings of this investigation. In other experiments conducted by the authors at Mach 6 and not discussed in this paper, some qualitative but less quantitative similarity is evident, and our conjecture is that plasma physics accordingly plays a more significant role. In Fig. 9, the total drag of the body

$$C_D = \left(2\pi \cdot \int_0^{d_3/2} p \cdot y \cdot dy + 2\pi \cdot \int_0^{d_1/2} \rho_a \cdot v_a^2 \cdot y \cdot dy \right) / q \cdot S$$

as a function of $n = p_{0j}/p_\infty$ is shown, where v_a and ρ_a are the velocity and the density in the jet exit, respectively. Here, the total drag of the body is understood to be the pressure drag plus the reaction force of the counterflow jet.

As indicated earlier, the calculations and experiments confirm the existence of the LPM and SPM configurations. The appearance of these regimes depends mainly on the pressure ratio P . Plasma effects, temperature, geometry, and perhaps other factors may be significant but have not yet been studied. LPM has appeared in

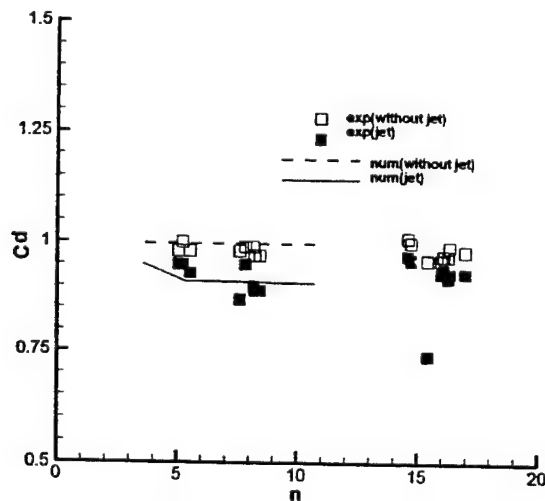


Fig. 9 Influence of the jet pressure ratio on total body drag.

the range $2 < P < 4.5$ in our studies. Outside this range, SPM was observed.

The main features of these configurations that were deduced primarily from Euler computations performed in this investigation are as follows:

1) For the SPM mode, the underexpanded jet forms a new body that moves upstream of the jetless bow shock and forms a single cell, as shown in Fig. 10. Conventional perfect gas nonplasma counterflow jets exhibiting this behavior have been previously studied.⁸

2) For the LPM mode, for some range of the pressure ratio P , the jet is compressed, and its cross section is decreased. It penetrates the jetless bow shock and forms the multicellular structure shown in Fig. 11. In this structure, a few small toroidal vortices are evident. Penetration may be relatively short or long. When the penetration is intermediate, suction, which is observed on the side surfaces of the body, can be significant. Long penetration and overblowing for a slender jet does not lead to significant decrease of the pressure on the side surfaces of the body. Here, the aerospike or long penetration jet is too far upstream and is of such high fineness ratio that it cannot significantly slenderize the body because its shock pattern is very weak and oblique and has a negligible attenuation of the jetless blunt-body bow shock system. Accordingly, an optimal range of parameters exists that maximizes drag decrease.

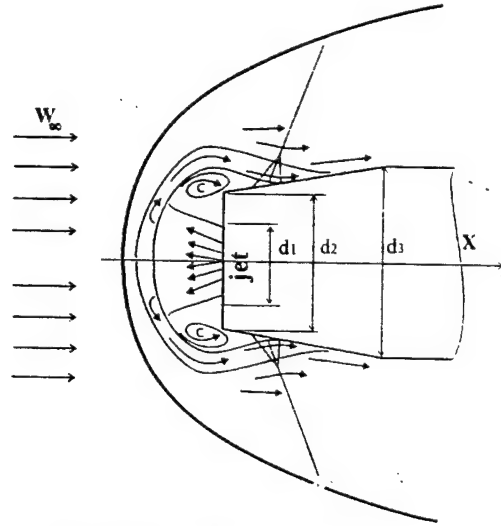


Fig. 10 Counterflow jet flow pattern, SPM.

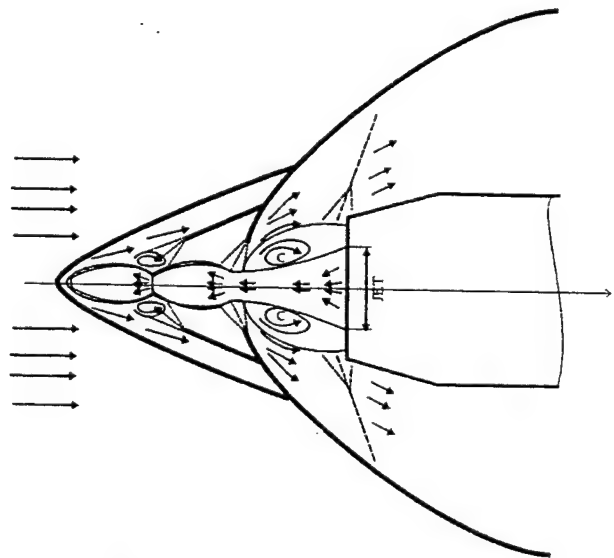


Fig. 11 Counterflow jet flow pattern, LPM.

The efficiency of plasma jet ejection in reducing drag may be estimated by comparing drag power to input power. Thus,

$$\eta = \Delta C_D \cdot q \cdot S \cdot V / Q_j$$

where ΔC_D is the reduction in drag coefficient due to the plasma jet from the value for the same body with the plasma jet off, q is the freestream dynamic pressure, S is the frontal area of the model, V is the freestream velocity, and Q_j is the electrical power used to develop plasma jet.

The value of η has been calculated for the tests discussed herein. At a freestream stagnation pressure of 1 atm, the LPM jet gave $\eta = 1.98$. For the SPM, this parameter was 0.5. This conclusively demonstrates the drag benefits of the LPM configuration. With flight-weight plasma generator units, this gain can be translated into more efficient drag reduction of hypersonic cruise vehicles such as blunted shapes for which the nose pressure drag is a dominant part of the drag buildup. Such drag reductions could have a substantial impact on aerodynamic efficiency (L/D) and result in higher payloads as well as reduced mission cost.

Qualitative Interpretations and Trends

Our calculations give trends similar to those observed by Romeo and Sterret^{20,21} for cold jets. They show bifurcations as well as qualitative details of the observed flow patterns reported by these authors.

For counterflow jets, the jet specific impulse (per area unit) is higher than the impulse in the external stream downstream of the normal shock wave. This consideration suggests as a governing parameter $P = P_{0j}/P'_{0f}$, which occurs in our calculations, where P_{0j} is the stagnation pressure in the jet and P'_{0f} is the stagnation pressure downstream of the normal shock wave.

SPM and LPM Regimes

The role of jet exit Mach number and temperature, as well as the ratio of nozzle to rim diameters, will be suppressed in this part of the discussion. (In all our calculations, this ratio was assumed to be in the range 0.2–0.25.)

Although SPM and LPM are the major modes, transitional regimes between these modes also exist. In particular, our experiments indicate different SPM regimes as shown in Fig. 12, which is also a validation of our computational model against experimental data for prediction of jet penetration and drag. We conjecture that these regimes are affected by P .

For low momentum of the jet compared to that behind the shock, SPM occurs. Here, the counterflow jet forms a reverse-circulation region whose slip line/shear layer reattaches on the side surface (Fig. 10).

An LPM regime forms when part of the jet is supersonic with a stable multibarrel shock structure. This can occur when the jet has sufficiently high momentum compared to that of the flow behind the normal shock. In this regime, the jet penetrates the flow ahead of the bow shock wave of the body with the jet off (jetless case). This creates a new oblique shock structure ahead of the bow shock that is altered from the jetless case. Our calculations suggest that a necessary condition for this regime's stability is reattachment of the eddy slip line on the rim face in contrast to its conical or cylindrical surfaces. The jet seems to be associated with a toroidal vortex and almost constant pressure inside the reverse-circulation region shown in Fig. 11. In our calculations, existence of this eddy is connected with the bifurcation of the flow at the reattachment point. These remarks pertain to the case considered in this study in which the jet diameter is small compared to the front face diameter. This case contrasts to that considered by Romeo and Sterret,^{20,21} where the jet and frontal diameters are nearly the same and the rim is small.

From the computations, one can see that the attachment point can move along the flat face containing the jet exit. As soon as the attachment point migrates to the side surface, the pressure in the recirculation zone decreases. This causes a decrease in size of this zone and, correspondingly, in attachment point migration back to its original position on the flat face. This bistable equilibrium is subsequently recycled into an oscillation unless a trigger such as

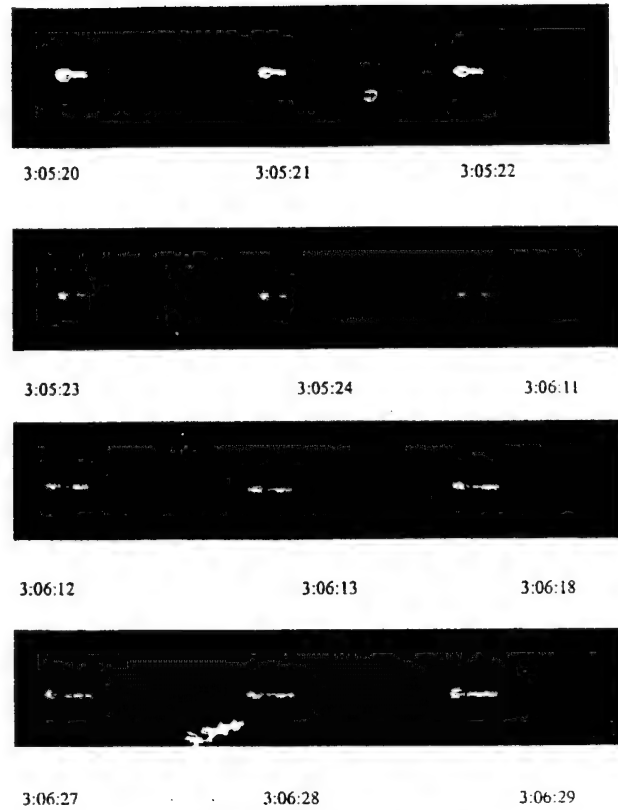


Fig. 12 Movie stills of LPM mode.

a downstream pressure perturbation disrupts it. If the jet becomes strongly underexpanded, the flow may transition directly to SPM. As a rule, the oscillation of the attachment point near the boundary of the flat face causes LPM perturbations involving periodic changes of its structure and length. Although, opportunities for these oscillations to occur, the LPM can be quite stable, as shown in Fig. 12. These movie stills from our tests show high dynamic stability of the jet in the LPM mode from an initial transient. This stability has practical implications for drag reduction practical application on blunt hypersonic vehicles where the forebody drag can have a major impact on payload.

For high P (strongly underexpanded jet), a single SPM shock forms again, in contrast to the split LPM configuration.

Jet Exit Mach Number Effects

The following discussion is based on our experiments and calculations.

$M_a > 1$

If the counterflow jet is supersonic and weakly underexpanded or overexpanded at the nozzle exit, multiple cells can arise. A weakly underexpanded jet exhibits small area changes along its length. Some perturbations cause Mach number increases with reduced pressure and shrinkage of the jet. This causes its specific impulse to grow, giving increased penetration. Strongly underexpanded jets exhibit substantial area increase, resulting in a specific impulse decrease, producing a shock wave upstream of the jet. If the impulse decreases still further, the flow reverts to the SPM regime. If the supersonic jet is weakly overexpanded, its cross section decreases. This leads to an increased specific impulse and an LPM configuration. Strongly overexpanded jets create a normal shock with a decreased specific impulse that leads to SPM.

$M_a = 1$

For sonic jets, supersonic and subsonic conditions can occur upstream of the jet similar to Laval nozzle flow. A weakly underexpanded jet can expand, giving supersonic flow. This leads to LPM. SPM can occur for strongly underexpanded or overexpanded jets.

$Ma < 1$

Here, the LPM regime can be associated with a convergent lip angle with acceleration to critical conditions and an upstream throat and farther upstream behavior already discussed for the choked case. We have observed this behavior in our computations, but only for high-temperature experiments.

To summarize, LPM flow in our calculations was observed for supersonic jets whose pressure differs little from the external jet pressure. It is not very important whether the nozzle exit is subsonic, sonic, or supersonic. If conditions exist for a supersonic transition and the jet is generally weakly underexpanded, LPM can occur. These are necessary but insufficient conditions. An associated vortex seems also to be a feature of this flow.

Effects of Separation

Some interesting studies that are useful in understanding the effect of the separated region in the LPM mode stem from the work of Ehrich,²² who extended the Zhukovskii hodograph method discussed by Milne-Thompson²³ to infinite slot two-dimensional (planar) jets in a crossflow. His closed-form solutions include counterflow jets as a special case. For the latter, penetration was limited if the flow was attached to the outside of the slot. In contrast, the penetration became infinite at a finite jet-to-freestream velocity ratio if the jet was separated over the slot.

Summary

Results of experimental and numerical studies of the influence of a thin counterflow, high-temperature jet on the aerodynamic characteristics of a blunt body in supersonic flow have been presented.

The experiments were conducted with plasma jet injection into supersonic and low hypersonic freestreams. They included balance, pressure distribution measurements, video and photographic visualization, and schlieren pictures. Two stable regimes of the plasma jet flow resembling ordinary perfect gas counterflow jets were found. These are SPM and LPM into the freestream. LPM produced the only substantial drag reduction, which was especially strong for transition from SPM to LPM.

Experimental pressure distributions over the surface of a truncated cone-cylinder model in the presence of a plasma jet were obtained. These distributions represent the first data of this type for onboard plasma jets and should be useful for separating aerodynamic heating from plasma physics phenomena in aerodynamic augmentation.

The experimental results were compared to Euler perfect-gas, hot-jet CFD models. Both SPM and LPM were obtained with these simulations. Based on our calculations, we believe that the bifurcation is driven by interaction of separated flow regions and the delicate role of reattachment points that interact with the flow and shock system on a global scale. These can be driven by the nozzle cavity flow and oscillations from the plasma generator. From a different perspective, we believe that the bifurcation is related to a nonuniqueness of the steady-state boundary value problem for the gasdynamic equations of motion, which may be an eigenproblem in a bifurcation stability sense. This indeterminacy relates to the classical incompressible problem of oblique collision of jets, which is nonunique to within an unknown constant. This nonuniqueness is related to the need to incorporate the flow history through determinism to assess the current state of the colliding jet flow. In this connection, conventional time-marching CFD codes may give path-dependent solutions rather than unique time asymptotics, due to a number of factors including stability of the temporal solution that might be an asymptotically bistable oscillation between the bifurcation SPM and LPM modes. We have correlated the LPM-SPM switch to a change in the position of the reattachment. We noticed migration of the attachment point from the forward face containing the jet exit to the inclined face and correlated this with LPM and SPM.

The numerical results are in reasonable agreement with the experimental data for supersonic freestreams, both for pressure distributions and drag, if the key stagnation pressure parameter P was adjusted within the experimentally observed range. This suggests that the dominant physics is fluid dynamics and that the plasma effects are relatively small at moderate supersonic Mach numbers. In particular, the large drag reductions associated with the LPM re-

sult from the resulting suction on the forward facing parts of the cone cylinder, namely, the conical face. Nevertheless, aerodynamic heating that controls much of the moderate Mach number flow has an important link to plasma processes, which are the only means of producing the intense energy densities and high temperatures in the plasma jet. These temperatures can be several thousand degrees Kelvin higher than those of conventionally heated jets. For hypersonic cases, the agreement of calculation and experimental results is only qualitative. We believe that this uncertainty is partly caused by plasma effects that were not taken into account. Future work will be focused on this aspect.

Acknowledgments

The financial support of The Boeing Company and Rockwell Scientific Company is acknowledged. Portions of this effort were also supported by the Air Force Office of Scientific Research, Air Force Materials Command, under Contracts F49620-92-C-0006 and F49620-96-C-0004. The authors thank A. N. Timoshevsky for advice on the plasma generator, A. A. Pavlov for advice on optical measurement, B. V. Postnikov and B. A. Pozdniakov for preparation of the equipment and participation in the experiments. The U.S. Government is authorized to reproduce and distribute reprints for government purposes, notwithstanding any copyright notation thereon. The views and conclusions herein are those of the authors and should not be interpreted as necessarily representing the official policies or endorsements, either expressed, or implied of the Air Force Office of Scientific Research or the U.S. Government.

References

- Aradailov, S. I., "Influence of Energy Output in a Shock Layer on Supersonic Flight of Bodies," *Izvestiya Akademii Nauk SSSR, MZhG*, No. 4, 1987, pp. 178-184 (in Russian).
- Bazhenova, T. V., Lyakhov, V. N., Pankova, M. B., and Kharitonov, S. M., "Numerical Simulation of a Thermal Non-uniformity in a Supersonic Flow on a Drag Coefficient of a Spherical Body," *Chislennoe Modelirovanie Nestatsionarnykh Gazodinamicheskikh i MGD Tsechenii*, 1989 (in Russian).
- Bergelson, V. I., Medvedyuk, S. A., Nemchinov, I. V., Orlova, T. I., and Hazins, V. M., "Aerodynamic Characteristics of a Body at Various Localization of a Thermal Needle," *Matematicheskoe Modelirovanie*, Vol. 8, No. 1, 1996, pp. 3-10 (in Russian).
- Borsov, V. Y., Rybka, I. V., and Yurev, A. S., "Influence of the Local Energy Input in a Hypersonic Flow on Drag of Bodies with Various Bluntness," *IFZh*, Vol. 67, No. 5, 1994, pp. 355-361 (in Russian).
- Chernyi, G. G., "The Impact of Electromagnetic Energy Addition to Air Near the Flying Body on its Aerodynamic Characteristics," *Proceedings of Weakly Ionized Gas Workshop*, AIAA, Reston, VA, 1998.
- Tretyakov, P. K., Fomin, V. M., and Yakovlev, V. I., "New Principles of Control of Aerophysical Processes Research Development," *Proceedings ICMAR-96*, Pt. 2, 1996, pp. 210-220.
- Fomin, V. M., Lebedev, A. V., and Ivanchenko, A. I., "Speckle Photography of Turbulence Variation After Shock Wave Passage," *Proceedings ICMAR-98*, Pt. 2, 1998, pp. 54-56.
- Finley, P. J., "The Flow of a Jet From a Body Opposing a Supersonic Free Stream," *Journal of Fluid Mechanics*, Vol. 26, Pt. 2, 1966, pp. 337-368.
- Kalinin, V. M., and Melbardt, A. M., "Parameters of Simulation in a Problem of the Supersonic Unexpanded Jet Efflux Forward to a Supersonic Flow," *Izvestia Akademii Nauk SSSR, MZhG*, No. 3, 1980, pp. 83-89 (in Russian).
- Yudintsev, Y. N., and Chirkashenko, V. F., "Interaction Regimes in a Counterflow Jet with a Supersonic Flow," *Gasodinamika i Akustika Struyinykh Tsechenii, Institute of Theoretical and Applied Mechanics*, Novosibirsk, Russia, 1979, pp. 75-106 (in Russian).
- Zhirikov, B. L., and Petrov, K. P., "Research of Interaction of Jets with a Counter Flow Flowing from a Frontal Surface of a Body of Revolution," *Sovremennye Problemy Aerodinamiki, Machinostroenie*, Moscow, 1987, pp. 114-122 (in Russian).
- Ganiev, Y. C., Gordeev, V. P., Krasilnikov, A. V., Lagutin, V. I., and Otmennikov, V. N., "Experimental Study of the Possibility of Reducing Aerodynamic Drag by Employing Plasma Injection," *Proceedings Third International Conference on Experimental Fluid Mechanics*, 1997, p. 6.
- Klimov, A., "Anomalous Supersonic Flow and Shock Wave Structure in Weakly Ionized Plasmas," *Proceedings 1st Workshop on Weakly Ionized Gases*, 1997.
- Leonov, S., "Experiments on Influence of Plasma Jet Lift and Drag of Wing," *Proceedings 1st Workshop on Weakly Ionized Gases*, 1997.
- Hornung, H. G., "The Forebody Drag of a Cone with a Counterflow Jet in Supersonic Flow," Internal Rept., 1997.

¹⁶Shang, J. S., Hayes, J., and Menart, J., "Hypersonic Flow over a Blunt Body with Plasma Injection," AIAA Paper 2001-0344, Jan. 2001.

¹⁷Lukianov, G. A., *Supersonic Plasma Jet*, Mashinostroenie, Moscow, 1985, 264p (in Russian).

¹⁸Chernyi, G. G., "High Velocity Supersonic Flow," *Fizmatlit*, 1959, 220p (in Russian).

¹⁹Korotaeva, T. A., Rakhimov, R. D., and Shashkin, A. P., "Computational Mesh Construction for Numerical Analysis of Three-Dimensional Supersonic Flow over Two Bodies," *Thermophysics and Aeromechanics*, Vol. 3, No. 3, 1996.

²⁰Romeo, D. J., and Sterret, J. R., "Exploratory Investigation of a Forward-Facing Jet on the Bow Shock of a Blunt Body in a Mach 6 Free Stream," NASA TN D-1605, Feb. 1963.

²¹Romeo, D. J., and Sterret, J. R., "Flowfield for Sonic Jet Exhausting Counter to Hypersonic Mainstream," *AIAA Journal*, Vol. 3, No. 3, 1965, pp. 544-546.

²²Ehrich, F., "Penetration and Deflection of Jets Oblique to a General Stream," *Journal of the Aeronautical Sciences*, Feb. 1953, pp. 99-104.

²³Milne Thompson, L. M., *Theoretical Hydrodynamics*, 3rd ed., Macmillan, New York, 1953.

²⁴Fomin, V. M., Maslov, A. A., and Malmuth, N. D., "Experimental Investigation of Counterflow Plasma Jet in Front of Blunted Body for High Mach Number Flows," *Proceedings of the 2nd Workshop on Magneto-Plasma Aerodynamics in Aerospace Applications*, IVTAN, Moscow, 2000, pp. 112-116.

²⁵Fomin, V. M., Maslov, A. A., and Malmuth, N. D., "Numerical Investigation of Counterflow Jet Penetration in Hypersonic Flow," *Proceedings of the 2nd Workshop on Magneto-Plasma Aerodynamics in Aerospace Applications*, IVTAN, Moscow, 2000, pp. 116-121.

P. Givi

Associate Editor

Dynamics of Slender Bodies Separating from Rectangular Cavities

V. I. Shalaev* and A. V. Fedorov†

Moscow Institute of Physics and Technology, Zhukovskii, 14080, Russia
and

N. D. Malmuth‡

Rockwell Science Center, Thousand Oaks, California 91330

Vertical and pitching motions (two degrees of freedom) of a thin body of revolution separating from a rectangular cavity in a subsonic stream are investigated using combined asymptotic and numerical methods. The analysis is based on explicit analytical solutions for the lift force and pitching moment obtained in our previous studies. Body trajectory dependencies on initial conditions, body parameters, and freestream velocity are studied. The problem is divided into three phases of the motion. In phase 1, the body is inside the cavity. In phase 2, the body crosses the shear layer, and in phase 3, the body is outside the cavity. For phases 1 and 3, analytical solutions of the body dynamics are obtained for typical cases. This analysis provides insight into the separation process and identifies governing lumped nondimensional parameters relevant to the body dynamics as well providing a model that can provide quick, computationally non-intensive estimates of store separation with a personal computer. The role of the nondimensional parameters in the dynamic stability eigenvalues is identified and found particularly useful in this connection. These parameters implicitly contain the effect of the shear layer. Numerical calculations for all three phases are in good agreement with a major portion of the free-drop experimental data obtained in a subsonic wind tunnel. However, there are cases when the agreement is only satisfactory. The discrepancy is associated with a pitching bifurcation when the body crosses the shear layer. It is shown that small variation of the initial conditions can trigger quick transition from one pitch angle trajectory to another and cause dramatic changes of the body trajectory outside the cavity.

Nomenclature

$a(x)$	= local body radius	X, Y, Z	= Cartesian laboratory frame with origin shown in Fig. 1a
a_0	= maximum body radius	X_c, Y_c, Z_c	= Cartesian moving body axes with origin at body c.g.
b_i	= coefficient defined after Eqs. (4), $i = 1, 2$	x, y, z	= Cartesian moving body axes at general location in body
b_{ij}	= coefficient defined after Eqs. (4), $i, j = 1, 2$	α	= pitch angle or angle of attack
c_z	= gravity force coefficient (Froude number), Eq. (2c)	$\alpha_{11}, \alpha_{12}, \alpha_{22}$	= coefficients defined after Eq. (3)
c_l	= lift force apparent mass, Eq. (2c)	γ	= angular velocity stability parameter, $\text{Re}(\lambda)$
c_m	= apparent pitch inertia, Eq. (2c)	$\Delta_1, \Delta_2, \Delta_3$	= coefficients defined after Eqs. (4)
G_1, G_2, G_3	= coefficients defined in Eq. (3d)	δ	= body half-thickness ratio, \hat{a}_0/\hat{l}_0
g	= gravity acceleration	ϑ	= azimuth angle
g_0, g_1, g_2	= body shape factors, Eq. (3c)	λ	= eigenvalue
$H(X, t)$	= vertical distance from body axis to slip surface	ρ	= density
H_0	= cavity depth	Φ	= near-field flow potential
I	= moment of inertia	Ω	= angular frequency of body oscillations, $-\text{Im}(\lambda)$
L	= lift force	ω	= pitch angular velocity
l_0	= body length	ω_a	= defined in Eq. (2b)
M	= pitch moment		
m	= body mass		
p	= pressure		
t	= time		
u, v, w	= flow velocity components		
V_a	= defined in Eq. (2b)		
V_r	= characteristic vertical speed		
V_0	= body initial vertical speed, see Eq. (2d)		

Subscripts

a	= body cross section of radius a
b	= body surface
c	= c.g.
e	= body base
0	= initial value
∞	= freestream

Superscripts

\wedge	= dimensional value
$+$	= inside the cavity

Introduction

MODELING of store separation from a cavity, even into a subsonic external stream is a very difficult problem that is the subject of the intensive application of current computational fluid

Received 12 October 2000; presented as Paper 2001-2996 at the AIAA 31st Fluid Dynamics Conference, Anaheim, CA, 11–14 June 2001; revision received 3 September 2001; accepted for publication 3 September 2001. Copyright © 2001 by the American Institute of Aeronautics and Astronautics, Inc. All rights reserved. Copies of this paper may be made for personal or internal use, on condition that the copier pay the \$10.00 per-copy fee to the Copyright Clearance Center, Inc., 222 Rosewood Drive, Danvers, MA 01923; include the code 0001-1452/02 \$10.00 in correspondence with the CCC.

* (Job title), (dept.).

† Associate Professor, (dept.). Member AIAA.

‡ Senior Scientist, Department of Material Sciences. Fellow AIAA.

dynamics. The motivation of the work described herein is the need for quick methods for certification and assessment of the physics of store separation from cavities. Similar rapid evaluation methods are needed for stage and cargo separations. A variety of computational methods are under development.¹⁻³ As contrasted to pure computational modeling, this paper discusses a combined asymptotic and numerical approach. It will be applied to solve aerodynamic problems relevant to separation of a thin body of revolution from rectangular cavities into subsonic or transonic flows.^{4,5} The separation process can be divided into three phases. In phase 1, the body is inside the cavity. In phase 2, the body crosses the shear layer that separates the cavity flow from the external flow. In phase 3, the body is outside the cavity. In many practical cases, viscous effects can be approximated with inviscid models. As an example, a vortex sheet representing an infinitesimally thin slip surface can be used to approximate the shear layer over a cavity. This approach is consistent with simulating the cavity shear layer interaction as a rational outer solution that is associated with viscous-inviscid interaction theory. This is an extension of the concept of transpiration velocities (outer limit of inner solution for asymptotic matching) that arises in boundary-layer viscous-inviscid interactions. It leads to a self-consistent simulation of the shear layer as an inviscid vortex sheet. Also, we time average the unsteady motions of the shear layer, because these are on a timescale that is at least three orders faster than the Froude scale of the dropping body. This is a self-consistent approximation that should be realistic for the practical case of high Reynolds number of the approaching boundary layer.

Also, the flow over the separating body can be modeled using slender body theory.⁶ In Refs. 4 and 5, effects of the side cavity walls were shown to be negligible in all phases of the separation process. In the analysis of this paper, the near-field flow associated with the body aerodynamics is governed by a system of nonlinear integro-differential equations. In Refs. 4 and 5, this problem was analyzed using asymptotic methods giving explicit analytical expressions for the lift force and pitching moment acting on the body in all three phases of the separation process. In the analysis, the slip-surface displacement is neglected. A more general case is when the slip surface is a free boundary supporting nonlinear boundary conditions and interacting with the solution. For the practically important case of small deflections, the boundary conditions can be linearized on the slip surface, on the length scale of the cavity. Local flow scales have larger deflections in which an iterative scheme needs to be used. The nondeflected slip surface corresponds to the initial iterate in such a small-perturbation scheme.

Problem Formulation

In this paper, we couple our previous results on the body aerodynamics with the body dynamics and analyze two-degree-of-freedom (2-DOF) vertical and pitching motions induced by aerodynamic and gravity forces during the separation process. The coordinate systems XYZ (attached to the cavity) and $oxyz$ (attached to the body center of gravity) are shown in Fig. 1. The oxy frame is inclined with respect to the XY frame at an angle of attack $\alpha(t)$. This frame can rotate around the oz axis with the angular speed $\omega(t) = d\alpha/dt$. The c.g. coordinates are expressed as $X_c = Z_c = 0$ and $Y_c(t)$; $H(X, t) = Y_c - \alpha X$ is the vertical coordinate of the body axis. Using scaling of the slender body theory,⁶ we introduce the nondimensional variables

$$\begin{aligned} X &= \bar{X}/\bar{l}_0, & Y &= \bar{Y}/\bar{a}_0, & Z &= \bar{Z}/\bar{a}_0, & x &= \bar{x}/\bar{l}_0 \\ y &= \bar{y}/\bar{a}_0, & z &= \bar{z}/\bar{a}_0, & t &= U_\infty \bar{t}/\bar{l}_0 \\ \alpha &= \bar{\alpha}/\delta, & V_c &= \bar{V}_c/\bar{V}_r, & \omega &= \delta U_\infty \bar{\omega}/\bar{l}_0 \end{aligned} \quad (1)$$

where the body half-thickness ratio δ is treated as a small parameter. Crossflow velocities and coordinates are normalized by δU_∞ and \bar{a}_0 , respectively. The streamwise and axial coordinates are scaled using \bar{l}_0 , and the pressure perturbation p is normalized with respect to $\rho_\infty U_\infty^2 \delta^2 \bar{l}_0^2$.

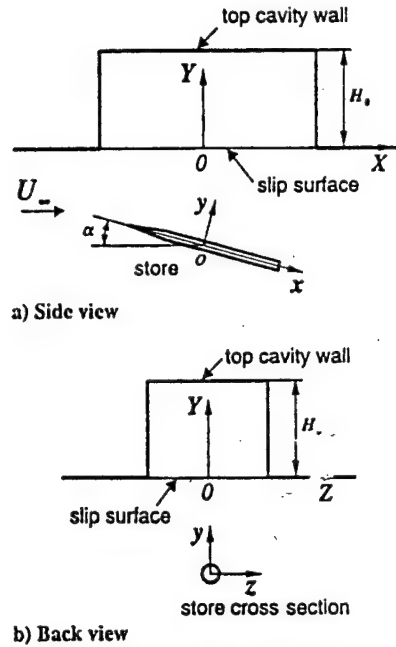


Fig. 1 Scheme of store separation.

As shown in Ref. 5, the equations for vertical and pitching body motions can be expressed in the form

$$\begin{aligned} \frac{d(V_c + c_l V_a)}{dt} &= c_l L(t) - c_g, & \frac{dY_c}{dt} &= V_c(t) \\ \frac{d(\omega + c_m \omega_a)}{dt} &= c_m M(t), & \frac{d\alpha}{dt} &= \omega(t) \end{aligned} \quad (2a)$$

$$\begin{aligned} V_a(t) &= \int_{x_0}^{x_r} \int_0^{2\pi} \Phi(x, \theta, t) a(x) d\theta dx \\ \omega_a(t) &= \int_{x_0}^{x_r} \int_0^{2\pi} \Phi(x, \theta, t) a(x) x d\theta dx \end{aligned} \quad (2b)$$

$$c_g = \frac{g \bar{l}_0}{\delta U_\infty^2}, \quad c_l = \frac{\pi \rho_\infty \bar{l}_0^3 \delta^2}{m}, \quad c_m = \frac{\pi \rho_\infty \bar{l}_0^3 \delta^2}{I} \quad (2c)$$

where x_0 and x_r are coordinates of the body nose and base, respectively, and Φ is the near field with respect to the body (inner) flow potential. We consider the Cauchy initial-value problem for Eqs. (2a) assuming that the body speeds, c.g. coordinate, and angle of attack are prescribed at the initial time $t = 0$ as

$$V_c(0) = V_0, \quad \omega(0) = \omega_0, \quad Y_c(0) = Y_0, \quad \alpha(0) = \alpha_0 \quad (2d)$$

Note that dV_a/dt and $d\omega_a/dt$ in Eq. (2a) represent the time derivative of the crossflow potential (incompressible harmonic inner solution) needed for the pressure in the crossflow plane from the unsteady Bernoulli equation. The terms L_1 and M_1 are integrals involving the square of the crossflow speed that also appear in the Bernoulli law for the pressure in the crossflow inner problem. These are determined from the square of the crossflow gradient of Φ .

In this paper, analytical solutions of the problem (2a-2d) for phase 1 are obtained for small lift forces compared to the weight. Slip-surface deflections are neglected, and Eqs. (2a-2d) are transformed into two decoupled ordinary differential equations with constant coefficients. A stability analysis of their solutions is performed, and behaviors of the pitch angle $\alpha(t)$ and the vertical coordinate $Y_c(t)$ are discussed for typical cases. In addition, the theoretical model for all three phases [in Eqs. (2) (without the stability linearizations)] is evaluated by comparison of the predicted trajectories with the experimental data of Ref. 7. The paper concludes with some parametric trajectory studies.

Phase 1: Body Inside Cavity

The lift force $L(t)$ and the pitching moment $M(t)$ acting on the body moving inside the cavity are derived in Ref. 5. They are expressed as integrals along the body axis with the integrands being a power series with respect to the parameters $q_1(x, t) = 0.5a/(H_0 - H)$ and $q = 0.5a/H$, where H_0 is cavity depth shown in Figs. 1a and 1b. If the body is far from the top cavity wall and the slip surface, then q_1 and q can be treated as small parameters. When terms of the order of $O(q^3, q_1^3)$ are neglected, the body cross section vertical velocity $V_a^+(t)$ and angular velocity $\omega_a^+(t)$ are expressed in the form

$$V_a^+(t) \equiv \alpha_{11}(t)V_c(t) - \alpha_{12}(t)\omega(t)$$

$$\omega_a(t) \equiv \alpha_{12}(t)V_c(t) - \alpha_{22}(t)\omega(t) \quad (3a)$$

$$\alpha_{11}(t) \equiv \pi[g_0 + G_0(t)], \quad \alpha_{12}(t) \equiv \pi[g_1 + G_1(t)]$$

$$\alpha_{22}(t) \equiv -\pi[g_2 + G_2(t)] \quad (3b)$$

$$g_0 \equiv \int_{x_0}^{x_e} a^2(x) dx, \quad g_1 \equiv \int_{x_0}^{x_e} a^2(x)x dx$$

$$g_2 \equiv \int_{x_0}^{x_e} a^2(x)x^2 dx \quad (3c)$$

$$G_0(t) \equiv 2 \int_{x_0}^{x_e} [q_1^2(x, t) - q^2(x, t)] a^2(x) dx \quad (3d)$$

$$G_1(t) \equiv 2 \int_{x_0}^{x_e} [q_1^2(x, t) - q^2(x, t)] a^2(x)x dx$$

$$G_2(t) \equiv 2 \int_{x_0}^{x_e} [q_1^2(x, t) - q^2(x, t)] a^2(x)x^2 dx \quad (3e)$$

This transformation helps to express the dynamic equations in a form convenient for further discussion of the body trajectory features. When Eqs. (3a–3e) are used, the trajectory equations (2a) can be integrated once and expressed in the form

$$\frac{dY_c}{dt} = -\frac{b_{22}(t)}{\Delta(t)} c_g t + \frac{\Delta_1(t)}{\Delta(t)} V_0 + c_l \pi \omega_0 b_1(t) \quad (4a)$$

$$\frac{d\alpha}{dt} = \frac{b_{21}(t)}{\Delta(t)} c_g t + \frac{\Delta_2(t)}{\Delta(t)} \omega_0 + c_m \pi V_0 b_2(t) \quad (4b)$$

where the coefficients are defined as

$$b_{11}(t) \equiv 1 + c_l \alpha_{11}(t), \quad b_{12}(t) \equiv c_l \alpha_{12}(t)$$

$$b_{21}(t) \equiv c_m \alpha_{12}(t), \quad b_{22}(t) \equiv 1 - c_m \alpha_{22}(t)$$

$$\Delta \equiv b_{11}(t)b_{22}(t) + b_{12}(t)b_{21}(t)$$

$$\Delta_1 \equiv b_{11}(0)b_{22}(t) + b_{12}(t)b_{21}(0)$$

$$\Delta_2 \equiv b_{11}(t)b_{22}(0) + b_{12}(0)b_{21}(t)$$

$$b_1 \equiv (1/\Delta)[(1 - c_m \pi g_2)[G_1(t) - G_1(0)] + c_m \pi g_1[G_2(t) - G_2(0)]$$

$$+ c_m \pi [G_1(0)G_2(t) - G_1(t)G_2(0)]$$

$$b_2 \equiv (1/\Delta)[(1 + c_l \pi g_0)[G_1(0) - G_1(t)] + c_l \pi g_1[G_0(t) - G_0(0)]$$

$$+ c_l \pi [G_1(0)G_0(t) - G_1(t)G_0(0)]$$

The first term of Eqs. (4a–4b) models the gravity effect, the second term comes from the initial conditions, and the third term arises from the boundary and initial conditions. The angular acceleration is proportional to the product of the pitching moment coefficient c_m , the gravity force coefficient c_g , and the value $g_1 + G_1(t)$ characterizing the displacement of the center of pressure from the c.g.⁸ Equations (4) can be solved numerically using, for example, the Runge–Kutta method. Note that the slip-surface effect and the top-wall effect rapidly decrease as the body moves away from these boundaries. Neglecting terms of the order of $O(q^2 + q_1^2)$, which are associated with the boundary effects, the solution of Eqs. (4) can be expressed in explicit analytical form:

$$Y_c(t) = Y_0 + V_0 t - \frac{1 - \pi c_m g_2}{2\Delta_0} c_g t^2$$

$$\alpha(t) = \alpha_0 + \omega_0 t + \frac{\pi g_1 c_m c_g t^2}{2\Delta_0} \quad (5a)$$

$$\Delta_0 = (1 + c_l \pi g_0)(1 - c_m \pi g_2) + c_l c_m \pi^2 g_1^2 \quad (5b)$$

Equations (5) show that the c.g. coordinate $Y_c(t)$ and the pitch angle $\alpha(t)$ are parabolic functions of time when the body moves in an unbounded fluid at rest.

It is also possible to obtain analytical solutions of Eqs. (4), when the lift and moment are small compared to the body weight. This is typical for many practical cases because the coefficients c_l and c_m are proportional to the air density to body density ratio, $\rho_\infty/\rho_b \ll 1$. For a body of uniform density, nondimensional ballistic parameters may be defined as

$$c_l = \frac{\rho_\infty}{\rho_b \pi g_0}, \quad c_m = \frac{\rho_\infty}{\rho_b \pi g_2}, \quad \frac{c_l}{c_m} = \frac{g_2}{g_0} \quad (6)$$

For the experimental conditions,⁷ the coefficients c_l and c_m as well as other basic parameters are shown in Tables 1 and 2, where the gravity force coefficient is calculated at the freestream speed $U_\infty = 77.1$ m/s.

If terms linear in c_l and c_m are retained in Eqs. (4), the approximate linear and angular trajectories are

$$Y_c = Y_0 + V_0 t - 0.5(1 - \pi c_l g_0) c_g t^2$$

$$\alpha = \alpha_0 + \omega_0 t + 0.5 \pi g_1 c_m c_g t^2 \quad (7)$$

The c.g. coordinate and the pitch angle are parabolic functions of time. In the first-order approximation, the vertical motion corresponds to a pure gravity drop. The lift force gives a small negative correction of the c.g. acceleration similar to the case of a plunging cylinder in the presence of a shear layer considered in Ref. 4. As will be shown, the analytical expressions (7) are consistent with trends of numerical solutions and experimental data.

Table 1 Physical parameters of models⁷

Model	δ	X_c	g_0	g_1	g_2
B1N1	0.31250E-01	0.51333E+00	0.86206E+00	0.68807E-01	0.66707E-01
B4N2	0.31250E-01	0.49500E+00	0.86206E+00	0.53002E-01	0.57596E-01
B5N5	0.32609E-01	0.62261E+00	0.85606E+00	0.16423E+00	0.12753E+00

Table 2 Aerodynamic and gravity acceleration coefficients for models⁷

Model	c_l	c_m	$c_g U_\infty^2$	c_g
B1N1	0.29915E-03	0.22204E-02	0.95585E+02	0.16080E-01
B4N2	0.72519E-03	0.38857E-02	0.95585E+02	0.16080E-01
B5N5	0.36773E-02	0.24684E-01	0.87786E+02	0.14768E-01

Phase 3: Body Outside Cavity

If the body is totally outside the cavity and moves into an external freestream, the lift force and pitching moment are again expressed as integrals along the body axis with the integrands being a power series with respect to the parameter $q = 0.5a/H$ (see Ref. 5). When these analytical solutions are analyzed the slip-surface effect on the body trajectory is obtained to be proportional to the quantity

$$\int_{x_0}^{x_e} q a^2 a_x dx + \int_{x_0}^{x_e} q^2 a^2 dx \sim \frac{\bar{q}}{3} + \bar{q}^2 g_0 + \mathcal{O}(\bar{q}^3 g_0) \quad (8)$$

where the over bars denote averaging along the body axis. For typical cases, the body shape factor is given by Eq. (3c), $g_0 = \mathcal{O}(1)$. The average distance parameter is $\bar{q} \leq 0.5$. Its maximum value $\bar{q} = 0.5$ corresponds to contact of the body surface with the slip surface. The maximum values of the first and second terms in Eq. (8) are $\frac{1}{6}$ and $\frac{1}{4}$, respectively. As the body drops, both terms decrease quickly, and the slip-surface effect vanishes. Thus, dominant terms are associated with the body drop in an unbounded uniform stream. In this case, the equations for the lift force and pitch moment can be reduced to

$$L = \pi \left[-g_0 \frac{dV_c}{dt} + g_1 \frac{d\omega}{dt} - (V_c - \alpha) a_e^2 + \omega (g_0 + x_e a_e^2) \right] \quad (9a)$$

$$M = \pi \left[-g_1 \frac{dV_c}{dt} + g_2 \frac{d\omega}{dt} + (V_c - \alpha) (g_0 - x_e a_e^2) + \omega x_e^2 a_e^2 \right] \quad (9b)$$

where $a_e = a(x_e)$ is the base radius ($a_e = 1$ for a cylindrical afterbody). These expressions were derived for bodies with a sharp nose, $a(x_0) = 0$. Substitution of Eqs. (9a) and (9b) into the trajectory equations (2a) and integration once give the linear ordinary differential equation (ODE) system (with constant coefficients)

$$\begin{aligned} \frac{dV_c}{dt} &= c_{11}(V_c - \alpha) + c_{12}\omega - c_{10} \\ \frac{d\omega}{dt} &= c_{21}(V_c - \alpha) + c_{22}\omega + c_{20} \end{aligned} \quad (10a)$$

$$c_{10} = \frac{1 - c_m \pi g_2}{\Delta_0} c_g, \quad c_{20} = \frac{c_m c_g \pi g_1}{\Delta_0}$$

$$c_{11} = \frac{c_l \pi}{\Delta_0} [c_m \pi g_1 (g_0 - x_e a_e^2) - (1 - c_m \pi g_2) a_e^2] \quad (10b)$$

$$c_{12} = \frac{c_l \pi}{\Delta_0} [(1 - c_m \pi g_2) (g_0 + x_e a_e^2) + c_m \pi g_1 x_e^2 a_e^2] \quad (10c)$$

$$c_{21} = \frac{c_l \pi}{\Delta_0} [(1 + c_l \pi g_0) (g_0 - x_e a_e^2) + c_l \pi g_1 a_e^2] \quad (10d)$$

$$c_{22} = \frac{c_m \pi}{\Delta_0} [(1 + c_l \pi g_0) x_e^2 a_e^2 - c_l \pi g_1 (g_0 + x_e a_e^2)] \quad (10e)$$

where Δ_0 is given by Eq. (5b).

We consider the Cauchy problem for Eqs. (10a) assuming that the body is totally outside the cavity for $t \geq t_0$, and its initial speeds, coordinate, and pitch angle are

$$V_c(t_0) = V'_0, \quad \omega(t_0) = \omega'_0, \quad Y_c(t_0) = Y'_0, \quad \alpha(t_0) = \alpha'_0 \quad (11)$$

From Eqs. (10a), the angular velocity ω and the function $W(t) = V_c(t) - \alpha(t)$ are solutions of the decoupled equations

$$\frac{d^2 W}{dt^2} - 2\gamma \frac{dW}{dt} + \kappa W + c_1 = 0, \quad \frac{d^2 \omega}{dt^2} - 2\gamma \frac{d\omega}{dt} + \kappa \omega + c_2 = 0 \quad (12)$$

where the constant coefficients are

$$\begin{aligned} \gamma &= \frac{c_m \pi a_e^2}{2\Delta_0} \left[x_e^2 - \frac{c_l}{c_m} + \pi c_l (x_e^2 g_0 - 2x_e g_1 + g_2) \right] \\ \kappa &= \frac{c_m \pi}{\Delta_0} [g_0 - a_e^2 x_e - c_l \pi a_e^2 (g_0 x_e - g_1)] \end{aligned} \quad (13a)$$

$$c_1 = \frac{c_m c_g \pi}{\Delta_0} (g_1 - x_e^2 a_e^2), \quad c_2 = \frac{c_m c_g \pi}{\Delta_0} (g_0 - x_e a_e^2) \quad (13b)$$

The characteristic (secular) equation for the eigenvalues of ODE system (10a) and its solutions are

$$\begin{aligned} \lambda^2 - 2\gamma\lambda + \kappa &= 0, & \lambda_1 &= \gamma + i\Omega \\ \lambda_2 &= \gamma - i\Omega, & \Omega &= \sqrt{\kappa - \gamma^2} \end{aligned} \quad (14)$$

Various cases significant for the trajectory stability will now be discussed.

Eigenvalues λ_1 and λ_2 Are Complex

If λ_1 and λ_2 are complex, then the trajectory parameters are expressed in the form

$$\begin{aligned} V_c(t) &= V'_0 + (d - c_2 \tau)/\kappa + e^{\gamma \tau} (A_1 \cos \Omega \tau + A_2 \sin \Omega \tau) \\ \omega &= -(c_2/\kappa) + e^{\gamma \tau} (B_1 \cos \Omega \tau + B_2 \sin \Omega \tau) \end{aligned} \quad (15a)$$

$$\begin{aligned} Y_c(t) &= Y'_0 + (V'_0 + d/\kappa)\tau - (c_2/2\kappa)\tau^2 + (e^{\gamma \tau}/\kappa) \\ &\times [(\gamma A_1 - \Omega A_2) \cos \Omega \tau + (\Omega A_1 + \gamma A_2) \sin \Omega \tau] \end{aligned} \quad (15b)$$

$$\begin{aligned} \alpha(t) &= \alpha'_0 - (1/\kappa) \{ c_2 \tau + \gamma B_1 - \Omega B_2 - e^{\gamma \tau} [(\gamma B_1 - \Omega B_2) \cos \Omega \tau \\ &+ (\Omega B_1 + \gamma B_2) \sin \Omega \tau] \} \end{aligned} \quad (15c)$$

where $\tau = t - t_0$ and $d = -\kappa(V'_0 - \alpha'_0) - c_1 - \gamma B_1 + \Omega B_2$. The coefficients A_1 , A_2 , B_1 , and B_2 are determined from the initial conditions (11) and Eqs. (10a). They are expressed as

$$\begin{aligned} A_1 &= -\frac{d}{\kappa}, & A_2 &= \frac{c_2}{\Omega \kappa} + \frac{\dot{V}_0 - \gamma A_1}{\Omega} \\ \dot{V}_0 &= \frac{dV(0)}{dt} = c_{11}(V'_0 - \alpha'_0) + c_{12}\omega'_0 - c_{10} \end{aligned} \quad (16a)$$

$$\begin{aligned} B_1 &= \omega'_0 + \frac{c_2}{\kappa}, & B_2 &= \frac{\dot{\omega}_0 - \gamma B_1}{\Omega} \\ \dot{\omega}_0 &= \frac{d\omega(0)}{dt} = c_{21}(V'_0 - \alpha'_0) + c_{22}\omega'_0 + c_{20} \end{aligned} \quad (16b)$$

Equations (15) indicate that the body motion includes two components. The first terms of Eqs. (15a) and (15b) correspond to body rotation with the constant angular speed $-c_2/\kappa$ and a vertical translation with uniform acceleration $-c_2/\kappa$. Also present is a drift with constant velocity $\alpha'_0 - (c_1 + 2\gamma B_1 - \dot{\omega}_0)/\kappa$ that depends on the initial angle of attack and angular velocity. These terms are associated with a nonoscillatory motion, which is called the mean state. The second component corresponds to periodic modulations of the mean state. These oscillations are neutral for $\gamma = 0$, unstable for positive γ , and stable for negative γ . For zero base radius $a_e = 0$, Eq. (13) specializes to

$$\begin{aligned} \gamma &= 0, & \kappa &= \Omega^2 = (c_m \pi / \Delta_0) g_0, & b_1 &= (c_m c_g \pi / \Delta_0) g_1 \\ & & & & b_2 &= (c_m c_g \pi / \Delta_0) g_0 \end{aligned}$$

This case corresponds to neutral oscillations. For heavy bodies with base radius $a_e = 1$ and small ballistic coefficients $c_l \ll 1$ and $c_m \ll 1$, we can linearize about c_l and c_m . Equations (13) yield

$$\gamma = \pi c_m (x_e^2 - c_l / c_m), \quad \kappa = \Omega^2 = c_m \pi (g_0 - x_e) \quad (17a)$$

$$\begin{aligned} c_1 &= \pi c_m c_g (g_1 - x_e^2), & c_2 &= \pi c_m c_g (g_0 - x_e) \\ d &= \pi c_l (\omega_0 + c_g) \end{aligned} \quad (17b)$$

Equations (17) show that oscillations are unstable for $x_2^2 > c_1/c_m$. This case fits the experimental conditions of Ref. 7. For $x_2^2 \leq c_1/c_m$, oscillations are stable or neutral. In all cases the increment is small, $\gamma \sim c_m \sim \Omega^2 \ll 1$.

The expressions for the vertical speed and angular velocity are

$$V_c = V_0' - c_2 \tau + A_1(e^{\gamma \tau} \cos \Omega \tau - 1) + A_2 e^{\gamma \tau} \sin \Omega \tau$$

$$\omega = -c_2 + e^{\gamma \tau} (B_1 \cos \Omega \tau + B_2 \sin \Omega \tau)$$

The first equation indicates that the c.g. oscillates near its mean state associated with free drop. If the body dynamics is stable, $\gamma < 0$, then the oscillations vanish as $\tau \rightarrow \infty$. Nevertheless, they induce the constant vertical velocity $-A_1 = c_1 \pi (\omega_0 + c_2) / \Omega^2$. The second equation shows that the angular velocity oscillates near its mean level, $\bar{\omega} = -c_2$, associated with free drop.

Eigenvalues λ_1 and λ_2 Are Real

If $\lambda_1 = \gamma + \nu$ and $\lambda_2 = \gamma - \nu$ [$\nu = \sqrt{(\gamma^2 - \kappa)}$] are real, then the solution of Eqs. (10a) or Eqs. (12) is

$$V_c(t) = V_0' + (d - c_2 \tau) / \kappa + e^{\gamma \tau} (A_1 \cosh \nu \tau + A_2 \sinh \nu \tau)$$

$$\omega = -(c_2 / \kappa) + e^{\gamma \tau} (B_1 \cosh \nu \tau + B_2 \sinh \nu \tau) \quad (18a)$$

$$Y_c(t) = Y_0' + (V_0' + d / \kappa) \tau - (c_2 / 2 \kappa) \tau^2 + (e^{\gamma \tau} / \kappa) [(\gamma A_1 - \nu A_2) \cosh \nu \tau + (\gamma A_2 - \nu A_1) \sinh \nu \tau] \quad (18b)$$

$$\alpha(t) = \alpha_0' - (1 / \kappa) \{ c_2 \tau + \gamma B_1 - \nu B_2 - e^{\gamma \tau} [(\gamma B_1 - \nu B_2) \cosh \nu \tau + (\gamma B_2 - \nu B_1) \sinh \nu \tau] \} \quad (18c)$$

where $d = -\kappa(V_0' - \alpha_0') - c_1 - \gamma B_1 + \nu B_2$ and the coefficients are

$$\begin{aligned} A_1 &= -(d / \kappa), & A_2 &= c_2 / \nu \kappa + (\dot{V}_0 - \gamma A_1) / \nu \\ B_1 &= \omega_0' + c_2 / \kappa, & B_2 &= (\dot{\omega}_0 - \gamma B_1) / \nu \end{aligned} \quad (19)$$

Again the body motion has two components. The first component is similar to the earlier case. It is associated with a pure gravity drop and can be treated as a basic state. The second component is relevant to an exponential drift from or toward the basic state depending on the signs of the eigenvalues. If $\lambda_1 < 0$ and $\lambda_2 < 0$, then the exponents decay as $\tau \rightarrow \infty$, and the body motion evolves from the initial conditions to the basic state, which includes rotation with constant angular velocity and translation with constant acceleration. If λ_1 and/or λ_2 are positive, then the exponential terms grow with time, and the body departs from its basic state (aperiodic divergence). If $\nu = 0$, then the second component of the body motion is governed by the sign of γ .

The aforementioned analytical solutions and stability characteristics of the body dynamics can be used for fast qualitative estimations of the body trajectory outside the cavity. To our knowledge, these results are new.

Results and Discussion

To calculate the body trajectory including all phases of the separation process Eqs. (2a) are numerically integrated using a fourth-order Runge-Kutta scheme (see Ref. 9). Our computational code includes a module that calculates the lift force and pitching moment for phases 1-3 using the analytical results of Ref. 5. The accuracy of the predictions can be related to the size of the perturbation parameters and uncertainties in the experimental launch conditions. (Because these data are referenced, their accuracy can be obtained from the authors.) In the best cases, the accuracy can be as good as a few percent when the aerodynamic forces are small compared to the weight and the characteristic pitch inertia with experimental initial conditions that matched those assumed in the theory. Large excursions can result if large-scale shear layer motions occur and other disturbances evolve in the external flow.

The combined asymptotic and numerical method described provides a means to calculate rapidly body trajectories. One trajectory is normally predicted in less than $\frac{1}{2}$ min using a personal computer Pentium 166. This quick-turnaround personal-computer-oriented tool

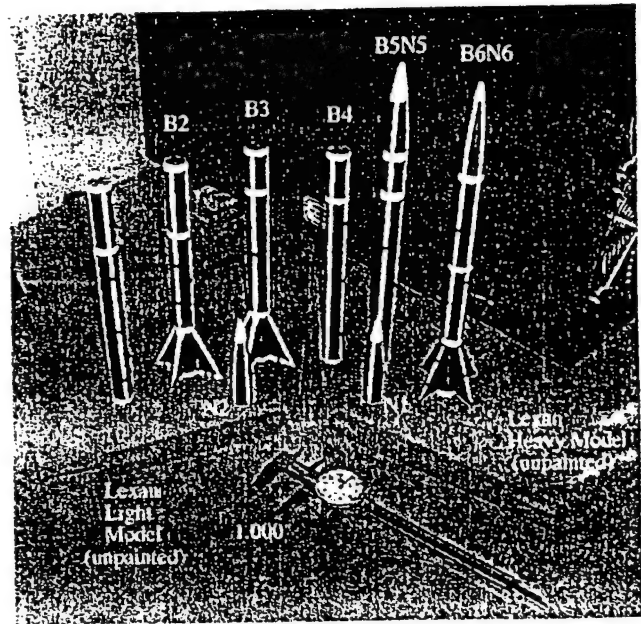


Fig. 2 Models for free-drop tests in the IIT wind tunnel.

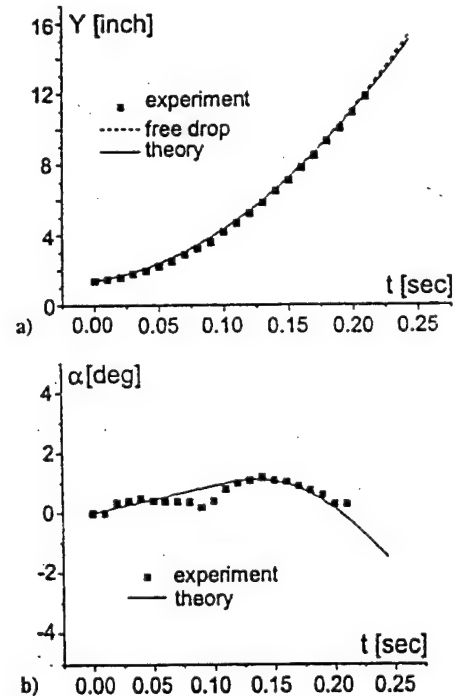


Fig. 3 Model B4N2, $U_\infty = 62.3$ m/s, $Y_0 = 1.42$ in., $\alpha_0 = 0$ deg, $V_0 = 8$ in/s, and $\omega_0 = 9$ deg/s.

will be compared to the subsonic experimental data⁷ in what follows.

Experimental Data

Drop tests⁷ were conducted in National Diagnostic Wind Tunnel of the Illinois Institute of Technology (IIT) Fluid Dynamics Research Center at the Mach number range $0.12 < M < 0.23$. The rectangular cavity 20 in. long, 41 in. wide, and 4 in. high was mounted on the top wall of the wind-tunnel test section. The models are bodies of revolution of radius $\bar{a}_0 = \frac{3}{8}$ in. and nose length $\bar{x}_n = 3.56$ in. (see Fig. 2). Two models (B1N1 and B4N2) are ogive cylinders 12 in. long. The third model (B5N5) has an elliptic nose and a total length of 11.5 in. The heaviest model, B1N1, has mass $m = 111.85$ g, moment of inertia $I = 0.0014$ kg \cdot m², and c.g. location $\bar{x}_0 = 6.16$ in. For model B4N2, $m = 46.14$ g, $I = 0.0008$ kg \cdot m², and $\bar{x}_0 = 5.94$ in. The lightest model, B5N5, has $m = 8.72$ g and $I = 0.000015$ kg \cdot m². In these experiments, bodies were dropped from a cavity in the IIT wind tunnel.

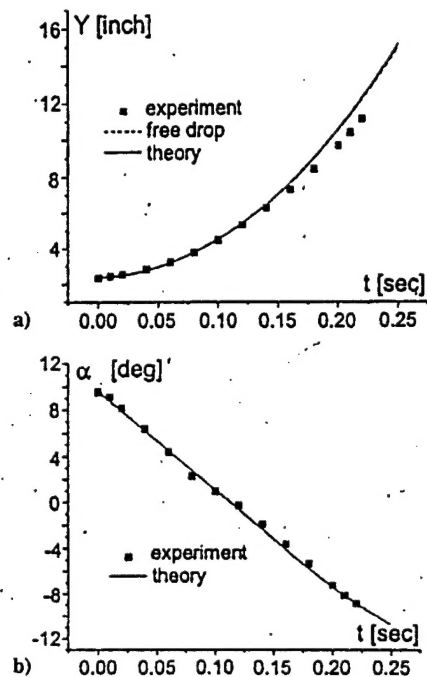


Fig. 4 Model B4N2, $U_\infty = 41.3$ m/s, $Y_0 = 2.4$ in., $\alpha_0 = 9.6$ deg, $V_0 = 2$ in/s, and $\omega_0 = -80$ deg/s.

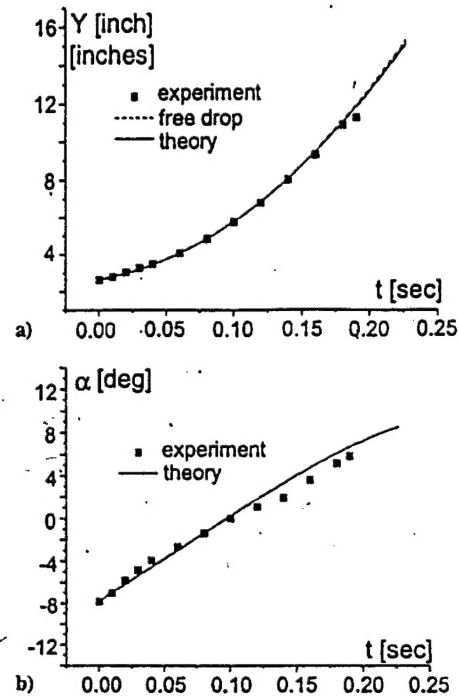


Fig. 6 Model B1N1, $U_\infty = 40.8$ m/s, $Y_0 = 2.65$ in., $\alpha_0 = -7.8$ deg, $V_0 = 15$ in/s, and $\omega_0 = 80$ deg/s.

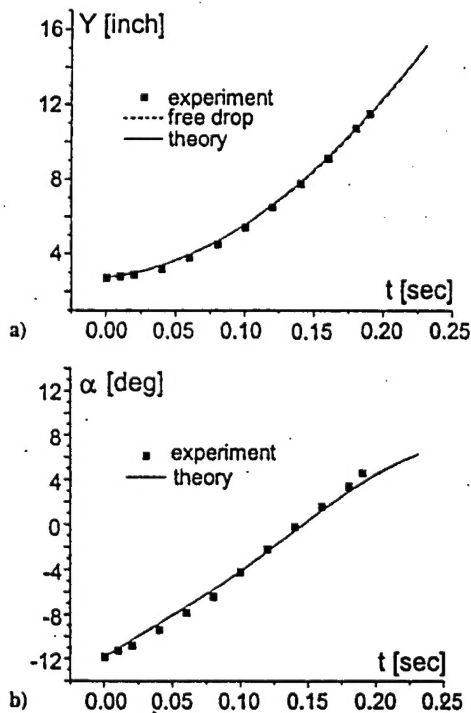


Fig. 5 Model B1N1, $U_\infty = 62.7$ m/s, $Y_0 = 2.72$ in/s, $\alpha_0 = -11.8$ deg, $V_0 = 9$ in/s, and $\omega_0 = 75$ deg/s.

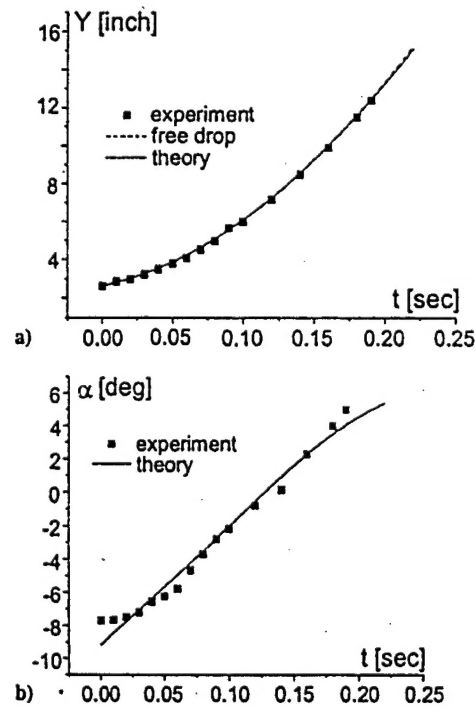


Fig. 7 Model B4N2, $U_\infty = 40.6$ m/s, $Y_0 = 2.65$ in., $\alpha_0 = -9.2$ deg, $V_0 = 15$ in/s, and $\omega_0 = 70.8$ deg/s.

The models were released by withdrawing pins, holding them at their noses and tails.

Comparison with Experiment

Preliminary analysis of the experimental data shows that during the release time $t_r \approx 0.03$ s, the initial angular and vertical velocities can be essentially affected by uncontrolled disturbances that may be induced by the release mechanism. During the release time, the gravity force may increase the pitch rate, if the model ends are not released simultaneously. This motivated identification of the actual initial angular speed $\hat{\omega}_0$ and vertical velocity V_0 by differentiating the experimental distributions of the pitch angle $\hat{\alpha}(\hat{t})$ and the c.g. vertical coordinate $\hat{Y}_c(\hat{t})$.

Figures 3a–10a show comparisons between predicted (solid lines) and experimental (symbols) c.g. trajectories for all three models. Dashed lines indicate the free-drop trajectories under the gravity force only. As already noted, the lift is small compared to the body weight. Figure 3 shows that the free drop in a vacuum is very close to the computational results and the experimental data for moderate angles of attack, especially for the heavier model, B1N1. However, the vacuum curve diverges from the experimental data if the body enters into the external stream at relatively large $\hat{\alpha}$. This is clearly seen in Figs. 4a, 8a, and 10a. In these cases, the theoretical prediction accounting for aerodynamic loads is in a good agreement with the experiment. Moreover, the theoretical model is capable of capturing trajectory nuances shown in Fig. 8a.

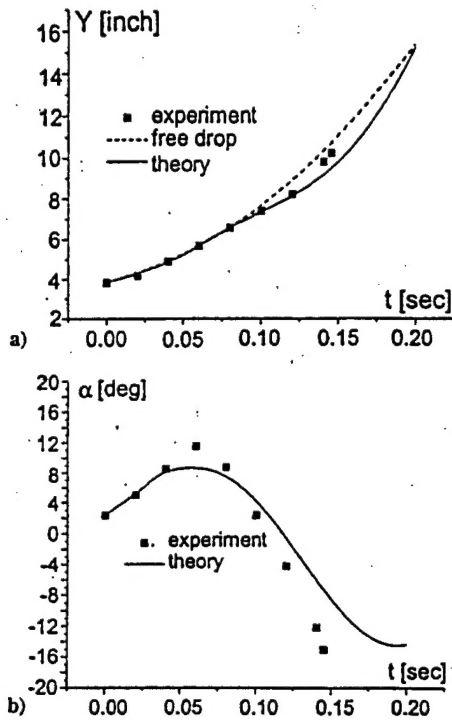


Fig. 8 Model B5N5, $U_\infty = 62.5$ m/s, $Y_0 = 3.85$ in., $\alpha_0 = 2.4$ deg, $V_0 = 19$ in/s, and $\omega_0 = 140$ deg/s.

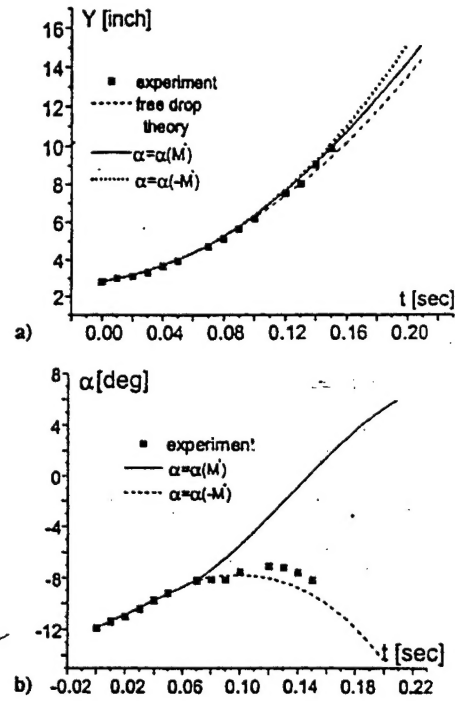


Fig. 10 Model B4N2, $U_\infty = 62.1$ m/s, $Y_0 = 2.8$ in., $\alpha_0 = -11.9$ deg, $V_0 = 15$ in/s, and $\omega_0 = 52.86$ deg/s.

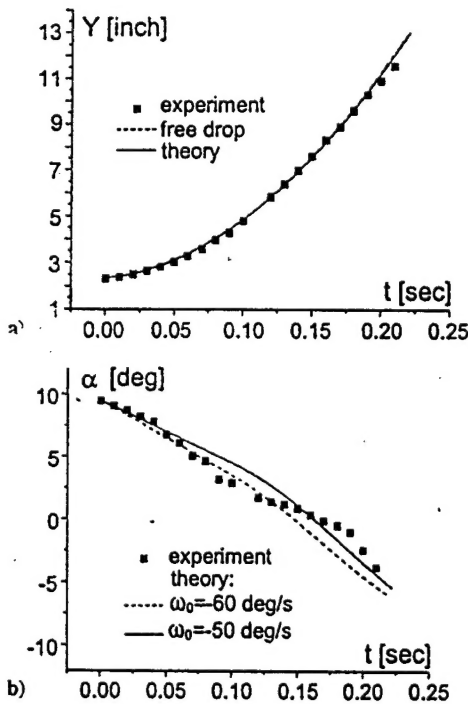


Fig. 9 Model B4N2, $U_\infty = 62.3$ m/s, $Y_0 = 2.33$ in., $\alpha_0 = 9.5$ deg, and $V_0 = 6$ in/s.

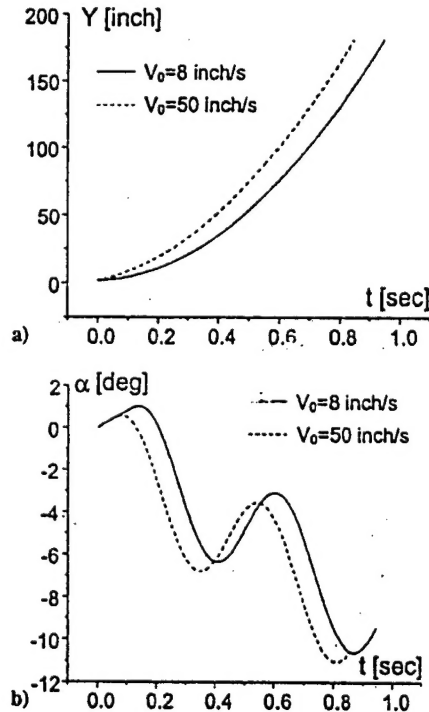


Fig. 11 Effects of initial vertical velocity: model B4N2, $U_\infty = 62.3$ m/s, $Y_0 = 1.42$ in., $\alpha_0 = 0$ deg, and $\omega_0 = 8$ deg/s.

Figures 3b–10b show a comparison between predicted (lines) and experimental (symbols) histories of the angle of attack $\hat{\alpha}(t)$. Figures 3b–6b show good agreement between the theory and the experiment. The agreement is only satisfactory for the cases shown in Figs. 7b–9b. Rough estimates indicate that the initial growth of $\hat{\alpha}$ (see Fig. 7b) may be associated with an initial pitch impulse generated by the release mechanism under a gravitational couple from the pins. In this case, both the initial angle of attack and angular speed were estimated from the experimental data. These were used as the initial conditions for the calculations. For the lightest model, B5N5 (see Fig. 8b), the discrepancy seems to be due to the difference between the actual nose shape (elliptic) and the shape used in our

calculations (parabolic ogive). Unfortunately, calculations were not possible for the actual nose because its geometry was not available. Note that the nose shape becomes more important at large pitch angles. The divergence of the predicted and experimental curves in Fig. 9b seems to be due to the flow inside the cavity, which is presently not included in our modeling. Namely, the nonuniform upwash field due to the recirculatory flow in the cavity has not been included. Such an upwash field will change the crossflow angle of attack from that due solely to the vertical speed of the body, which has been accounted for in the approximate model described here. This can be thought of as a first estimate of the flow physics. The effect of the upwash field can be considered a refinement of this

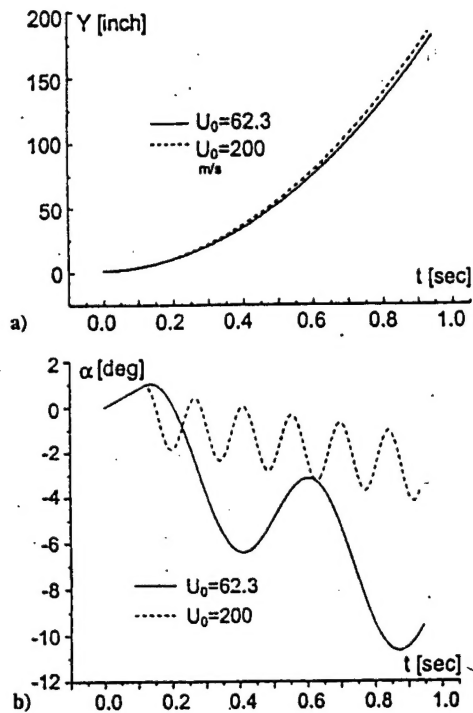


Fig. 12 Effect of freestream velocity on the body trajectory: model B4N2, $Y_0 = 1.42$ in., $\alpha_0 = 0$ deg, $V_0 = 8$ in./s, and $\omega_0 = 8$ deg/s.

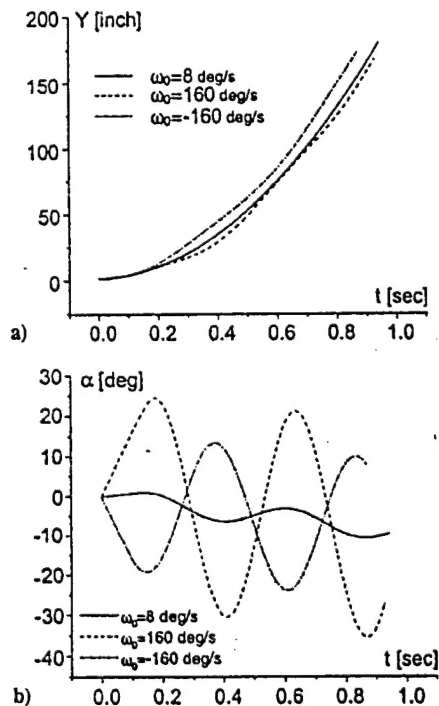


Fig. 13 Influence of the initial angular speed on the body trajectory: model B4N2, $U_\infty = 62.3$ m/s, $Y_0 = 1.42$ in., $\alpha_0 = 0$ deg, and $V_0 = 8$ in./s.

model in which this recirculatory flow can be estimated from the empty cavity flow. An inviscid approximation for the latter is given in Ref. 4 for deep cavities. (Deep cavities are almost bridged at their top end by the shear layer in contrast to shallow cavities for which the shear layer will collide with their bottom.) Further refinements would include the interaction of the moving body with this nonuniform flow for both deep and shallow cavities. Pitch oscillations observed in phase 1 (body is totally inside the cavity) clearly indicate the presence of this effect, which may also explain the substantial difference between the theory and the experiment shown in Fig. 10b.

As indicated earlier, the pitch behavior in phase 3 (body is outside the cavity) strongly depends on the entry condition, which is a

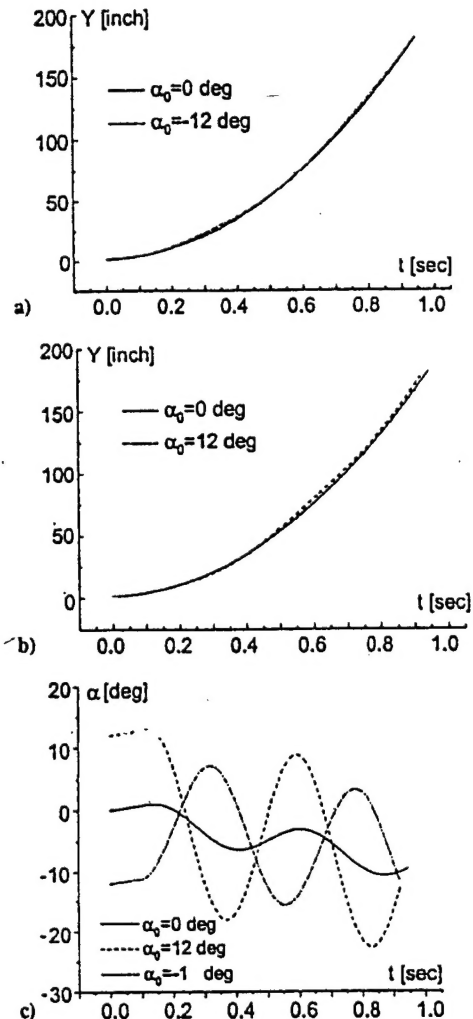


Fig. 14 Influence of the initial pitch angle on the body trajectory: model B4N2, $U_\infty = 62.3$ m/s, $Y_0 = 1.42$ in., $V_0 = 8$ in./s, and $\omega_0 = 8$ deg/s.

function of the angular velocity, vertical speed, and their derivatives. For the case shown in Fig. 10b, the shear layer displacement from its basic state into the cavity may cause a phase jump of the right-hand-side term in Eq. (2a) from 0 to 180 deg. Such a jump affects the pitch history outside the cavity. This is illustrated in Fig. 10b by the dotted line that was calculated with the opposite sign of the pitching moment. It is seen that this curve is in a good agreement with the experimental data. On the other hand, experimental curves, shown in Figs. 5b, 6b, and 7b for approximately the same initial conditions, have a regular behavior, that is, they are in a good agreement with the computations performed without changes of the sign of pitching moment. These findings suggest that there is a bifurcation in the pitch history $\alpha(t)$ when the body enters into the external stream. The trajectory equations allow such a bifurcation because the aerodynamic forcing terms of Eqs. (2a) are nonlinear (quadratic) functions of speeds V and ω . One of two possible trajectories is selected when the body crosses the shear layer. Therefore, phase 2 serves as a trigger of the pitch bifurcation. Accurate modeling of this mechanism is important for prediction of the pitch history and store trajectory in the next phase, when the store is outside the cavity. To verify this hypothesis additional theoretical, numerical, and experimental studies are needed.

Parametric Studies

Parametric studies of the body trajectory were conducted for different initial conditions, body parameters, and freestream speeds. The results are shown in Figs. 11–15. Variations of the initial vertical velocity cause not only c.g. acceleration but phase shift of the pitch angle (see Fig. 11). In accord with the analytical solution discussed earlier, an increase of the freestream velocity leads to a substantial increase of the mean pitching angle and the pitch oscillation

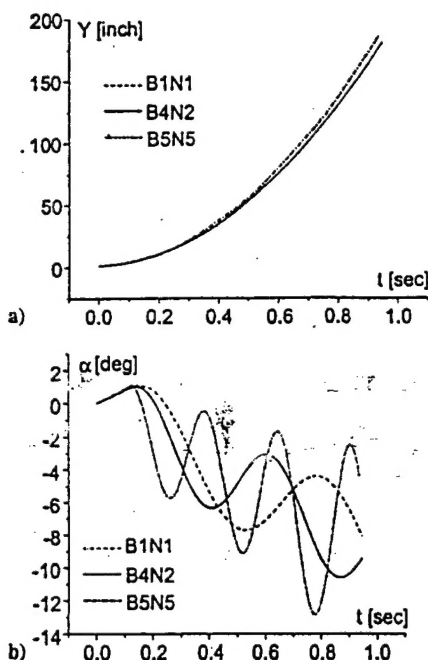


Fig. 15 Trajectories of different models: $U_\infty = 62.3$ m/s, $Y_0 = 1.42$ in., $\alpha_0 = 0$ deg, $V_0 = 8$ in/s, and $\omega_0 = 8$ deg/s.

frequency (see Fig. 12), while the c.g. trajectory is changed slightly. Figure 13 shows that the pitch oscillation amplitude increases and the phase shift occurs as the initial angular speed increases. Amplification of the pitch oscillations is stronger in the case of positive ω_0 with the c.g. trajectory also noticeably affected. The effect of the initial pitch angle is similar to the effect of ω_0 (compare Figs. 14 and 15). However, the variation of the c.g. trajectory in this case is smaller.

Trajectory dependencies on the body shape are shown in Fig. 15. The calculations were performed for three experimental models of Ref. 7 under the same initial conditions. As expected, the highest amplitude and frequency of the body oscillations correspond to the lightest model, B5N5. It is also seen that the body trajectories outside the cavity are consistent with the analytical solution discussed earlier.

Conclusions

This paper discussed modeling of 2-DOF vertical and pitching motions of thin bodies of revolution separating from a rectangular cavity into an external freestream. The problem is analyzed using combined asymptotic and numerical methods. The body dynamic equations include aerodynamic forces and moments, which are predicted using approximate analytical solutions obtained in our previous studies within the framework of the slender body theory. Different phases of the separation process were analyzed using small perturbation theories. This leads to simplifications of the trajectory equations and their integration in closed form for different typical cases associated with phase 1 (body is inside the cavity) and phase 3 (body is outside the cavity). These analytical solutions provide explicit dependencies of the body trajectory on the flow and body characteristics, which allows identification of the critical parameters and insight gained into the physics of the separation process.

The numerical code predicting the trajectories for all three phases of store separation was validated by comparison with the experiment. For a major portion of the data, the calculations are in a good

agreement with experiment. Moreover, the theory is able to capture nuances of the body pitching observed experimentally. These results confirm our theoretical model. However, there are cases when the agreement is only satisfactory. The body separation is affected by more complex flow phenomena, which are not captured by our model. One discrepancy seems to be due to the slip-surface displacement induced by the shear layer instability and/or self-excited oscillations of the cavity flow. These effects can lead to the pitching moment phase jump from 0 to 180 deg during phase 2, when the body crosses the shear layer. The jump may trigger quick transition from one pitch angle trajectory to another for phase 3, when the body is outside the cavity. Our calculations showed that this interpretation is consistent with the experimental data indicating the existence of two substantially different pitching trajectories for approximately the same initial conditions. Because nonlinear dynamic equations are involved, the body trajectory may have a bifurcation point associated with phase 2. Although this transitional phase is relatively short, its aerodynamics may determine the selection between possible trajectories outside the cavity. Further theoretical and experimental studies are needed to establish and clarify the bifurcation mechanism. Our future work will extend this model to transonic speeds.

Acknowledgments

Portions of this effort was supported by the Air Force Office of Scientific Research, Air Force Materials Command under Contract F49620-92-C-0006 and F49620-96-C-0004. The U.S. government is authorized to reproduce and distribute reprints for government purposes, notwithstanding any copyright notation thereon. The views and conclusions herein are those of the authors and should not be interpreted as necessarily representing the official policies or endorsements, either expressed, or implied of the Air Force Office of Scientific Research or the U.S. government.

References

- Goodwin, F. K., Dillenius, M. F. E., and Nielsen, J. N., "Prediction of Six-Degree-of-Freedom Store Separation Trajectories at Speeds up to the Critical Speed. V.1. Theoretical Methods and Comparison with Experiment," U.S. Air Force Flight Dynamics Lab., AFFDL-TR-72-83, 1972.
- Wood, M. E., "Application of Experimental Techniques to Store Release Problems," *Proceedings of NEAR Conference on Missile Aerodynamics*, 1988.
- Stanek, M. J., Sinha, N., Ahuja, V., and Birkbeck, R. M., "Acoustic-Compatible Active Flow Control for Optimal Weapon Separation," AIAA Paper 99-1911, 1999.
- Malmuth, N. D., Fedorov, A. V., Shalaev, V., Cole, J., Khokhlov, A., Hites, M., and Williams, D., "Problems in High Speed Flow Prediction Relevant to Control," AIAA Paper 98-2695, June 1998.
- Malmuth, N. D., Shalaev, V. I., and Fedorov, A. V., "Combined Asymptotics and Numerical Methods for Store Interactions," Final TR Contract CF49620-96-C-0004, Air Force Office of Scientific Research/NM, Oct. 1998; available from Defense Technical Information Center [online database], URL: <http://stient.dtic.mil>.
- Cole, J. D., *Perturbation Methods in Applied Mathematics*, Waltham, MA, 1968.
- Malmuth, N., Hites, M., and Williams, D., "Photographic Investigation of the Dynamics of an Ogive Model Near a Cavity at Subsonic Mach Numbers," Final Rept. Fluid Dynamics Research Center, Illinois Inst. of Technology, Chicago, IL, Jan. 1998.
- Nielsen, J. N., *Missile Aerodynamics*, McGraw-Hill, New York, 1960.
- Korn, G. A., and Korn, T. M., *Mathematical Handbook*, McGraw-Hill, New York, 1968.

P. Givi
Associate Editor